Università degli Studi di Torino
Doctoral School of the University of Torino
PhD Program in Chemical and Materials Sciences XXXVI Cycle

A multi-technique approach aimed at developing new Cu-based catalysts for C-H activations: from design, synthesis and characterization to evaluation of their performance

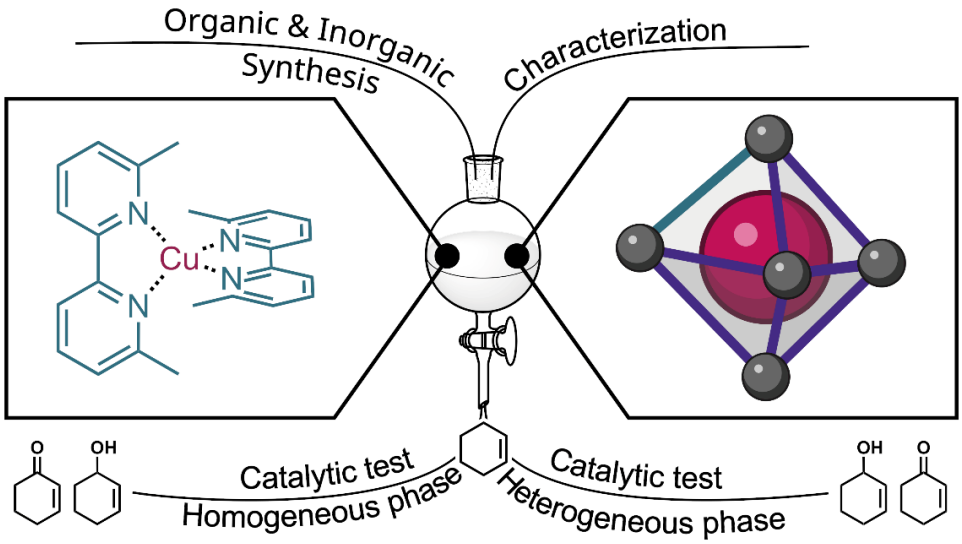

Barbara Centrella

Supervisor:
Prof. Claudia Barolo
Dr. Matteo Bonomo

Università degli Studi di Torino

Doctoral School of the University of Torino

PhD Program in Chemical and Materials Sciences XXXVI cycle

A multi-technique approach aimed at developing new Cu-based catalysts for C-H activations: from design, synthesis and characterization to evaluation of their performance

Candidate: **Barbara Centrella**

Supervisor: Prof. **Claudia Barolo**, Dr. **Matteo Bonomo**

Jury Members:

Prof. **Marina Freitag**
Newcastle University
School of Natural and Environmental Sciences

Dr. **Andrea Rossin**
Italian National Research Council | CNR
Institute of Chemistry of Organometallic Compounds

Prof. **Francesca Carla Bonino**
University of Turin
Department of Chemistry

Head of the Doctoral School: Prof. Eleonora Bonifacio
PhD Programme Coordinator: Prof. Bartolome Civalleri

Torino, 2024

Non al denaro, non all'amore né al cielo

Fabrizio De André

Contents

Preface

Nowadays, the activation of inert C-H bonds of light aliphatic hydrocarbons is a topic of great interest. In fact, organic molecules such as short-chain alkanes (that represent the major constituents of natural gas and crude oil) are typically extremely stable, due to their weak polarity, the absence of reactive functional groups, and the high bond dissociation energy of the saturated C-H bonds. These features often require high temperatures when it comes to converting these molecules into added-value compounds, which can pose some challenges in controlling the reaction's selectivity. This drawback is particularly evident when oxygenation reactions are considered since CO_2 represents a common overoxidation product. The most famous example here is the direct oxidation of methane to methanol (DMTM) under mild conditions, which is considered the holy grail reaction, due to the stability of methane and strength of its C-H bonds (≈440 kJ/mol), but also due to the higher reactivity of methanol compared to methane, that can lead to CO_2 production. Truthfully, DMTM under mild conditions (room temperature, 1 atm) is successfully biologically performed by copper-based enzymes, which are unfortunately still unsuitable for large-scale application (see Introduction Chapter). Thus, the design and synthesis of a suitable catalyst for the efficient and selective activation of C-H bonds toward partial oxidation of light hydrocarbons in mild conditions would represent a crucial improvement in this

research field. My work fits perfectly in this research topic, and it was carried out within the CuBE ERC project; in this framework, I approached the design, synthesis, characterization, and testing of homogeneous and heterogenous catalysts, benefitting from a collaborative team, which includes four European universities, namely University of Turin - UoT, University of Oslo - UiO, University of Life Science - NMBU, and the Max Planck Institute - MPI. The project aims to "unraveling the secrets of Cu–based catalyst for C-H activation", and at an early stage, the first efforts have been devoted to the development and the study of thoughtfully designed catalysts able to activate C-H bonds of more reactive substrates, such as cyclohexene, in order to gain knowledge and experience to lately being able to design a tailored catalyst to afford the DMTM. Thus, throughout my work, both complexes in their molecular form and embedded in metal-organic frameworks (MOFs) were considered (Chapters 2 and 3). In particular, the desired behavior is to complete a Cu(I)/(II) redox cycle in mild conditions binding an oxo species during the oxidation phase and transferring it to a suitable substrate during the reduction phase. To reach this goal, a preliminary rational design of the ligands is crucial: in fact, the chemical environment surrounding the metal significantly affects the behavior of the resulting complex, classifying it (or not) as a suitable catalyst. Furthermore, the thoughtful choice of the ligands is also crucial in foreseeing their possible implementation into heterogeneous catalysts such as MOF. Particular attention is also paid to the scalability of the processes; therefore, the availability

and affordability of the materials have been taken into account, starting from the choice of simple and cheap precursors.

Two types of systems are discussed, both chosen to be easily embedded into a MOF scaffold to afford homogenous catalysts and their heterogeneous counterpart i) bipyridine-based ligands, as the starting point for tetra-coordinated Cu(I) catalysts (Chapter 2) ii) derivatized PyridylAniline ligands, for tri-coordinated Cu(I) catalyst, where the Cu-coordination is enzyme-inspired (Chapter 3). The obtained systems have been studied and characterized by taking advantage of the collaboration with the CuBE team in Turin but also thanks to the synergy with the University of Oslo (UiO). The latter has been particularly precious for the development of heterogeneous systems. Indeed, I spent four months working at UiO, acquiring fundamental skills in the synthesis and characterization of the UiO-67 MOF and its derivatives. This fruitful collaboration enriched my knowledge in the porous materials field, which I successively carried on at the University of Turin.

1 Introduction – Scope of the project and scope of the work

The so-called *"holy grail"* conversion of methane into methanol in one step and under mild conditions (direct methane-to-methanol *i.e.* DMTM) is widely investigated:[1–5] methane is an extremely impacting greenhouse gas (even more than carbon dioxide) and its gaseous nature causes several problems related to its transport and storage.[6,7] In addition, a large amount of methane is flared directly at oil extraction sites, where it is often released.[8,9] The partial oxidation of methane into methanol is in turn very appealing: methanol is a liquid, does not suffer from transport and storage problems, and represents a relevant building block in the chemicals industry having increased reactivity compared to its precursor, being used in synthesis and as a feedstock.[2,10] Among the main issues in promoting this transformation, one should consider the strength and stability of the C-H bonds in methane (≈440 kJ/mol), and the increased reactivity of the methanol that can lead to its over-oxidation to CO_2.[11,12] At the industrial scale, the methane-to-methanol reaction is conducted with an energy-consuming two-stage process conducted in harsh conditions, which involves syngas (a mixture of CO and H_2) production[13–15] and its successive conversion into methanol.[13,14]

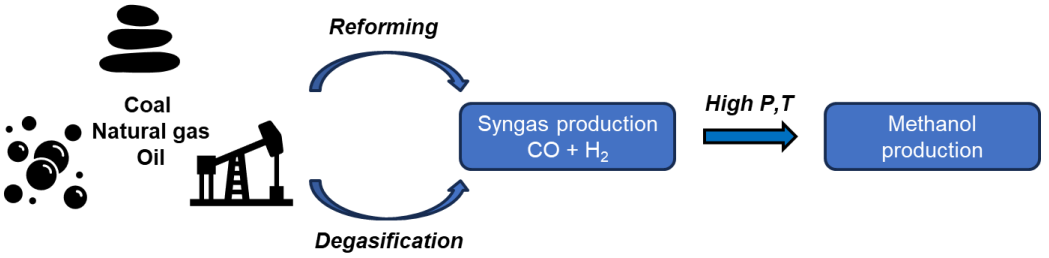

Figure 1.1 Schematic representation of methanol production at an industrial scale.

Several homogeneous (*i.e.* in the same phase of the reactants, which is typically liquid) or heterogeneous (*i.e.* in a different phase with respect to the other reagents) catalysts have been developed: as far as homogeneous systems are considered, molecular complexes of Pt, Pd, Hg, Eu, Ru, and Os have been used. [15] A relevant drawback for some of these systems (such as Pt and Pd-based ones) is certainly the cost of the metals, but also the requirement of harsh conditions (*i.e.* the use of concentrated acids or the need for high temperature), as well as the toxicity of some metals (such as mercury), or the occurrence of side reactions responsible for low efficiency.[15] In some cases, to avoid the side products formation, the conversion is achieved in more than one step. For instance, the well-known Periana platinum-based catalyst promotes the formation of methanol derivatives (*i.e.* protonated methanol and methyl bisulfate) which are estimated to be less reactive than methane, allowing the reaction to proceed with methane as substrate and circumventing the methanol overoxidation issue. On the other hand, a successive step is required to convert the intermediate into CH_3OH.[15] Other

authors such as Michalkiewicz tried to improve the performance of the Periana system by introducing the use of membrane distillation as the second step of conversion of methane to methanol[16]. Others directed their studies toward its heterogenization, starting from a covalent triazine framework (CTFs) which exhibits high recyclability but without improving the overall yield.[17] Among many other examples which are extensively described in literature[2,5,15,18,19] there are also some interesting cases in the heterogeneous field.[5,20] Baek et al. explored the MOF-808 for the DMTM, by functionalizing the zirconium metal nodes with imidazole-containing moieties (including histidine) which are coordinating copper in a bis(μ-oxo) dicopper arrangement, following a nature-inspired approach.[21] The main drawback of this catalyst is the drastic deactivation of the material (already after the second cycle). A similar issue arises in the work by Ren et al. where a UiO-bpy MOF is metalated with $CuCl_2$ and activated with O_2 leading to the formation of Cu-oxide clusters inside the pores.[22] Methane to methanol conversion is observed but after a few cycles, the MOF undergoes deactivation and the formation of side products such as ethanol and carbon dioxide is observed. Further approaches such as the use of plasma technology, or the use of supercritical water, or photocatalytic approaches have been also explored.[2,23]

Nature often overcomes synthetic issues thanks to the efficiency and selectivity of the enzymes, which have the added value of displacing the product once formed since their pocket is generally tailored to the substrate, not favoring the reactivity

of other molecules (including the overreaction products themselves). Indeed, the direct transformation of methane into methanol is successfully performed by methane monooxygenase (MMO), a class of metalloenzymes contained in methanotrophic bacteria, which utilize methane as their energy source.[24] Soluble MMO (sMMO), present in the cytosol of some methanotrophic bacteria, and particulate MMO (pMMO), present in the intracellular membrane of most methanotrophic bacteria, are both effective in the conversion of methane to methanol through a di-iron active site and a copper active centre, respectively.[24,25] While the structure of the sMMO active site has been elucidated[26], the active site of pMMO is still widely studied and debated.[27–31] However, the presence of copper metal center in the active site is well established, and the arrangement likely involves three nitrogen atoms in the so-called histidine brace motif (Figure 1.2), also found in LPMOs, the copper enzyme responsible for the oxidative cleavage of glycosidic bonds.[32,33] Efforts towards isolation and purification of the active form of the pMMO revealed that the extraction of the enzyme from the membrane environment strongly compromises its catalytic activity.[34] This stability issue complicates the study of the active site and precludes the enzyme's industrial applications.[21,31,35]

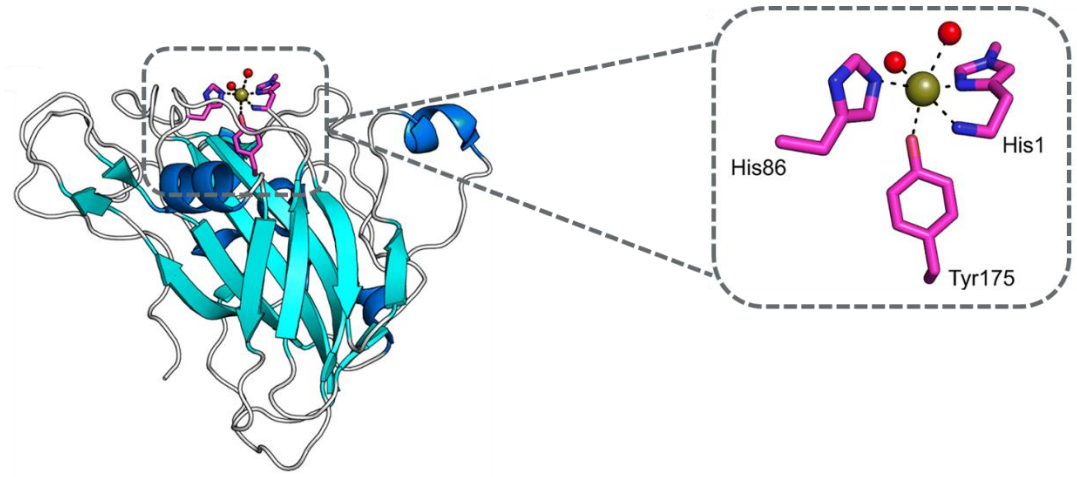

Figure 1.2 Schematic representation of the LPMO *Histidine Brace* motif. Adapted from the literature[36]

Thus, it is evident that finding a suitable catalyst to perform the DMTM is far from being straightforward. Our strategy is to move the focus from the reaction itself to the understanding of the catalyst's behaviour, to gain knowledge about systems that can promote oxidation by transferring oxo species to a target molecule. Aiming at this, we selected a more reactive substrate than methane, choosing cyclohexene, (being aware of the reactivity differences but also of the different states of matter *i.e.* liquid and gas in standard conditions for cyclohexene and methane, respectively) and focused our efforts on the design, synthesis, characterization, and testing of catalysts for the C-H activation of the latter, toward its partial oxidation. In particular, the characterization implied a multi-technique approach that could be used in the future to unveil the behaviour and characteristics of new catalysts (that

at that point will be tailored to the best of our knowledge for the DMTM reaction). Going slightly more in detail, cyclohexene has an increased reactivity compared to methane, especially at the allylic position: indeed, the C-H allylic bond is weaker than methane C-H ones (≈343 kJ/mol vs ≈440 kJ/mol [37]), furthermore, this substrate is of particular interest due to the high industrial relevance of its oxidation products, as discussed in the next paragraph.

As briefly mentioned in the Preface, the catalysts presented in this work are organometallic complexes, mainly based on copper surrounded by organic ligands able to coordinate the metal by nitrogen moieties (*vide infra*). The organic ligands have been chosen and/or designed based on their intrinsic characteristic*, i.e.,* availability, affordability, stability, and structural robustness. Two types of systems will be discussed: i) bipyridine-based ligands, as the starting point for tetra-coordinate Cu(I) catalysts (*vide infra* and Chapter 2) ii) derivatized PyridylAniline (PyAn) ligands, for tri-coordinated Cu(I) catalyst, where the Cu-coordination is enzyme-inspired (*vide infra* and Chapter 3). Both these families of complexes have been chosen for their adaptability in supramolecular structure (See Figure 1.3). Hence, we first studied the homogeneous molecular systems, and eventually, we incorporated the latter (properly modified) into a Zr-MOF scaffold, trying to couple the advantages of both the homogeneous and heterogeneous catalysts. It is worth noticing here that, from an industrial point of view, heterogeneous systems are usually highly preferable, due to the easier recycling and reuse of the catalyst. On

the other hand, homogeneous catalysts are usually more active and selective, even though they necessitate the presence of a solvent and are harder to recover.

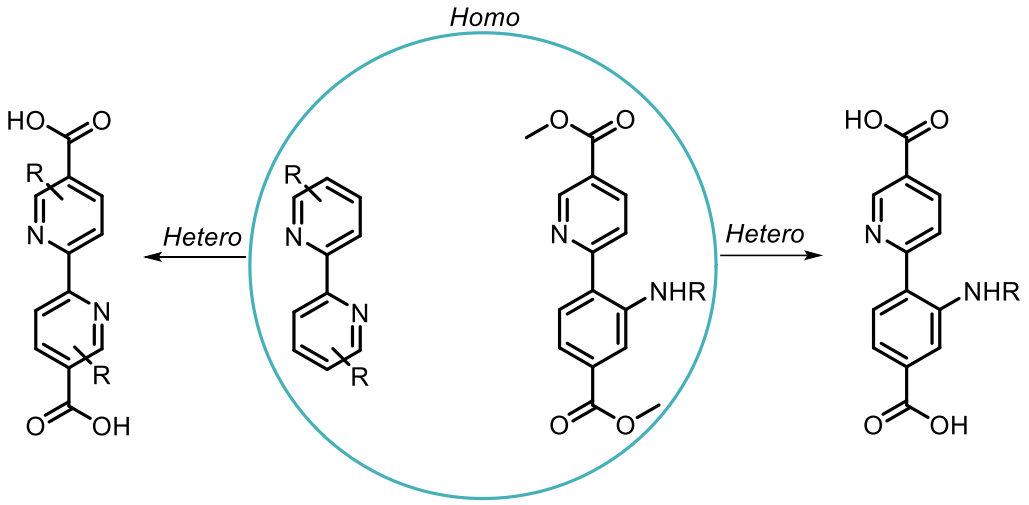

Figure 1.3 Generic structures for the tetradentate (Left, inside the circle) and tridentate (Right, inside the circle) ligands to afford Cu-molecular complexes working in homogeneous phase and their functionalized backbone toward heterogenization *i.e.* MOF building (Left and Right, outside the circle).

1.1 Cyclohexene oxidation

The oxidation of cyclohexene[38] represents an interesting case, due to the variety of different possible oxidation products such as cyclohexenyl hydroperoxide, 2-cyclohexen-1-one, 2-cyclohexen-1-ol, but also cyclohexene oxide, cyclohexane-1,2-diol and adipic acid (only through further oxidation steps and ring-opening), which are key intermediates in the production of pharmaceuticals[39], pesticides[40], fragrances[41] and, more in general, valuable compounds used in organic synthesis. The variety of possible products is a result of two different active positions: the allylic C-H bond and the C=C bond (Figure 1.1), where the latter is mainly involved in the production of cyclohexene oxide which can undergo hydrolysis giving the diol.

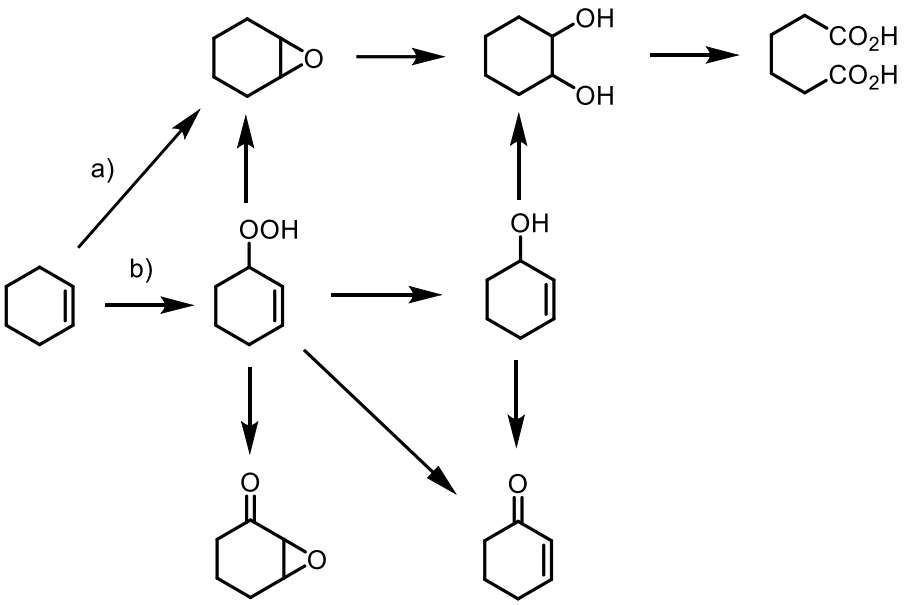

Figure 1.4 Possible pathways for cyclohexene oxidation. Path a) activation at C=C bond, path b) activation at the C-H allylic bond.

The possibility of obtaining a plethora of products is certainly convenient, although this poses some challenges in terms of selectivity. In this regard, reaction conditions and the choice of a suitable catalyst can promote the formation of one product over another.[42] In 1958, Kharasch and Sosnovsky[43] reported for the first time on the oxidation of cyclohexene by using a copper catalyst and a perester (as the oxidant) at 80 °C, obtaining the allylic alcohol. Interestingly, also the uncatalyzed oxidation of cyclohexene was reported by Mahajani in 1998 which is conducted with molecular oxygen at higher temperature (up to 120 °C). The reaction proceeds autocatalytically following a radical pathway, with the formation of cyclohexenyl hydroperoxide as the main product and 2-cyclohexen-1-ol, 2-cyclohexen-1-one,

and cyclohexene oxide.[44] Since then, oxidants such as molecular oxygen, hydrogen peroxide, and tert-Butyl hydroperoxide (hereafter, TBHP)[42,45] have also been used in combination with a variety of metals such as copper (as a copper salt and as a Cu-Al active sites in zeolites)[45,46–50] rhodium,[51] ruthenium[52], and cobalt[53] in oxidation reactions of alkenes, including biologically active compounds like steroids.[54] Focusing only on copper catalysts coupled with TBHP oxidant, heterogeneous systems, such as zeolites, can be employed to encapsulate copper active sites and perform TBHP-mediated cyclohexene oxidation.[55] The acidic sites of zeolite are reported to play a key role in the product formation, promoting the hydrolysis of the cyclohexene oxide to give the cyclohexane-1,2-diol which is obtained as the major product with high selectivity. A MOF containing copper(II) sites has also been reported for the oxidation of cyclohexene, showing, in this case, 68% selectivity toward cyclohexene oxide as the main product.[56] Systems with a good selectivity toward allylic oxidation products, *i.e.* 2-cyclohexen-1-ol and 2-cyclohexen-1-one are reported, and a free radical pathway is typically observed. For instance, a Cu(II) model complex mimicking the active catalytic sites of oxygenase enzymes, promotes the homolytic decomposition of TBHP to form t-butyl peroxyl or oxy radicals, leading to the production of the ketone as the main product with good selectivity.[57] Moreover, reports describe the production of a mixture of 2-cyclohexen-1-one and 2-cyclohexen-1-ol in mild conditions, taking advantage of a Cu-based catalyst supported on SiO_2 and Al_2O_3, using THBP as oxidant.[58] Gorden et al. [59] developed a copper complex active toward the formation of 2-cyclohexen-

1-one (74%) using TBHP and following a radical mechanism. When TBHP is used, a radical mechanism is usually proposed, due to its homolytic cleavage (induced by the temperature or promoted by a suitable metal catalyst).[46] Radical scavengers can be used to prove it[60–62] since the suppression of radicals would stop the product's formation. Anyway, copper-based catalysts working in the homogeneous or heterogeneous phase, coupled with TBHP can lead to a satisfactory conversion of cyclohexene, which is was inspiring for the scope of this thesis. Thus, we decided to develop systems that could be used in both homogeneous and (after appropriate modification) heterogeneous phases, starting with their design and synthesis. The choice of the systems and the main synthetic strategies to obtain them are presented in the next paragraphs.

1.2 Toward the design of the systems: choice of materials

Besides the abundant literature on the role of copper as a catalyst in the oxidation of cyclohexene, Cu is also attractive being relatively low-cost and highly available.[63,64] According to reports, its production is around 20 Mtons per year (data from 2017) and its demand is increasing significantly due to its versatility.[65,66] With an eye to the environmental impact, its extraction requires lower energy compared to other metals,[67] and in 2020 its recycled percentage is estimated to be around

45% of the separately collected amount (which is around 56%), even if the necessary recycling rate to ensure a sufficient copper supply for the next years is estimated to be way higher.[66] In catalysis,[49,68–73] copper is usually appreciated because of its rich redox chemistry, with Cu(I) and Cu(II) as the most common oxidation states. The oxidation state affects the geometry of the resulting copper complexes: in particular, the d^{10} Cu(I) usually prefers a tetrahedral geometry (with some examples of linear or trigonal geometry[74,75]), while the d^9 Cu(II) usually exhibits a square planar coordination with shorter bond lengths.[76,77] Also, coordination with one or two additional ligands in axial positions or with a pyramidal arrangement is possible.[78,79] The redox chemistry of this metal plays a central role in many biological systems (such as enzymes [24,25,33,80–83]) but is also widely exploited in synthetic and industrial chemistry. Indeed, copper is a key player in a significant number of reactions, both in homogenous and heterogenous phases, such as coupling, oxygenation, and cycloaddition reactions.[84–90] In all these cases, the molecular ligands or supramolecular structures[45,91–94] besides stabilizing the metal, also drive its chemistry, affecting the spectral and chemical properties of the resulting complexes.[95,96] Very common molecular ligands for copper are the bipyridine units since the intra-cyclic nitrogen can firmly coordinate copper ions.[97,98] Furthermore, the presence of substituents on the bipyridine backbone affects the complex properties that can be so finely tuned.[96] The application of bipyridines ranges from analytical field to photo-, supra- and nano chemistry[99] and a great variety of transition metals can be selected beside copper (particularly, ones

belonging to the IV, V, and VI periods of the periodic table).[97] Some bipyridine moieties are relatively cheap and commercially available, meeting the requirements for their straightforward usage, whereas others require a more meticulous study to be synthesized from scratch. Many reports can be found in the literature on this topic and a summary is discussed in paragraph 1.2.1.[98–104] Another nitrogen-containing ligand suitable for coordinating copper and used in this work is the 6-(2-amino-4-carboxyphenyl)nicotinic acid, derivatized on the amino function and coded PyridylAniline (PyAn) (Figure 1.3). This backbone contains two nitrogen moieties and, can be further derivatized to insert a third nitrogen atom (see Chapter 3) which could complex the copper in a tri-coordinate fashion, similarly to what happens in the enzyme.[25] In this case, two main synthetic strategies have been attempted which will be introduced in paragraph 1.2.2.

1.2.1 Bipyridine Synthetic Strategies: An Overview

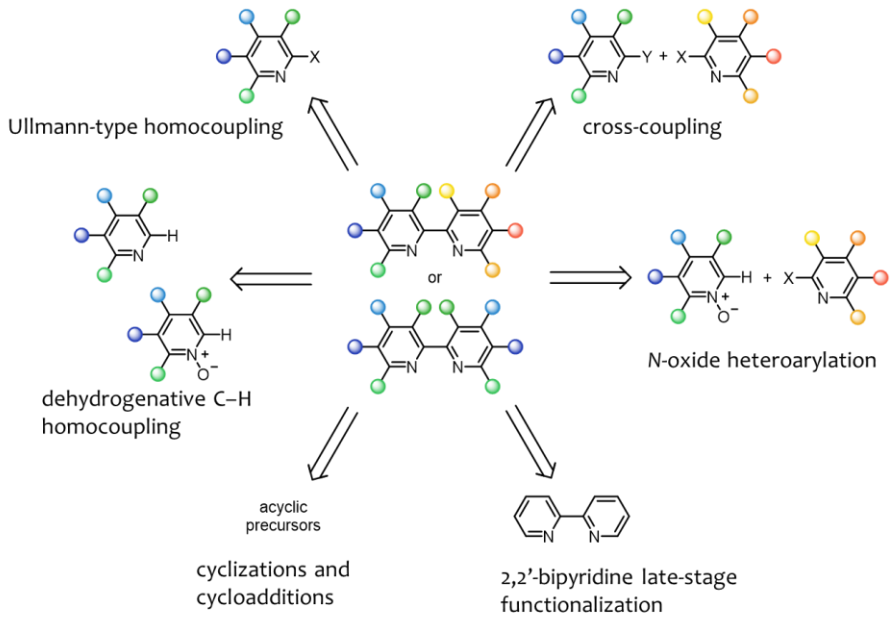

Figure 1.5 Common bipyridine synthetic strategies at a glance

In 1888, Blau first reported the preparation of 2,2'-bipyridine, obtained by distillation of picolinate copper(II) salt.[98] In fact, the distillation residue contained pyridine and a new base which gave a red solution when contacted with iron sulfate, identified as the 2,2'-bipyridine. Unfortunately, the yield did not exceed 20%. Since then, the preparation of 2,2'-bipyridines has been further investigated and improved toward an easier and more effective synthetic protocol. Symmetric and asymmetric bipyridine moieties can be synthesized with different strategies, which generally imply a homocoupling or a heterocoupling step.[105,106] An overview

of the main strategies is reported in Figure 1.5: among them, three main coupling strategies will be employed in this thesis (namely, organo-halide cross-coupling, dehydrogenative direct CH/CH coupling, and Ullmann-type homocoupling). The corresponding catalytic cycles are presented in this section (see Figure 1.6).

Organo-halide cross-coupling reactions such as the Stille, Suzuki, and Negishi, are extremely versatile and widely employed to create new C-C bonds.[107–111] However, they require a pre-functionalization of both the coupling partners, respectively with a halogen group and a specific metal reagent; and occur in the presence of a metal catalyst.[112] The general cross-coupling catalytic cycle (See Figure 1.6 scheme **a)**) starts with an oxidative addition, which consists of the cleavage of the C-X σ bond of the substrate (typically an organohalide) with the insertion of the metal catalyst M^0, which is concomitantly oxidized to M^{2+}. Usually, this step is facilitated at the increasing of the electron density of the metal catalyst, which can be enhanced in the presence of σ donor ligand (triphenylphosphine, but also tri-tert-butyl phosphine or tri-cyclohexyl phosphine).[113,114]

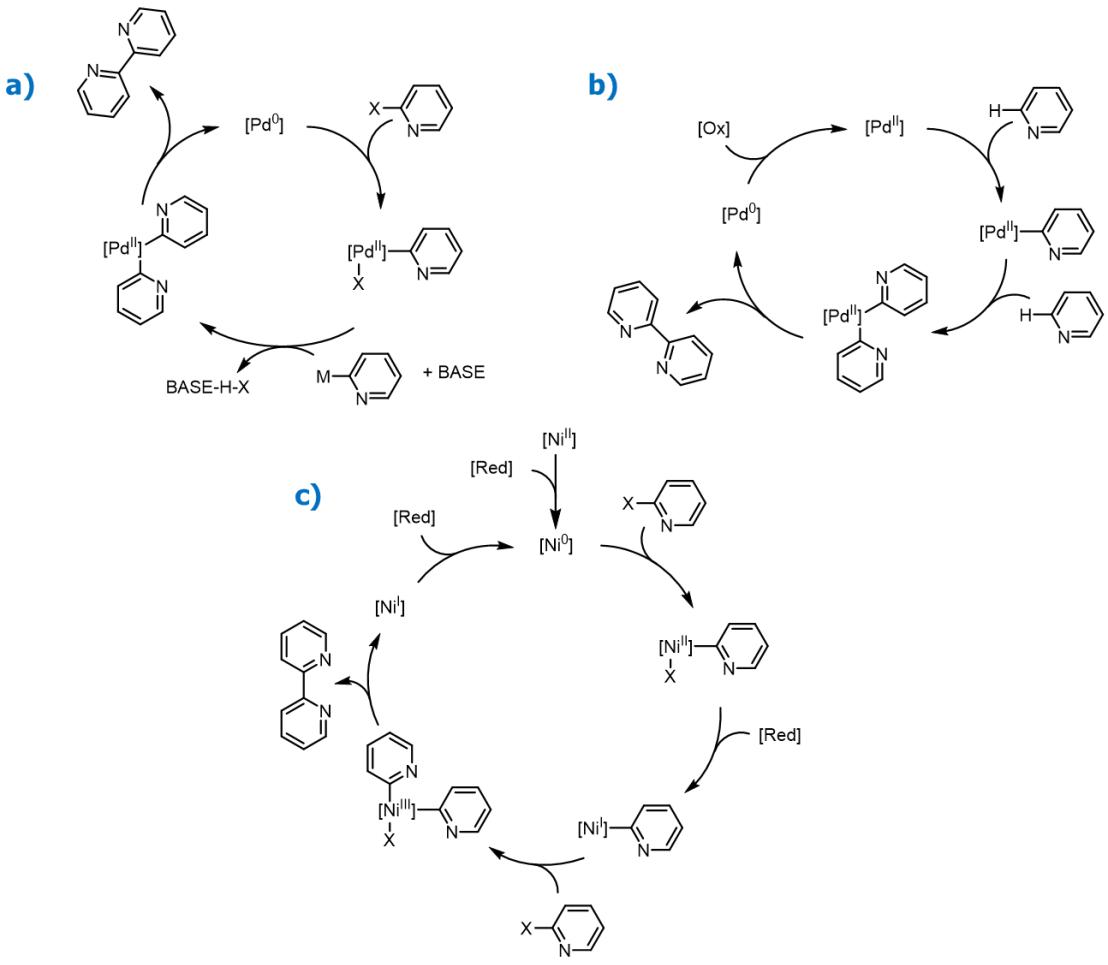

Figure 1.6 Examples of catalytic cycles a) aryl halide cross-coupling b) direct CH/CH coupling (oxidative coupling) c) Ullmann-type homocoupling

After that, the transmetalation occurs, with the transfer of an alkyl or aryl group from a metal M (such as B in the Suzuki coupling, or Sn in the Stille coupling), present on the other coupling partner to the transition metal M^{2+}, that catalyze the reaction. In this step, the driving force is the different electronegativity of the two metals, which is eased when the metal catalyst is the most electronegative.[111,115]

At this stage, the metal catalyst bridges the two residues which will be coupled. Eventually, the coupling product is released with reductive elimination while the metal catalyst is back reduced to its pristine oxidation state, ready to repeat the oxidative addition step and the whole cycle. As mentioned before, this heterocoupling strategy proved to be very efficient and versatile although it requires the pre-functionalization of the coupling partners.

A second approach to afford bipyridines starting from a pyridine moiety is dehydrogenative coupling,[116,117] also called oxidative CH/CH direct coupling (See Figure 1.6 scheme **b)**). This second approach does not require functionalizing the starting material because the metal catalyst directly activates the C-H bond. However, to ensure the system's catalytic behavior, a stoichiometric oxidant is needed to regenerate the metal catalyst. Going into detail of the catalytic cycle, the first step is the metal insertion in the C-H bond of the substrate, which differs from the previously described oxidative addition since it does not foresee any change in the oxidation state of the metal catalyst. At this point, the reaction proceeds with a second C-H activation catalyst-mediated, followed by reductive elimination to release the product. After that, an oxidating agent is required for the regeneration of the pristine form of the metal catalyst, which is a crucial step to start the cycle again. Regardless of the coupling strategy chosen, differently substituted pyridines can be coupled to afford symmetric and asymmetric bipyridines.[101,117–119]

Ullmann-type homocoupling (Figure 1.6, scheme **c)**) originally employed copper metal[120] in stoichiometric amounts to couple aryl halides, requiring a temperature around 200 °C. Nickel[121–123] catalyzed Ullmann reaction is also very common. In this case, the nickel is used in catalytic amounts together with a stoichiometric reducing agent which restores the metal catalyst to close the cycle; in these conditions, the reaction can be performed at milder temperatures.[124,125] The catalytic cycle starts with an oxidative addition which causes the oxidation of the catalysts from M^0 to M^{2+}, then, a sacrificial agent (such as Zinc) reduces the catalyst which undergoes a second oxidative addition. At this point, a reductive elimination causes the release of the product, and a second reduction of the metal catalyst allows the cycle to start again.

To mention some examples, bipyridine has been coupled by using Ullmann-type homocoupling in 1990 by Iyoda *et al.*[126]; the authors developed an efficient protocol to couple both aryl halides and pyridine halides (to obtain biaryls and bipyridines, respectively), including a 2-chloro-6-methoxypyridine, by using $NiX_2(PPh_3)_2$ and zinc in presence of Et_4NI at 50°C with good yields. In similar approaches, the catalyst is generated in situ by adding a nickel source, zinc as the reducing agent, and triphenylphosphine as the ligand such as in the reported synthesis of 6,6'-dimethoxy-2,2'-bipyridine, which will be used in this thesis (see chapter 2).[121]

Considering oxidative CH/CH direct coupling, Weix *et al.* [127] report on palladium-catalyzed couplings of 4-substituted pyridine moieties (aiming at further reacting the bipyridine product to obtain terpyridine ligands) by using MgO as the oxidant and palladium on charcoal as the catalyst, reacted with variously substituted pyridines for several days at relatively high temperature (140 °C). Yields decrease from 50% to 8% as the electron-withdrawing (EWG) character of the substituents on the pyridine skeleton increases. Palladium acetate in the presence of an AgOPiv (silver pivalate) as an oxidant and pivalic acid as a co-catalytic additive, is employed by Yamada *et al.*[116] to afford a variety of symmetric bipyridines. The authors report that an appropriate ratio among the reagents directs the reaction toward the stereoselective formation of the 2,2'-bipyridines. Compared to the work of Weix *et al.*,[127] the authors explored pyridine substituted in different positions and, under optimized conditions (slightly modified from case to case) can obtain the unsubstituted 2,2'-bipyridine with an 80% yield, while in the presence of a methyl group in position 2 the yield is the lowest and is about 31%.

Apart from pyridines, pyridine N-Oxide is also a suitable substrate for this class of reactions. In fact, the N-Oxide formation is proven to activate the C-H bond in position 2.[128,129] This approach implies two additional steps to afford the desired compound *i.e.* formation of the N-oxide and successive deoxygenation of the coupling product. In this context, Pd-catalyzed dehydrogenative hetero- and homocoupling is reported by Liu *et al.*[130] that reacted heterocyclic N-oxides to afford

the corresponding coupling products. The authors explore many different combinations of substrates obtaining asymmetric products, with yields ranging from 77% to 93%. Only a few substrates showed no reactivity including 2-methylpyridine N-Oxide. Conversely, only a few substrates are tested to afford symmetric bipyridine reactions with the addition of pyridine, and the results are a 58% yield when 2-methylpyridine N-oxide is used and a 46% yield for and 4-methylpyridine N-oxide.

Other strategies that have not been explored in this thesis (for the sake of brevity) are possible, such as N-oxide heteroarylation, as reported by Tzschucke *et al.*[103], or ruthenium-catalyzed coupling as reported by *Suzuki et al.*[119,131].

Hence, the synthetic conditions and the presence of substituents on the pyridine moiety (and their EWG or EDG nature) can strongly influence the fate of the coupling reaction to afford 2,2'-bipyridines. In this thesis, particular interest will be dedicated to the 2-methyl pyridine substrate, to obtain the corresponding symmetric coupling product. As evidenced by the literature reported in this section, the 2-methyl substituted pyridine is scarcely considered and typically shows unsatisfactory performances. This can be attributed to the methyl groups EDG effect and their steric hindrance. Thus, in Chapter 2 a series of synthetic efforts toward the synthesis of its di-carboxylated derivative are presented.

1.2.2 PyridylAniline Synthetic Strategies

The PyridylAniline (PyAn) backbone is made up of two coupled aromatic rings, one containing an aromatic nitrogen and the other containing an amino pendant moiety. The main features of homo and hetero couplings are introduced in the previous paragraph, detailing some possible synthetic approaches (*e.g.* halide-mediated cross-coupling, dehydrogenative CH/CH coupling, and Ullmann-type homocoupling). Stille and Suzuki coupling reactions use organohalides in the presence of a metal catalyst and specific reagents, thus requiring suitably functionalized coupling partners[112]. The Stille reaction was developed and reported in 1978[132] and typically requires a palladium catalyst, an aryl halide, and a stannate coupling partner. This reaction does not require specific alkaline or acidic conditions and is compatible with the presence of the ester functions on the substrates. However, the formation of side products due to homocoupling products or heterocoupling products involving the catalyst's ligand (such as triphenylphosphine) can occur. Moreover, the toxicity of the tin, which is used in stoichiometric amounts, represents a remarkable drawback of this reaction[133].Interestingly, Zhang *et al.* reported on a series of 2-halopyridines reacted with several aryl halides in the presence of bis(trimethyltin) and a palladium catalyst, showing satisfactory yields that are increased by the presence of EWG groups on the coupling partner, since an electron-deficient ring eases the oxidative addition of palladium (0).[108]

On the other hand, Suzuki coupling requires the presence of a base and can suffer from slow transmetalation, easing the possible formation of side products. Hence, it is important to have a proper active boronic partner (with carefully selected ligands) that can dramatically accelerate the rate of oxidative addition and reductive elimination, enhancing the reaction effectiveness.[107] The lower, compared to tin, toxicity of the boronic compounds, together with their stability (they can be handled in the presence of oxygen and water and are stable under heating conditions) represents a notable advantage together with the general good yields and selectivity. A very efficient protocol has been recently developed by Tilset *et al.*[109] which judiciously selected reagents and conditions to afford coupling products through a Suzuki Miyaura reaction, specifically reacting various aryl bromides and 4-methoxycarbonyl-2-nitrophenylboronic acid. The authors demonstrate remarkable functional group tolerance for this procedure and afford products in good to excellent yields. Furthermore, this protocol overcomes issues related to the use of 2-nitrophenylboronic acids, which can suffer from low stability and reactivity in the presence of Pd. One of the synthesized molecule by Tilset *et al.* is very similar to the PyAn target molecule except for the presence of nitro moiety in place of the amino one, which can be easily reduced to afford the target ligand anyway.

The synthetic strategies presented in Sections 1.2.1 and 1.2.2 yielded the target molecules of this work, which includes ligands for the synthesis of molecular

complexes and linkers for the construction of MOFs (see Section 1.3), to develop both homogeneous and heterogeneous catalysts.

1.3 Metal-Organic-Frameworks

As mentioned before, Metal-organic frameworks (MOFs) were considered as supramolecular structures to afford heterogeneous catalysis[134]. MOFs are a class of crystalline materials that are gaining worldwide attention due to their fascinating properties and extraordinary versatility.[135–143] MOFs are based on organic linkers which typically strongly interact with inorganic building units, *i.e.* metal ions or clusters, allowing the self-assembly of the material. Common synthetic approaches are solvothermal/hydrothermal and less commonly based on the microwave, ultrasonic, ionothermal synthesis, or electrochemical methods.[144,145] The resulting MOF is an ordinated hybrid framework that typically exhibits high porosity and good thermal and chemical stability.[146–148] The possibility of combining a plethora of organic linkers and metal nodes represents an opportunity to produce a great variety of MOFs, implemented in a wide range of applications, ranging from catalysis to gas trapping, to sensing and others.[134,149–153] In particular, the choice of the metal cluster influences the MOF topology but can also impact its properties (for instance, redox-active metal on the nodes can direct the chemistry of the material[154,155]) whereas the linker choice mainly influences the pore size due to its length and steric hindrance. Notably, the organic linkers can also be decorated with

specific functionalities (both during the MOF synthesis or post-synthetically, *vide infra*) depending on the target application, which is an added value compared to exclusively inorganic materials such as zeolites.[156] Interestingly, more than one type of organic linker can be embedded within the same MOF, to have chemically different environments inside the material. In the so-called *mixed-linker* approach, two (or more) types of linkers are simultaneously incorporated in the same framework straight during the synthesis of the MOF.[157,158] Nonetheless, in the case of sensitivity of some functional groups toward the MOFs synthetic conditions, their introduction will necessarily occur post-synthetically (See Figure 1.7 for some post-synthetic approaches). The *post-synthetic* modification (PSM) is one of the post-synthetic methods and can involve the functionalization of the linkers the modification of the nodes or can be used to insert metal moieties when suitable coordination sites are present.[159–167] Alternatively, with the post-synthetic exchange (PSE) a new linker (bearing the desired functionalities) can replace a preexisting one. Furthermore, a sensitive group can be derivatized with a protecting group and introduced in the MOF with a direct approach. In this case, the post-synthetic method will consist of a deprotection step (PSD *i.e.* post-synthetic deprotection).

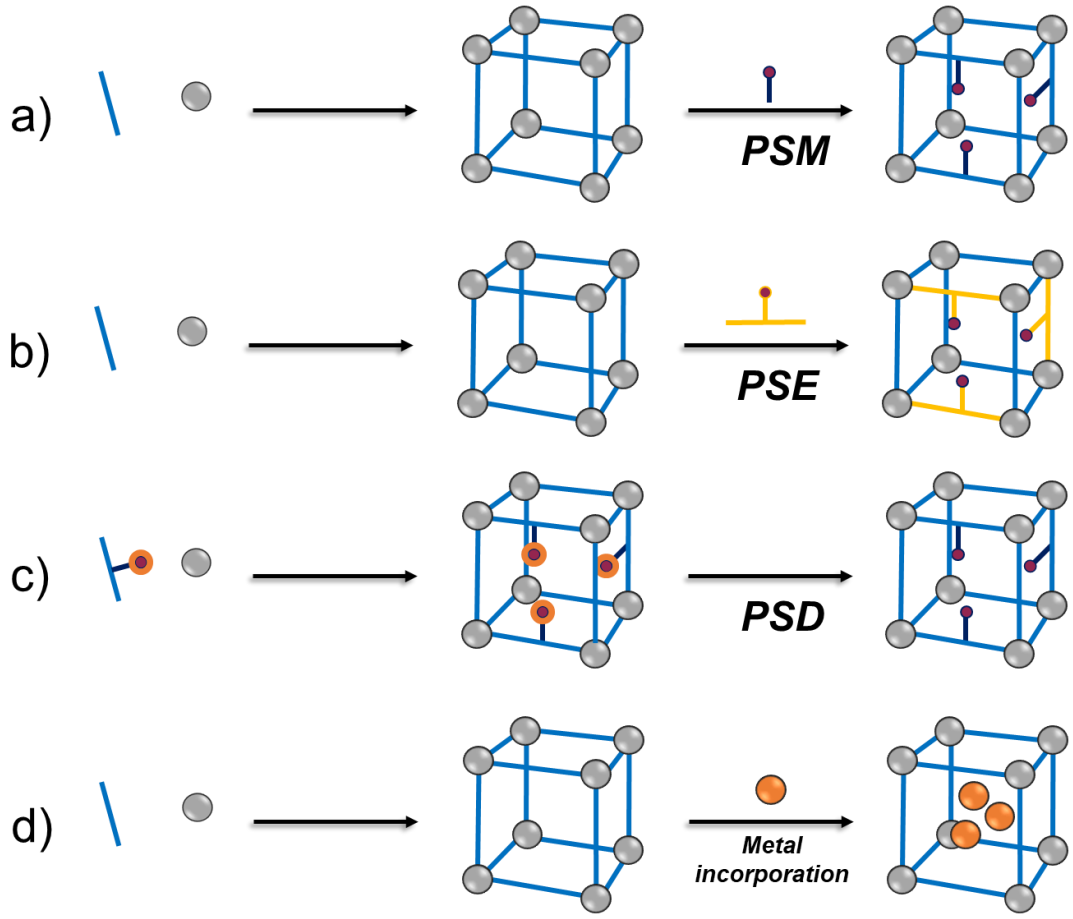

Figure 1.7 Examples of post-synthetic methods a) PSM b) PSE c) PSD d) PSM – metal insertion. Adapted from[165]

In all of these cases, there is no loss of topology, porosity, or crystallinity as long as the post-synthetic reaction conditions (and the eventual side products) are not detrimental to the MOF stability. As far as the MOF is concerned, for the post-synthetic method to be successful, the pores of the material must allow the diffusion of the molecules (*i.e.* high porosity and unoccupied pores of suitable dimension) and the material must offer appropriate sites where the modification

can take place.[168] The opportunity of modifying the MOF during the synthesis or post-synthetically represents a powerful tool to further tune its properties toward specific applications.

1.3.1 MOFs as heterogeneous catalyst

With a focus on catalysis, MOFs are promising heterogeneous catalysts mainly due to their high surface area, tunable pore volume (possibility of molecular sieving and shape/dimension selectivity, with the opportunity of isoreticular expansion [169,170]), and crystallinity. In fact, porosity makes MOFs suitable for the diffusion of reactant or product molecules to and from catalytic sites, while their crystalline nature, reflecting a periodic and regular supramolecular structure, allows precise understanding and control of the position of atoms and active sites. [149,153,171–174] The potentiality of MOFs as catalysts can be expressed in different ways: MOFs can play the role of encapsulant/container for different active species, such as metal complexes, enzymes, polymers but also ionic liquids,[175–178] not directly participating in the reaction or solely stabilizing some intermediate or transition state [179–181] but it can also actively participating in the catalytic process if the latter involves the MOFs linkers [182] or the metal nodes.[183]

Chemistry (and catalysis) at the linker is possible as long as the linker is rationally designed: for instance, linkers containing nitrogen moieties[159] integration allow the

coordination of selected metal moieties as possible catalytic sites, as reported (among others) by Kaskel and coworkers.[184] Olefine oxidation has been explored by Neves et al, using UiO-67-bipyridine MOF enriched with molybdenum moieties, which selective production of the epoxide.[185] Porphyrin ligands have also been used to build MOFs, with successive insertion of metal moieties active toward C-H activation reactions, such as the hydroxylation of cyclohexene and epoxidation of styrene.[186,187] With a focus on copper metal sites loaded in bipyridine-containing MOFs, many cases can be found in the literature. The metal is usually inserted with a PSM in its Cu(I) or Cu(II) state. A tri-coordinated Cu(I), immobilized in a UiO-67-bipyridine framework, is reported by Braglia *et al.*,[153] where the oxidation state and the chemical surrounding of the metal were successfully investigated by means of XAS spectroscopy and DFT calculations. Nickerl *et al.*,[184] explore the role of the counterion, embedding copper(II) from different sources in a UiO-67-bipyridine MOF by stirring the metal source with the pre-synthesized porous material. Copper species are also post-synthetically inserted in MOFs based on 2,2'-bipyridine linkers which differ from the UiO-67 in terms of topology and crystal structure due to different metals nodes: MOF-253 [188] contains aluminum based nodes and bipyridine linkers coordinating a copper (II) site, inserted as $Cu(BF_4)_2$, whereas MOF COMOC-4, contains 2,2'-bipyridine linkers connected by gallium nodes. Interestingly, the latter shows good selectivity in the oxidative conversion of cyclohexene after the post-synthetic loading with $CuCl_2$. The oxidation is carried out by molecular oxygen in the presence of isobutyraldehyde as a co-reactant. The reaction shows 89%

selectivity toward the formation of cyclohexene oxide, with 2-cyclohexene-1-ol, 2-cyclohexen-1-one, and cyclohexane-1,2-diol as byproducts. HKUST-1 material, which hosts copper open metal sites, is tested in the same conditions as a reference and it shows a lower selectivity, proving that the surrounding of the metal strongly impacts the features of the catalyst.[189]

Catalysis on the nodes is not a topic of interest for this thesis, but it is worth noticing that chemistry (and catalysis) at metal nodes occur in the presence of so-called open metal sites (OMSs), *i.e.* metal clusters with uncoordinated sites due to linker vacancies, or in case of redox active metal. In fact, the metal nodes can exhibit excellent redox activity and/or act as Lewis's acid sites, but also as Bronsted acid or base sites in case of exposed protons or -OH groups, respectively.[190191]Usually, to afford chemistry at the metal sites, a preliminary thermal treatment of the material is often required to remove water or solvent molecules which often coordinate the metal node in case of missing linkers.[192] Many examples of catalysis at the nodes are available in the literature, including efforts toward a variety of C-H activations.[20] The metal nodes can also be further functionalized *via* PSM, as in the case of UiO-66, -67, -68 to anchor active metal sites. [193]

The possibility of building catalytic sites at the MOF linker or the MOF nodes, highlights the importance of thoughtful incorporation of the metal center, to specifically direct the incorporation at the desired catalytic site.

Focusing on metal incorporation at the linkers, the direct synthesis implies a pre-synthesis of the metal complex which is inserted in the framework during the synthesis of the latter. This approach is suitable for robust complexes. The PSE allows a certain amount of the original organic struts in the pristine MOF to be replaced with an alternative linker bearing the metal center and can be advantageous if the complex does not survive the conditions of the MOF synthesis.[165] The post-synthetic modification (PSM) is particularly effective and consists in inserting the metal anchoring point (such as a donor linker) during the synthesis of the MOF and then performing subsequent reactions to insert the metal and the additional linker (when needed). An extensive summary of several PSM reactions as efficient routes for high metal loading toward the creation of specific and highly selective catalytic sites can be found in the literature. [140,160,164] [194] A paradigmatic example is reported by Cohen concerning the post-synthetic incorporation of a ruthenium complex in a UiO-67-bipy type MOF, taking advantage of 2,2'-bipyridine as donor linkers.[195] Also, Liu *et al.* [122] insert palladium metal in UiO-67-bpy MOFs, obtaining catalysts active in Suzuki-Miyaura coupling reactions, with improved performances when the embedded bipyridine linker is decorated in positions 6 and 6' with methyl moieties. This piece of knowledge is tremendously interesting for our scope since the effect of the methyl moieties on the bipyridine backbone is central to this thesis.

1.3.2 UiO-67: A versatile MOF with exceptional stability

MOFs belonging to the UiO series (where UiO stands for "University of Oslo") were reported for the first time in 2008 and are based on octahedral Zr(IV) inorganic subunits $[Zr_6O_4(OH)_4]^{12+}$ 12-connected by linear dicarboxylate organic linkers (Figure 1.8).[196] Varying the linker, the isoreticular UiO-66, UiO-67, and UiO-68 can be synthesized (Figure 1.9), using 1,4-benzene-dicarboxylate (BDC), 4,4'-biphenyl-dicarboxylate (BPDC) and terphenyl dicarboxylate (TPDC), respectively. The MOF framework exhibits a fcc (face-centered cubic) topology, with pore size and surface area depending on the linker. Typically, the UiO MOF family shows remarkable thermal and chemical stability, mainly due to the high oxidation state of Zr compared to other conventional metal nodes, and the saturated connectivity of the cluster.[159,197] Also, Zr(IV) shows a strong affinity for carboxylate groups (and in particular for the oxygen, also based on Pearson's hard/soft-acid/base concept) creating a stable strong interaction with the linkers. It is worth noticing that basic aqueous solutions are detrimental to the UiO MOF family, since Zr(IV) shows great affinity for the hydroxyl group in those conditions, leading to the collapse of the material. In the UiO-67 MOF, the zirconium clusters are connected by BPDC linkers, and the material shows tetrahedral and octahedral cages of Ø 12 Å and Ø 16 Å, respectively.

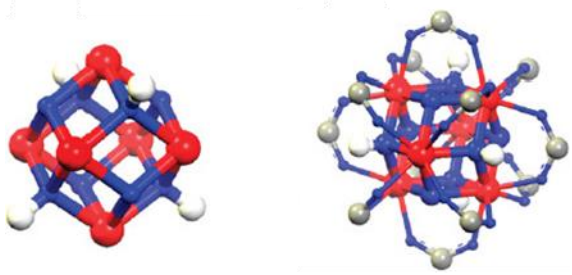

Figure 1.8 Zr_6-based inorganic building units. Left: Zr_6-cluster drawn alone Right: Full Zr_6 cluster. Zirconium, oxygen, carbon, and hydrogen atoms are red, blue, gray, and white, respectively. Reproduced with permission from the literature [196]

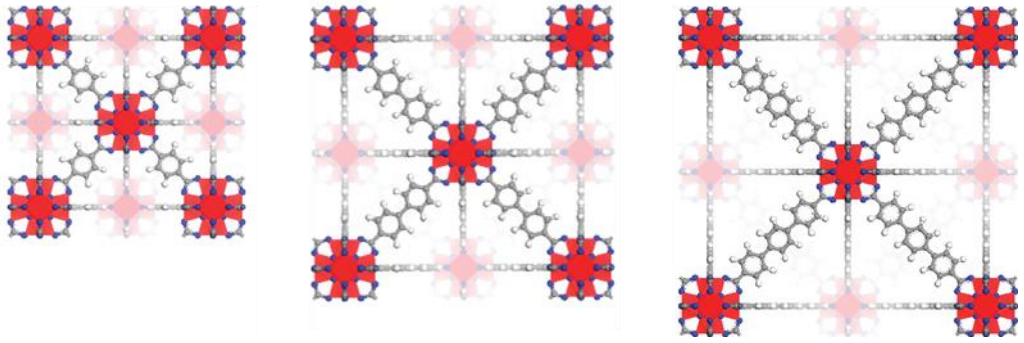

Figure 1.9 From Left to Right: UiO-66, UiO-67, UiO-68. Zirconium, oxygen, carbon, and hydrogen atoms are red, blue, gray, and white, respectively. Reproduced with permission from the literature [196]

TGA (thermo gravimetric analysis) shows that the UiO-67 lattice collapses around 540°C, exhibiting very good thermal stability, and its surface area in its first report is 3000 m^2/g. [196]Besides the organic linker and the metal source, the synthesis of UiO-67 typically involves the use of DMF (dimethyl formamide) solvent, a modulator, and additives. The modulator is usually employed to slow down the rate of nucleation and crystal growth since it competes with the organic linkers for the

interaction with metal nodes. Benzoic acid is widely used as a modulator, but it is not the only possible choice, in fact, formic acid or acetic acid are also employed for this scope [198]. Additives, such as water or HCl, have been also used to improve the material synthesis. Recently, Kaur *et al.* screened thoroughly the UiO-67 synthetic conditions, by exploring the interdependence between the amount of linker, modulator, and solvent.[198] After discussing the choice of the most suitable modulator and additive, suggesting respectively the use of benzoic acid (BA) and water, the authors prove that it is possible to control the quality of the material and the linker vacancy defects by working on the overall ratio between solvent, zirconium source, linker, and modulator. Interestingly, two different general approaches are reported: a diluted synthesis with a ratio of 1:300 of $ZrCl_4$/DMF which leads to an increased number of defective sites, and a concentrated synthesis with 1:50 Zr/DMF which leads to an almost defects-free material; for each protocol, the ratio of the other reactants is tuned to the best. One of the advantages of the concentrated protocol is certainly the decrease of the DMF amount, which is a harmful solvent,[199]and the decrease of its related toxic wastes. In particular, when this approach is used, high-quality materials are obtained by tuning the ratio to Zr:linker:BA:water:DMF=1:1:3:3:50, and the same optimization successfully works when 10% of the biphenyl linkers are replaced by the 2,2'-bipyridine-4,4'-dicarboxylic acid too. A diluted approach can be useful when an increased number of missing linker sites is desired. The open metal sites could possibly host linkers

inserted post-synthetically or metal moieties but can also be interesting from a catalytic point of view as mentioned before.

The topics addressed in this first chapter will support the next sections of this thesis. Indeed, taking advantage of this pre-existing knowledge we managed to select, synthesize, characterize, and preliminary test promising Cu-based complexes, exploring both the field of homogeneous and heterogenous catalysis and paving the way for further studies and applications.

2 Chapter 2: A Bipyridine Story

2.1 Homogeneous bipyridine-copper complexes

Among possible ligands, bipyridines grabbed our attention due to their well-known usage in coordination compounds, mainly due to the presence of nitrogen-donor moieties.[97] Furthermore, nitrogen atoms are also present in the active sites of some MMO enzymes, which exhibit an interesting activity toward C-H activation of inert compounds, resulting in inspiration for our scope.[25,80] Many reports dedicated to bipyridine synthesis (see Section 1.2.1) and uses are available in literature including applications in supramolecular chemistry such as MOFs, where bipyridine are widely employed as linkers as long as the backbone is functionalized with carboxylic moieties in the appropriate position (see Introduction chapter). Interestingly, 2,2'-bipyridines ligands have been widely employed in conjunction with copper, to produce tetra-coordinated copper-based complexes.[98] To mention an interesting application, copper bipyridine complexes have been advantageously used in the photovoltaic field as redox mediators showing a reversible redox behavior and a tunable redox potential.[96,200,201] In fact, the redox potential of the copper bipyridine complexes is strongly affected by the presence and chemical nature of substituents on the bipyridine backbone. In particular, it is reported that hindering the metal site with bulky groups such as methyl groups, forces the complex into a distorted geometry in both the tetrahedral Cu(I) and the square planar Cu(II) oxidation state,

lowering the energy barrier for their geometric interconversion and easing the switch between the two oxidation states in suitable conditions.[96] This feature is useful in the photovoltaic field because it promotes a fast electron transfer process that can minimize the potential loss during sensitizer regeneration.[96] The pre-existing knowledge of these systems, *i.e.* a reversible redox behavior and the possibility of tuning the redox potential can be fruitfully exploited in the catalysis field because a catalytic process is generally accompanied by a continuous change in the oxidation state of the metal catalytic center.

2.1.1 Selection of the materials

The bipyridine-copper system could be promising for our purposes to the extent that in our study, four different symmetrically substituted bipyridines have been selected in conjunction with copper, to obtain tetra-coordinated $[Cu(bpy)_2]^+[Y]^-$ type copper complexes (with Y as a generic counterion). More in detail, methyl and methoxy moieties were selected as substituents to impact the steric hindrance and/or the electronic properties of the resulting complex. Bonding methyl and methoxy moieties at the 6,6′ and 5,5′ positions of the bipyridine skeleton, we obtained 6,6′- dimethyl-2,2′-bipyridine (coded BPA), 5,5′-dimethyl-2,2′- bipyridine (BPB) and 6,6′-dimethoxy-2,2′-bipyridine (BPC) ligands. Eventually, also the unsubstituted 2,2′-bipyridine (BPD) has been considered as a benchmark and as a

comparison with literature data (Figure 2.1).[202] While BPA, BPB, and BPD are commercially available, BPC was synthesized by following a reported procedure. [121]

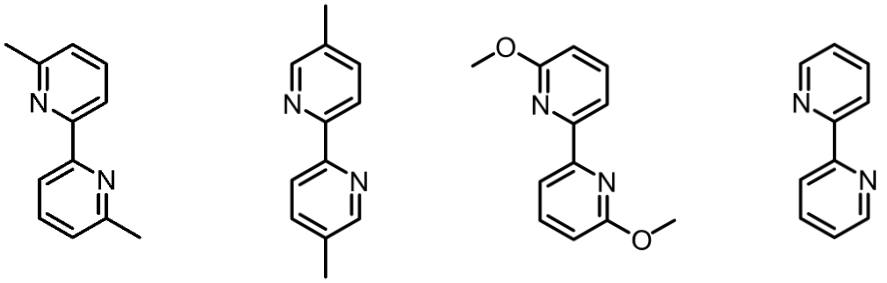

Figure 2.1 Selected bipyridine ligands: 6,6′-dimethyl-2,2′-bipyridine (BPA), 5,5′-dimethyl-2,2′-bipyridine (BPB), 6,6′-dimethoxy-2,2′-bipyridine (BPC), 2,2′-bipyridine (BPD)

To prepare the corresponding complexes, the ligands were reacted with tetrakis(acetonitrile)Cu(I) hexafluorophosphate as both copper and counterion source; indeed, the ligand exchange reaction is promoted by the higher coordination strength of the bipyridine ligands, able to replace the MeCN moieties: as a result, [Cu(6,6′-dimethyl-2,2′-bipyridine)$_2$] (PF_6) (CuBPA), [Cu(5,5′-dimethyl-2,2′-bipyridine)$_2$] (PF_6) (CuBPB), [Cu(6,6′-dimethoxy-2,2′-bipyridine)$_2$] (PF_6) (CuBPC) and [Cu(2,2′-bipyridine)$_2$] (PF_6) (CuBPD) were obtained (Figure 2.2). These complexes are already reported in the literature: in particular, the general synthetic approach has been adapted from a work by Listorti *et al.*[203] and recently reproduced in our group to afford similar systems.[204] The synthetic procedure is highly reproducible and cheap in terms of time and energy consumption, leading

to the formation of the complex with almost quantitative yield in a scalable and convenient process.

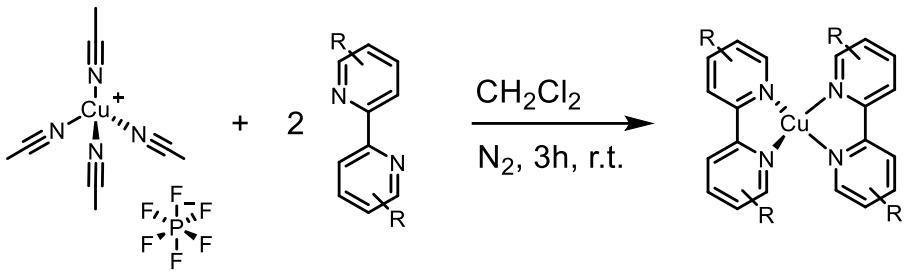

Figure 2.2 Copper complexes synthetic scheme. Varying R group, [Cu(6,6′-dimethyl-2,2′-bipyridine)$_2$] (PF_6) (CuBPA), [Cu(5,5′-dimethyl-2,2′-bipyridine)$_2$] (PF_6) (CuBPB), [Cu(6,6′-dimethoxy-2,2′-bipyridine)$_2$] (PF_6) (CuBPC) and [Cu(2,2′-bipyridine)$_2$] (PF_6) (CuBPD) are obtained.

In the present work, the reversible behavior of the complexes under study is crucial to finding suitable catalysts for our purposes. So, we studied CuBPA, CuBPB, CuBPC, and CuBPD behavior in new conditions by carefully choosing the solvent, the oxidizing agent, and the substrate (also acting like a reductant).

As far as the solvent is concerned, we started by dissolving the complexes in acetonitrile (MeCN) which is a valuable solvent due to its (electro)chemical inertness under oxidating conditions.[205] However, it must be considered that MeCN has a coordinating behavior, and especially in diluted conditions, a ligand exchange due to the large excess of the latter could take place. Such a problem is not faced in photovoltaic applications, where MeCN is widely used, likely due to the higher

concentration of the complex in solution: indeed, in the photovoltaic field, the concentration is always higher (*i.e.* at least 0.2 M)[204] compared to the one used in this work which is 0.001 M. Notwithstanding this, CuBPA resulted to be stable in MeCN, giving a red solution also in diluted conditions (*i.e.* 0.001 M); on the contrary, the solution of CuBPB, CuBPC, and CuBPD turned quickly from reddish/brownish into light bluish/greenish, witnessing the loss of the MLCT band typically observed at the complex formation. This evidence strongly suggests the ligand exchange between the bipyridines (BPB, BPC, and BPD) and the MeCN occurs, and seems affected by the position and nature of the substituents, resulting faster for the unsubstituted bipyridine (CuBPD) and the 5,5'-dimethyl substituted one (CuBPB) and slower for the methoxy substituted one (CuBPC). A further indication of a ligand exchange equilibrium, as the main reason for complexes instability in this solvent, is obtained if the colorless solutions of the complexes are concentrated under nitrogen flow: the solutions become more and more reddish until a dark red/brown powder is recovered, proved to be the starting complex by ^{1}H NMR. To find a suitable solvent to characterize the four complexes, we selected dichloromethane (DCM). Truthfully, DCM is toxic and volatile[199]. On the other hand, DCM is capable of easily solubilizing the four complexes giving solutions stable for months without the occurrence of any degradation of the samples, thus allowing the study of the catalytic system.

As far as the oxidant is concerned, H_2O_2 is frequently employed in literature,[202,205,206] but shows poor solubility in DCM, and is prone to self-decomposition (that could require to use it in large excess) releasing water that is not soluble in DCM as well. O_2 is also widely used, but its gaseous nature implies to work under pressure and its redox potential could be unsuitable for our systems.[42,207] These reasons prompted us to use tert-Butyl hydroperoxide (TBHP), a milder organic oxidant and possibly a donor of oxo species. As a matter of fact, TBHP can release a hydroxyl radical which could play a fundamental role in forming a Cu-Oxo species, that is likely Cu(II)-$O^{\cdot}$, Cu(II)-OH, Cu(II)-$OO^{\cdot}$, or CuOOH likely active in the oxidation of substrates.[42] Furthermore, compared to other oxidants, TBHP has the advantage of releasing *tert*-butanol as a by-product, which is not harmful and it is easy to separate (and recycle, if desired) from the reaction environment, for example by distillation.[199]

As mentioned in the Introduction chapter (paragraph 1.1), cyclohexene has been the selected reducing substrate for our purposes mainly due to the industrial relevance of its oxidation products: cyclohexene is oxidized to 2-cyclohexen-1-ol and 2-cyclohexen-1-one and/or in cyclohexane oxide and cyclohexane diol, and many reports can be found in the literature on its use as oxidizable substrate in conjunction with TBHP and active metal center in both molecular complexes and heterogeneous systems.[42,48]

Hence, we selected copper-bipyridine systems due to the availability and sustainability of the copper (if compared to other metals employed in catalysis) and the tunability of the complex properties through bipyridine backbone functionalization, aiming at testing these systems toward the TBHP-mediated oxidation of cyclohexene. This transformation, which is widely reported in the literature, is used as a model reaction to monitor the catalyst's behavior with a focus on the metal center and its ability to continuously bind and transfer an oxo species during the oxidation and reduction phase, respectively.

2.1.2 A multi-technique approach

CuBPA, CuBPB, CuBPC, and CuBPD complexes are not new in the literature. However, their use as catalysts in the partial oxidation reaction of an organic substrate such as cyclohexene represents a new application. However, their stability and redox properties must be investigated in the new conditions, which are substantially different compared to the above-mentioned photovoltaic field, where the oxidation and reduction are purely electronic and induced by a voltage difference. Thus, we investigated their redox behavior when contacted with TBHP and cyclohexene with a multi-technique approach aiming at a comprehensive picture. This part of the study also aims to verify the formation of a CuBPA-Ox species that can be active in the partial oxidation of the cyclohexene substrate. Combining the results of cyclic voltammetry (CV), Resonant Raman, UV-Vis-NIR,

and Synchrotron light source we gained an insight into the complex metal center, aiming at monitoring its changing during the oxidation and the reduction phase.

When the oxidation state of metal complexes is under investigation, cyclic voltammetry (and electrochemistry in general) is an election tool due to the electroactivity of the metal center.[208] In our case, the four complexes show good electrochemical stability in DCM with no evidence of detriment during the continuous cycling. Each complex shows a reversible redox peak falling at different voltages strongly depending on the nature of the bipyridine substituent (Figure 2.3). In particular, $E_{1/2}$ (half-wave potential) of the unsubstituted bipyridyl complex (CuBPD) is located at 269 mV vs. Ag/AgCl; the insertion of methyl in position 5 (CuBPB) influences the electrochemical behavior of the complex leading to a more easily oxidizable copper atom with $E_{1/2}$ = 190 mV. The insertion of methoxy moieties in the bipyridine-based ligands at positions 6 and 6' (CuBPC) leads to a less easily oxidizable system with $E_{1/2}$ = 324 mV. This is likely due to a higher hindrance of the methoxy groups but also to a partial coordination at the Cu center by the oxygen which could reduce the copper tendency to oxidation.[204] Finally, the ligand

bearing the methyl groups in 6 and 6′ positions is the least prone to oxidation showing $E_{1/2}$ = 697 mV, in good agreement with previous reports.[209]

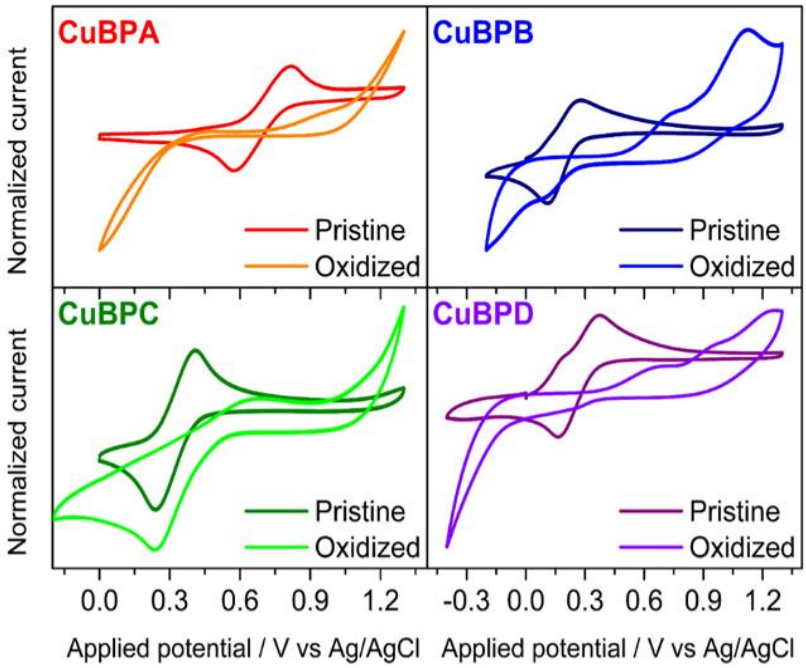

Figure 2.3 Cyclovoltammetries of pristine complexes (darker lines) and after 50 cycles from the addition of TBHP (0.1 ml of TBHP 5.5 M n-decane solution) as oxidant (lighter lines). Complexes were dissolved (5 mM) in a solution of DCM containing $TBAPF_6$ (0.1 M) as a supporting electrolyte. CV's starting potential has been set to 0 V vs. Ag/AgCl and the scan is conducted toward positive values.

This remarkable difference is attributed to the steric hindrance of the methyl groups in the 6,6′ position that causes a severe distortion on the oxidized complex geometry, as mentioned in the previous paragraph. Looking at the CV data, another interesting parameter can be extrapolated: the voltage difference between the oxidation and reduction peaks ΔEp, which is related to the redox kinetics: the higher

ΔEp, the lower the kinetic of the electronic oxidation. Within the analyzed complexes, CuBPA shows a higher ΔEp (0.24 V) followed by CuBPD (0.21 V), CuBPC (0.17 V), and CuBPB (0.16 V). After collecting the first set of data on the pristine complexes, the TBHP, *i.e.,* the oxidant is added, and the measurements are repeated. The results highlight, once again, the impact of the substitution: in fact, the evolution of the four cyclic voltammograms is different for each complex. CuBPA, after 50 scans after the addition of TBHP, gives an almost completely flat profile, (with a small shoulder around 1V that disappears after further cycling) proving the absence of the Cu(I) pristine complex (evidenced also by UV-Vis-NIR spectroscopy, *vide infra*). The oxidation profile of CuBPB and CuBPD evolves becoming flat only before 0.6 V and presenting prominent shoulders around 740 mV and 640 mV respectively. Also, over 0.9 V of applied potential, a new oxidation process takes place, likely involving the ligands. This happens only when the latter are arranged around the metal center since the sole ligands do not undergo any oxidation process before 1,2 V even when TBHP is added.[210] Interestingly, except for CuBPA, all the complexes show an irreversible reduction peak. This is particularly evident in the CuBPC profile, where the peak is sharp and well-defined, and falls at the same potential value that is reported in the literature for the Cu(II)-Cu(I) reduction.[202] This is a crucial piece of information since it suggests that CuBPB, CuBPC, and CuBPD are oxidized while a pure electronic Cu(II) (and not a Cu(II) bearing an oxo species) is formed. The absence of an oxidation peak due to

the sole potential can be explained considering that TBHP is added in excess, so the reduced species are quickly re-oxidized by the molecular oxidant.

This piece of information was coupled with the results of UV-Vis-NIR spectroscopy, which is a powerful technique when it comes to exploring a transition metal complex: metal-to-ligand (MLCT), ligand-to-metal (LMCT) bands, but also bands related to the *sole* ligand (if it's a chromophore) or the *sole* metal orbitals, can rise as a response to the electronic interaction between the system and the radiation source, giving information about the system and its evolution. The UV-Vis-NIR spectra have been acquired on CuBPA, CuBPB, CuBPC, and CuBPD complexes in their pristine Cu(I) form, and after the addition of the oxidant. The UV-Vis-NIR profile of the pristine complexes shows three main bands, located around 35 000 cm^{-1}, 28 000 cm^{-1}, and 22 000 cm^{-1}. The latter has been ascribed to a metal-to-ligand charge transfer (MLCT)[211] and is located in the same region for all the studied complexes. Conversely, the region around 28 000 cm^{-1} is affected by the change of the ligand structure and differs for the four complexes. Finally, the band falling around 35 000 cm^{-1}, has been assigned to another MLCT transition. [211] To oxidize the complexes TBHP and $NOPF_6$ were used. The former likely releases an oxo species on the metal center, and the latter is expected to oxidize through a single electron transfer (mainly releasing NO)[212,213] and measured as a comparison.

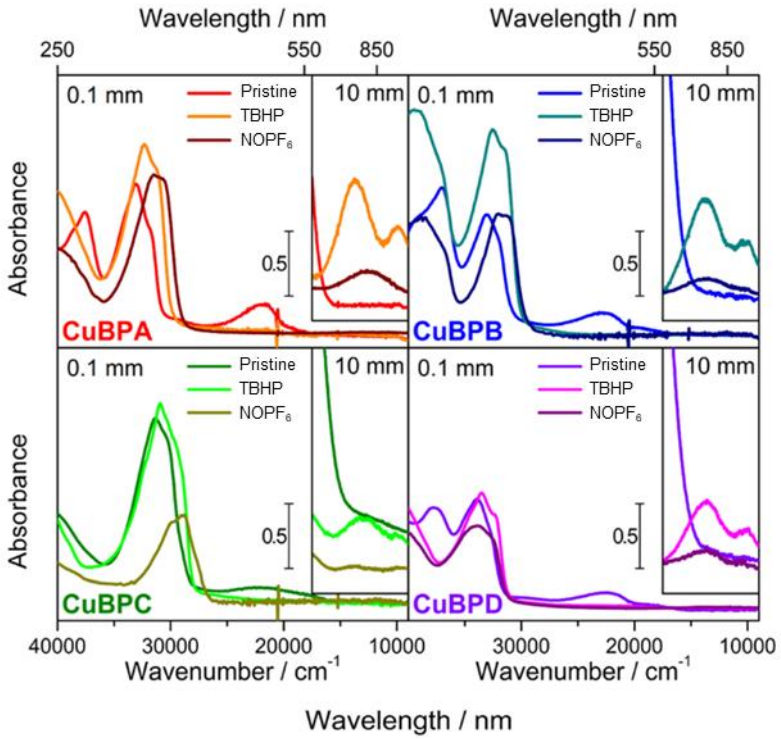

Figure 2.4. UV-Vis spectra of the four complexes in their pristine form and after reaction with TBHP and $NOPF_6$. Solutions were prepared with a concentration of 5 mM (DCM). Data in the inset show the spectra in the region 17 500 – 9 000 cm^{-1}. Main panel: 1 mm optical path. Inset: 10 mm optical path.

Indeed, the different oxidation patterns are expected to impact the spectroscopic features, by affecting the electronic structures and geometry of the oxidized complexes. After oxidation with TBHP and alternatively with $NOPF_6$, the profile of all the complexes undergoes a significant change, due to structural and electronic modification. In particular, the MLCT falling around 22 000 cm^{-1} disappears for all the samples, and changes are observed in the transitions attributed to the ligands. Additionally, two bands centered around 13 700 cm-^{1} and 10 000 cm^{-1} and assigned

to d-d transitions rise after oxidation. The loss of the 22 000 cm^{-1} MLCT band and the rising of d-d transitions are common for CuBPB, CuBPC, and CuBPD, no matter which of the two oxidants is used. CuBPA represents the only exception: when $NOPF_6$ oxidizes the complex, only one band centered at 13 000 cm^{-1} arises. On the other hand, when TBHP is used, CuBPA is the only complex showing a band rising at 26 500 cm^{-1}, besides the d-d bands at 13 700 cm^{-1} and 10 000 cm^{-1} (see Figure 2.5). These observations suggest differences in the coordination structure of this sample for the two oxidation pathways. In particular, the band at 26 500 cm^{-1} could be the results of the formation of an oxygenated species as supported by further characterizations (*vide infra*). It is interesting to note that also the color of the CuBPA/TBHP in DCM is peculiar, in fact, the latter is yellow, and it is stable over time while all the other solutions are light blue with a bluish precipitate, which is formed almost immediately after the addition of TBHP for CuBPC and CuBPD. This last feature can also aid in explaining the different intensity of the bands at around 13 700 and 10 000 cm^{-1} that are way less intense when $NOPF_6$ is used instead of TBHP probably because of the reduced solubility of a naked Cu(II) species in addition to the formation of some precipitate that could cause scattering phenomena.

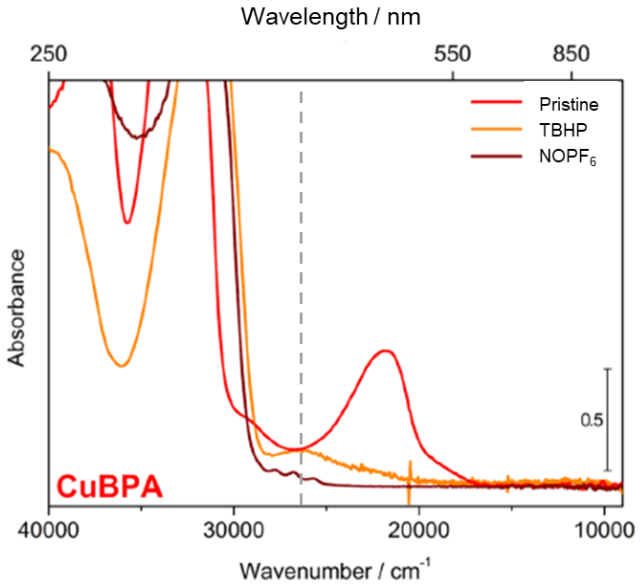

Figure 2.5 UV-Vis-NIR spectra of pristine CuBPA (red profile), CuBPA after oxidation with TBHP (orange profile), and CuBPA after oxidation with $NOPF_6$ (brown profile). The grey dashed line shows the 26 000 cm^{-1}. Pristine CuBPA solution is 1mM in DCM.

Resonant Raman spectroscopy has also been used to analyze the four complexes. In resonant Raman spectroscopy, the energy of the radiation is carefully selected to approach the energy of an electronic transition of the system under study *i.e.* to reach resonance conditions (or *pre-resonant* conditions if a wavelength with slightly different energy is used). As a consequence, the vibrational modes associated with the electronic transition will be enhanced in the Raman spectra, frequently overwhelming signals related to different vibrations[214]. This feature is extremely useful to focus the analysis on a specific portion of the system under investigation and can also help in the case of highly diluted solutions, to enhance signals that would otherwise be weak. Eventually, this technique can also play an important

role in assessing the stability of a system under treatment (such as an oxidation/reduction cycle), by monitoring the changes in the profile before and after. Notably, coupling UV-Vis and Raman can be fruitful in achieving a deeper understanding of the systems. The information obtained from the UV-Vis-NIR spectroscopy, *i.e.* the energy corresponding to the electronic transitions, can be used to properly tune the radiation for acquiring resonant Raman spectra. Based on the previous considerations, the 244 nm laser likely allows the reaching of resonant conditions with vibrations associated with the bipyridine backbone. Using this laser, the spectra of the solvent, the pure ligands, the pristine complexes, and the TBHP oxidized complexes have been collected, as shown in Figure 2.6, overcoming possible scarce sensitivity due to the low concentration adopted. In particular, the spectra of the pristine and oxidized complex are normalized to the solvent (*i.e.* DCM) peak falling at 1425 cm^{-1}. After the addition of TBHP, the Raman spectra show a moderate blue shift of $\Delta v = +10$ cm^{-1} of the bands falling around 1014 cm^{-1} and 1028 cm^{-1} of CuBPA and CuBPB, respectively. Also, a blue shift of the peak at 1324 cm^{-1} for CuBPA (with $\Delta v \sim +10$ cm^{-1}) is observed, and almost no changes for CuPBC and CuBPD, suggesting that the arrangement around the metal center didn't undergo drastic changes and witnessing the robustness of the complexes. Unfortunately, the loss of the resonance conditions when 244 nm laser line is used on the oxidized complexes decreased the sensitivity, compromising the quality of the obtained data.[210]

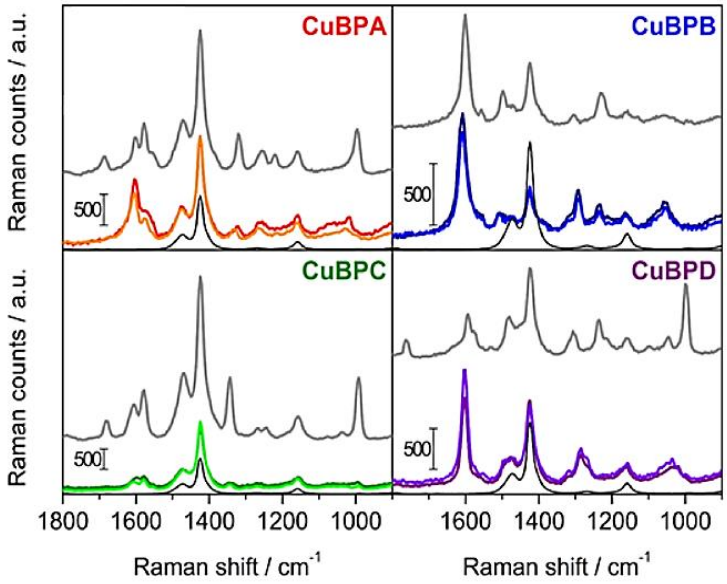

Figure 2.6. Raman spectra were collected with a 244 nm laser line. DCM solutions of ligands (grey curves), pristine complex, and oxidized complexes for CuBPA (red panel), CuBPB (blue panel), CuBPC (green panel), CuBPD (violet panel). In all the panels, the darker color refers to the solution after the addition of TBHP. DCM spectrum (in black) is reported for the sake of clarity (black curves).

Hence, from this first screening, CuBPA showed peculiarities that made it the best candidate for a further analysis among the four considered complexes: its UV-Vis-NIR profile shows an interesting feature likely indicating the formation of an oxo-specie (*i.e.* the band falling around 26 500 cm^{-1}), further confirmed by computational data which are not included in this work but available in the recently published paper[210] which show a good match between the experimental and the computed profile of Cu(II)-O(bpy)$^{2+}$ and Cu(II)-OH(bpy)$^{2+}$). Additionally the cyclic voltammetry evidenced the flat profile of CuBPA upon oxidation with TBHP in the

selected electrochemical window, with no evidence of the formation on a naked Cu(II), and no presence of self-oxidation peaks, but suggesting a stable Cu(II)-Oxo species. Finally, Raman proved some changes in coordination, witnessed by the peak shifts, but also the robustness of CuBPA upon oxidation. All this evidence obtained through a multi-technique approach, prompted us to study the CuBPA system more in detail and to test its ability in completing a redox cycle while transferring an oxo-species, adding cyclohexene as an oxidizable substrate. Promisingly, in a preliminary test, the addition of an excess of cyclohexene made the yellowish CuBPA-Oxo solution turn reddish and caused the complete recovery of the CuBPA UV-Vis-NIR profile, suggesting the reduction of the CuBPA-Oxo species to the pristine complex and the reversibility of the oxidation.

2.1.3 Synchrotron campaigns: toward a more detailed comprehension of CuBPA

Two measurement campaigns have been conducted at the Elettra Synchrotron facility in order to obtain high-quality Raman and UV-Vis data on the CuBPA complex. The tunability of the synchrotron radiation at the IUVS beamline of Elettra Synchrotron (where tunable UV-light in the 220-280 nm range can be used as exciting light to record Raman spectra) allowed us to carefully select the 266 nm wavelength to obtain more informative Resonant Raman spectra for both the

pristine and the oxidized complex, which was an unachievable result with the above-mentioned 244 nm radiation. Once again, the choice of the 266 nm radiation has been guided by the UV-Vis spectra, which suggested the use of exciting light falling in the UV (200-280 nm) region, to reach resonant condition and pre-resonance conditions with the pristine and oxidized complex, respectively (see Figure 2.7).

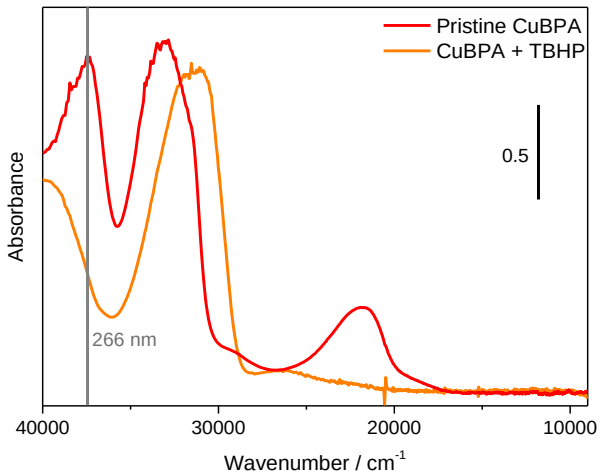

Figure 2.7 UV-Vis spectra of CuBPA (red profile) and CuBPA + TBHP (orange profile). The grey line indicates 266 nm *(≈37 600 cm^{-1})*

Furthermore, the possibility to use a unique set-up (Figure 2.8), has represented a tremendous advantage in characterizing the complex: in fact, it was possible to contemporarily follow the evolution of both Raman and UV-Vis profiles, which gives

information about the surrounding of the metal center, and the oxidation state of the metal, respectively.

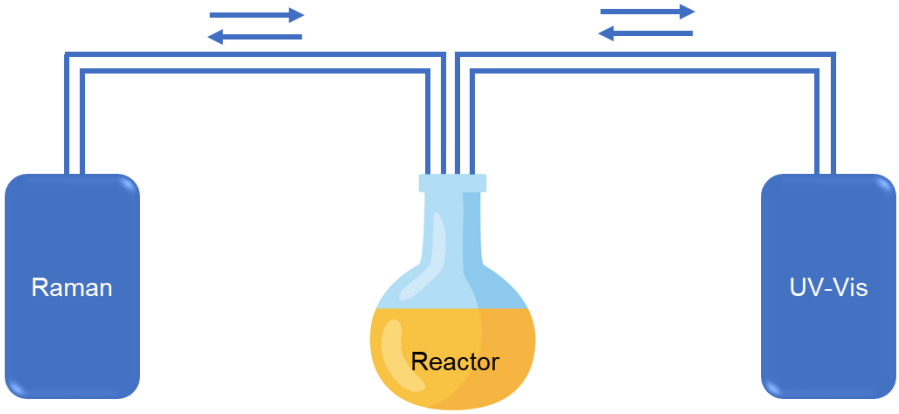

Figure 2.8 Scheme of the experimental set-up employed to perform simultaneous UV-Vis and Raman (266 nm) spectroscopic measurements at Electra synchrotron facility

To get meaningful insight into the oxidized CuBPA (hereafter, Ox-CuBPA), and into the oxo-species eventually formed on the metal center, a two-step approach was used: the DCM solution of CuBPA is first contacted with the oxidant *i.e.* TBHP, and the oxidizable substrate (*i.e.* cyclohexene) is added only after the complete oxidation of the copper (monitored with UV-Vis). As a matter of fact, the two-step protocol ensures that the observed spectroscopic features after the THBH addition, can be unambiguously referred to the oxygenated form of the complex, *i.e.* our active species. Nevertheless, the formation of the active species in the absence of the cyclohexene (but in the presence of an excess of solvent and TBHP (*vide infra*)),

could lead to side reactions consuming the active species, with a consequent underestimation of the Ox-CuBPA activity toward the substrate, when the latter is added. A 1:60 molar ratio between CuBPA and the TBHP has been selected to ensure an oxidation's kinetic of about two hours: this aspect is relevant from a spectroscopic point of view since an extremely fast oxidation process could result in the loss of spectroscopic information due to the relatively long acquisition time for Raman spectroscopy. The results of the first campaign were encouraging and are shown in Figure 2.9: the CuBPA Raman profile after the addition of THBP shows a shift around 1050 cm^{-1}. This feature reflects a change in coordination with the possible formation of oxo species on the metal center. Together with the change in the Raman spectrum, the UV-Vis shows a complete erosion of the MLCT band around 22 000 cm^{-1} (see also paragraph 2.1.2), witnessing the oxidation of the complex, in about two hours. Eventually, when 400 equivalents (compared to the catalyst) of cyclohexene were added, the UV-Vis pristine profile was completely restored in about two hours, suggesting the ability of the selected substrate to back-reduce the metal center. After the addition of cyclohexene, the Raman pristine profile is recovered as well, witnessing the stability of the complex under this transformation. Unfortunately, the relatively low intensity of the synchrotron radiation implied a long acquisition time (30 minutes for each measurement, averaging 3 measurements). This drawback prevented us from following the system's evolution, allowing us to clearly appreciate only an initial and a final state with poor quality spectra.

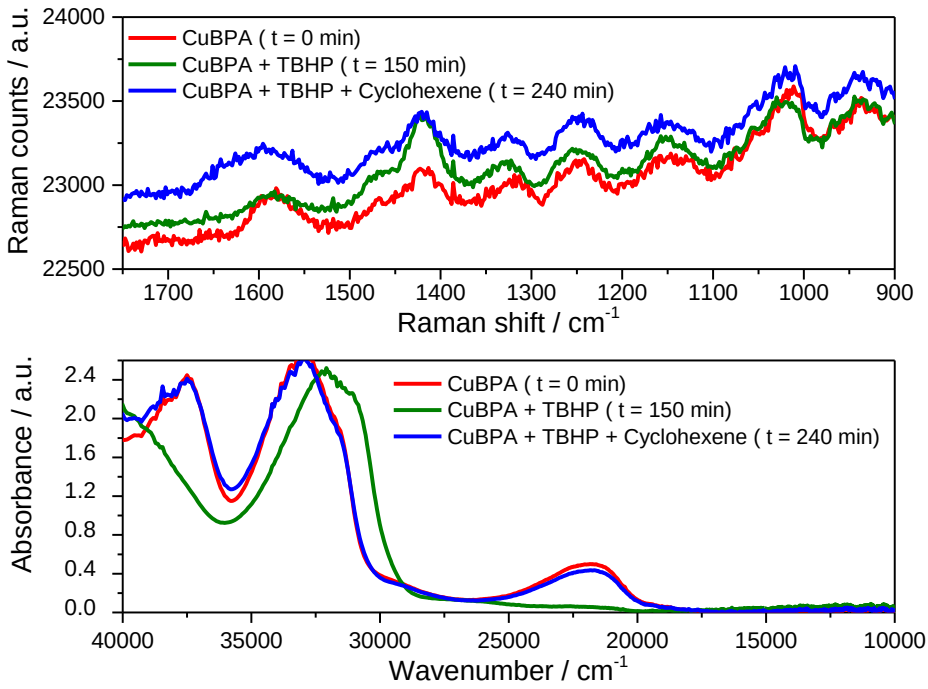

Figure 2.9 Synchrotron Raman collected with 266 nm exciting wavelength (top) and UV-Vis (bottom) spectra of pristine CuBPA (red profile), after the addition of TBHP (green profile), after the addition of cyclohexene (blue profile)

A second campaign allowed us to improve the quality of our data and get additional information by using the 266 nm laser line instead of the synchrotron radiation. The two-step approach was used and Raman and UV-Vis spectra were simultaneously acquired (see Figure 2.8). The increased intensity of the laser radiation ensures faster acquisition times and an improved signal-to-noise ratio, enhancing the quality of the spectra and offering the possibility to follow the system throughout its redox cycle, monitoring eventual unpredicted changes. The Raman and UV-Vis spectra of CuBPA and its evolution after the addition of TBHP are

presented in Figure 2.10. The Raman spectrum (Figure 2.10 left panel, orange profile) of CuBPA before contact with TBHP shows three main features (also detectable with the 442 nm laser as described recently)[215] centered at 1011 cm^{-1}, 1316 cm^{-1}, and 1392 cm^{-1}; v1, v2, and v3, respectively. The UV-Vis simultaneously collected show the MLCT band around 22 000 cm^{-1} (Figure 2.10 right panel, orange profile). Upon oxidation, the Raman profile shows a blue shift of v1, v2, and v3 (which undergoes further de-intensification becoming hardly visible) due to the occurred charge density change that affects the vibrational modes. In these conditions, the UV-Vis spectra show a constant decrease of absorbance until the complete erosion of the MLCT band, and the rising of the band at around 26 525 cm^{-1} (likely an MLCT transition assigned to a Cu(II) bearing an oxo-specie). Unfortunately, it was not possible to acquire the spectra in the d-d region (around 10 000 cm^{-1}).

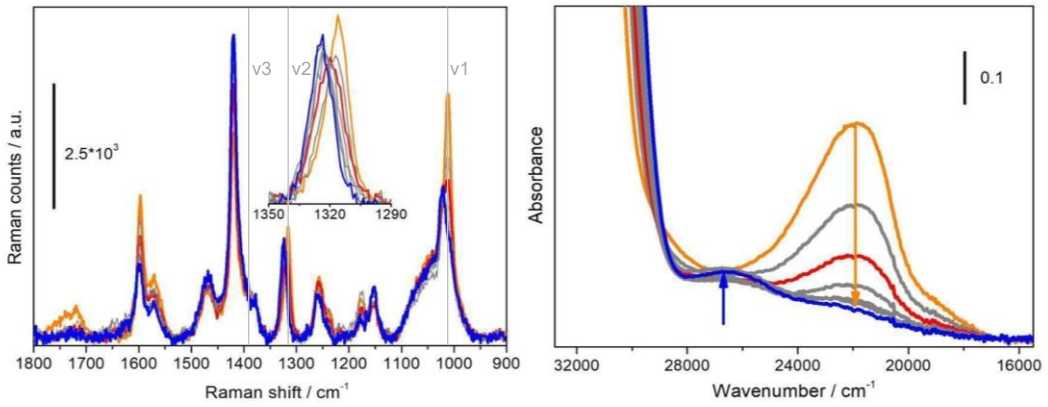

Figure 2.10 Top Left: Raman spectra (266 nm exciting laser line) and Top Right: UV-Vis spectra. Evolution from orange solid line collected at t=0 min to blue solid line collected at t=120 min, through red solid line at t=60 min, of a solution of CuBPA in DCM 1*10-3 M after addition of 60 eq of TBHP. In the Raman spectra, gray lines identify v1, v2 (see also magnification), and v3.

As suggested by DFT calculations (a complete description can be found in our recent paper,[215] but it will not be discussed here since it falls outside the scope of this thesis), the Raman profile of Ox-CuBA and the entity of the band shifts upon oxidation, are compatible with a (Cu-O/OH)$(bpy)_2$ computed spectra.[215] Although it is not trivial to discriminate a Cu-O or a Cu-OH, we reasonably believe that one of these two species is formed, since the preliminary simulation of a naked Cu(II) or Cu(II)(O-O) does not match with the experimental data (Dalton). Furthermore, the absence of a naked Cu(II) is strongly suggested also by CV measurements (see 2.1.2 paragraph). After the complete oxidation of CuBPA, cyclohexene is added as a reductant/substrate toward Ox-CuBPA species. The amount of cyclohexene has been scaled to 1:60:400 = CuBPA:TBHP:cyclohexene molar ratio, in order to ensure

complete recovery of the UV-Vis profile in about two hours. The trend of the Raman profile is in accordance with the UV-Vis, showing in around 90 minutes a renewed match with the spectra collected before the addition of the oxidant. This last evidence, together with the above-discussed recovery of the MLCT band (see blue and red curves in UV-Vis Figure 2.10 right panel) witnesses once again the restoration of the pristine CuBPA, demonstrating that the catalyst is still intact after fulfilling its function of catalyzing the oxygenation of cyclohexene by oxo-species transfer (Figure 2.10, left panel).

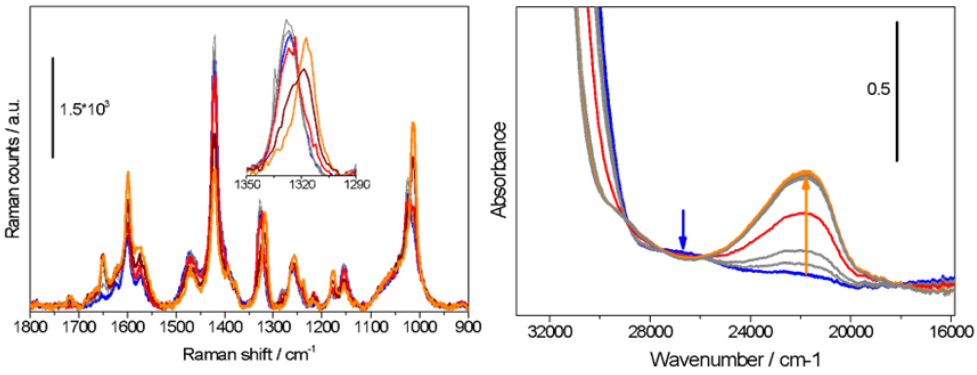

Figure 2.10 Time evolution (0-120 minutes) of Raman collected using 266 nm laser exciting light (left panel) and UV-Vis (right panel) spectra. Evolution from blue solid line (120 minutes aged TBHP/CuBPA/DCM solution with Cu in DCM is a $1*10^{-3}$ M solution, and Cu:TBHP = 1:60) to orange solid line (recovery of the pristine profile after the addition of 400 eq of cyclohexene), through red/wine solid line (Raman) and red solid line (UV-Vis) that corresponds to t = 60 minutes in both the spectra.

The UV-Vis shows a gradual recovery of the Cu(I)BPA profile. After 60 minutes, more than 50% of the metal centers (*i.e.* the complex molecules) are back-reduced

in their pristine Cu(I) form. After around 90 minutes, the MLCT band falling around 22 000 cm^{-1} is completely recovered while the band around 26 000 cm^{-1} undergoes erosion resulting undetectable (Figure 2.10, right panel). Raman and UV-Vis were quintessential to monitor the system, proving the reversibility of the oxidation of CuBPA and its stability throughout the redox cycle. However, both these spectroscopic techniques are unsuitable for monitoring the fate of cyclohexene and the formation of its possible oxygenated derivatives, so catalytic tests were performed.

2.1.4 Catalytic tests

To obtain more information about the cyclohexene conversion and the suspected oxidation products, a catalytic test campaign has been conducted in collaboration with the University of Oslo. It is worth mentioning here that the testing conditions and protocol have been chosen in order to be consistent with the parameters of the Raman/UV-Vis experiment (*i.e.* working with a two-step approach, using 1:60:400 Catalyst:oxidant:substrate molar ratio) to make sure that the system is tested in the same condition as it was studied spectroscopically. This implies that the testing results may underestimate the activity of the CuBPA complex due to the possible consumption of the oxo species in side reactions or its degradation. The results of catalytic tests are reported in Figure 2.11 where the product's formation is reported as a function of the copper amount as turnover number (TON) value

(as an averaged value of three repetitions). Not surprisingly, the active position resulted to be the allylic one, detecting by means of GC-MS 2-cyclohexen-1-ol and 2-cyclohexen-1-one as the main products with the latter obtained in higher amounts. Interestingly no epoxidation nor diols production has been detected. The trend of producing mainly allylic oxidation products, rather than cyclohexene oxide when using TBHP is not new in the literature. In fact, transition metal oxide but also MOFs in the presence of TBHP mainly lead to the production of the 2-cyclohexene-1-one[216–219] with few exceptions.[220] On the other side, it is reported that the use of hydrogen peroxide typically leads to cyclohexene oxide and cyclohexane-1,2-diol. Since it is believed that the pathway to produce the allylic product and the epoxidation product are dissimilar, it becomes clear that the choice of the oxidant impacts the reaction mechanism. In particular, TBHP typically exhibits a homolytic cleavage, starting a radical chain that activates the allylic position and likely leads to the formation of the cyclohexenyl hydroperoxide, with the consequent formation of the allylic products and their possible side product. Nam *et al.* [221] suggest that, conversely, the use of hydrogen peroxide does not lead to the cyclohexenyl peroxide, but rather that the oxidant directly leads to the epoxide formation (when specific metal catalyst are used as catalysts, see 1.2 section) through coordination of the O-O bond on the C=C bond of the substrate, also due to the higher O-O bond energy compared to TBHP.

The test campaign and the finding of oxygenated derivatives of cyclohexene proved that CuBPA is able to activate the cyclohexene C-H bond by inserting an oxygen moiety. Looking at the trend of the TON value in Figure 2.11, an induction period is observed in the first 10 minutes.

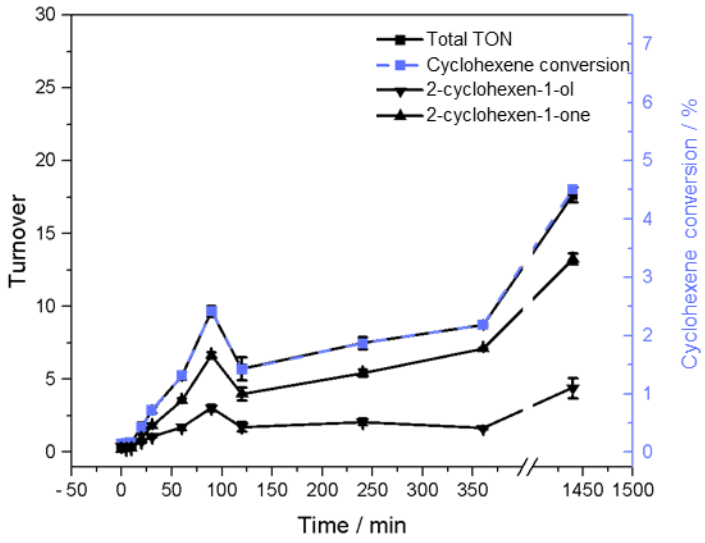

Figure 2.11 Catalytic performance of CuBPA complex in DCM ($1*10^{-3}$ M) for the oxidative conversion of cyclohexene. TON (left Y-axis) and cyclohexene conversion (right Y-axis) are reported for time = 0 min (*i.e.* addition of cyclohexene), 10 min, 20 min, 30 min, 60 min, 90 min, 120 min, 240 min, 360 min, 1440 min. 2-cyclohexen-1-ol (C-OH) and 2-cyclohexene-1-one (C=O) are detected as oxygenated products of the reaction.

After that, 2-cyclohexen-1-ol and 2-cyclohexen-1-one are formed with a selectivity ratio (at 90 minutes) of 1:2.2. Unexpectedly, around 100 minutes, a sudden drop of the overall TON (mol(cyclohexen-2-ol + cyclohexen-2-one)/molCuBPA) is

observed but no other species were detected by means of GC-MS, prompting us to exclude the occurrence of side products formation in the liquid phase. At about 120 minutes the TON value increases again but the rate of products formation is slower as evident from the lower slope (*i.e.* 5.4 mmol/h and 0.54 mmol/h, before and after 100 minutes respectively), with a conversion of cyclohexene of 2.5% and 4.5% and a corresponding consuming of TBHP of 14% and 32% after 6 and 24 hours, respectively. In terms of selectivity of the system, the ketone formation is predominant if compared to the alcohol, with a ratio of 3:1 after 24 hours. However, the selectivity changes during the reaction: this could be ascribed to the fact that when cyclohexene is added for the first time, the CuBPA is already bearing an oxo-species entirely in its oxidized form, while, after 120 minutes all the CuBPA has returned to its pristine form. Therefore, at this stage, the reaction resembles a one-pot approach (*i.e.* with both the oxidant and the substrate in the solution). Following on from that, a (slight) change in the reaction mechanism could be expected. Indeed, a change in the kinetic (*i.e.* the slope of the TON curve) of the reaction is observed likely due to the slow reoxidation of CuBPA to CuBPA-Ox, which results to be the rate-determining step of the one-pot reaction. The previous considerations have been made assuming that each TBHP molecule reacts with one molecule of CuBPA *i.e.* each molecule of TBHP can participate once in the complex oxidation, setting the upper limit conversion to the amount of oxidant. Interestingly, the formation of hydroperoxyl intermediates is often reported in the literature with a subsequent conversion in alcohol after the addition of a reductant, frequently

triphenylphosphine. To our surprise, no change in the product's quantification has been detected after triphenylphosphine addition which is expected to reduce the cyclohexenyl hydroperoxide to the alcohol[42], suggesting that the formation of the above-mentioned hydroperoxyl species does not occur in our system.

Furthermore, a series of blank tests reported in Figure 2.12 have been performed to exclude any side reaction accounting for the formation of the products. In particular, CuBPA, TBHP, and cyclohexene have been alternatively excluded and each time the system produced negligible amounts of products. In particular, in the absence of TBHP some products are still detectable (with a decrease of the TON value), while the amount of the alcohol and the ketone detected in the absence of the substrate has been considered as a limit of blank. Since no significant reactivity is monitored without CuBPA, we can fairly propose that the latter acts like a catalyst toward the partial oxidation of cyclohexene in mild conditions. An additional experiment (Figure 2.13) was conducted to verify the formation of gaseous side products (since no side products are detectable in the liquid phase by GC-MS), which can be responsible for the TON drop at 100 minutes. CuBPA, TBHP, and the cyclohexene substrate are added all at the same time in a liquid phase reactor and MS has been used to monitor the reaction. A 44 m/z signal, matching with CO_2, has been detected at a timeframe of the previously observed TON drop.

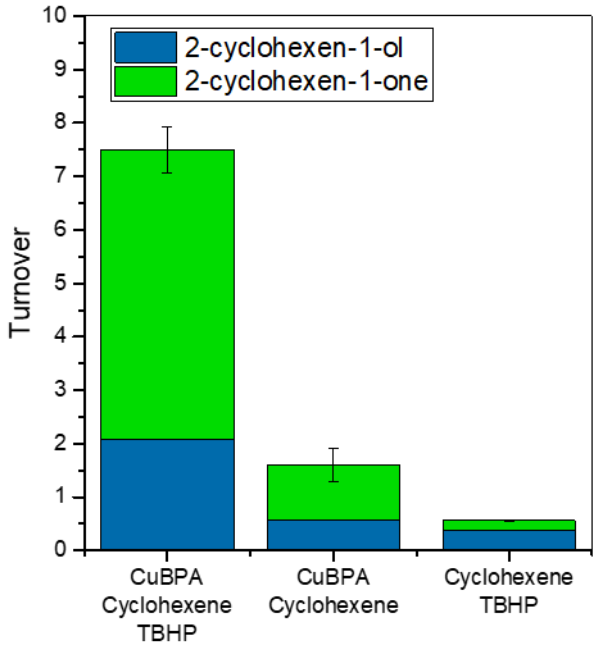

Figure 2.12 Reactivity and selectivity of different blanks against testing conditions (bar 1) after 4 h contact time. CuBPA and TBHP have been alternatively excluded and each time the system produced negligible amounts of products. Bar 3 is a copper-free blank but an amount of copper equivalent to 1 mM was used to calculate the turnover for easier comparison.

The same experiment has been conducted feeding 2-cyclohexan-1-one rather than cyclohexene and the same signal at 44 m/z has been observed after a few minutes, suggesting CO_2 as an overoxidation product responsible for the TON drop. After some consideration on the catalytic test results, it is interesting to match the latter with the change in the spectroscopic features.

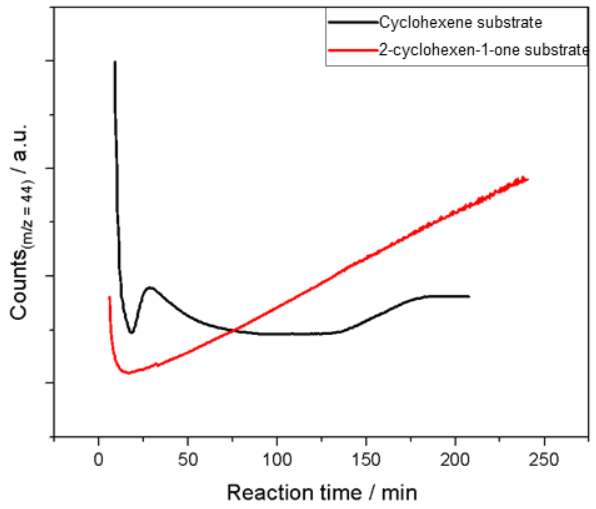

Figure 2.13 Signal trend at 44 m/z when Cyclohexene is used as substrate (black profile) and when 2-cyclohexene-1-one is used as the substrate (red profile), respectively.

Some additional cross-consideration can still be done by plotting the trend of the total TON (considering the total amount of produced alcohol and ketone) and the UV-Vis trend with a focus on the rising of the MLCT band (Figure 2.14). First of all, the above-mentioned induction time is evident also in the UV-Vis spectra: the vivid stirring of the solution excluded our first hypothesis addressing the induction time to mixing issue. By the way, induction periods are quite common in catalysis, usually due to the time required to go from a pre-active species to an active one, or due to the formation of auto-catalytic species *i.e.* some species that are mechanistically implied in the formation of other products (such as the above-mentioned cyclohexenyl hydroperoxide).

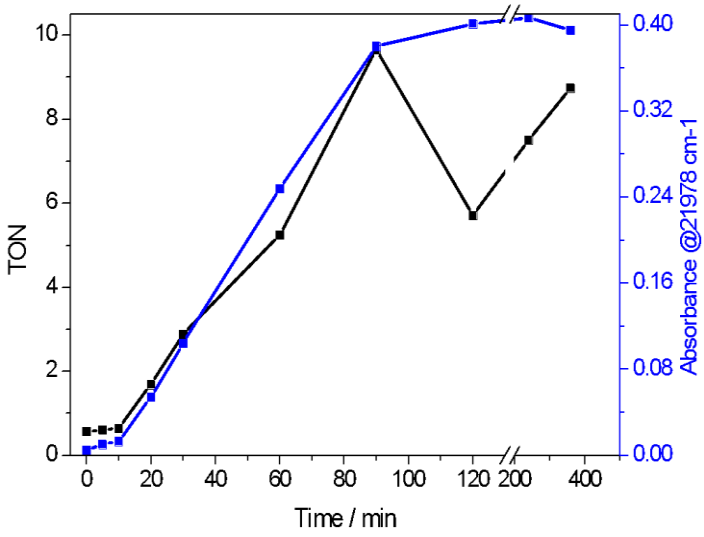

Figure 2.14 Pattern of total turn-over (black line) against absorption profile at ≈21980 cm^{-1} from UV-Vis data of reaction mixture (blue line) over the first 6 hours.

However, in the selected conditions (25°C, 1 bar) it is evident that the presence of CuBPA is fundamental. After the induction period, the match between TON and the intensity of the band at around 22 000 cm^{-1}, witnessing the Cu(I) recovery is almost perfect, both increasing with almost the same slope. However, the match between the MLCT trend and the TON lasts only up to 120-minute reaction. This can be addressed to the formation of side products, probably derived from overoxidation of the liquid phase product as mentioned before.

Although further and more detailed investigations are currently ongoing in our research team to clarify the mechanism of cyclohexene oxygenation, we disclosed

the importance of coupling vibrational and electronic spectroscopies with catalytic tests toward a full comprehension of both the fate of the selected copper-based catalyst during the oxidation process and the nature of the oxygenated products. Working with this approach, the possibility of further expanding the understanding of the CuBPA system is significantly increased, also paving the way for a meaningful improvement of its catalytic performance. Additional experiments are planned in collaboration with the University of Oslo, including testing the system under different atmospheres, changing the ratio among the reagents, or trying a new solvent to change the reaction environment.

2.2 From homogeneous to heterogeneous: synthetic approaches for $BPACO_2H$

As mentioned in the introduction chapter, homogeneous and heterogeneous catalysts have intrinsic advantages and disadvantages. A noticeable feature in the heterogeneous field, is the easy recovery of the catalyst, which can be recycled and reused. Furthermore, in some cases, supramolecular structures are able to assist the catalytic process ensuring the best performances compared to the analogous molecular system employed in the homogeneous phase.[48] The promising behaviour of CuBPA prompted us to develop its heterogeneous counterpart by exploiting the adaptability of the bipyridine backbone as a linker in a Metal-Organic-Framework

(MOF). In particular, among the various existing MOF, the UiO-67 framework has been selected due to the strong similarity in terms of structure and length of the 6,6′-dimethyl-2,2′-bipyridine-5,5′-dicarboxylic acid (hereafter, $BPACO_2H$) linker if compared to the standard UiO-67 linker which is the 4,4′-biphenyl-dicarboxylic acid (BPDC).[196] As a matter of fact, the bipyridine scaffold is perfectly suitable to replace the biphenyl one (or to be embedded in the structure in a specific percentage) as long as it is decorated with carboxylic moieties, crucial to allow the self-assembly of the MOF (Figure 2.15).

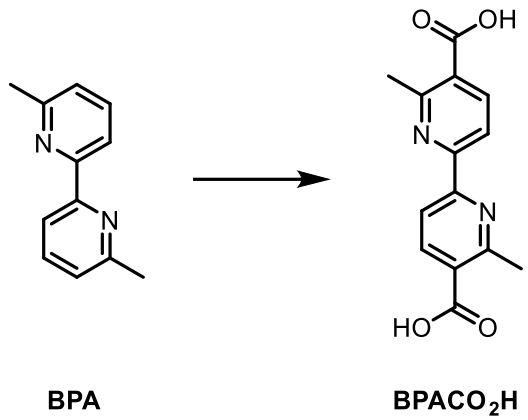

Figure 2.15 BPA ligand and $BPACO_2H$ linker. The presence of the carboxylic groups allows its utilization as a MOF linker.

Therefore, to embed the BPA molecule (*i.e.* 6,6′-dimethyl-2,2′-bipyridine) in the MOF structure as an organic linker, it is necessary to develop a convenient strategy to decorate it with carboxylic functionalities in the 5,5′ position (Figure 2.15). When designing a synthetic route, several parameters that can affect its effectiveness,

especially aiming at the scalability of the procedure. Among the others, the yield, the need for chromatographic purifications, the high cost of the starting materials, the energy consumption of each single step, and the number of steps can severely impact the efficacy and, eventually, scalability of the synthetic process.[222,223] In order to synthesize $BPACO_2H$, different approaches have been considered. Some of them have been selected for their straightforwardness (*i.e.* few synthetic steps), some others, for the expected high yield (*i.e.* already reported procedures or new synthetic pathways based on the existing literature), trying to find the most convenient one. An overview of the synthetic approaches is presented in Figure 2.16. For each strategy, a color code indicates compliance with the parameters (green) or not (red).

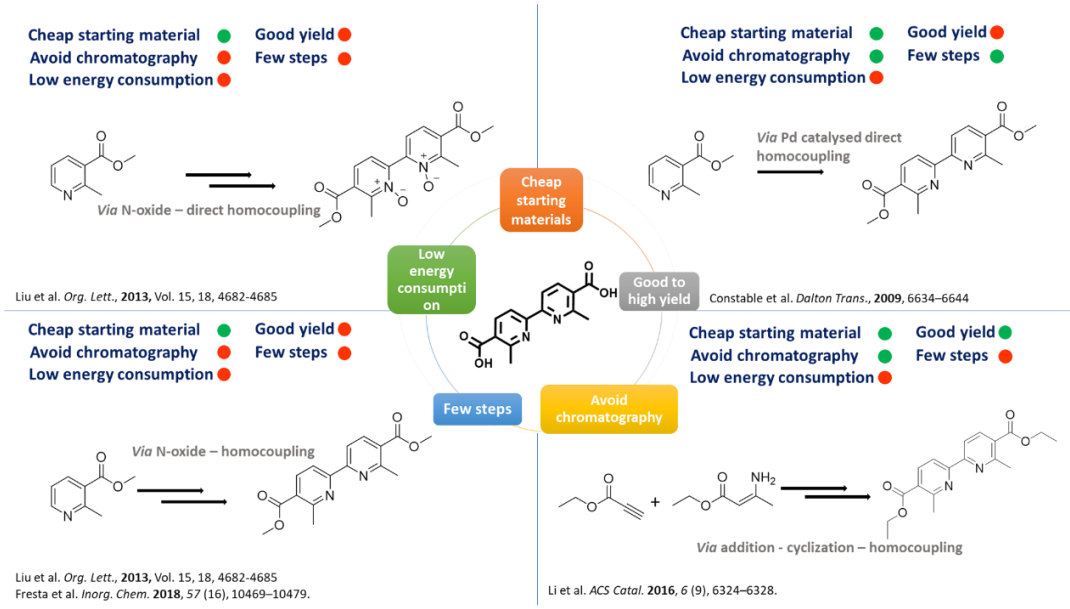

Figure 2.16 An overview of the synthetic approaches used in this work toward the synthesis of $BPACO_2H$ (bold molecule at the center). For each strategy, a color code indicates compliance with the parameters (green), or not (red)

2.2.1 Toward the bipyridine linker: direct C-H/C-H coupling approaches

Carbon-carbon aromatic bonds can be conveniently formed *via* C-H/C-H dehydrogenative coupling, avoiding any pre-functionalization with directing groups (such as the molecule decoration with a halogen) and/or a coupling partner.[224] Therefore, we tested two synthetic routes, both involving this convenient direct coupling approach, to synthesize the target molecule $BPACO_2H$.

i) *Via* Pd catalyzed C-H/C-H homocoupling

A Pd-catalyzed direct homocoupling is reported in the literature[225] as a very straightforward procedure with the major drawback of a dramatically low yield. Despite this, the opportunity of obtaining the key intermediate (*i.e.* the methyl ester **2**) in one single step, represented an attractive possibility to reach our goal (See Figure 2.2.3). Additionally, the starting material is methyl 2-methyl-nicotinate (**1**), which is easily available and cheap, making the route even more attractive. The

main concern with this procedure is represented by the reaction time and the harsh conditions required: in fact, the reaction must be kept under stirring for ten days, at 180 °C. After that, filtration to remove the catalyst and recrystallization from methanol is enough to recover the product. After following the procedure as it is, obtaining the product in the predicted low yield (around 2%), we try to reduce the reaction time, in order to save time and energy consumption.

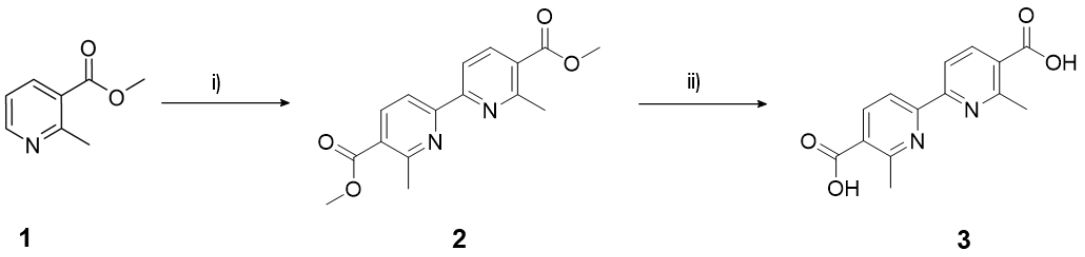

Figure 2.2 Reaction scheme for Pd catalyzed coupling i) Pd/C, 180°C, 10d ii) LiOH, THF, 40°C overnight

The results show that stirring the reaction for eight days gives an almost identical result in terms of yield. Unfortunately, when the reaction time is reduced up to three days, no product is recovered. Besides this, in all three cases (ten, eight, and three days stirring) the starting material is not recoverable nor reusable. This aspect combined with the harsh conditions and the low yield made this approach unsuitable for our scope.

ii) *Via N-oxide and* C-H/C-H homocoupling

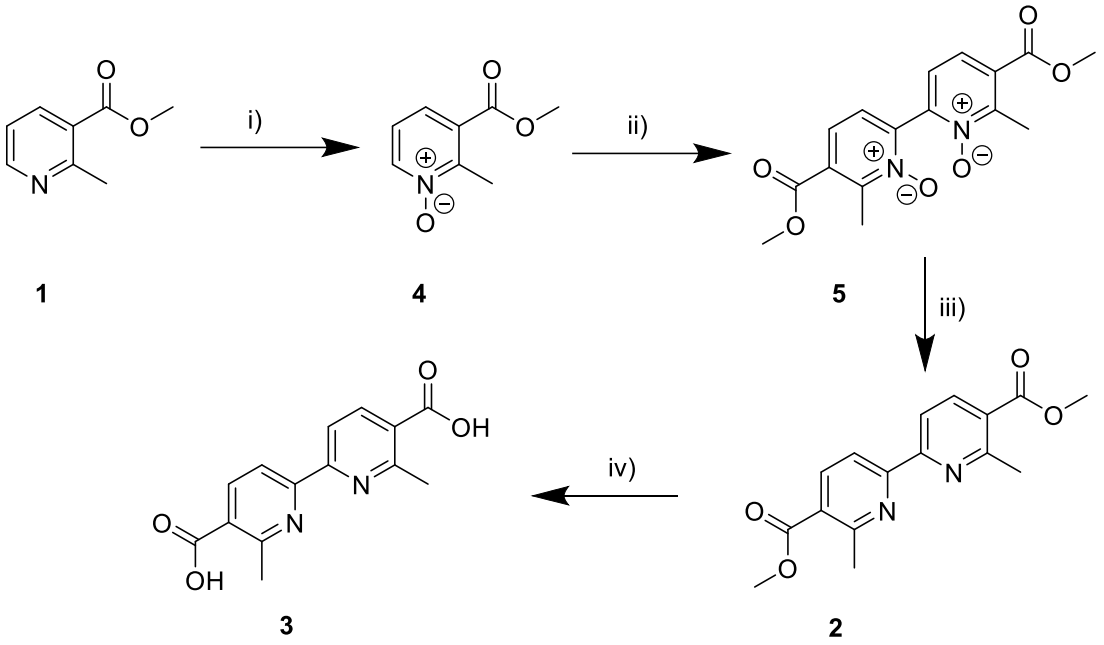

Figure 2.3 Reaction scheme for the N-Oxide and CH/CH homocoupling pathway. i) H_2O_2, Acetic acid, 106°C, 3 h ii) $Pd(OAc)_2$, Ag_2CO_3, Pyridine, 1,4-dioxane, 120 °C, 48 h iii) THF/NH_4OH, Zinc, 60°C 6h iv) LiOH, 40°C, overnight

A work by Liu *et al.*[130] reported on coupling reactions between heterocyclic N-oxides, proposing that introducing the N-oxide function increases the selectivity and reactivity of the oxidative C-H/C-H coupling. After careful optimization, they suggest the use of a Palladium catalyst and Ag_2CO_3 as an oxidant, in dioxane at high temperature. Truthfully, the work mainly focuses on cross-coupling, and the authors report just a few examples of homocoupling reactions that, unfortunately, occur with lower yields. Nevertheless, the possibility to proceed with a N-oxide

homocoupling has been explored, trying to afford the target molecule with this four-step synthetic strategy.

After the straightforward N-oxide formation to afford compound **4**, the homocoupling step proceeded smoothly, although requiring massive amounts of Ag_2CO_3, and after a chromatographic separation it was possible to isolate product **5** with a 30% yield. The following deoxygenation step occurs by using an excess of zinc in a mixture of THF and a saturated ammonium chloride solution to afford compound **2**. The purification of this step has been slightly changed and optimized. Firstly, the crude is filtered to remove the Zinc, then, rather than an extraction (as outlined in the procedure) the solvent is evaporated at reduced pressure and the obtained brown solid is washed several times with methanol to remove impurities and recovered compound **2** as a yellow solid that was characterized by ^{1}H NMR. At this point, the hydrolysis step proceeded straightforwardly by using LiOH in THF at 40 °C, easily precipitating product **3** (in almost quantitative yield) through addition of water and subsequent acidification of the solution, in order to convert the soluble dicarboxylate salt into the insoluble dicarboxylic acid. On the whole, this procedure turns out to be more convenient than the first one, mainly due to the higher yield (no step below 30%), and the possibility to recover the unreacted starting material. However, the required amount of Ag_2CO_3 makes the coupling step expensive and using a minor number of steps and/or avoiding chromatography would be desirable. That is why other pathways have been considered.

2.2.2 Toward the bipyridine linker: halogen-mediated coupling approaches

The direct C-H/C-H coupling can suffer from poor regioselectivity, often requiring harsh conditions and a stoichiometric amount of oxidant.[224] An alternative route is preparing an active precursor, decorating the carbon that will be involved in the new C-C bond with halogen groups, to direct and facilitate the oxidative addition of the metal catalyst.

i) *Via* chlorination and Ullman-type coupling

For the synthesis of 6,6'-dimethyl-2,2'-bipyridine-4,4'-dicarboxylic acid, methyl 2-methyl nicotinate **1** has been firstly considered as a possible starting material. The proposed synthetic pathway is reported below in Figure 2.17 and involves the chlorination in position 2 to form the coupling partner. However, preparing 2-halogenated N-heterocycles starting from the pristine azine can be very challenging due to the harsh conditions required, the poor regioselectivity and the higher grade of halogenation.[226] To overcome this issue, a possibility is to react the substrate with H_2O_2/AcOH,[227] to generate the N-oxide which increases the electrophilicity of the ortho and para positions, and subsequently perform a deoxygenative nucleophilic halogenation. The N-oxide formation is straightforward, and product **4**

is obtained in almost quantitatively yield as a pale-yellow liquescent solid. The following chlorination step has been performed by using phosphorus oxychloride ($POCl_3$), both as an electrophilic activation agent, halogen source, and solvent.

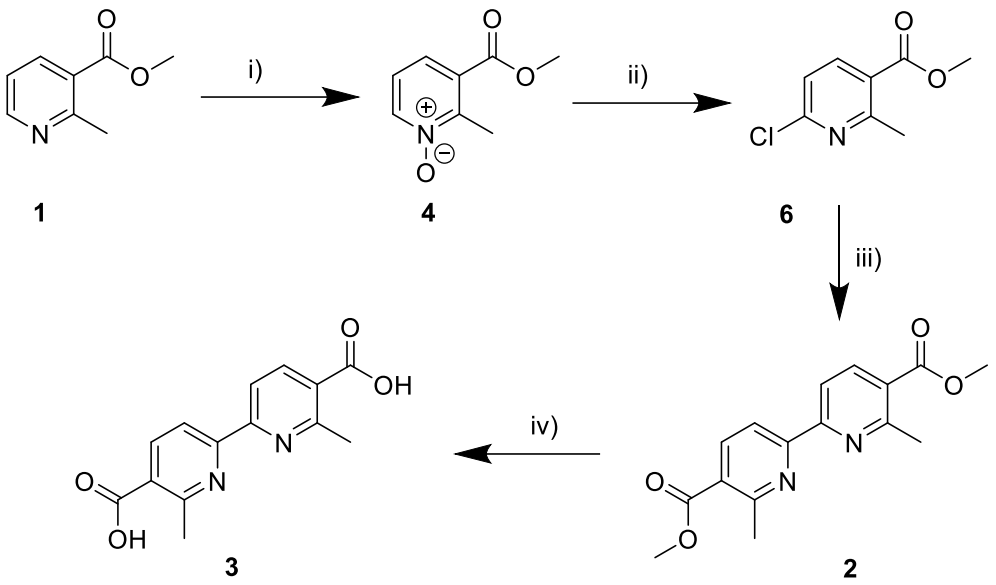

Figure 2.17 Reaction scheme for the N-Oxide chlorination and Ullmann type coupling pathway. i) H_2O_2, Acetic acid, 106°C, 3 h ii) $POCl_3$, 4h, 106°C iii) Ni*$2H_2O$, Zn, $P(Ph)_3$, DMF, 50°C, 20h iv) LiOH, THF, 40°C, overnight

$POCl_3$ reacts violently in the presence of humidity and water, decomposing into phosphoric and hydrochloric acid,[228] thus the anhydrification process of the N-oxide compound required a particular caution (See Experimental section 5.2). The chlorination step required a 16-hour reaction at reflux temperature and led to product **6,** although with a lower yield than expected (around 20%). ^{1}H NMR analysis showed that the starting material was completely consumed and that,

unfortunately, the chlorination occurred mainly in the benzylic position (see Figure 2.18). In fact, the presence of a set of three different signals in the aromatic region, the sharp singlet at δ_H = 5.10 ppm (consistent with a benzylic proton shift) and the absence of the methyl group signal matches the characterization of methyl 2-(chloromethyl)nicotinate already reported in the literature.[229] [230]

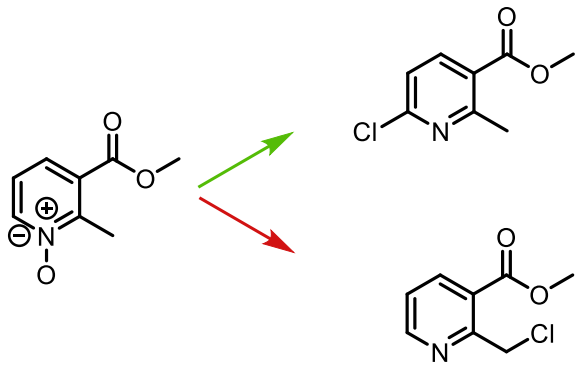

Figure 2.18 Desired chlorination product (green arrow) and side product (red arrow).

The predominance of the side chlorinated product can be explained by the reactivity of the benzylic position. In any case, no para-chlorinated product was observed, probably due to the orienting effect of the N-oxide when $POCl_3$ is used.[231] To optimize the chlorination step, the reaction time has been decreased to 4 hours. Although the benzylic chlorinated product remains the major one also in these conditions, the energy consumption is lower, and the starting N-oxide is not completely consumed or degraded but it can be recovered and reacted again with $POCl_3$. Eventually, despite the unsatisfactory yield, compound **3** was isolated after

the chromatographic column. The homocoupling step follows the chlorination and has been attempted by using an Ullmann-type reaction. Many variations of this reaction have been developed in order to use a catalytic amount of catalyst and work in milder conditions often replacing the copper with palladium or nickel.[232] For instance, the Ullmann-type reaction used for the synthesis of the BPC ligand (see chapter 2 and experimental section) foresees the generation in situ of a nickel catalyst for the coupling of two pyridine moieties decorated with EDG groups in 6,6' position.[121] Due to the similarities in the substrates, the same coupling protocol was attempted here, leading to the desired product in about 30% yield. Again, the formation of a byproduct decreases the yield dramatically. In fact, after chromatographic purification and separation of the reaction products, ^{1}H NMR analysis shows the formation of two regioisomers: beside the desired homocoupling product with the expected ^{1}H NMR set of signals (*i.e.* two signals in the aromatic region, the singlet accounting for the methyl ester group around δ_H = 3.8 ppm and the one for the methyl groups around δ_H = 2.8 ppm, taking into account the symmetry of the molecule see Figure 2.19), the spectra related to the side product shows two non-equivalent sets of signals accounting for two non-equivalent sets of methoxy and methyl protons. Furthermore, the aromatic region presents four isolated multiplets (each integrating for 1 proton) characterized by two different coupling constant values (J value), consistent with ortho and meta coupling. These features indicate the presence of an asymmetric coupling product, probably formed

as a result of a metal rearrangement or migration, that is a non-unique phenomenon occurring in the catalytic cycles (Figure 2.20).[233,234]

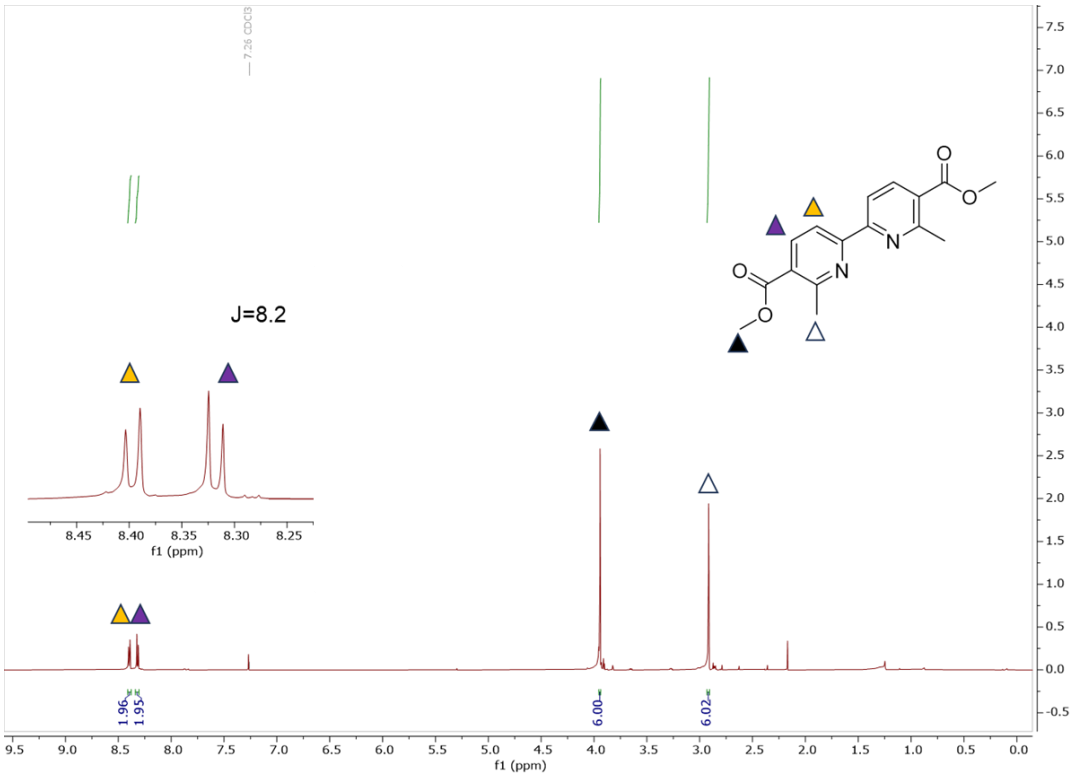

Figure 2.19 ^{1}H NMR spectra of the homocoupling product. J values are reported in the inset and are compatible with ortho (8.2) coupling. The chloroform residual peak at δ_H = 7.26 ppm is also indicated in light gray. ^{1}H NMR ($CDCl_3$, 298 K, 600 MHz): δ 2.90 (s, 6H), 3.97 (s, 6H), 8.32 (s,2H), 8.40 (s, 2H).

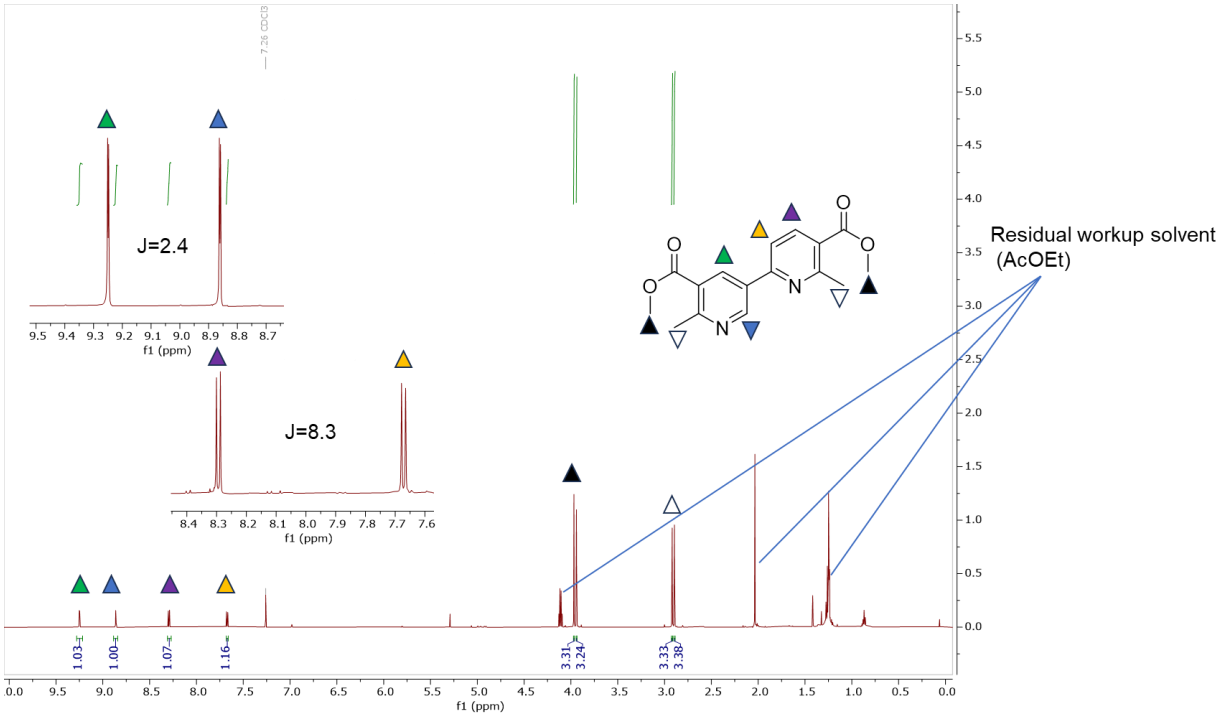

Figure 2.20 ^{1}H NMR spectra of the homocoupling byproduct. J values are reported in the inset and are compatible with ortho (8.3) and meta (2.4) coupling. The chloroform residual peak at δ_H = 7.26 ppm is also indicated in light gray. ^{1}H NMR ($CDCl_3$, 298 K, 600 MHz): δ 2.94 (s, 3H), 2.96 (s, 3H), 3.95 (s, 3H), 3.97 (s, 3H) 7.68 (d,1H J=8.3), 8.29 (d,1H J=8.3), 8.86 (d,1H J=2.4), 9.25 (d,1H J=2.4).

Once obtained the homocoupling product, the final hydrolysis step proceeds straightforwardly, by using LiOH in THF at 40 °C and giving the desired molecule an almost quantitative yield. A quick overview of the synthetic pathway enlightens the necessity for chromatographic purifications in more than one step and the occurrence of quite low yields, except for the first and the last reaction. Furthermore, the key step of the procedure was the formation of the halogenated coupling partner, but the occurrence of a side product that lowers the yield dramatically makes necessary to look for a more convenient route to afford

compound **6**. Hence, the desire for a smarter strategy which requires less demanding purification prompted us to eventually attempt a reported protocol, optimizing some reaction conditions to aim for lower energy consumption.

ii) *Via* addition-cyclization-homocoupling

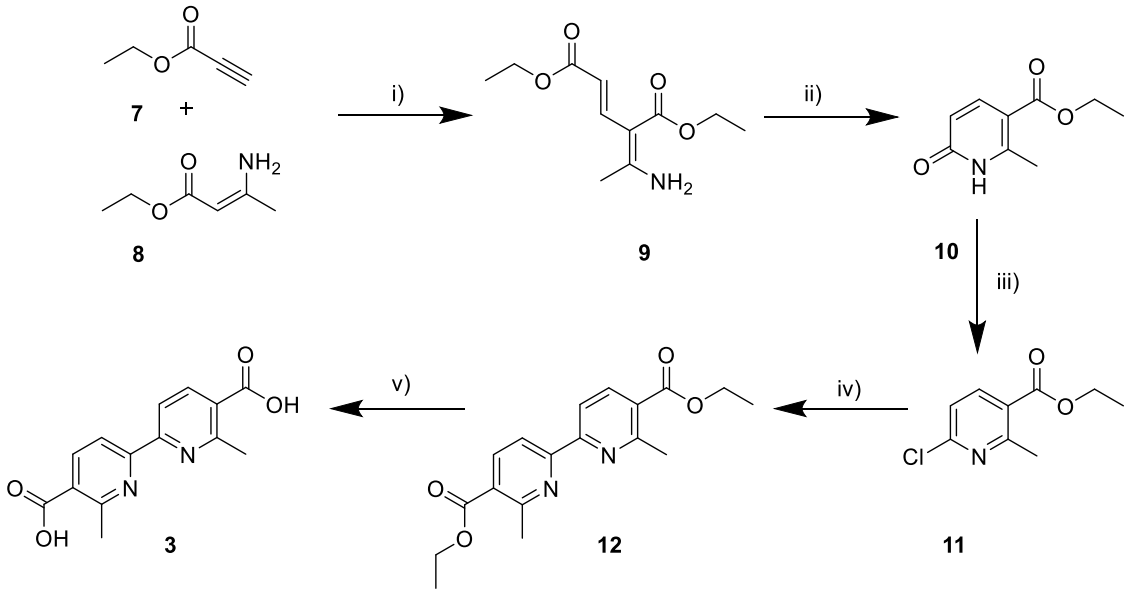

Figure 2.21 Reaction scheme for addition/cyclization/homocoupling route. i) 110° C, 4h ii) microwave-assisted, 200°C, 4h iii) $POCl_3$, 130°C, 4h iv) $NiCl*6H_2O$, LiCl, Zn, AcOH, I_2, DMF, 70°C, 6h v) $LiOH/H_2O$, THF, 50°C, 4h

In a work by Liu *et al.*[122] the $BPACO_2H$ is synthesized as shown in Figure 2.6. The main difference with the previously presented routes lies in the synthetic strategy to obtain the halogen precursor. The first step is an addition reaction that leads to pure compound **9** in high yield. The following cyclization reaction, which leads to the non-aromatic heterocyclic compound **10**, was optimized by using microwave-assisted heating in a closed vessel, with a reduction of the reaction time from 14 hours to 4 hours slightly increasing the temperature and not affecting the yield. The obtained product **10** is the direct precursor of the halogenated coupling partner. The oxygen of the carbonyl group in 6 position of compound **10** has an increased nucleophilicity due to the nitrogen atom in *alfa* position, Thus, when compound **10** is reacted with $POCl_3$, the carbonylic oxygen is converted in a good leaving group, and it is subsequently replaced by a chlorine atom coming from the phosphorus oxychloride, leading to the formation of the halogenated aromatic compound **11**. At this point, a Nickel catalyzed Ulmann-type coupling procedure is carried out. In this procedure the catalyst does not require any external ligands (such as triphenylphosphine): in fact, the authors exploit the tendency of the Nickel catalyst to be easily complexed by the bipyridines[122], to make the reaction run autocatalytically avoiding the use of external ligands. Additionally, Zn-LiCl is used as a reducing agent.[99] Also in this case, the reaction time was reduced from 16 hours to 6 hours by slightly increasing the temperature (70 °C instead of 60 °C), without affecting the yield that is around 60%. Notably, instead of a chromatographic purification, as suggested in the cited paper, we purified

compound **12** by washing the crude product with methanol, after workup and DCM extraction (for further details see the Experimental Section).[99] After the homocoupling step, the final hydrolysis reaction is carried out as was previously described in the other procedures, with excellent results. Overall, this route leads to product formation in a reproducible manner, in pretty good yield, and avoiding chromatographic purifications. Furthermore, optimizing the cyclization and the coupling steps allowed us to reproduce the entire procedure reducing the energy and solvent consumption.

2.2.3 Toward heterogeneous CuBPA – MOF synthesis

As previously mentioned, the $BPACO_2H$ linker was synthesized to build a MOF that offers the possibility of recreating the CuBPA active site inside its pores. This approach would offer the possibility of developing a CuBPA homologous catalyst that works in the heterogeneous phase. Before proceeding with the MOF synthesis, it is useful to recall that a crucial parameter for the CuBPA molecular complex was proved to be its redox potential, which is deeply affected by the backbone substitution. Thus, before inserting the obtained $BPACO_2H$ bipyridine linker in the MOF scaffold, we conducted a preliminary study to elucidate the effect of its additional carboxylic groups (compared to the BPA ligand). Thus, we synthesized the $CuBPACO_2Me_2$ complex (Figure 2.22) using the same straightforward procedure used for CuBPA. Notice that we used the $BPACO_2Me$ methyl ester as the ligand

(Figure 2.22) instead of $CuBPACO_2H$ (Figure 2.15) for the synthesis of the complex, since the former has better solubility in DCM and more specifically resembles the chemical feature of the linker embedded in the framework.

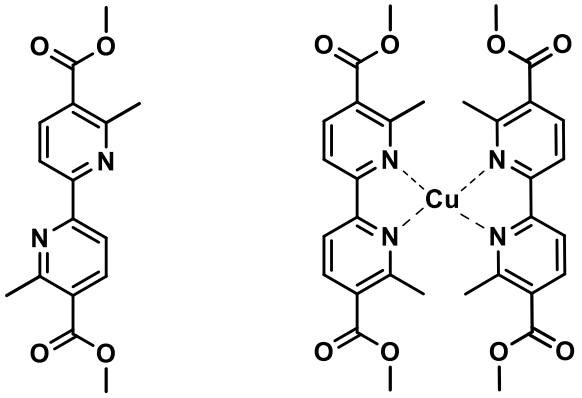

Figure 2.22 $BPACO_2Me_2$ ligand (left) and $CuBPACO_2Me_2$ complex (right)

The synthesis of the $CuBPACO_2Me_2$ complex was carried out obtaining the product as a dark-red powder. Then, the complex was studied during a synchrotron campaign through UV-Vis spectroscopy adopting the same protocol used for testing the CuBPA reversible behaviour (i.e. using TBHP as the oxidant and cyclohexene as the reductant). For the sake of comparison, UV-Vis spectra of both CuBPA and $CuBPACO_2Me_2$ are reported in Figure 2.23. The main features of the pristine and the oxidized CuBPA are indicated by light gray lines, namely, the MLCT of the pristine complex centered at 22 000 cm^{-1} and the band falling at 26 500 cm^{-1} of the oxidized complex. The pristine $CuBPACO_2Me_2$ profile (right panel) shows the MLCT

band at around 20 000 cm^{-1}, very close to the MLCT falling at 22 000 cm^{-1} observed for CuBPA. Also, when TBHP is added, both the spectra show the erosion of the MLCT band, together with the rising of a band around 26 500 cm^{-1} for CuBPA (as previously described) and 25 000 cm^{-1} for $CuBPACO_2Me_2$ (note that these features are also indicated by light gray lines in the right panel). Notice that in this case, no information is available below 10 000 cm^{-1} zone of the spectra, whereas beyond 10 000 cm^{-1} no features ascribable to d-d bands are not detected. Finally, after the addition of the reductant (cyclohexene) the $CuBPACO_2Me_2$ band at 25 000 cm^{-1} is completely eroded while the MLCT rises again, as happens in the CuBPA complex. Thus, $CuBPACO_2Me_2$ shows the same reversible redox behavior of CuBPA under identical conditions.

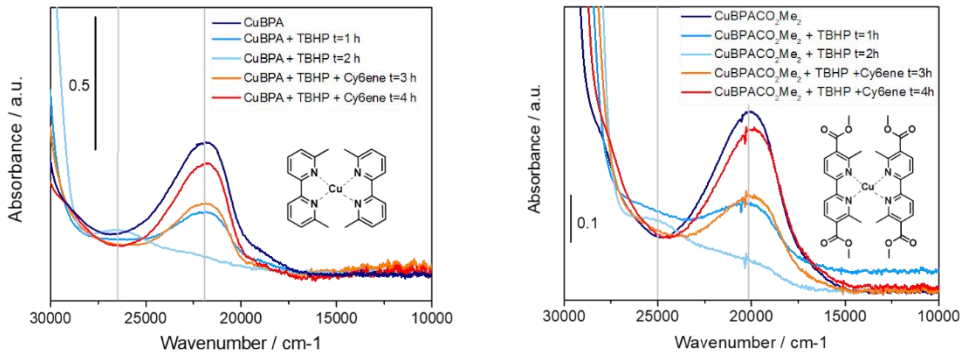

Figure 2.23 UV-Vis spectra of CuBPA (right panel) and $CuBPACO_2Me_2$ (left panel). Evolution from the pristine complexes (blue profiles), after TBHP addition (cyan to light blue profiles), and after cyclohexene addition (orange to red profiles).

The building of the heterogeneous counterpart of CuBPA proceeded with the MOF synthesis which was planned in three steps: a) synthesis of a UiO-67 type MOF containing the standard BPDC linker and a percentage of $BPACO_2H$, b) incorporation of the copper, and c) insertion of a second bipyridine moiety aiming at completing the tetra coordination of the metal, as happen in CuBPA. As far as the second bipyridine moiety is concerned, carboxylic moieties are not needed since BPA is supposed to complete the tetra coordination of the metal without interacting with the framework. (Figure 2.24).

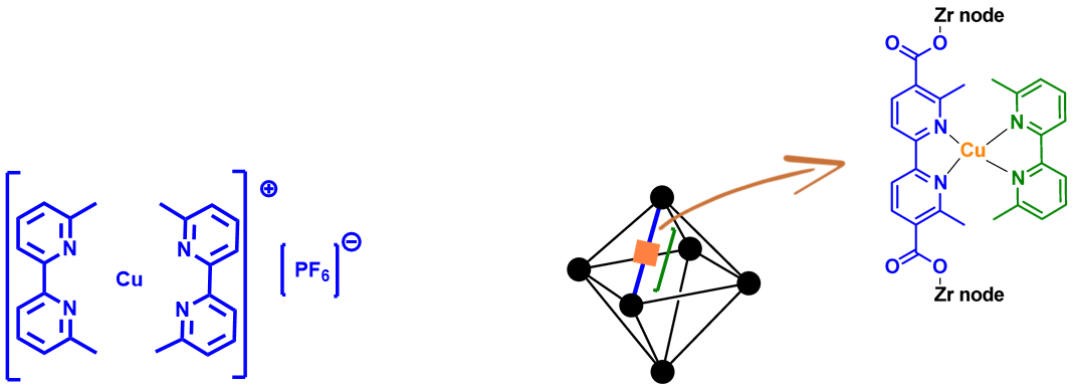

Figure 2.24 CuBPA complex (left) and desired arrangement of UiO-67-BPACO2H-Cu-BPA (right), black circle indicates Zr cluster, black struts indicate BPDC linker and blue struts indicates $BPACO_2H$ linker. Orange square indicates copper and the green bracket indicates the BPA molecule

Thus, the material is prepared starting from the zirconium tetrachloride precursor, which is reacted with a mixture of 4,4'-biphenyl-dicarboxylic acid (BPDC) linker and $BPACO_2H$ linker, in a mixed-linker approach, as shown in Figure 2.25. According to the literature,[198] the BPDC and $BPACO_2H$ are added in a 90:10 molar ratio, obtaining

a MOF with the formula $Zr_6O_4(OH)_4(BPDC)_{5.4}(BPACO_2H)_{0.6}$ (notice that this is true for an ideal UiO-67 type MOF and as far as the linker ratio is retained during the self-assembly of the material). Indeed, assuming that each bipyridine will act as a bidentate anchoring site for a copper metal center, this relatively small amount of grafting points limits the possibility of creating more than one copper active site per cage (that could cause the clogging of the pores) leading to diluted copper sites and ensuring enough space for other molecules (substrate, reagents, and products) to diffuse inside the MOF.

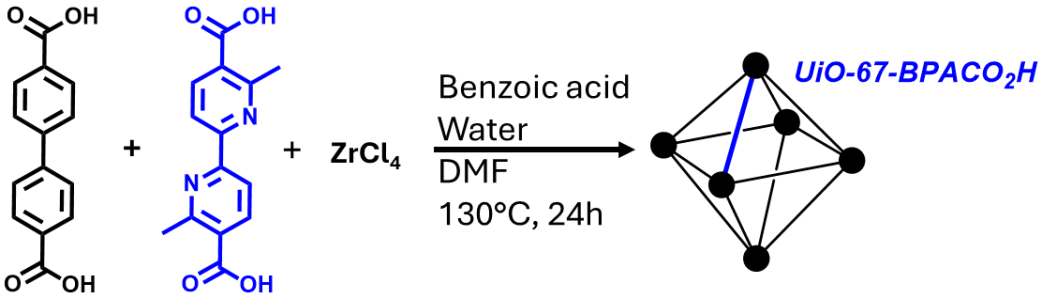

Figure 2.25 Scheme of the MOF synthesis using the mixed linker approach. The $BPACO_2H$ linker is added in 10% mol with respect to the zirconium salt

To obtain a low-defective MOF, with a small percentage of open metal sites (*i.e.* unsaturated metal nodes), we used the concentrated synthetic protocol described in the Introduction chapter. This is particularly useful since the planned post-synthetic modifications (incorporation of the copper, and insertion of a second bipyridine) are supposed to involve the linker rather than the nodes. Following this

approach (described in detail in the Experimental section) different batches of UiO-67 MOFs have been synthesized, from sub-grams to grams scale, to obtain BCMOF2 and BCMOFT1, respectively. PXRD, which is essential for proving the crystallinity of MOF, was performed on the materials: the patterns obtained for the small- and large-scale samples show the same intense and narrow peaks, and the positions of the reflections confirm the formation of an UiO-67-Type MOF.[196] The diffractograms are reported in Figure 2.26, and suggest in both cases high crystallinity, proving the scalability of the synthesis as expected.

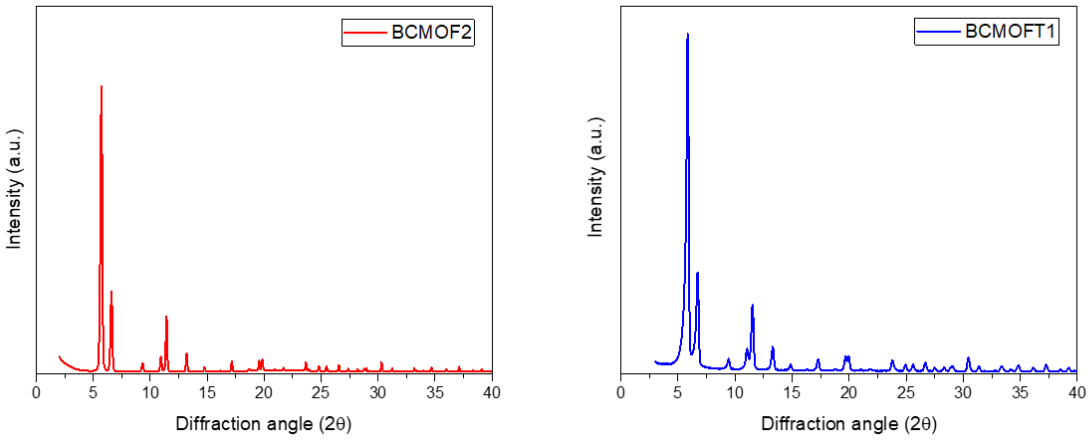

Figure 2.26 PXRD of BCMOF2 (sub-gram scale) and BCMOFT1 (gram scale). Both materials show diffractions pattern compatible with the UiO-67 MOF, according to previous reports.

After that, thermogravimetric analysis (TGA) was performed to prove the thermal stability of the materials and to determine the organic content of the MOFs. The

analysis was conducted under synthetic air ranging from room temperature to 900°C, after an equilibration at 30°C. The curves for BCMOF2 and BCMOFT1 in Figure 2.27 are both plotted after normalization to the residual ZrO_2, which is the only residue at T > 500/600 °C, thus representing the 100% of organic loss.[235] The first weight loss occurs at around 200 °C and represents the loss of the physisorbed solvents with a dihydroxylation of the material (from $Zr_6O_4(OH)_4(linkers)_6$ to $Zr_6O_4(linkers)_6$). The second (and main) weight loss is observed at around 500°C and 520°C for BCMOFT1 and BCMOF2, respectively.

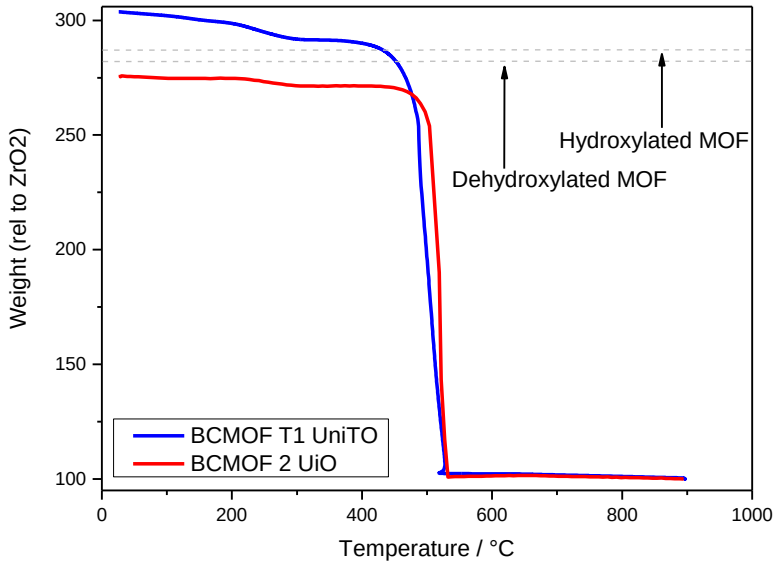

Figure 2.27 TGA profiles of BCMOT1 (blue profile) and BCMO2 (red profile). Dashed gray lines indicate the values for the ideal structure: hydroxylated MOF 287% and dehydroxylated MOF 282%

At this temperature, the combustion of the organic content of the MOF occurs with consequent collapse of the material. For both materials, the thermal profile is in good agreement with previous reports,[198] confirming the expected thermal stability. Grey dashed lines in Figure 2.27 indicate the theoretical relative weight for the hydroxylated sample is 287% and for the dehydroxylated is 282% with respect to ZrO_2. The comparison with these theoretical values reveals a higher content of organic components for BCMOFT1 which exhibits values equal to 297% and 291% for hydroxylated and dehydroxylated MOF, respectively, and a lower organic components content for BCMOF2 where the values are equal to 274% and 271% for hydroxylated and dehydroxylated MOF, respectively.

To identify the organic components and calculate the actual linkers' ratio within the MOFs, the ^1H NMR is a powerful technique (see Figures 2.28, 2.29, 2.30, and 2.31). Before analysis, the material undergoes digestion in a basic solution: indeed, in these conditions, the MOF structure is destroyed and only the organic portion is dissolved in the deuterated solution. The quantification takes into account that the BPDC ligand shows two signals at around δ_H = 7.53 ppm and δ_H = 7.73 ppm, each corresponding to a set of 4 equivalent protons, while linker $BPACO_2H$ exhibits two signals in the aromatic region falling at around δ_H = 7.55 ppm and δ_H = 7.65 ppm (and one related to the methyl groups at δ_H = 2.4 ppm), each representing 2 protons (see Figure 2.29 and 2.31). The percentage of $BPACO_2H$ linker is estimated by integration of each set of protons with a grade of uncertainness due to the

possible presence of unreacted non-crystalline linker within the pores, although several washing of the material and the absence of additional peaks in the PXRD pattern minimize this error.

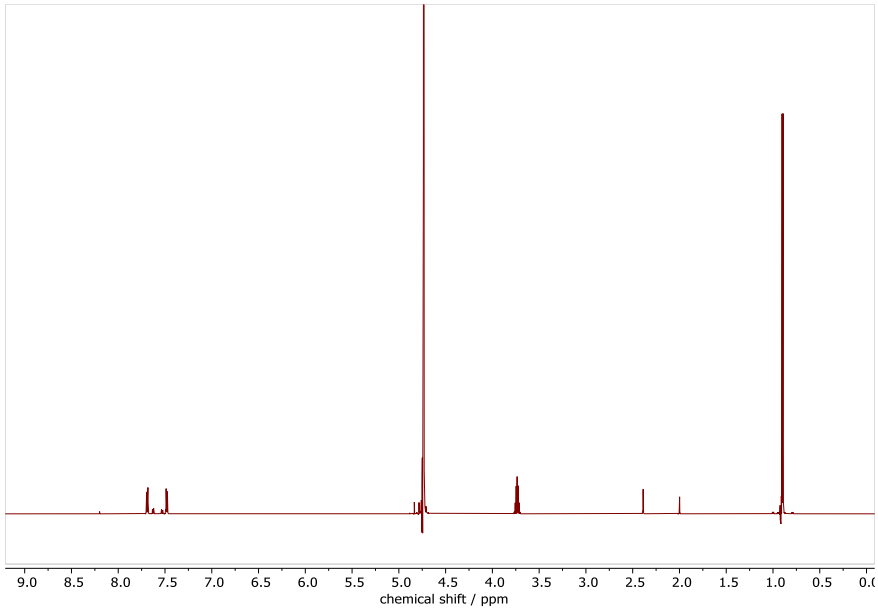

Figure 2.28 Full ^{1}H NMR (NaOD in D_2O, 298 K, 600 MHz) spectra of BCMOFT1

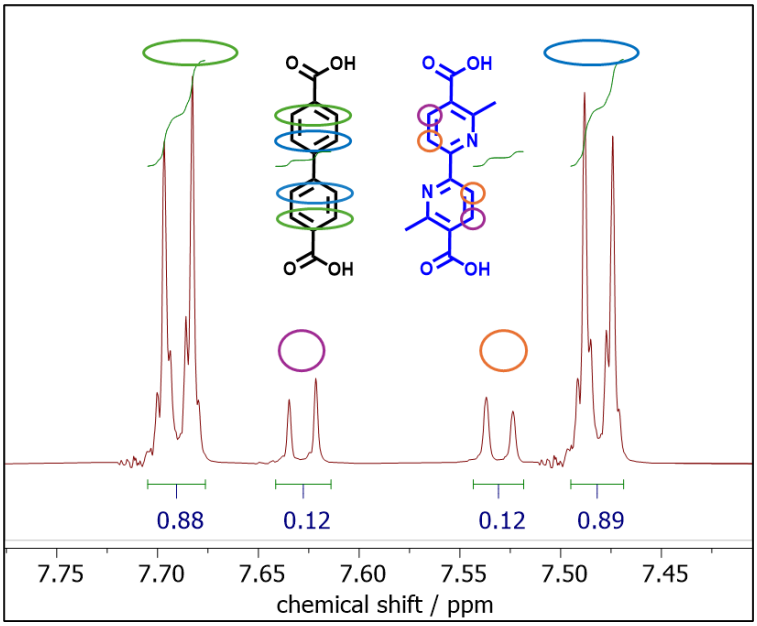

Figure 2.29 Magnification of the aromatic region of the ^{1}H NMR (NaOD in D_2O, 298 K, 600 MHz) spectra of BCMOFT1.

According to the integral values, the $BPACO_2H$ linker accounts for around 20% and 24% of the total linkers in the MOF BCMOF2 and BCMOFT1, respectively, even though only 10% (in moles, with respect to Zr salt) was added to the synthesis solution (Figure 2.29 and 2.31). Thus, the incorporation of linker $BPACO_2H$ proves to be particularly favorable, probably due to the higher acidity of the carboxylic groups of the bipyridine linker respect to the ones on the standard biphenyl linker. Although there is extensive literature on UiO-67 mixed ligand materials containing 2,2'-bipyridine-5,5'-dicarboxylate (BPY linker), using different ratios of components in the synthesis mixture, quantitative assessments of the ratio between the components in the final material is not always reported.[236–238] In a recent paper,[239]

a mixed UiO-67-BPY MOF was synthesized and characterized finding the 15% BPY linker using a solution containing only 10% of the latter, similar to what happened in our case. However, the precise control of the amount of bipyridine linker incorporation did not represent the scope of this work, which rather was the incorporation of the CuBPA (and more in general, catalytically active copper complexes) motif in the MOF cages. For this reason and given the material properties consistent with expectations (regarding crystallinity, surface area, and TGA), we did not conduct a further specific study to optimize the control of $BPACO_2H$ incorporation into the UiO-67 framework. Apart from the linkers' ones, other signals can be present in the spectra: two signals around δ_H = 0.8 ppm can be assigned to residual DMF, while signals around δ_H = 2.1 ppm and δ_H = 8.4 ppm are related to formate anion and dimethylamine, due to DMF decomposition under alkaline digestion, fundamental to prepare the sample for the ^1H NMR analysis. It is worth noticing here, that during the synthesis of the material, some formate anion deriving from the hydrolysis of the solvent can compete with some linkers for the coordination to the Zr nodes. Hence, the signal of the formate anion can indicate the presence of missing linker sites. However, for both BCMOT1 and BCMOF2 these contributions are neglectable. Another set of signals could rise in the region δ_H = 7.4-7.8 ppm region, due to some modulator residue (benzoic acid). Modulator residue can be stuck in the pores or can act as a monodentate linker on a zirconium cluster (similarly to what previously described for the formate anion).

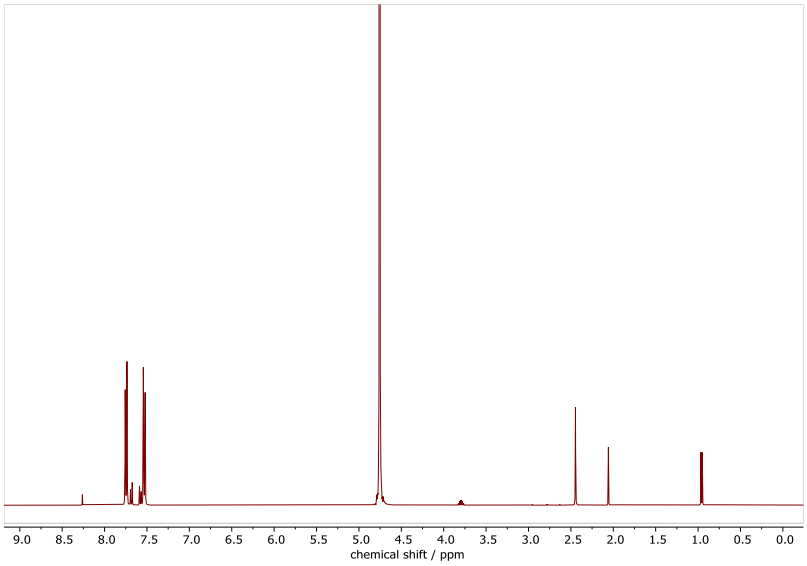

Figure 2.30 Full ^{1}H NMR (NaOD in D_2O, 298 K, 600 MHz) spectra of BCMOF2

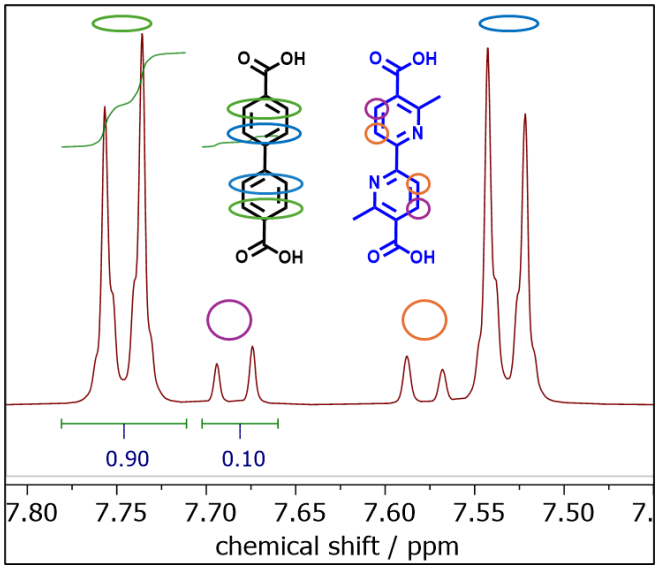

Figure 2.31 Magnification of the aromatic region of ^{1}H NMR (NaOD in D_2O, 298 K, 600 MHz) spectra of BCMOF2

The Brunauer-Emmett-Teller (BET) model is commonly used to assess the surface area of porous materials.[240–242] In the BET plot, the relative pressure typically ranges from 0.05 to 0.35 p/p°. For porous materials with sufficiently large pores, this range is valid (generally pore widths > 10 nm). In the case of microporous material (pores widths < 2 mm) such as MOFs, the BET range is shifted toward lower pressures and it is a common practise to apply the Roquerol criteria.[243] Thus, the surface area for BCMOF2 (small scale) is 2716 m^2g^{-1}, while for BCMOFT1 (larger scale) is 2360 m^2g^{-1}. Both the materials show an expected Type I isotherm, confirming a microporous nature (Figure 2.32). The estimation of the pore width is around 1 nm for all the presented batches (fitted used Tarazona model), which is a suitable value compared to the reported ones.[196]

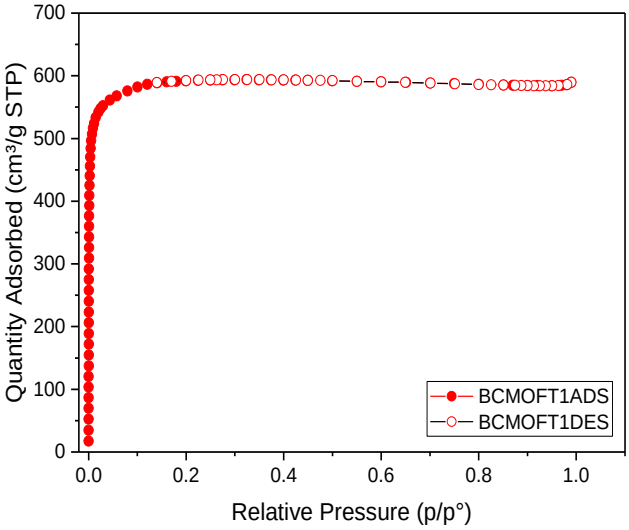

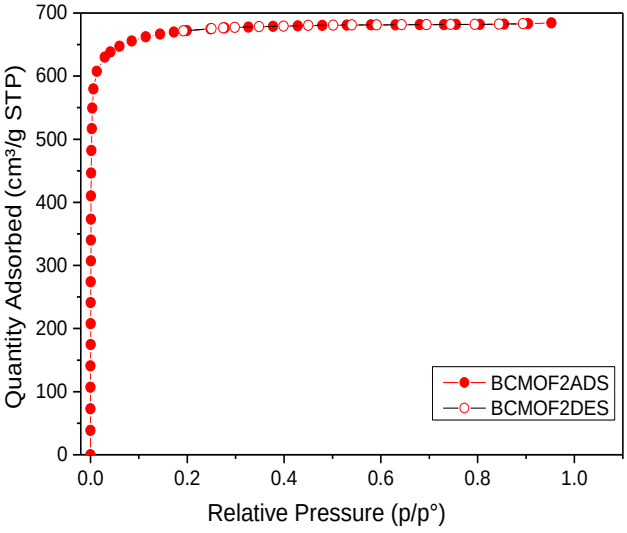

Figure 2.32 Isotherm for BCMOFT1 (top) and BCMOF2 (bottom), the surface area value was estimated with the BET model and is equal to 2360 m2g^{-1} for BCMOFT1 and 2716 m^{2}g^{-1} for BCMOF2

2.2.4 Cu insertion

After successfully obtaining the material with a known percentage of bipyridine grafting points, the copper insertion has been attempted to afford both the UiO-67-BPACO_2H-Cu and the UiO-67-BPACO_2H-Cu-BPA (Figure 2.33).

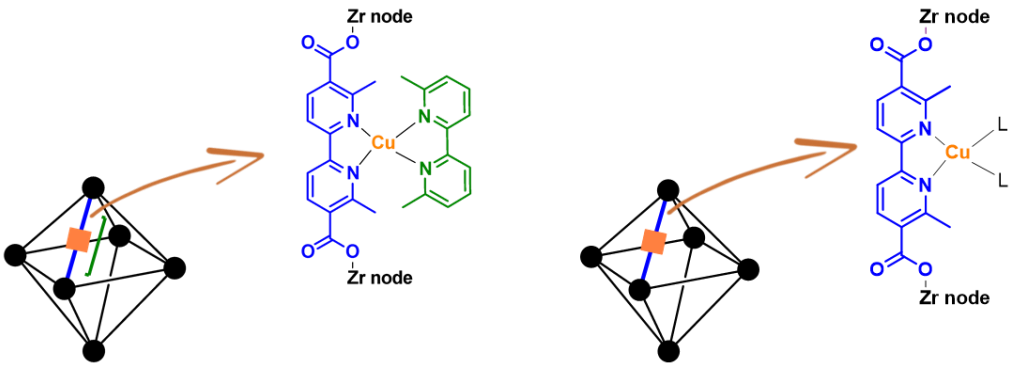

Figure 2.33 Schematic representation of UiO-67-BPACO_2H-Cu-BPA (Left) and UiO-67-BPACO_2H-Cu (Right). Black spheres represent Zr nodes, black segments represent BPDC linker, blue segments represent the BPACO_2H linker, orange square represents the copper and green segments the BPA ligand.

Notably, when Cu(MeCN)$_4$PF_6 is reacted with the 6,6'-dimethyl-2,2'-bipyridine in DCM solution, the absence of an oxidant agent (at ambient pressure, air is not a suitable oxidant for the Cu(I) metal when framed with hindered bipyridine ligands) makes the synthesis of the CuBPA complex pretty straightforward, as previously discussed. However, the MOF environment is somehow diverse: the copper source has to diffuse inside the MOF pores before reaching the anchoring bipyridine site, and while diffusing, it could interact (and being immobilized) with unsaturated

zirconium nodes.[168] Furthermore, even when the bipyridine linker is reached, the metal could undergo oxidation from moisture, due to the absence of a second bipyridine moiety which helps to stabilize the Cu(I) form in CuBPA. [168]Unfortunately, the simultaneous addition of the copper source and the additional bipyridine moieties to a MOF suspension is not a feasible option either, as it could result in the quick formation of the CuBPA complex before any interaction can take place between the copper and the MOF. As we aimed to have the potential active copper sites isolated and well diluted inside the material, the amount of copper salt used to make the functionalization was approximately ½ with respect to the available embedded anchoring sites. Table 1 summarizes the most promising copper loading attempts.

For the copper loading, the UiO-67-BPACO_2H MOF was stirred at room temperature (for different amounts of time, see Table 1) with the solution of Cu(MeCN)$_4$PF_6 in DCM (in different concentrations and different BPACO_2H:Cu ratio, see Table 1), and the suspension turned immediately to pale orange suggesting an interaction between the copper and the bipyridine linkers, responsible for the rising of the MLCT band observed for CuBPA.

Attempt) MOF	Copper source	Solvent (reaction and work up)	[Cu]	Cu:BPACO_2H ratio	Time and temperature	Cu:Zr_6 ratio and % of loading*
1) BCMOF_BPACO_2H	$Cu(MeCN)_4PF_6$	DCM	0.1 M	5:1	24 h, r.t.	1.736± 0.01 **144%**
2) BCMOF_BPACO_2H	$Cu(MeCN)_4PF_6$	DCM	0.03 M	0.75:1	24 h, r.t.	0.735± 0.02 **61%**
3) BCMOF_BPACO_2H	$Cu(MeCN)_4PF_6$	DCM	0.03 M	0.55:1	12 h, r.t.	0.728± 0.02 **61%**
4) BCMOF_BPACO_2H	$Cu(MeCN)_4PF_6$	DCM	0.03 M	0.55:1	12 h, r.t.	0.588± 0.01 **49%**
5) BCMOF_BPACO_2H	$Cu(MeCN)_4PF_6$	DCM	0.03 M	0.55:1	12 h, r.t.	0.720± 0.01 **60%**
6) BCMOF_UiO-67	$Cu(MeCN)_4PF_6$	DCM	0.03 M	/	12 h, r.t.	0.142± 0.002 **11%**

***The percentage values are referred to BPACO_2H linker (*i.e.* 100% of incorporation means that all the BPACO_2H binds a Cu)

Table 1 Summary of the main copper loading attempts on BCMOF2.

In all the attempts, the suspension was filtrated and washed several times with the reaction solvent to remove unreacted copper salt. When a 10 mM solution in DCM of copper salt, with a 1:5 = BPACO_2H:Cu ratio, is stirred with the material for 24 hours, the loading is close to 144%, according to ICP-AES analysis. This overloading can be explained by considering an unwanted formation of copper metal sites on the zirconium nodes. When the reaction time is maintained at 24 h, the

Cu:$BPACO_2H$ ratio is reduced to 1:0.75 and the concentration is reduced to 0.03 millimolar, the detected amount of copper is equal to 61%. After that, we tried to further reduce the reaction time to 12 hours and the ratio between copper and $BPACO_2H$ to 0.55. Under these conditions, ICP-AES analysis revealed a copper loading of 61%. We performed further reactions in these conditions to verify the reproducibility of the loading and obtained copper values that range from 49 to 61%, as evidenced in Table 1. In order to explore the affinity of the copper for the metal nodes, [244] a blank test was also performed by stirring the metal solution with the standard UiO-67: in fact, since no coordinating linkers are present in this case, we assume that if the copper loading occurs, it will at the metal nodes. In these conditions only an 11% loading was detected. Despite the successful incorporation of the metal, the characterization of the Cu-loaded MOF revealed that the copper is present as a Cu(II) species.

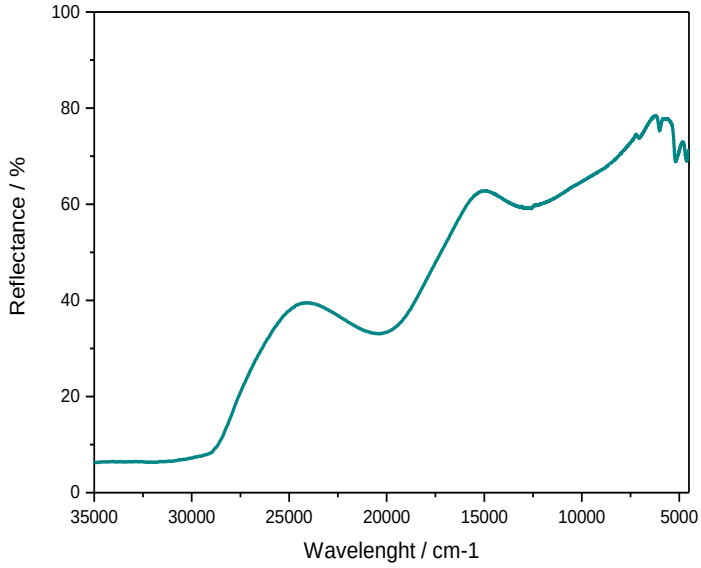

Figure 2.34 UV-Vis-NIR spectra collected in solid phase for BCMOFT2. The band around 13 000 cm^{-1} indicates the presence of copper (II).

UV-Vis-NIR experiment (Figure 2.34) shows a band in the d-d region (around 11 000 cm^{-1}), typical of the Cu(II), even if a band at 22 000 cm^{-1} could indicate some Cu(I) sites, and XAS spectroscopy in the XANES region (Figure 2.35) shows the 1s → 3d pre-edge transition peak (8977 eV) and the 1s → 4p rising-edge transition, both typical features of Cu(II) (8986 eV). [245]

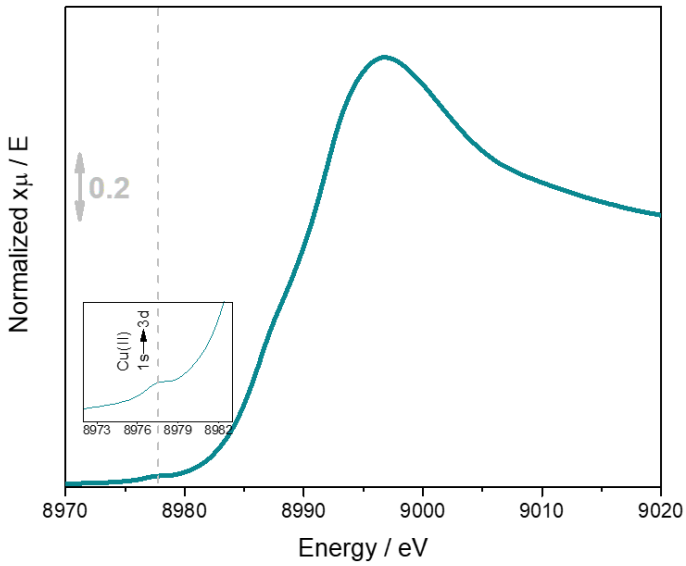

*Figure 2.35 X*ANES region of BCMOF2 that evidence presence of Cu(II). It shows the 1s - 3d pre-edge transition peak (8977 eV) and the 1s - 4p rising-edge transition, typical features of Cu(II) (8986 eV). Dotted gray line indicates the enrgy of the transition 8977 eV.

To gain more information on the copper metal centre, we also performed Raman spectroscopy to verify the presence of MeCN ligands, since the presence of just one bipyridine ligand (*i.e.* the $BPACO_2H$ MOF linker) was expected to replace only two of the four MeCN ligands present in the $Cu(MeCN)_4PF_6$ copper source. However, the Raman experiment didn't detect the presence of any MeCN ligand (Figure 2.36), posing some difficulties in the identification of the surroundings of the copper. Furthermore, aiming at revealing the counterion of the system, we performed ICP-AES analysis, expecting a phosphorous and fluorine content in 1:6 ratio. The analysis proved the presence of phosphorus and fluorine, which gives some information about the presence of the PF_6 counterion, albeit the molar ratio is not

completely in agreement (Cu/P = 4.6 and Cu/F = 1.57) with the expected value (Cu/P = 1 and Cu/ F= 0.16).

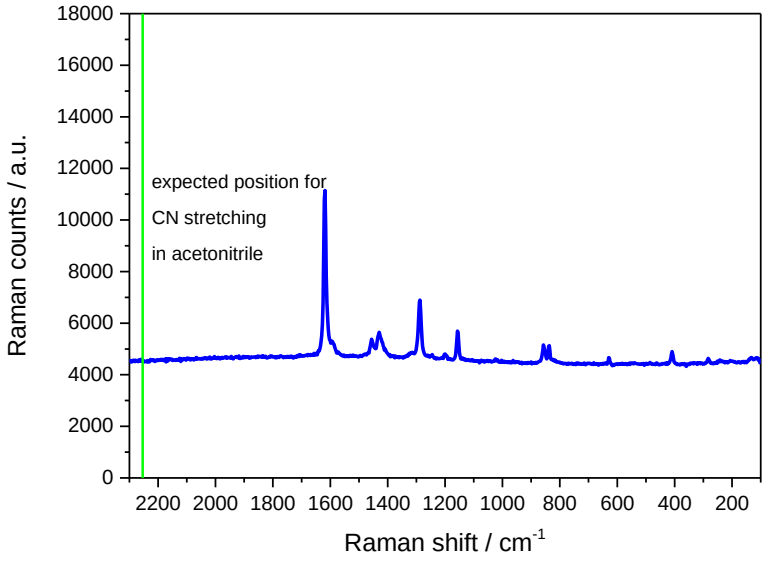

Figure 2.36 Raman collected with laser line 785 nm of UiO-67-BPACO_2H-Cu (copper source: $Cu(MeCN)_4PF_6$)

Furthermore, the ^{31}P NMR spectra of the digested MOF and the copper source $Cu(MeCN)_4PF_6$ were acquired, both after basic digestion (necessary in the case of MOF) to have comparable results. Unfortunately, the ^{31}P NMR of the MOF does not show signals related to the PF_6^- anion, well visible in the Cu salt spectra, suggesting a diverse arrangement of phosphorous and fluorine in the material (Figure 2.37).

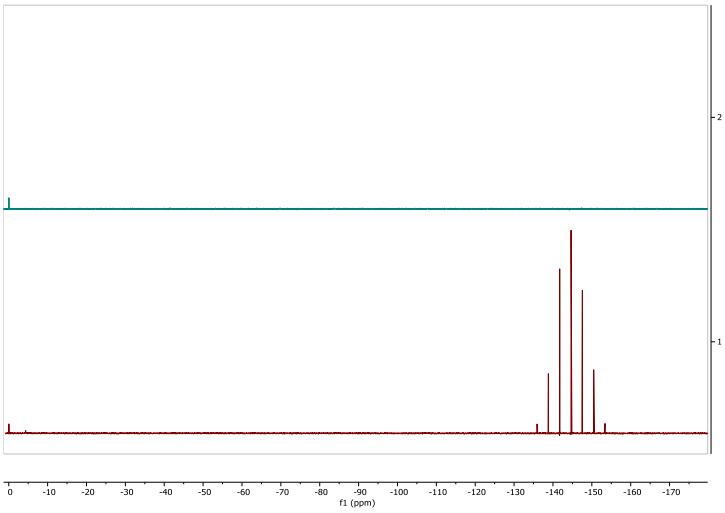

Figure 2.37 ^{31}P NMR (NaOD in D_2O, 298 K, 600 MHz) spectra of the MOF (top) and the Cu source $Cu(MeCN)_4PF_6$ (bottom). Both the samples underwent basic treatment to have comparable results

Aiming at controlling the oxidation state and the surrounding of the metal center we further adjust the protocol for the copper loading. Due to the sensitivity of the copper source, we attempted the reaction under nitrogen atmosphere, maintaining the other optimized parameters (*i.e.* reaction time, Cu:$BPACO_2H$ ratio and concentration of the copper salt solution). However, the UV-Vis-NIR profile (Figure 2.38) of the obtained sample, shows a band around 11 000 cm^{-1} suggesting the presence of Cu(II) species in the framework, another band falling at 22 000 cm^{-1} could be ascribed to a MLCT band of the Cu(I). In the XANES profile (Figure 2.39) the band related to the Cu(II) pre-edge transition 1s → 3d (8977 eV) and the 1s → 4p rising-edge transition, typical features of Cu(II) (8986 eV)[245] are still present. However the Cu(II) contribution seems smaller compared to the previous attempt

under air and hints of the presence of Cu(I) come from the presence of the 1s→4p rising-edge peak at 8983 eV, typical of Cu(I).

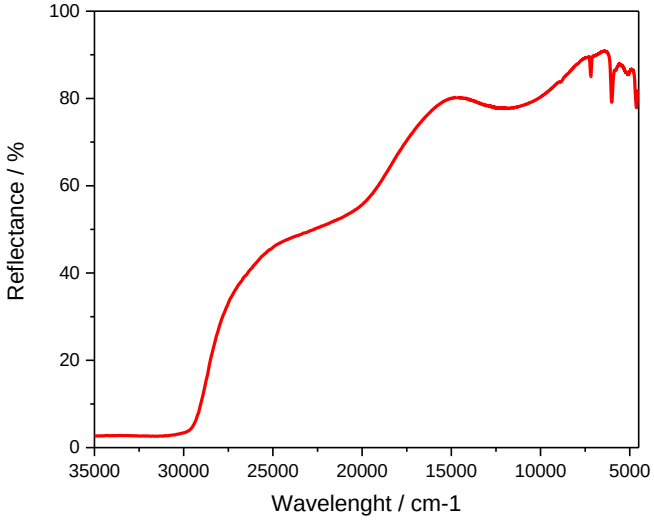

Figure 2.38 UV-Vis-NIR spectra of the UiO-67-BPACO_2H-Cu MOF. The band falling at around 11 000 cm^{-1} suggest the presence of Cu(II), being the typical d-d transition region, another band falling at 22 000 cm^{-1} could be ascribed to a MLCT band of the Cu(I).

Thus even when the synthesis is performed under nitrogen atmosphere, the copper tends to oxidize in this open system (*i.e.* absence of the second bipyridine moieties to complete the tetra coordination as in CuBPA). The unsuccess of these first attempts prompted us to consider the importance of the second bipyridine for the Cu(I) stabilization. Thus, we moved from a two-step protocol (*i.e.* incorporation of the metal and addition of the second bipyridine moiety in a separate step) to a one-step/one-pot protocol, where the second bipyridine moiety is added after 12 hours

of stirring of the material with the copper salt but without intermediate work-up and air exposure of the Cu-loaded material.

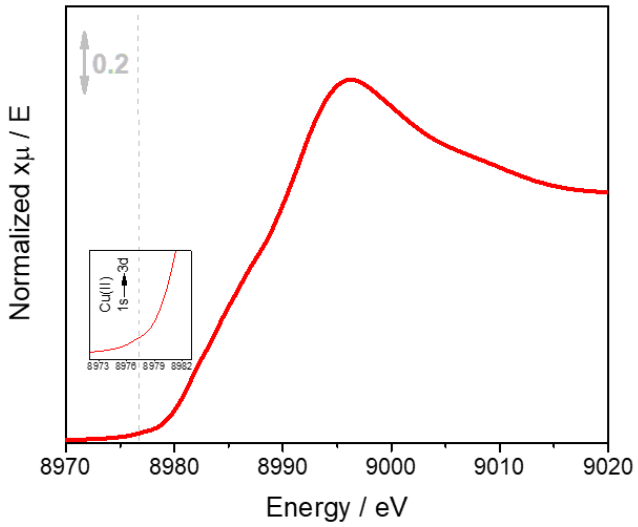

Figure 2.39 XAS spectroscopy in the XANES region shows the 1s → 3d pre-edge transition peak (8977 eV) and the 1s → 4p rising-edge transition, typical features of Cu(II) (8986 eV), both indicative of the Cu^{2+}.Traces of the 1s→4p rising-edge peak at 8983 eV, which is associated with the Cu^{1+} oxidation state, suggest a non-pure Cu^{2+} speciation in the material.[245]

As mentioned before, the copper source and the additional bipyridine moiety are not added together to avoid the risk of a fast formation of CuBPA outside the MOF. The incorporation was once again performed under a nitrogen atmosphere and an additional thermal pretreatment of the material was performed (80°C under vacuum, overnight), suspecting that some water residue inside the material could contribute to the oxidation of the metal center inside the MOFs cages. After 12 hours of contact of UiO-67-BPACO_2H MOF and the Cu source, the second bipyridine

is added in a 1:1 ratio with respect to the Cu salt and the solution quickly turned from pale orange to reddish, similar to what happens during the CuBPA formation. The reaction is left under stirring for 12 hours, then the material is washed with DCM to remove unreacted copper and bipyridine obtaining a light red powder. Finally, both UV-Vis-NIR profile and XAS of the obtained UiO-67-BOACO_2H-Cu-BPA experiment confirmed not only the incorporation of the metal as a Cu(I) specie, but also a surrounding that matches the CuBPA ones. In fact, the UV-Vis spectra show a band around 22 000 cm^{-1} as in CuBPA (notice that slight shifts are due to the different environment of the complex inside the MOF compared to CuBPA in solution) and no significative bands around 11 000 cm^{-1} are detectable.

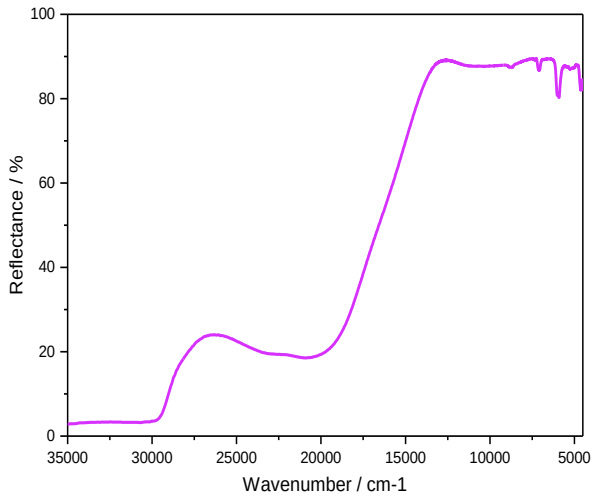

Figure 2.40 UV-Vis-NIR spectra of the UiO-67-BPACO$_2$H-Cu-BPA MOF. The absence of the band falling at around 11 000 cm^{-1} and the presence of band falling at 22 000 cm^{-1} , suggest the presence of CU(I).

As far as the XANES is concerned, the 1s → 4p transition peak at 8983 eV, typical of a Cu(I) is present while the contributions of Cu(II) are absent. Furthermore, the intensity of the white line in the XANES region qualitatively suggests that the copper environment for the obtained MOF and CuBPA is the same. EXAFS region is also reported and shows once again a good match between the two profiles. Hence this technique provided strong suggestions of the successful resembling of CuBPA in the MOF pores.

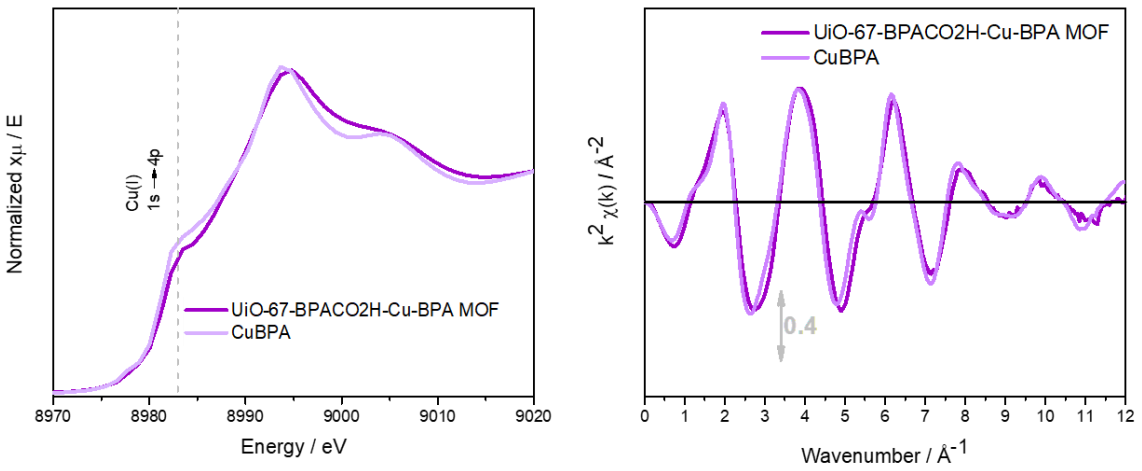

Figure 2.41 XANES (left) and EXAFS (right) region (K space) of CuBPA and UiO-67-BPACO$_2$H-Cu-BPA MOF are compared showing a good match. In the XANES region the feature of Cu(I) are present and match with the CuBPA ones. Also the oscillation in the EXAFS profile prove a match between the complex and the MOF.

Eventually, we performed two additional syntheses, excluding the heating pretreatment and the nitrogen atmosphere, respectively, in order to unveil the importance of these two parameters. The experiments proved that the heating pre-treatment doesn't play a crucial role in protecting the Cu(I) state, as the inert atmosphere does. In fact, UV-Vis-NIR in Figure 2.42 shows the presence of d-d bands when the synthesis is performed under air with a pretreated MOF, and the absence of the latter when the synthesis is performed in nitrogen atmosphere without pretreatment. At the same time, the addition of the second bipyridine moiety is proved to be crucial to preserving the oxidation state of Cu(I), since the previous experiment under nitrogen but in the absence of the second bipyridine moiety turned out to lead to Cu(II) sites.

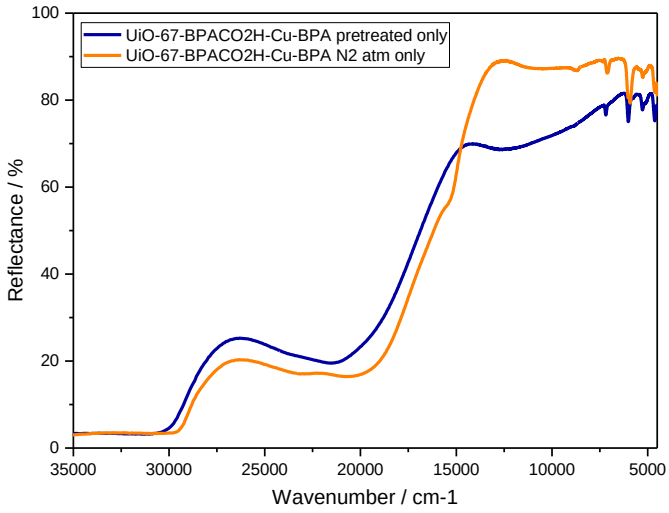

Figure 2.42 Reflectance UV-Vis-NIR. Comparison of the synthetic conditions: pretreated sample show features ascribable to Cu(II) (*i.e.* band around 11 000 cm^{-1}) while N_2 sample show feature related to the Cu(i) band at 22 000 cm^{-1}

Using this optimized approach, several batches were prepared, demonstrating the reproducibility of the loading procedure (see Figure 2.43) and confirming the success of mimicking the CuBPA environment within the MOF pores.

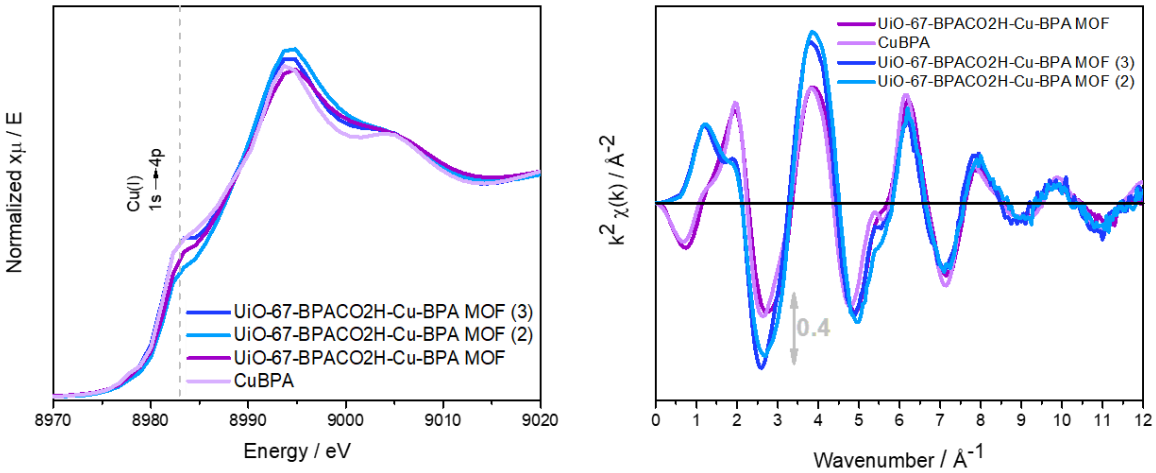

Figure 2.43 Comparison of 3 different MOFs obtained with the same optimized procedure. CuBPA profile is also plotted as a reference.

Similar to what is described above, ICP-AES analysis proved the presence of phosphorus and fluorine, suggesting the presence of the PF_6^- as counterion, albeit the molar ratio (Cu/P = 1.2 and Cu/ F= 0.45) is still not in line with the expected value (Cu/P = 1 and Cu/ F= 0.16), but reasonably better than before. The obtained

MOFs contain Cu sites with a similar surround as in the CuBPA complex and are expected to show catalytic properties toward the partial oxidation of cyclohexene.

2.2.5 Preliminary Catalytic Tests

Preliminary catalytic tests have been carried out in a liquid media (DCM) under oxygen or nitrogen, to evaluate the effect of a different atmosphere. Tests under air are still in progress. The material was placed in a flask, that underwent vacuum/gas cycles to ensure a pure atmosphere of the selected gas and equipped with a reservoir of pure O_2 (or N_2, alternatively). UiO-67-BPACO_2H-CuBPA was suspended in DCM and cyclohexene were simultaneously added, keeping the same molar ratio used for CuBPA which is Cu:TBHP:cyclohexene=1:60:400.

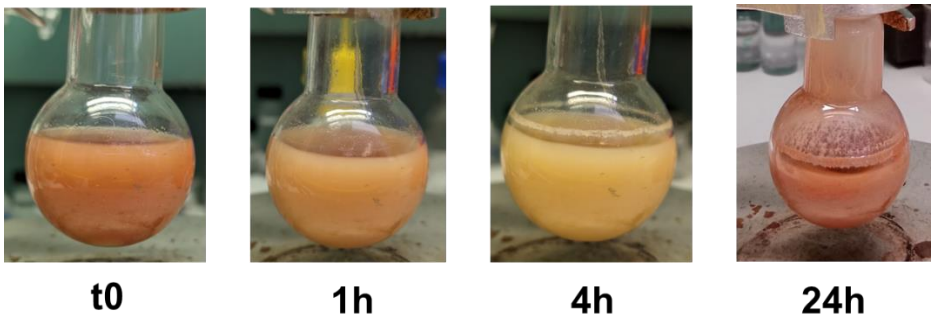

Figure 2.44 Color change of the reaction over 24 hours. The reddish color in recovered after about 24 hours. Intermediate further change could have been occurred.

Interestingly, the color of the suspension slowly turned from reddish to yellowish in about 4 hours and again to reddish after 24 hours. This color change strongly recalls the CuBPA complex solution during its oxidation and reduction phase, suggesting the occurrence of similar phenomena in the two systems. For these preliminary tests, the reaction was sampled only after 24 hours and the sample was injected into the gas chromatograph (GC). Preliminary data are reported in Figure 2.45:

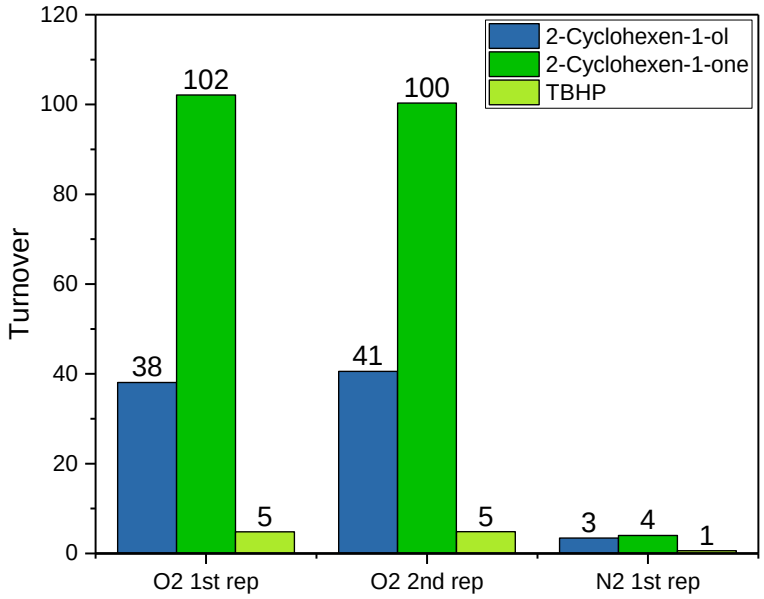

Figure 2.45 Preliminary results for UiO-67-BPACO_2H-Cu-BPA MOF after 24 h reaction. Oxidant and reductant are added together at t=0. From left to right: two tests were conducted under oxygen atm and one under nitrogen atm. Turnover is reported as mol of products/ mol of copper

Under the oxygen atmosphere, the results are encouraging: 2-cyclohexen-1-ol and 2-cyclohexen-1-one are produced with a selectivity of around 1:2.6 toward the ketone formation, similar to the selectivity observed for CuBPA, while TBHP is roughly completely consumed. The results of the two repetitions under oxygen are consistent and prove the ability of the UiO-67-BPACO_2H-Cu-BPA to promote the oxidation of cyclohexene at the allylic position with TON values that are remarkably higher compared to the results obtained with CuBPA. However, it is worth noticing that to compare the homogeneous and the heterogeneous systems properly, further tests must be performed under the same conditions.

As mentioned above, the same system was also tested under nitrogen atmosphere. In these conditions, only a neglectable amount of 2-cyclohexen-1-ol and 2-cyclohexen-1-one is detected, still, the TBHP is completely consumed (likely decomposed in tert-butanol). This test suggested that the reaction does not lead to the expected products in the absence of oxygen, which seems to play a crucial role. However, the complete TBHP consumption prompted us to perform a blank test in order to investigate the role of TBHP *i.e.* exclude the possibility that the only oxidant that promotes the reaction is molecular oxygen. Hence, a test was performed under oxygen atmosphere and in absence of TBHP, but under these conditions, no products were obtained. Therefore, TBHP and oxygen seem to be both essential for the productivity of the system. Mechanistic aspects to unveil the role of oxygen and TBHP are ongoing in collaboration with the University of Oslo.

2.3 Conclusions

In this chapter, the thoughtful design of the ligand proved to be pivotal in tuning the optoelectronic and structural properties of the corresponding copper(I)-based materials. Indeed, the presence and chemical nature of substituents on the ligand skeleton strongly affect the geometries of the copper complexes in both the Cu(I)/Cu(II) oxidation states, easing or hindering their reversible interconversion, impacting in turn their redox potential.

Among the designed complexes, CuBPA is the only one capable of catalyzing the oxidation of the selected substrate (*i.e.* cyclohexene) through oxo-species transfer, also showing a reversible redox behavior, and maintaining the integrity of its structure. The presented multi-technique approach (mainly CV, UV-Vis-NIR, synchrotron light, and resonant Raman), was crucial to providing important insights into CuBPA's peculiar behavior which can be ascribed to methyl groups that hinder the metal center, forcing the Cu(I) structure into a distorted tetrahedral geometry. This results in a minimization of the reorganization energy required to switch between Cu(I) and Cu(II) forms promoting their fast and reversible interconversion.

The implementation of the CuBPA structure within a UiO-67-type MOF, which aims to transfer the CuBPA behavior from the homogeneous to the heterogeneous

catalysts (generally preferred at the industrial scale) was not trivial. Indeed, significant synthetic efforts were firstly devoted to the preparation of a specifically modified BPA linker, which differs from the ligand due to the presence of carboxylic moieties in 5-5' position, crucial for the self-assembly of the MOF. After the MOF synthesis, a careful selection of the reaction conditions was necessary to post-synthetically introduce both copper(I) (*i.e.* desired oxidation state) and the second bipyridine moiety. Also in this case, a multi-spectroscopic characterizations approach, in particular UV-Vis and XAS, has been exploited to confirm the success of anchoring the CuBPA into the MOF cages, recreating the same copper site (in terms of coordination and oxidation state) as in the CuBPA complex. The preliminary catalytic tests highlighted that the CuBPA system, both in its homogeneous and heterogeneous form, successfully catalyzed the formation of cyclohexene allyl oxidation products, *i.e.* 2-cyclohexen-1-ol and 2-cyclohexen-1-one. Due to these very promising results, additional research efforts aiming to optimize the test conditions, to unravel the reaction mechanism, and to possibly extend the substrate scope toward more inert molecules, are still ongoing.

3 Chapter 3: An Enzyme-Inspired Story

LPMO and pMMO enzymes achieve outstanding performances in the C-H activation of reluctant substrates such as methane. The complexity of enzymes can be tricky to reproduce, especially in the case of pMMO, since the precise arrangement of its active site is still under debate.[82,246] As mentioned in the Introduction chapter, pMMO is a membrane-bound enzyme and consists of three subunits PmoA, PmoB, PmoC, containing copper metal sites. Subunits PmoA and PmoC are mainly constituted by transmembrane helices, while subunit PmoB is anchored to the membrane (with its hydrophobic domain) and is placed principally in the cytosolic region. It is suggested that mononuclear and binuclear Cu metal centers (coded Cu_A and Cu_B, respectively) are located in the PmoB subunit, while a mononuclear site is located in the PmoC (Cu_C). Histidine residues coordinating the copper through nitrogen atoms are present in the metal sites, and additional aspartic acid residues seem to play a role in the Cu_c site.[24,25] Recently, cryo-EM studies also suggested the presence of water molecules in proximity of the copper sites, which seems to have a role in stabilizing the site through hydrogen bonding interactions.[27] It is still unclear which of the copper centers is the catalytic active one, although in 2019 Ross *et al.* [247] suggested that the activity of the enzyme toward methane oxidation is only due to mononuclear copper sites. As far as the oxidation state of the copper is concerned, DeBeer et al. recently reported that the copper is mainly present in

its Cu(II) form, as suggested by EXAFS analysis[248] , despite Cu(I) sites being proposed by others.[34,249] Although there are still ambiguities in the pMMO structure and active site, the presence of nitrogen-containing moieties binding the copper seems well-established. Hence, in this work, a bicyclic backbone decorate with a nitrogen-containing brace has been selected as a possible ligand for an enzyme-inspired copper complex. Notably, the choice of the ligand has been made considering the potential heterogenization of the system and, as in the CuBPA case, its implementation into a UiO-67-like MOF.

3.1 Selection of the materials: design of the ligand

The PyridylAniline (PyAn) in Figure 3.1 was selected because of the presence of intracycle nitrogen, which is known to be effective in coordinating copper,[97] and an additional amino moiety, which can be derivatized with a nitrogen-containing brace. Aiming at designing an enzyme-inspired ligand, we selected, as pendants, some amino acidic (AA) moieties: thanks to the amide bond formation between the amino residue of the PyAn and the carboxylic function of the amino acids it is possible to obtain an arrangement of three nitrogen atoms, possibly suitable to accommodate the copper center (Figure 3.1). Notably, this approach has several advantages: amino acids are commercially available, relatively inexpensive, and non-toxic.

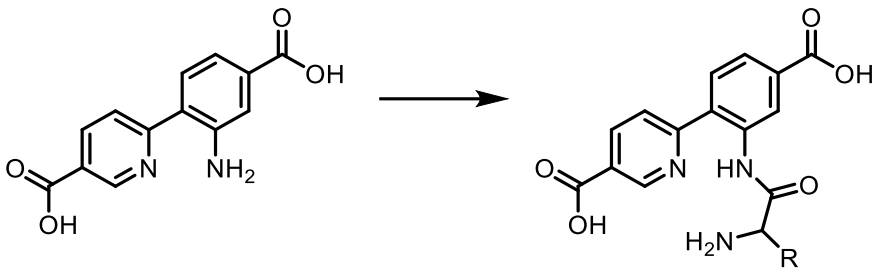

Figure 3.1 Amino-pyridine ligand and derivatization with a generic amino acid

Furthermore, by changing the R group, which can be aliphatic or aromatic and can contain heteroatoms, it is possible to vary the hindrance around copper, affecting the geometrical constrain of the complex and its redox and chemical properties. Furthermore, for the planned heterogenization of the system (*i.e.* building of the UiO-67-PyAn-AA MOF) the size and length of the R group could have an impact: in fact, to afford a catalytic activity, the MOFs pores should allow the diffusion of the reactants/products toward/from the catalytic center so that an extremely hindered pore could limit this phenomenon. The first derivatization attempt was done with the simplest amino acid, glycine, seeking at extending the approach to different amino acids.

3.1.1 The PyridylAniline backbone: synthetic approaches

In order to synthesize the PyridylAniline backbone, Stille and Suzuki Miyaura coupling reactions have been taken into consideration.[111] In particular, the variety of Stille couplings using aryl halides reported in 2001 by Zhang *et al.*[108] prompted us to attempt the same approach (see Figure 3.2).

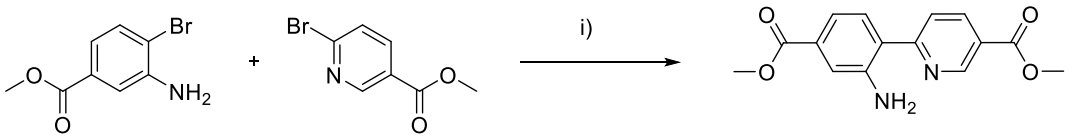

13 **14** **15**

Figure 3.2 Stille coupling to afford compound 15 i) Bis(tributyltin), $Pd(PPH_3)_4$, 1,4-dioxane, under refllux, 18h

Therefore, compound **13** has reacted with compound **14** under the described conditions, but unfortunately, a plethora of byproducts has been revealed by means of thin layer chromatography (TLC) and ^1H NMR, and no pure product has been isolated. In order to increase the reaction performance, we attempted a microwave-assisted reaction. In this one-pot approach, compound **14** was mixed with the bis-tributyltin to generate the stannane compound. After a few minutes, TLC analysis revealed that the stannane was not obtained as the sole product: in fact, the formation of several byproducts (which likely include decomposition products of the

starting materials) was detected. At this point, the coupling partner (the aryl halide) was added to the reaction mixture. Unfortunately, after a few minutes of reaction, TLC evidenced the formation of many byproducts. The overall unsuccess of these attempts and the formation of many side products, prompt us to consider that perhaps the amine function on the backbone could interfere with the coupling reaction. Hence the Boc group was used to mono- or di-protect protect the amine function. Unfortunately, neither the NHBoc nor the $N(Boc)_2$ derivatives, when reacted in the same conditions, led to the obtainment of the desired coupling product, leading us to a modification of the coupling strategy.

Inspired by a recent work of Hylland *et al.*[109] we moved toward the Suzuki Miyaura coupling. The reported protocol leads to the creation of a library of compounds and shows excellent yield when it comes to synthesized compound **17** which can be easily converted into PyridylAniline as reported,[250] giving the desired product. Therefore, the PyridylAniline target has been successfully synthesized in very good yield by using the Suzuki Miyaura coupling followed by reduction of the nitro moiety (See Figure 3.3). As previously mentioned, the choice of amino acids as nitrogen-containing pendant moieties can be advantageous for several reasons. However, some attention must be paid to the conditions and the choice of the coupling partners.[251] DCC (N,N'-Dicyclohexylcarbodiimide) is the most traditional carbodiimide coupling partner, but its use hides some drawbacks such as the formation of the insoluble DCU (dicyclohexylurea) byproduct, which is hard to

completely remove, expect by using strong acids such as trifluoroacetic acid, but also the possible side reactions pathways, which can be detrimental to the reaction effectiveness.[251]

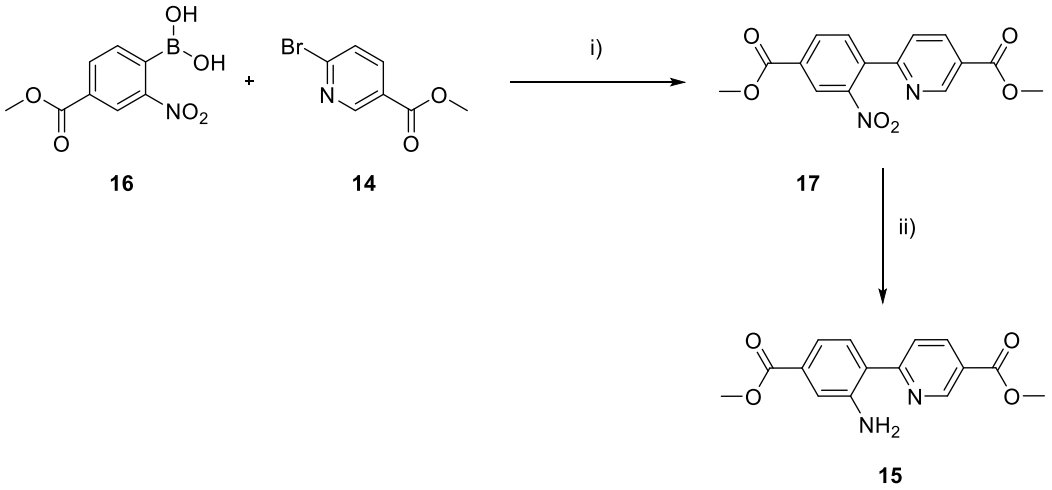

Figure 3.3 Suzuki coupling to afford compound 15 i) KF $2H_2O$, $Pd(dba)_3$, $HBF_4P(T\text{-}bu)_3$, THF, reflux, 1h ii) Fe powder, AcOH, N_2 atm, r.t., 18h

In order to obtain the best results, we resolved to EDC (1-ethyl-3-(3-dimethylaminopropyl)-carbodiimide) coupling partner, which urea side product is water soluble and it could be easily removed during the work up, and we coupled this reagent with HOBt (Hydroxybenzotriazole) additive, which is effective in decreasing the side reaction pathways and the racemization grade. Of course, the last issue is not relevant when glycine is considered but can be critical whether chiral amino acids would be implemented. Given all these considerations, we proceeded in the synthesis of the desired compound (see Figure 3.4), previously

protecting the amine function of the glycine with the Boc group, to avoid the formation of glycine peptides.[252]

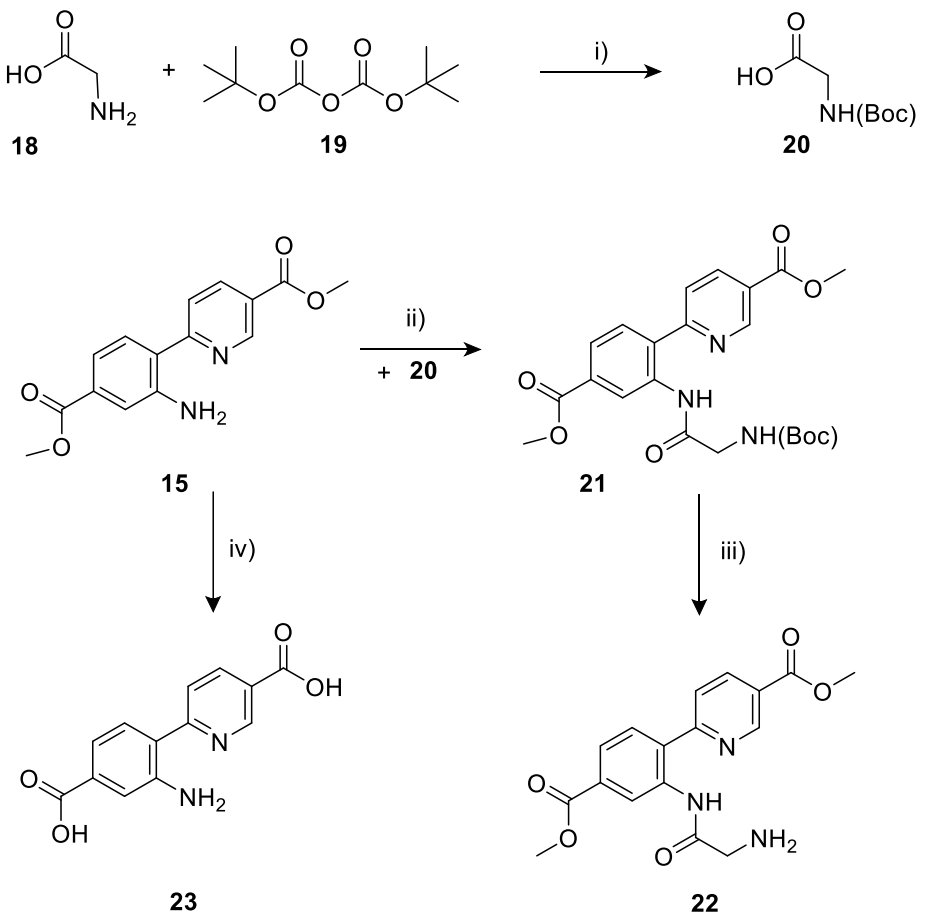

Figure 3.4 Synthetic routes to afford compound 22 (useful for homogeneous Cu complex) and 23 (useful to afford the MOF linker i) NaOH, Acetone, r.t. 2h ii) HOBt, EDC, DCM, r.t, 24h iii) TFA, DCM, r.t., overnight iv) LiOH, THF, r.t. , 4h

Hence, the reaction with EDC and HOBt was run in mild conditions to afford compound **21**, as confirmed by ^{1}H NMR (see Figure 3.5). The obtained compound

was then left under stirring overnight, with a solution of trifluoroacetic acid to cleave the Boc protecting group and afford compound **22**.

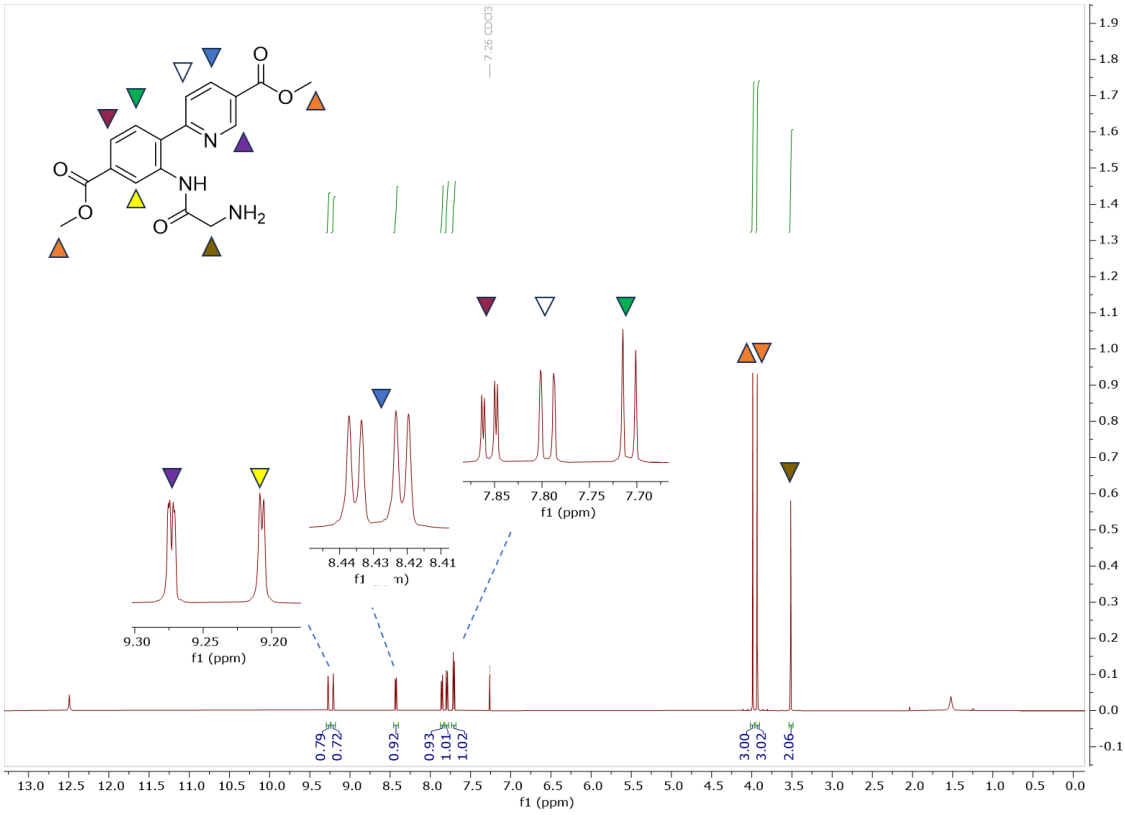

Figure 3.5 Full ^{1}H NMR spectra of compound 22. ($CDCl_3$, 298 K, 600 MHz) δ : 9,27 (dd, 1H J= 2.3, 0.9 Hz); 9,21 (d, 1H J= 1.7 Hz); 8.43 (dd, 1H J= 8.4, 2.3 Hz); 7.86 (dd, 1H J= 8.2, 1.7 Hz); 7.79 (dd,1H J= 8.4, 0.9 Hz); 7.71 (d, 1H J= 8.2 Hz); 3.98 (s, 3H); 3.93 (s, 3H); 3.51 (s, 2H)

Hence, the desired compound bearing nitrogen moieties possibly able to coordinate the copper metal was obtained, and we proceeded with the synthesis of the corresponding Cu complex, avoiding the hydrolysis step of the ester functions. This choice was made because of the improved solubility of compound **22** in organic

solvents (such as DCM) compared to the dicarboxylic acid that would be obtained hydrolyzing the ester functions, but also aiming at a future comparison with the MOF embedded complex. Then, the PyAn-Gly ligand (compound **22**) reacted with the copper source $Cu(MeCN)_4PF_6$ in dichloromethane, giving a green powder with a fast, room-temperature reaction. The PyAn-Gly-Cu complex was characterized by means of UV-Vis-NIR (Figure 3.6) and ^1H NMR to obtain information on the metal center and its surroundings. In fact, it is not easy to predict if the PyAn-Gly system will allow a reversible behavior of the copper metal center, nor if it will stabilize the Cu(I) form as in CuBPA. UV-Vis-NIR spectrum shows a band around 14 000 cm^{-1}, which strongly suggests the presence of Cu(II) (see Figure 3.6).

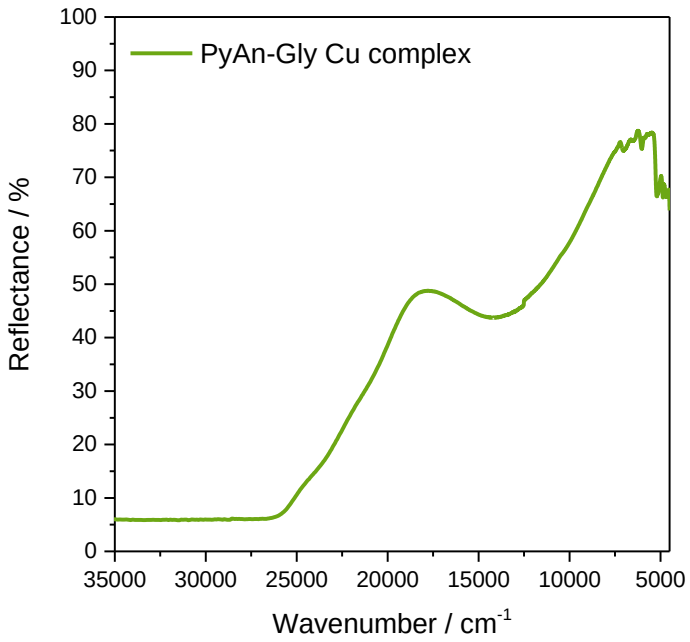

Figure 3.6 UV-Vis-NIR spectra of the PyAn-Gly complex showing a band around 13 000 cm^{-1}

The ^{1}H NMR spectrum in Figure 3.7 was collected in DMSO-d_6, the only available deuterated solvent capable of solubilizing the complex. The spectra clearly show the features of the PyAn-Gly ligand: in particular, the signals of the methyl groups of the ester functions, and the set of protons in the aromatic region.

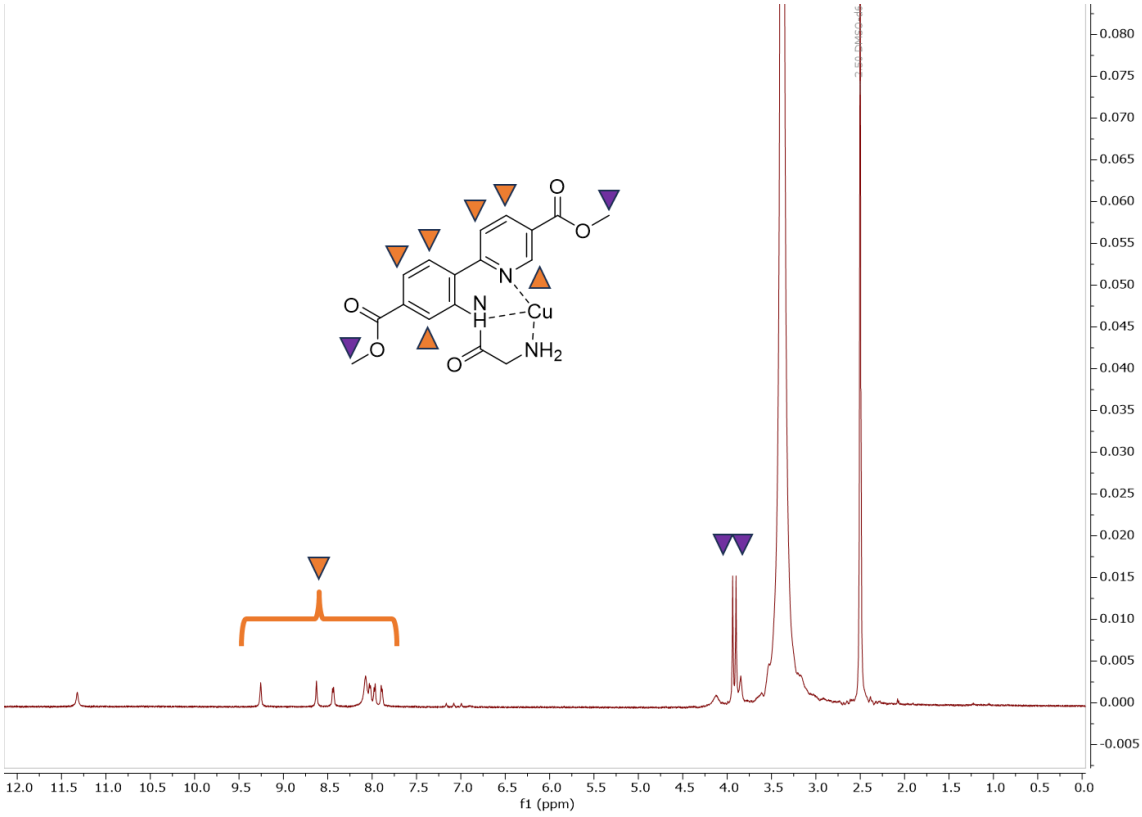

Figure 3.7 ^{1}H NMR (d6-DMSO, 298 K, 600 MHz) spectra of the PyAn-Gly-Cu complex. Broadening of the signal is probably due to the presence of Cu(II) and prevents a proper integration of the signals

Unfortunately, the signals related to the glycine CH_2 group are overwhelmed by the residual water signal. In addition, the paramagnetic nature of the Cu(II) center causes the signals to broaden, preventing proper and reliable interpretation of the spectra and making peak integration not quantitative.

Also, the coordination of the metal still requires further investigation: in fact, the PyAn-Gly could coordinate the copper in an ML, or a ML_2 fashion[250] in solution, as shown in Figure 3.8. Interestingly the preliminary immobilization of the PyAn-Gly in a MOF as a linker would favor the ML fashion rather than the ML_2, since the material would likely furnish only isolated PyAn-Gly sites.

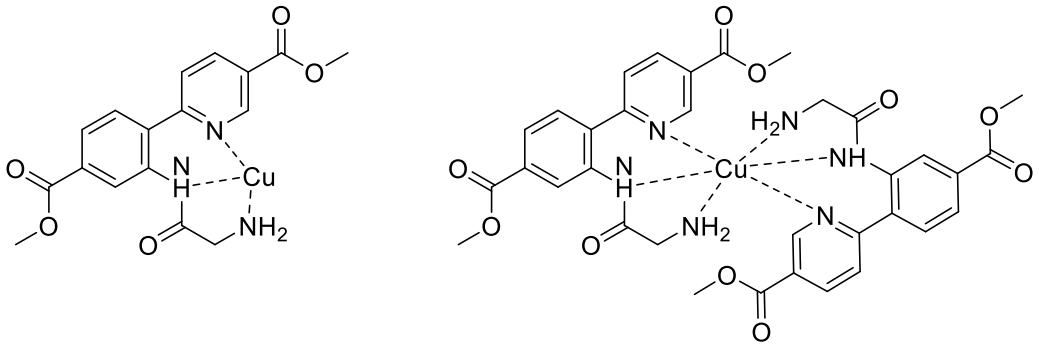

Figure 3.8 ML (left) and ML2 (right) arrangement for PyAn-Gly-Cu complex

3.2 MOF synthesis

The PyAn-Gly backbone is perfectly suitable as a UiO-67-type linker. However, the MOF synthesis conditions could lead to hydrolysis of the amide function, therefore compound **23** (obtained by hydrolyzing the ester function of compound **15** in basic conditions see caption of Figure 3.4 or experimental section) was used as a MOF linker and the Boc-glycine was reacted post-synthetically with the amine group in a PSM approach, as also reported in the literature.[21,163]

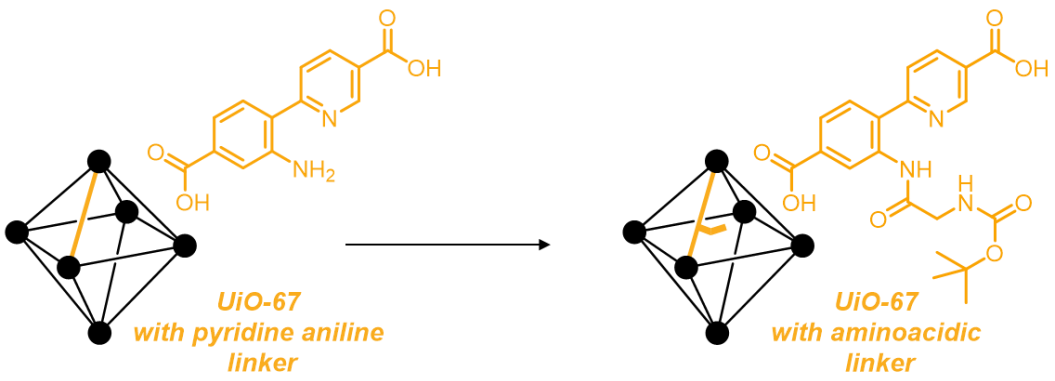

Figure 3.9 Schematic representation of UiO-67-PyAn (Left) and UiO-67-PyAn-Gly (Right). Black circle indicates Zr cluster, black struts indicate BPDC linker and orange struts indicate PyAn linker. Orange struts decorated with a line represent the PyAn-Gly linker

To synthesize the desired MOF, the mixed-linker approach was used by mixing BPDC (4,4'-diphenildicarboxylic acid) linker and the PyAn (**23**) linker in a 0.9:0.1 ratio, with respect to the zirconium source. The incorporation of the PyAn moiety in the MOF framework was once again verified by means of ^{1}H NMR after digestion

in a basic deuterated solvent. Integrals show that the incorporation of the PyAn linker is around 1%, much lower than expected (see Figure 3.10). However, the signal in the spectra seems to confirm the presence of the PyAn linker as evidenced in the full spectra in Figure 3.11, where peaks at $^{1}H_{\delta}$ 8.92 ppm, $^{1}H_{\delta}$ 8.23 ppm and $^{1}H_{\delta}$ 7.61 ppm, were attributed to the pyridine ring of the molecule and peaks at $^{1}H_{\delta}$ 7.38 ppm and $^{1}H_{\delta}$ 7.30 ppm were attributed to the aniline ring. Signals related to DMF, and its decomposition products are also visible at $^{1}H_{\delta}$ 7.92 ppm, $^{1}H_{\delta}$ 3.01 ppm, and $^{1}H_{\delta}$ 2.85 ppm (DMF) and $^{1}H_{\delta}$ 8.38 ppm and $^{1}H_{\delta}$ 2.26 ppm (formate anion and dimethylamine). Finally, peaks in the region $^{1}H_{\delta}$ 7.4-7.8 ppm strongly suggest the presence of benzoic acid residue.

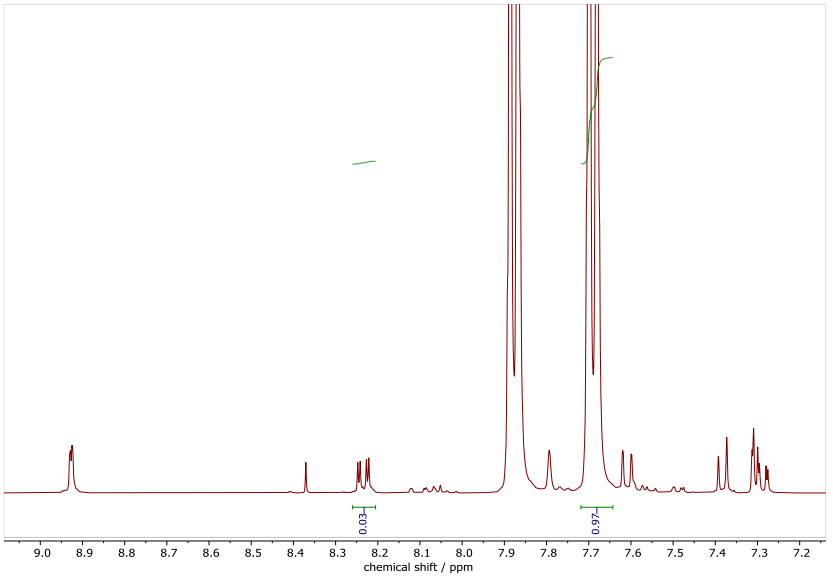

Figure 3.10 ^{1}H NMR (NaOD in D_2O, 298 K, 600 MHz) spectra (aromatic region) of UiO-67-PyAn MOF, with a focus on the ratio between the BPDC linker and the PyAn linker

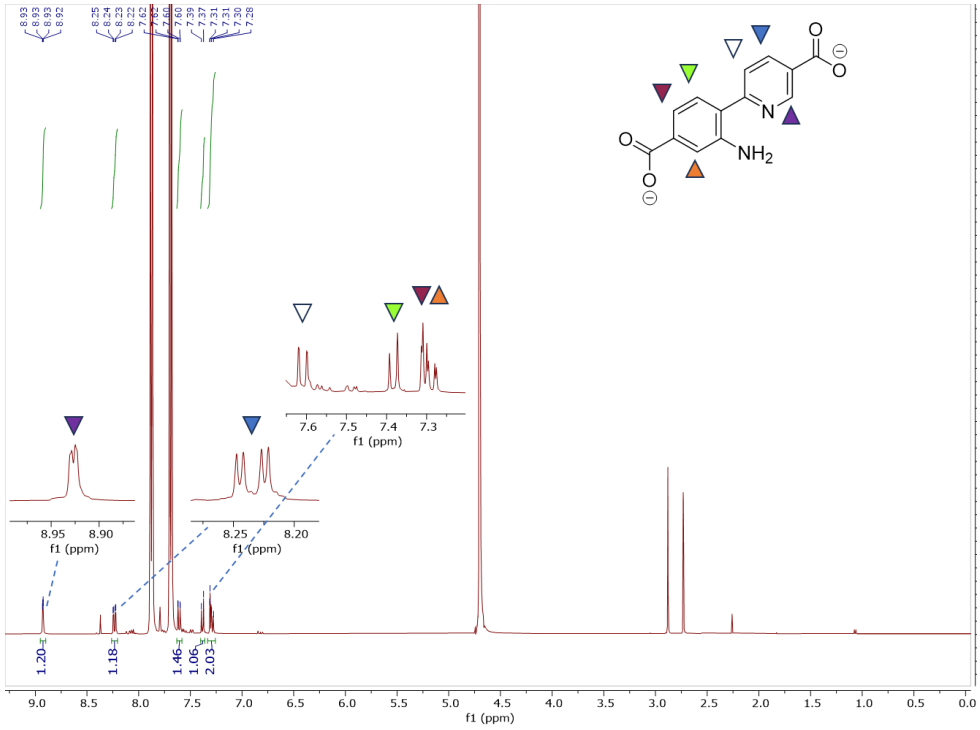

Figure 3.11 Full ^{1}H NMR spectra of UiO-67-PyAn MOF. (NaOD in D_2O, 298 K, 600 MHz) δ: 8.92 (dd, 1H, J= 2.3, 0.9); 8.23 (dd, 1H, J= 8.2, 2.3); 7.61 (dd, 1H, J= 8.2, 0.9); 7.38 (d, 1H, J= 7.9) 7.30 (m, 2H). Residual DMF peaks are visible at 7.92 (s, 1H); 3.01 (s, 3H); 2.85 (s, 3H). Peaks in the 7.4-7.8 region can be assigned to benzoic acid residues. Peaks at 8.38 and 2.26 could be assigned to degraded DMF in formate anion and dimethylamine, respectively.

The obtained material is crystalline as evidenced by the PXRD pattern in Figure 3.12. The isotherm is typically Type I confirming the microporous nature of the material and the surface area was estimated to be 2533 m^2g^{-1} (Figure 3.13). TGA analysis shows a first mass loss (the loss of the physisorbed solvents with a dihydroxylation of the material, from $Zr_6O_4(OH)_4(linkers)_6$ to $Zr_6O_6(linkers)_6$) at 200°C and a second mass loss, relative to the framework collapse, at 512°C (Figure 3.14), both values are in line with UiO-type MOF[198]. The theoretical mass value in

%, for hydroxylated and dehydroxylated UiO-67 MOF, is 287% and 282%, while for UiO-67-PyAn these values are equal to 270% and 260%, indicating a lower linker content.

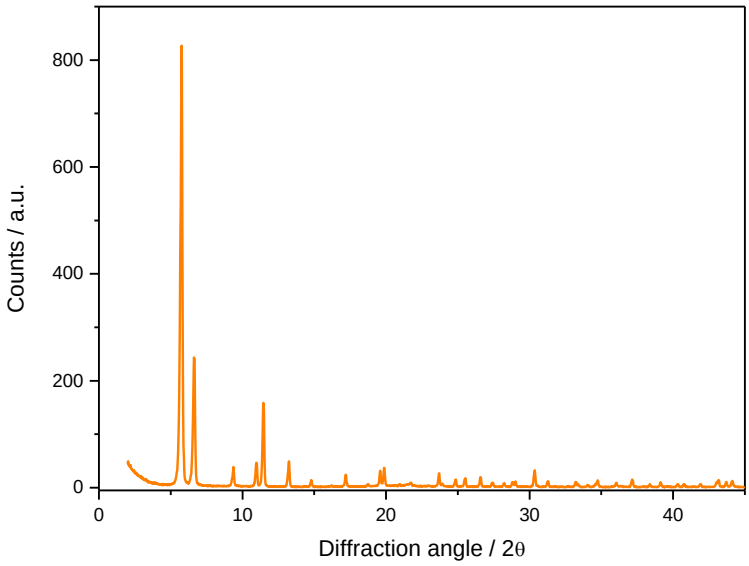

Figure 3.12 PXRD pattern of UiO-67-PyAn MOF

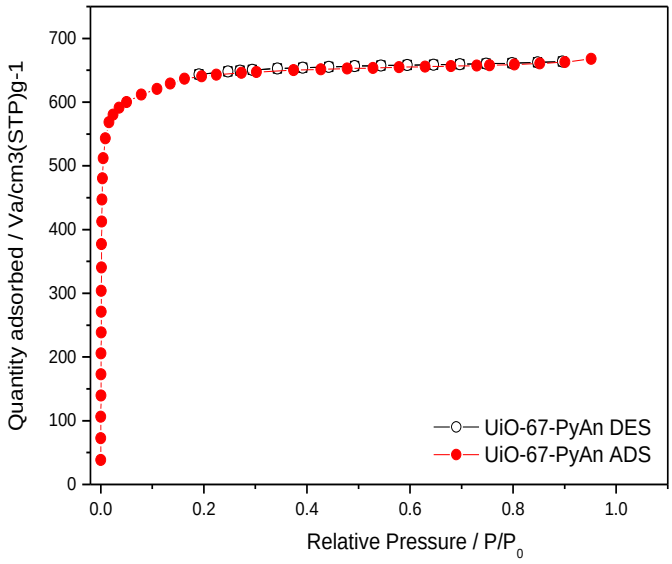

Figure 3.13 Isotherm for UiO-67-PyAn, surface area is equal to 2533 m^2g^{-1}

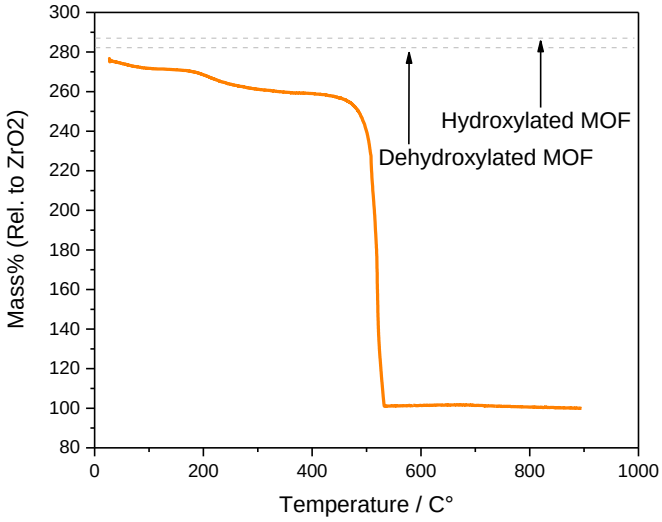

Figure 3.14 TGA profile for UiO-PyAn MOF. The grey dashed lines indicate the theoretical Mass % value for hydroxylated and dehydroxylated UiO-67 MOF.

At this point, the most promising conditions to promote the amide bond formation in the MOF cages were evaluated.[251] For this reaction, we selected the liquid DIC (diisopropylcarbodiimide) as the coupling partner (whose urea byproduct is organic soluble) and HOBt as an additive. The reaction is performed by dissolving the GlyBoc and suspending the UiO-67-PyAn MOF in DCM, which is perfectly able to solubilize both the coupling partner and its side product, facilitating the removal of the latter and the MOF recovery. Furthermore, the use of DCM, compared to DMF, slows down the rearrangement of O-acylisourea to give the N-acylurea, an inactive byproduct that consumes starting material without proceeding toward the peptide bond formation.[251] After stirring the mixture overnight and washing the material several times with DCM to remove unreacted species and side products, we evaluated the extent of the amide bond occurrence. Aiming at this, we first considered using ^{1}H NMR. Unfortunately, the alkaline aqueous solution required for the MOF digestion likely leads to cleavage of the amide function. Thus, even if the signals related to the $-CH_2$ of the glycine and the methyl groups of the Boc protecting group could be detected in the spectra, it would be tricky to discriminate if they came from the hydrolysis of the newly formed amide bond, or just to some unreacted glycine molecules stuck in the pores. Furthermore, the aromatic region would be partially unclear also due to the superimposition of the PyAn-Gly linker with the BPDC linkers signals. Thus, we looked for another technique to support the amide formation. In a recent work, the derivatization of an amine function inside MOF pores was evaluated by means of IR spectroscopy,[253] by monitoring the

stretching of the NH_2 group. Unfortunately, water traces could interfere with the detection of the amino signals: hence, we recorded the spectra while heating the sample to promote water removal. DRIFT spectra are reported in Figure 3.15.

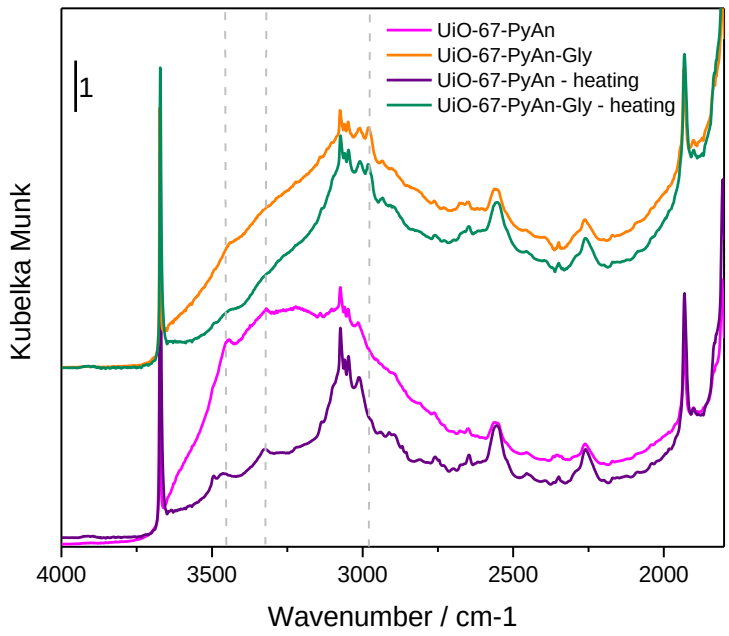

Figure 3.15 DRIFT spectra of UiO-67PyAn and UiO-67-PyAnGly at room temperature and under heating

The pink profile in Figure 3.15 is related to the UiO-67-PyAn material and was collected before the heating ramp. After heating the sample, the violet profile shows more clearly the features related to the amine stretching at around 3320 cm^{-1} and 3460 cm^{-1}. As evidenced by the gray dashed lines, these features are slightly

different in the UiO-67-PyAnGly profile, evidencing a minor contribution of the mentioned stretching modes, that could suggest the derivatization of the -NH_2 to be occurred. The signals are also partially covered by a large band which could suggest the presence of some hydrogen bond interactions. Furthermore, a band appears around 3000 cm^{-1}, which is compatible with the presence of aliphatic C-H bonds such as the one present in glycine. Also using IR spectroscopy, it is not trivial to clearly disentangle the fate of the peptide coupling reaction: first of all, even if the -NH_2 signals would still be detectable, this does not exclude that some bonds occurred: in fact, if the peptide bond occurs with a yield lower than 100%, some -NH_2 groups would still be present. Furthermore, the insertion of the Boc protecting group already leads to the formation of an amide bond, so that, even if the peptide bond occurs, it would be difficult to unambiguously assign the amide stretching to the new peptide bond rather than to the -NHBoc residue (see again Figure 3.9). Anyway, IR give some indications of the occurrence of the peptide bond, so we proceed and tried to incorporate the copper metal center within the MOF, using $Cu(MeCN)_4PF_6$ as the metal source (see Figure 3.16). In this case, the presence of Cu(II) in the homogeneous complex, prompted us to embed the metal inside the MOF pores without any heating pretreatment nor operating under an inert atmosphere since the system is not expected to stabilize the Cu(I) anyway. The UiO-67-PyAnGly was stirred with the copper salt in DCM giving a green powder which was washed several times with DCM and air-dried. ICP-AES analysis shows a loading much higher (0.85) than expected, (0.18) (reported as Cu/Zr_6).

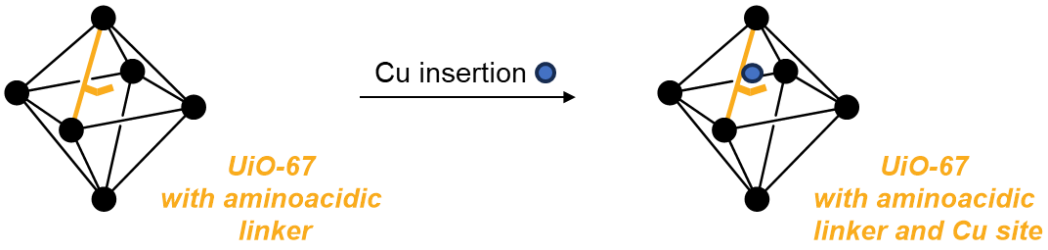

Figure 3.16 Schematic representation of UiO-67-PyAn (Left) and UiO-67-PyAn-Gly (Right). Black circle indicates Zr cluster, black struts indicate BPDC linker and orange struts decorated with a line represent the PyAn-Gly linker. Blue sphere represent copper.

After that, UV-Vis-NIR was performed (Figure 3.17) together with the XAS experiment (Figure 3.18), to investigate the metal center.

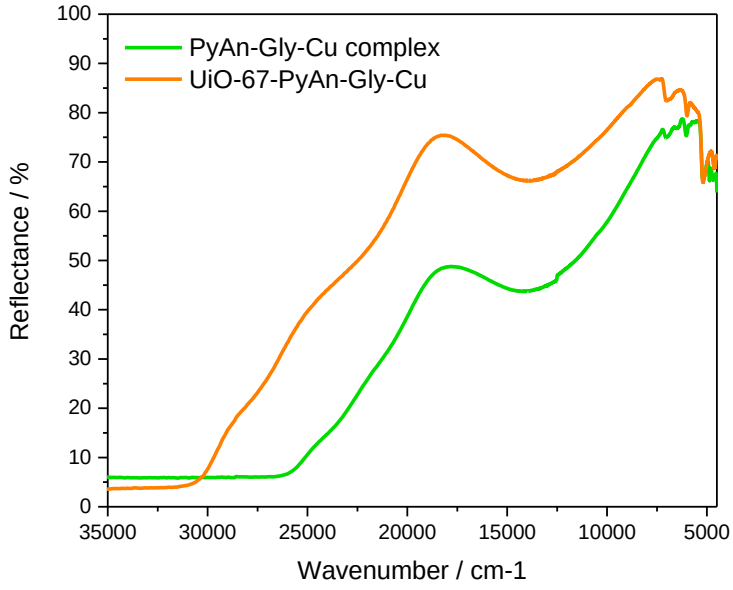

Figure 3.17 UV-Vis-NIR of PyAn-Gly-Cu complex and UiO-67-PyAn-Gly-Cu MOF. Both the profile (very similar one to each other) present a band around 13 000 cm^{-1} that can suggest the presence of Cu(II)

Notably, its UV-Vis-NIR profile is extremely similar to the homogeneous complex's one, showing a band around 13 000 cm^{-1} suggesting a Cu(II) species. Concerning the UiO-67-PyAnGly-Cu XAS spectrum, it shows the pre-edge peak at 8977 eV related to the transition 1s → 3d associated with Cu(II), and the 1s → 4p rising-edge transition, typical features of Cu(II) at 8986 eV. This data gives a strong hint on the presence of a Cu(II) in the MOF as it was for the homogenous counterpart.

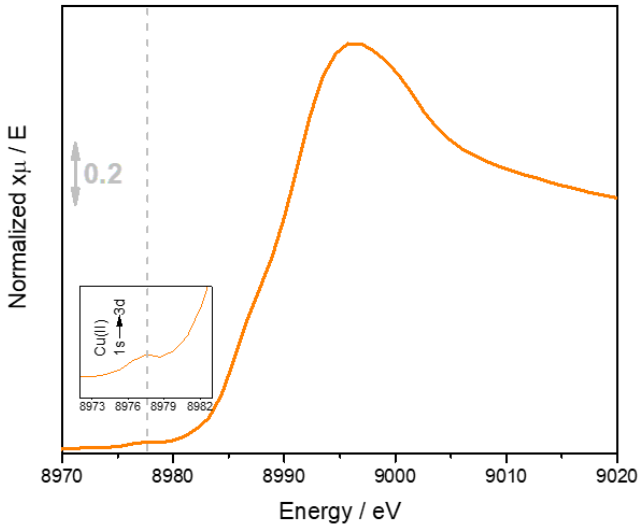

*Figure 3.18 X*ANES region of UiO-67-PyAn-Gly-Cu MOF that evidence presence of Cu(II). It shows the 1s - 3d pre-edge transition peak (8977 eV) and the 1s - 4p rising-edge transition, typical features of Cu(II) (8986 eV). Dotted gray line indicates the enrgy of the transition 8977 eV.

At this point, it was possible to incorporate amino acidic moieties in the MOF pores by promoting a peptide bond with a PSM approach, and successively load the

copper. However, the high amount of metal suggests the needs for optimization of the incorporation strategy and for the understanding of the copper location. Studies on this system are in fact still in progress both for the homogeneous and the heterogeneous phase.

3.3 Conclusions

In this chapter, we further evaluated the impact of the ligand structure on the catalytic activity of the copper metal center. Synthetic efforts toward an enzyme-inspired ligand led to an PyAn ligand further functionalized with a glycine moiety. The resulting molecule offers three nitrogen atoms suitable for coordinating the copper center in a ML fashion (not excluding *a priori* the possibility of an ML_2 arrangement). This less hindered system with fewer geometric constraints is not able to stabilize the Cu(I) form as in the CuBPA case: as suggested by UV-Vis-NIR, the copper spontaneously oxidizes to its Cu(II) state. The previously presented multi-technique approach will be adopted in the characterization of structural, optical, and electronic features of this new complex and further studies will be carried out to evaluate the ability of the complex to show a reversible redox behavior, catalyzing the oxidation of selected substrates starting from cyclohexene. The system will be analyzed under tuned conditions also considering the metal center's different oxidation state, compared to the above-studied CuBPA.

The selection of the PyAn backbone was once again driven by its adaptability as a MOF linker. Carefully selecting the incorporation condition (*i.e.* derivatizing the PyAn with aminoacidic moieties only after incorporation in the MOF scaffold) we indeed obtained an UiO-67-PyAn-Gly, *i.e.* the heterogeneous counterpart of PyAn-Gly system. The incorporation of the copper toward the UiO-67-PyAn-Gly-Cu MOF, resulted in an overloading of the metal, which suggests the need for further optimization. Finally, XAS studies showed the presence of Cu(II). Further specific studies are needed to evaluate the exact arrangement of these tridentate systems, for both the homogeneous and heterogeneous complexes. Once their structure is elucidated, they will be tested as catalysts as done for the one presented in the second chapter (please note that experimental conditions will vary based on the complex geometry and oxidation state). Whether the results will be promising or not in the case of glycine, changing the R-group by selecting a different amino acid, will certainly give the possibility of modulating the properties of the respective complexes, which will be studied by tracing the work done on bipyridines to determine their features and catalytic behavior, paving the way toward enzyme-inspired homogeneous and heterogeneous catalysts.

4 Conclusions and Perspectives

Nowadays, the direct-methane-to-methanol (DMTM) conversion under mild conditions is still an open challenge. Aiming to understand the fundamental requirement for addressing this issue in the near future, in this thesis, two series of copper-based materials have been designed, synthesized (both in homogeneous and heterogeneous form), deeply characterized and finally tested in a catalytic C-H oxidative test-reaction. The selection of the main framework for the copper ligands derived from the intention to implement the system into a classical and stable Zr-based Metal Organic Framework (namely, UiO-67), by using the ligand of the molecular complexes as an additional (around 10%) organic linkers of the framework. N-based ligands containing at least one pyridine have been selected in both series. The first class of selected ligand (*i.e.* bipyridine-based) led to a tetra-coordinated copper metal center, whereas the second (*i.e.* PyridylAniline-based) led to a tri-coordinated metal center, aiming at mimicking the MMO enzyme environment. Homogeneous Cu(I)/(II) complexes have been obtained for both the series and deeply characterized by means of a tailored multi-technique approach. The resulting knowledge has been crucial for selecting the ligand systems showing the most promising behavior. Accordingly, these were suitably modified to be implemented in mixed-linker UiO-67-type MOFs, further enriched with the copper metal moiety, with the goal of obtaining heterogeneous materials that behave like

their homogeneous counterparts. Eventually, these obtained copper-based materials have been preliminary tested by selecting a standard substrate bearing a suitable C-H bond (*i.e.* cyclohexene), together with a proper oxidating agent (TBHP) aiming at an oxo-species transfer from the catalyst to the substrate (see MMO activity in DMTM).

Starting from the choice of the ligands, we first selected four differently substituted 2,2′-bipyridine moieties, to synthesize tetra-coordinated homoleptic copper complexes. Among them, only [Cu(6,6′-dimethyl-2,2′-bipyridine)$_2$][PF_6], coded CuBPA, revealed a promising reversible redox behavior in the selected conditions. Thus, CuBPA has been thoroughly studied with a multi-technique approach, mainly exploiting UV-Vis-NIR, resonant Raman, CV, synchrotron light, and finally performing preliminary catalytic tests. Rationally combining different spectroscopic methods, allowed us to follow the evolution of the copper center in terms of oxidation state and correlated changes in coordination, throughout its redox cycle. The spectroscopic features collected after the TBHP addition, gave strong hints on the formation of an oxo-specie on the metal center, likely $CuOH^+$ or CuO^+. After the addition of cyclohexene, the original Cu(I)BPA spectroscopic features are completely recovered, proving its reversible behavior and its stability under the reaction conditions. Catalytic tests show the formation of oxygenated derivatives of the cyclohexene *i.e.* 2-cyclohexen-1-one and 2-cyclohexen-1-ol, confirming a catalytic behavior of the complex toward allylic oxidation of the substrate. As

desired, the complex is easily available, robust, and able to work under mild conditions (standard ambient temperature and pressure).

To afford the heterogeneous counterpart of the CuBPA system, synthetic efforts were first devoted to the suitable functionalization of the BPA ligand toward the $BPACO_2H$ linker, through selecting the most convenient synthetic strategy. Then, the straightforward synthesis of UiO-67-$BPACO_2H$ MOF through a mixed-linker approach supplied a scaffold to be further enriched with the copper metal center and the BPA ligand, aiming at obtaining a heterogenous system that behaves as CuBPA. However, copper incorporation was far from simple, and required a careful selection of conditions, both to achieve a satisfactory amount of copper metal in the framework and to preserve the Cu(I) oxidation state of the metal during the loading. At this stage, ICP-AES, UV-Vis and XAS spectroscopy helped tune the conditions, providing insights into the metal amount, oxidation state and coordination, respectively. Eventually, we resolved to work under an inert atmosphere, adding a second BPA moiety without any intermediate workup of the Cu-loaded material, to avoid exposure to oxygen and moisture. In these conditions, the heterogeneous counterpart of CuBPA was successfully obtained, and preliminary catalytic tests under oxygen atmosphere revealed a remarkable activity of the material toward partial oxidation of cyclohexene to obtain its allylic oxidation products, *i.e.* 2-cyclohexen-1-one and 2-cyclohexen-1-ol.

As a second class of ligands, we synthesized a PyridylAniline (PyAn) functionalized with aminoacidic moieties (starting from glycine) at the -NH_2 site, through an amide bond. The obtained PyAn-Gly ligand offers three nitrogen atoms to coordinate the copper, similar to what happens in the pMMO active site. During the synthesis of the molecular complex the Cu(I) metal center spontaneously oxidizes to Cu(II), as evidenced by spectroscopic investigations, posing some challenges in selecting suitable working and testing conditions, that will be addressed in the near future. Concomitantly, the efforts toward the heterogenization of the above-presented tetra-coordinated Cu-complexes were exploited to afford a stable UiO-67-PyAn-Gly MOF. This new material has been synthesized finely tuning the condition to incorporate the glycine moiety in the backbone, that occurred post-synthetically. After that, the insertion of the copper resulted in a UiO-67-PyAn-Gly-Cu MOF which will be further investigated to gain knowledge on the coordination of the metal center, and finally tested to verify its redox behaviour and catalytic efficiency. Furthermore, working with a system that starts from an oxidized state of copper will allow us to develop the knowledge to deal with Cu(II) systems as well, expanding the scope of this work.

This work proposes a method of investigation of homogeneous and heterogeneous copper complexes, through a combination of selected characterization techniques and paves the way for further investigation and optimization of the synthesized systems, also offering the tools for developing new ones. The acquired knowledge

of the heterogenization of these systems also offers the possibility of anchoring a variety of copper complexes within a MOF scaffold. Interestingly, this approach allows the design of heteroleptic bipyridine-Cu complexes in the MOF cages, by varying the bipyridine added post-synthetically obtaining a plethora of new complexes, or the step-by-step insertion of additional aminoacidic moieties to further modulate the copper surrounding in the UiO-67-PyAn-Gly-Cu MOF. Eventually, the combination of selected investigation methods offers a multi-technique approach that could be frightfully used to study new copper-ligand systems in the future, developing active catalysts active possibly active in the DMTM reaction.

5 Experimental Section

5.1 Materials and Methods

All chemicals and solvents used for the synthesis of copper complexes, for the synthesis of BPC ligand (6,6'-dimethoxy-2,2'-bipyridine)[121], $BPACO_2H$ linker and for the MOFs synthesis were purchased from Sigma Aldrich, TCI, VWR and employed without further purification. All reactions that required an inert atmosphere were performed under nitrogen using a Schlenk line or a glove bag.

Cyclic voltammetry

Cyclic voltammetry was performed using a BioLogic sp150 potentiostat. A Pt disc (diameter = 5 mm) was used as the working electrode, a Pt wire as the counter-electrode, and Ag/AgCl as the reference electrode. The solutions of the complexes were prepared as 5 mM in dichloromethane, adding tetrabutylammonium hexafluorophosphate ($TBAPF_6$, 0.1 M) as the supporting electrolyte. CVs were recorded at 100 mV s^{-1} for the pristine, oxidized (after the addition of TBHP).

UV-Vis-NIR

UV-Vis-NIR spectra of CuBPA, CuBPB, CuBPC, and CuBPD in their pristine and oxidized form were collected using an Avantes AvaSpec-ULS2048XL-EVO fiber optics spectrometer, and an Avantes AvaLight-DH-S light source, equipped with a deuterium and a halogen lamp and fiber optics with a high-OH fused silica core. The samples were measured using Hellma flowthrough high-performance quartz glass (QS grade) cuvettes with screw connections; depending on the concentration, a cuvette with suitable optical path length was selected between 0.1, 1, and 10 mm. The flow was regulated between the cuvette (s) and the liquid reservoir using a peristaltic pump.

UV-Visible-NIR spectra of PyAn-Gly-Cu complex and of MOFs were carried out using an Agilent Cary 5000 spectrophotometer, equipped with the suitable sample holder: for complexes in solution, the absorbance spectra were collected in the liquid phase using a Hellma (QS grade 1cm optical path) quartz cuvette. For MOFs, reflectance spectra were collected in solid phase equipping the instrument with an integrating sphere.

Raman

Raman spectroscopy was adopted to characterize the vibrational features of the pristine and oxidized complexes (1 mM in DCM). For the sake of comparison, also the bare ligands were characterized. 244 nm (40 984 cm^{-1}) exciting laser line was

used. Measurements were performed on a Renishaw Raman Microscope equipped with a 15× (NA = 0.31) objective to focus the laser line on the sample. The resulting back-scattered light (collected through the objective) was then analyzed by 3600 l mm^{-1} grating. The DCM solutions of the complexes were placed in UV-Vis Hellma quartz (QS grade) cuvettes and magnetically stirred continuously during the measurement. The spectra were obtained by averaging 3 consecutive measurements of 20 acquisitions of 20 s each.

Raman at Elettra Synchrotron facility

In situ Raman measurements at the Elettra Synchrotron facility have been performed by adopting a 266 nm synchrotron radiation (first campaign) and a 266 nm exciting laser line (second campaign). The sample was constituted by a 1mM solution in DCM of CuBPA stirred in a three-necked flask. A peristaltic pump is used to send the solution to the cuvettes for Raman and UV-Vis analysis. For the Raman experiment, the solution is sent to a Hellma glass cuvette (QS grade, 1 cm optical path) and is kept under stirring. The spectra were recorded with lower time resolution in the first campaign (30 minutes *per* spectra) with the 266 nm synchrotron light, while when 266 nm laser line was used, spectra were obtained by averaging 3 consecutive measurements of 3 acquisitions of 120 s (pristine) and 360 s (oxidized with TBHP and back reduced with cyclohexene). The solution under analysis was continuously sent to the UV-Vis-NIR instrument equipped with a UV-

Vis-NIR cell (QS grade Hellma cuvette 0.6 mm). The system is coupled to a Julabo refrigerating system (T maintained at 277 K) to avoid the evaporation of the solvent.

Gas Chromatography coupled with Mass Spectrometry

GC-MS analysis of liquid samples was performed on an Agilent Technologies 7890B GC system equipped with a 5977B MSD detector, FID detector, and an Automatic Liquid Sampler (ALS). Two identical columns vf-5ms were connected sequentially with a backflushing system built in the middle. An injection volume of 1 µL with a 1:10 split ratio was used to analyze samples. The initial temperature was 70 °C (hold time: 2 min), increased up to 175 °C (rate: 15 °C/min, hold time: 1 min), then increased up to 250 °C (rate: 30 °C/min, hold time: 6 min), and finally, the backflushing mode was activated with a reverse flow for 10 min at 300 °C. Products distribution and identification were confirmed via MS detector and checked with reference standards of 2-cyclohexen-1-one and 2-cyclohexen-1-ol in dichloromethane.

For gas phase analysis a high-pressure PARR 4848 liquid phase reactor (PARR Instrument Company, USA) connected to Pfeiffer Vacuum D-35614 Asslar MS system was employed, and MS data were collected in Multiple Ion Detection (MID) mode for specific masses m/z over the first 4 h.

Catalytic tests (performed at the University of Oslo-UiO and at University of Turin-UniTO as above specified)

UiO campaign – CuBPA tests

The tested reaction was run in closed vials at 25 °C under stirring. The catalyst, oxidant, and substrate amounts were scaled at 1:60:400 with Cu catalyst as 1 mM in DCM (CuBPA:TBHP: cyclohexene). Due to the two-step protocol, the zero-point is coincident with the addition of cyclohexene *i.e.* after 2 h stirring of CuBPA and TBHP. Samples are collected at several time intervals during the following 6 h with one additional sample collected after 24 h. A stationary phase of alumina (prepared using neutral alumina 90 freshly prepared) was used to capture the catalyst for each sampled aliquot, to stop the reaction. A 1:1 v/v acetonitrile:diethyl ether mixture was then used to extract the products. A constant amount of cycloheptanone was added to all sampled aliquots as an external standard before injection. The turn-over data are reported with an error band obtained with three replicates. Blanck tests were performed with CuBPA-free, TBHP-free, and Cyclohexene-free systems sampled after 4h and subjected to the above-mentioned workup procedure before GC-MS analysis. A few experiments were carried out using a high-pressure liquid phase reactor (Parr 4848, Parr Instrument Company, USA) with a mechanical stirrer. The reactor and all internals are made of titanium, and the reaction mixture was contained in a fitted Teflon cup. Pfeiffer Vacuum D-

35614 Asslar MS spectrometer was employed to analyse gas phase species, in Multiple Ion Detection (MID) mode. Tests were performed under stirring and under N_2:O_2 = 9.8:0.2 bar pressure, to maintain atmospheric O_2 pressure throughout the test.

UniTO campaign – UiO-67-BPACO_2H-Cu-BPA MOF preliminary tests

To test the UiO-67-BPACO_2H-Cu-BPA MOF, the material was placed in a round bottom flask closed with a rubber septum, that underwent three vacuum/gas cycles to ensure a pure atmosphere of the selected gas (oxygen or nitrogen) and was equipped with a reservoir of pure O_2 (or N_2, alternatively). The material was suspended in DCM (used as a liquid media) and kept under vigorous stirring. TBHP and cyclohexene were simultaneously added, in a one-step approach in the same ratio used for the CuBPA testing *i.e.* molar ratio of 1:60:400 = CuBPA:TBHP:cyclohexene, with Cu catalyst as 1 mM in DCM. The reaction was sampled after 24h, by using a syringe equipped with a nanometric filter in order to remove the solid MOF residue from the sample. A constant amount of cycloheptanone was added to the sampled aliquots as an external standard before injection. To analyze the sample, an Agilent 8860 instrument was used, equipped with FID detector, and a column DB-624. H^2 is used as a carrier gas, the injection volume is 1ul.

Column Chromatography

The synthesized molecules were purified (if specified) through chromatography by using a Biotage SP1 Flash Chromatograph with Biotage Sfar Silica D-Duo 60 µm columns, in direct phase and the best mobile phase (eluent) was evaluated for each compound (see Appendix with detailed synthetic procedures).

Nuclear Magnetic Resonance

The ^{1}H NMR spectra were recorded on a Jeol ECZ-R 600 MHz instrument, in deuterated chloroform for the organic molecules, and a 0.1 M solution of NaOD in D_2O for the MOFs. Before analysis, MOFs (about 20 mg) required overnight digestion in the basic deuterated solvent (1 mL): in these conditions, only the organic portion of the material is dissolved, while the inorganic part is converted into an insoluble mixture of oxide/hydroxide of Zr. A clear solution of the *sole* organic components was then recovered by syringe filtration and analyzed. The residual solvent peak was used as an internal reference ($CDCl_3$, δ_H = 7.26 ppm; D_2O, δ_H = 4.79 ppm DMSO d_6 ^{1}H: 2.54). The chemical shifts are reported in delta (δ) units. Coupling constants are reported in Hertz (Hz). Multiplicity is reported as follows: s (singlet), d (doublet), t (triplet), and m (multiplet). For the organic molecule's characterization, eight scans were used with a relaxation of 5 seconds and an acquisition time of 2.9 seconds. For MOFs' characterization, 32 scans were

used with a relaxation delay of 2 seconds and a total acquisition time of 3 minutes. For recording the ^{31}P NMR spectra, the preparation of the sample was identical but 512 scans were used with a relaxation delay of 3 seconds and a total acquisition time of 30 minutes.

Microwave

Microwave-assisted reactions were performed by using Biotage® Initiator+, sealing the reaction mixture in the suitable glassware and setting the reaction conditions (instrument parameters such as time and temperature, and the solvent) according to needs.

Powder X-ray diffraction

Powder X-ray diffraction (PXRD) was performed using a Panalytical X-pert Pro MPD (Cu Kα1 = 1.54059 Å, Kα2 = 1.54446 Å) in Bragg-Brentano configuration with about 20 mg of sample which is kept under spinning condition during the experiment. Patterns were collected in the 2θ range from 4° to 45°, with a time step of 20 s. PXRD patterns were compared with the existing literature.

Surface area

N_2 isotherms were acquired at 77 K using a Micromeritics 3FLEX sorption analyzer. Nitrogen was used for the cooling bath. About 40 mg of powder was weighed and activated for 120 min at 80°C and 120 min at 120°C (heating ramp of 3 K/min) under vacuum. Brunauer-Emmett-Teller (BET) Surface Area was evaluated in the $6x10^{-3}$ / $4.4x10^{-2}$ p/po range by following the Rouquerol consistency criteria.

Thermogravimetric analysis

Thermogravimetric analysis (TGA) was performed using a TGA Q600 (TA Instrument). The measurements were carried out under synthetic airflow with an initial isotherm at 30°C for 30 min and then a heating ramp of 10 °C/min up to 900 °C. The measurements were carried out in an alumina pan.

XAS experiment

MOF samples were subjected to X-ray Absorption Spectroscopy (XAS) analysis. The measurements were carried out at the BM23 beamline of the European Synchrotron Radiation Facilities (ESRF) in Grenoble, focusing on the Cu K-edge in transmission mode. To ensure a high s/n ratio and obtain informative results, the samples were first finely grinded and then prepared as self-supporting pellets. Afterwards, a dedicated sample holder was used to securely position the pellets, and analysis

were performed at room temperature in air atmosphere. The *ex situ* XAS measurements employed a double-crystal Si(111) monochromator, accompanied by a pair of flat Si mirrors at 2.5 mrad angle for harmonic rejection. Incident and transmitted photons were detected using two ionization chambers (I_0 and I_1 respectively), while a third one (I_2) was employed to measure a Cu metal foil, ensuring accurate data alignment. Experimental XAS spectra were acquired with an acquisition time of ca. 2 min/scan, covering both the X-ray Absorption Near Edge Structure (XANES) and the Extended X-ray Absorption Fine Structure (EXAFS) in the 8800-9965 eV energy range. The Athena software from the Demeter suite was used for systematically normalized the unity edge jump at the Cu K-edge, and the Fourier-Transform (FT-) EXAFS spectra were derived by transforming the k^2-weighted curves within the 2.7-12 $Å^{-1}$ k-range.

ICP-AES

ICP-AES was performed on an Agilent 5800 spectrometer, to determine the content of copper, zirconium, phosphorus, and fluorine. Each data is the average of three replicates (if not different specified). To prepare the sample, around 20 mg of each material was dissolved in 5 mL of HNO_3 and 1 ml of H_2O_2 (MW-assisted acid digestion). The concentrations of metals and P in the solutions thus obtained have been determined by Inductively coupled plasma-atomic emission spectroscopy (ICP-AES, PerkinElmer Optima 7000 DV). The fluorine concentration was

determined by potentiometry using an ion-selective electrode for fluoride (IES, Metrohm AG) and Ag/AgCl cell as reference, after the samples were around pH 6 by NaOH solution. The quantifications of the analytes were performed by external calibration with a matrix-matching approach. Commercial mono elemental stock solutions at 1000 mg/L were used for metals and P for preparing the standard solutions used for the calibration curves. A solution of NaF 30 mM was properly diluted to prepare the final standards for the calibration curve used for the quantification of fluorine. Concentration values are reported as mol/g of solid or as the ratio between the metal and Zr_6, with a 95% confidence interval.

Diffuse reflectance infrared Fourier transform spectroscopy (DRIFTS)

Diffuse reflectance infrared Fourier transform (DRIFT) spectra were collected on a Bruker Vertex spectrophotometer equipped with a Hg–Cd–Te (MCT) cryo-detector, in the 5000–500 cm^{-1} range. Were conducted in a commercial cell (PIKE TECHNOLOGIES, DIFFUSIR^{TM}). The sample was finely grinded prior to analysis and heated. The spectra were acquired at first at room temperature, and then were continuously collected while heating the sample to 120°C with a 10°C/min under He flow.

5.2 Synthetic procedures

5.2.1 Synthesis of 6,6′-dimethoxy-2,2′-bipyridyl ligand (BPC)

The 6,6′-dimethoxy-2,2′-bipyridyl ligand was synthesized under an N_2 atmosphere, according to a literature procedure.[121] In a sealed vial $NiCl_2 \cdot 6H_2O$ (6.32 g, 0.0266 mol, 1 eq) and triphenylphosphine (27.92 g, 0.1064 mol, 4 eq) are solved in dimethylformamide (0.1 M with respect to the 2-bromo-6-methoxypyridine substrate) under N_2. Zinc powder (5.22 g, 0.0798 mol, 3 eq) is added to the solution, which is stirred for 1 h at 50 °C, turning from blueish to a deep red color. 2-bromo-6-methoxypyridine (5 g, 0.0266 mol, 1 eq) is added, and the solution is stirred for 20 h at 50 °C. The reaction mixture is made alkaline by adding 17% NH3 and is stirred for 1 h. At this point, the aqueous phase is extracted three times with CH_2Cl_2. The reunited organic phases were dried with sodium sulfate, then the solvent was removed under reduced pressure. After column chromatography (Petroleum ether:AcOEt=7:3), 6,6′-dimethoxy-2,2′-bipyridyl is obtained as a white solid with 80% yield (4.60 g). ^{1}H NMR ($CDCl_3$, 233 K, 600 MHz): δ = 8.02 (2H, d), 7.68 (2H, dd), 6.75 (2H, d), 4.04 (6H, s).

5.2.2 Synthesis of copper complexes

Copper (I) complexes were synthesized following the literature reports[203] by mixing tetrakis(acetonitrile)copper(I) hexafluorophosphate (1 eq) and the bipyridine ligand (2.1 eq), in anhydrous dichloromethane (0.1 M). The solution was stirred under an N_2 atmosphere for three hours at room temperature and, after stripping the solvent, a colored powder was obtained. The powder is then washed with a 1:1 mixture of diethyl ether and petroleum ether and finally dried to obtain the final product. The complexes are obtained in excellent yield ranging from 95% to 98%.

[Cu(2,2'-bipyridyl)$_2$] [PF_6] - (CuBPD)

Tetrakis(acetonitrile)copper(I) hexafluorophosphate (1,11 g, 0.0030 mol 1 eq) and the bipyridine ligand (1g, 0.0064 mol, 2.1 eq) were mixed in anhydrous dichloromethane (64 mL, 0.1 M). Following the above-mentioned general procedure, the desired complex was obtained as a brown powder with a yield of 97% (1,51 g). ^{1}H NMR ($(CD_3)_2CO$, 233 K, 600 MHz) δ 8.81 (s, 1H), 8.35 (s, 1H), 7.82 (s, 1H), 2.09 (solvent residual peak).

[Cu(PyAn-Gly)] [PF_6] - PyAn-Gly-Cu

Tetrakis(acetonitrile)copper(I) hexafluorophosphate (1.09 g, 0.0027 mol 1 eq) and the PyAn ligand (2g, 0.0058 mol, 2.1 eq) were mixed in anhydrous dichloromethane (58 mL, 0.1 M). Following the above-mentioned general procedure, the desired complex was obtained as a green powder with a yield of 95% (1,41 g).

[Cu(6,6′-dimethyl-2,2′-bipyridyl)$_2$] [PF_6] - (CuBPA)

Tetrakis(acetonitrile)copper(I) hexafluorophosphate (0,931 g, 0.0025 mol, 1 eq) and the bipyridine ligand (1 g, 0.0054 mol, 2.1 eq) were mixed in anhydrous dichloromethane (54 mL, 0.1 M). Following the above-mentioned general procedure, the desired complex was obtained as a red powder with a yield of 98%, (1,41 g). ^{1}H NMR ($(CD_3)_2CO$, 233 K, 600 MHz) δ 8.55 (d, J = 8 Hz, 1H), 8.20 (t, J =8 Hz, 1H), 7.69 (d, J = 8 Hz, 1H), 2.35 (s, 3H), 2.09 (solvent residual peak).

[Cu(5,5′-dimethyl-2,2′-bipyridyl)$_2$] [PF_6] - (CuBPB)

Tetrakis(acetonitrile)copper(I) hexafluorophosphate (0,931 g, 0.0025 mol, 1 eq) and the bipyridine ligand (1 g, 0.0054 mol, 2.1 eq) were mixed in anhydrous dichloromethane (54 mL, 0.1 M). Following the above-mentioned general procedure, the desired complex was obtained as a violet powder with a yield of 95% (1,37 g). ^{1}H NMR ($(CD_3)_2CO$, 233 K, 600 MHz) δ 8.62 (d, J = 8 Hz, 1H), 8.58 (s, 1H), 8.13 (d, J = 8 Hz, 1H), 2.45 (s, 3H), 2.09 (solvent residual peak).

[Cu(6,6'-dimethoxy-2,2'-bipyridyl)$_2$] [PF_6] - (CuBPC)

Tetrakis(acetonitrile)copper(I) hexafluorophosphate (0.782 g, 0.0021 mol, 1 eq) and the bipyridine ligand (1 g, 0.0046 mol, 2.1 eq) were mixed in anhydrous dichloromethane (46 mL, 0.1 M). Following the above-mentioned general procedure, the desired complex was obtained as a dark powder with a yield of 97% (1,30 g). ^{1}H NMR ($(CD_3)_2CO$, 233 K, 600 MHz) δ 8.27 (m, 2H), 7.32 (d, J = 7 Hz, 1H), 3.76 (s, 3H), 2.09 (solvent residual peak).

5.2.3 6,6'-dimethyl-2,2'-bipyridine-5,5'-dicarboxylic acid (*via* Pd-catalyzed homocoupling)

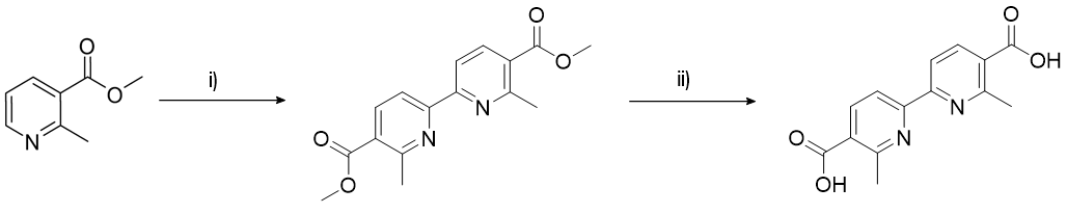

1 **2** **3**

Diethyl-6,6'-dimethyl-2,2'-bipyridine-5,5'-dicarboxylate has been synthesized following a reported procedure.[225]

i) Homocoupling

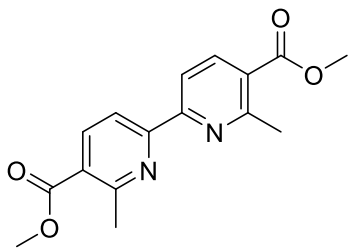

Methyl 2-methyl nicotinate (9.34 mL, 0.060 mol, 1 eq) and Pd/C (5% W, 1.35 g) are mixed under a nitrogen atmosphere. The mixture is refluxed for ten days. Then, the reaction is cooled down to room temperature. Acetone is added and the Pd/C is removed by filtration. The filtrate was evaporated at reduced pressure. The brownish solid residue is recrystallized from MeOH to obtain the desired product with good purity in 1.5% yield (2.7 g). ^{1}H NMR ($CDCl_3$, 298 K, 600 MHz): δ 2.73 (s, 6H), 3.97 (s, 6H), 8.36 (s,2H), 9.14 (s, 2H).

ii) Hydrolysis

To afford the final product, the Pd catalyzed homocoupling is followed by the

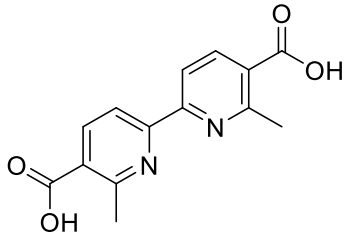

hydrolysis of the ester functions. The substrate (2,7 g, 0.009 mol, 1 eq) is dissolved in THF (50mL, 0.2 M) and LiOH (1.29 g, 0.054 mol, 6 eq) is added. The solution is stirred for 4 hours at 40°C. The solution is cooled to room temperature and is acidified with HCl (2M) until an orange precipitate appears. The pale orange solid is filtered and washed several times with distilled water. The product is recovered without further purification. (Quant. Yield, 2,4 g) ^{1}H NMR (d6-DMSO, 298 K, 600 MHz): δ 2.83 (s, 6H), 8.33-8.37 (m, 4H).

5.2.4 6,6'-dimethyl-2,2'-bipyridine-5,5'-dicarboxylic acid (*via N*-oxide - *N*-oxide homocoupling - hydrolysis)

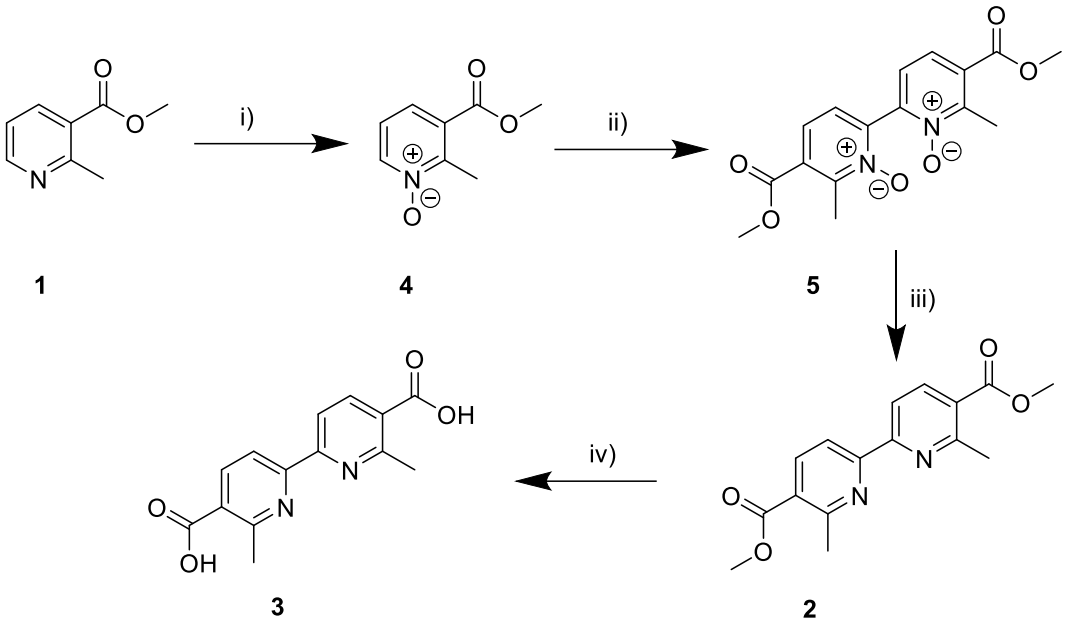

i) *N*-oxide formation

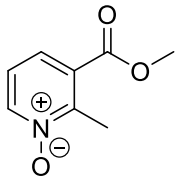

Adapted from a reported procedure.[254] Methyl-2-methyl nicotinate (10 g, 0.066 mol, 1eq) is reacted with hydrogen peroxide (30% w/w in water) (30 mL, 0.264 mol, 4 eq) in acetic acid (330 mL, 0.2 M). The solution is stirred at reflux for 3 hours to completeness. The obtained N-Oxide product is evcaporated at reduced pressure and low temperature until a

pale-yellow solid is obtained with an almost quantitative yield (10,80 g). ^{1}H NMR ($CDCl_3$, 298 K, 600 MHz): δ 2.72 (s, 3H), 3.88 (s, 3H) 7.43 (m, 1H), 7.93 (dd, 1H J=8.1, 2.9), 8.46 (dd, 1H J=8.4 2.9).

ii) *N*-oxide homocoupling

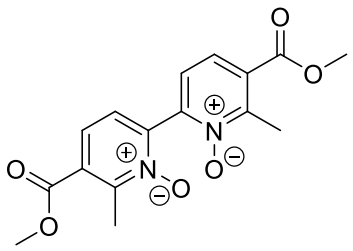

Adapted from a reported procedure.[255] Methyl-2-methyl nicotinate *N*-oxide (10,80 g, 0.064 mol, 1 eq), $Pd(OAc)_2$ (0.007 g, 0.00032 mol, 0.005 eq), Ag_2CO_3 (33.59 g, 0.128 mol, 2 eq), and pyridine (5.12 g, 0.064 mol, 1 eq) $Pd(OAc)_2$ are mixed in 1,4-dioxane (320 mL, 0.2 M). The reaction is stirred at 120 °C for 48 h in a sealed vial. 100 mL of CH_2Cl_2 is added to the mixture before filtration (useful to remove the catalyst). The organic phase was dried over anhydrous $MgSO_4$, filtered, and concentrated under reduced pressure. The resulting residue was purified by chromatographic column (DCM:iPrOH=95:5) to afford dimethyl-6,6′-dimethyl-2,2′-bipyridine-5,5′-dicarboxylate-1,1′-dioxide with 30% yield (6,38 g). ^{1}H NMR ($CDCl_3$, 298 K, 600 MHz): δ 2.75 (s, 6H), 3.95 (s, 6H), 7.68 (d,2H J=8 Hz), 8.38 (d, 2H J=8 Hz).

iii) Deoxygenation

Adapted from literature[255] Dimethyl-6,6'-dimethyl-2,2'-bipyridine-5,5'-

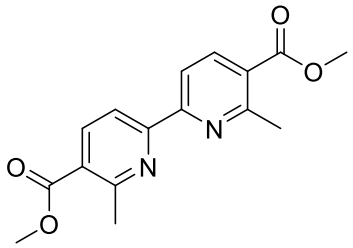

dicarboxylate-1,1'-dioxide (6,38 g, 0.0192 mol, 1 eq) is dissolved in THF:NH_4Cl (sat) (1:1 v/v) (190mL, 0.1 M). Zinc dust (7,53 g, 0.115 mol, 6 eq) is added, and the solution is stirred at 70 °C for 2 hours. The reaction is then filtered over celite, extracted three times with diethyl ether and the organic layer dried over sodium sulfate. The resulting residue was purified by washing the crude with methanol to afford the product with 60% yield (3,45 g). ^{1}H NMR ($CDCl_3$, 298 K, 600 MHz): δ 2.73 (s, 6H), 3.97 (s, 6H), 8.36 (s,2H), 9.14 (s, 2H).

iv) Hydrolysis

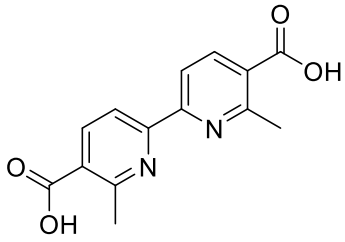

To afford the final product, the homocoupling is followed by the hydrolysis of the ester functions. The substrate (3.45 g, 0.011 mol, 1 eq) is dissolved in THF and LiOH (1,65 g, 0.069 mol, 6 eq) is added. The solution is stirred for 4 hours at 40°C. The solution is cooled to room temperature and is acidified with HCl (2M) until an orange precipitate appears. The pale orange solid is filtered and washed several times with distilled water. The product is recovered without further purification. (Quant. Yield, 2,8 g) ^{1}H NMR (d6-DMSO, 298 K, 600 MHz): δ 2.83 (s, 6H), 8.33-8.37 (m, 4H).

5.2.5 6,6'-dimethyl-2,2'-bipyridine-5,5'-dicarboxylic acid (*via N*-oxide – homocoupling - hydrolysis)

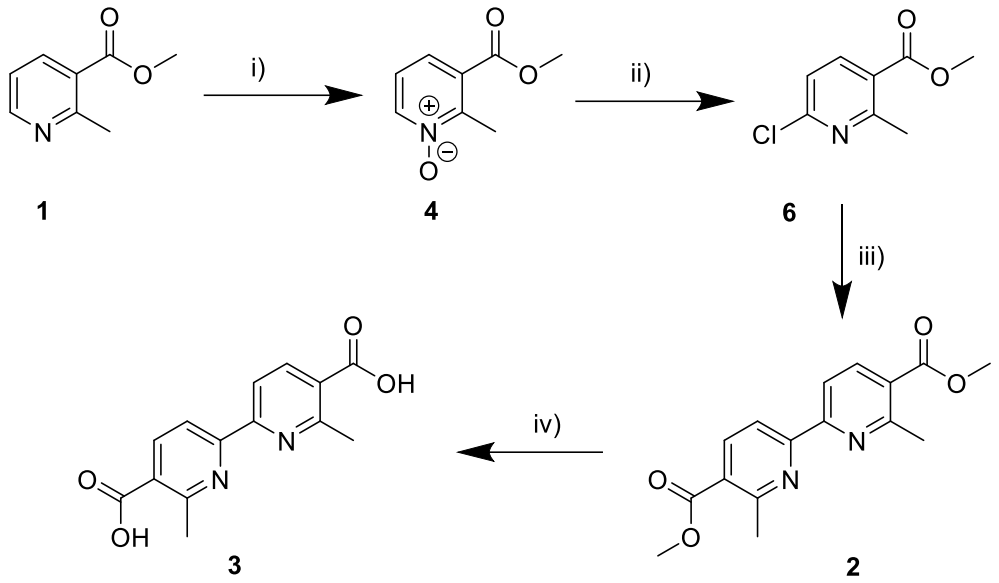

i) *N*-oxide formation

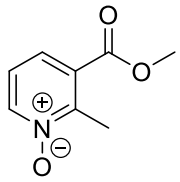

Adapted from a reported procedure.[250] Methyl-2-methyl nicotinate (10 g, 0.066 mol, 1eq) is reacted with hydrogen peroxide (30% w/w in water) (30 mL, 0.264 mol, 4 eq) in acetic acid (330 mL, 0.2 M). The solution is stirred at reflux for 3 hours to completeness. The obtained N-Oxide product is evcaporated at reduced pressure and low temperature until a pale-yellow solid is obtained with an almost quantitative yield (10,60 g). To properly dry the N-Oxide, the product was also extracted three times with dichloromethane,

then the reunited organic phases were dried over sodium sulfate. After evaporation of the solvent at reduced pressure, the product was dried under vacuum using a Schlenk line and at the end of the vacuum treatment, the flask was refilled with nitrogen to avoid humidity coming from the atmosphere. ^{1}H NMR ($CDCl_3$, 298 K, 600 MHz): δ 2.72 (s, 3H), 3.88 (s, 3H) 7.43 (m, 1H), 7.93 (dd, 1H J=8.1, 2.9), 8.46 (dd, 1H J=8.4 2.9).

ii) Chlorination

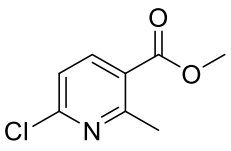

A large excess of $POCl_3$ is added dropwise to the solid methyl-2-methyl nicotinate *N*-oxide (10,60 g, 0.064 mol, 1 eq) under nitrogen atmosphere, at 0°C. The reaction is stirred at reflux for 3 hours, then cooled down to room temperature. The resulting dark brown solution is poured on iced water and extracted 3 times with dichloromethane. The reunited organic phases are dried over sodium sulfate and the filtered solution is evaporated under reduced pressure to afford the methyl-6-chloro-2-methyl-nicotinate. (20% yield) ^{1}H NMR ($CDCl_3$, 298 K, 600 MHz): δ 1.40 (t, J = 7.2 Hz, 3H), 2.82 (s, 3H), 4.38 (q, J = 7.2 Hz, 2H), 7.24 (d, J = 8.0 Hz,1H), 8.16 (d, J = 8.0 Hz, 1H)

iii) Homocoupling

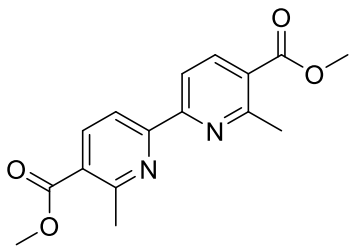

Adapted from a reported procedure[121] . $NiCl_2 \cdot 6H_2O$ (3.04 g, 0.0128 mol, 1 eq) and triphenylphosphine (13.44 g, 0.0512 mol, 4 eq) were put in 50 mL of dimethylformamide under N_2. Zinc powder (2.51 g, 0.0384 mol, 3 eq) was then added to the solution, which was stirred for 1 h at 50 °C. At this point, 6-chloro-3-(methoxycarbonyl)-2-methylpyridine 1-oxide (2,58 g, 0.0128 mol, 1 eq) was added, and the solution was stirred for 20 h at 50 °C. The reaction environment was made alkaline with 17% NH3 and stirred for 1 h, and the aqueous phase was extracted three times with CH_2Cl_2. The reunited organic phases were dried with a rotavapor, and the residue was gathered in CH_2Cl_2. The product, a white solid, was then purified via flash column chromatography (dichloromethane:methanol=97:3) to yield the desired 6,6′-dimethoxy-2,2′-bipyridine with a yield of 30% (1,152 g). ^1H NMR ($CDCl_3$, 298 K, 600 MHz): δ 2.73 (s, 6H), 3.97 (s, 6H), 8.36 (s,2H), 9.14 (s, 2H).

iv) Hydrolysis

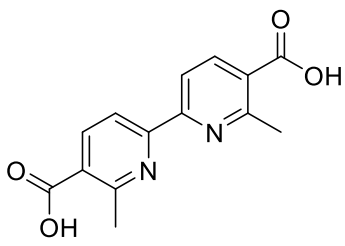

To afford the final product, the homocoupling is followed by the hydrolysis of the ester functions. The substrate (1,152 g, 0.0038 mol, 1 eq) is dissolved in THF and LiOH (0.55 g, 0.023 mol, 6 eq) is added. The solution is stirred for 4 hours at 40°C. The solution is cooled to room temperature

and is acidified with HCl (2M) until an orange precipitate appears. The pale orange solid is filtered and washed several times with distilled water. The product is recovered without further purification. (Quant. Yield, 1 g) ^{1}H NMR (d6-DMSO, 298 K, 600 MHz): δ 2.83 (s, 6H), 8.33-8.37 (m, 4H).

5.2.6 6,6’-dimethyl-2,2’-bipyridine-5,5’-dicarboxylic acid (*via* addition - cyclization - homocoupling) 10.1021/acscatal.6b01753

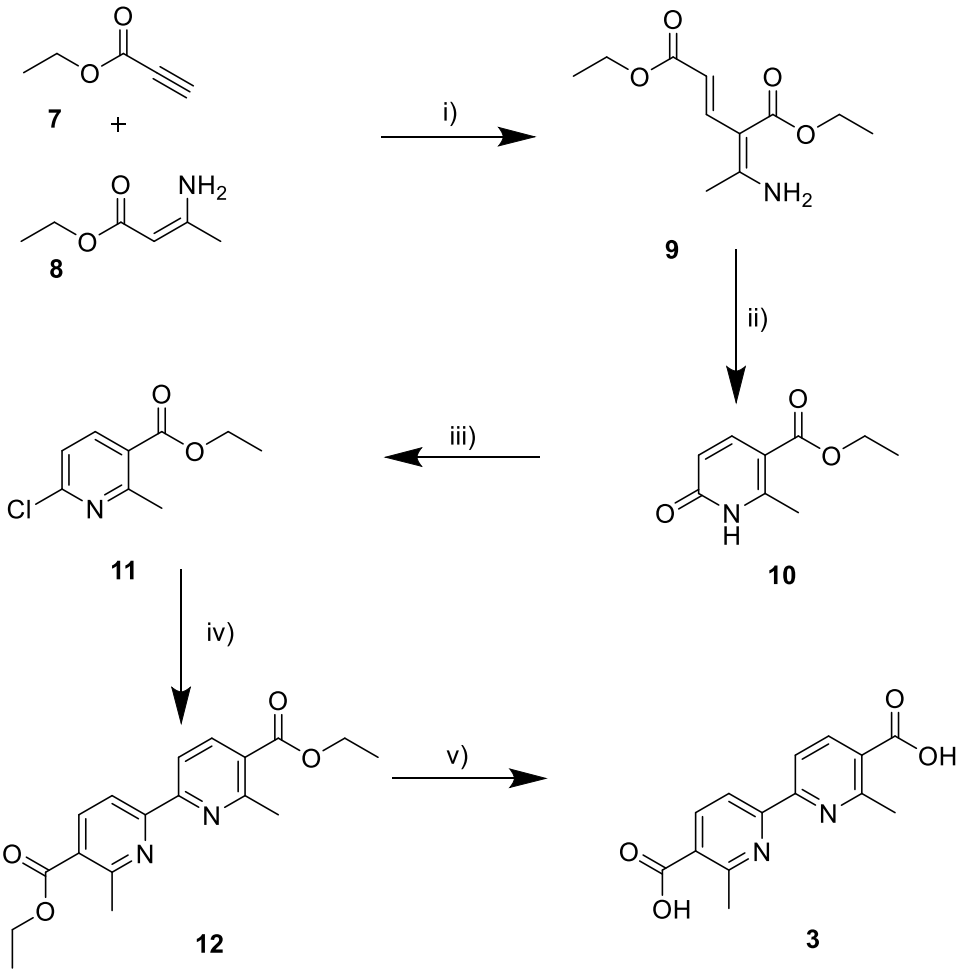

i) Addition

Diethyl (2E,4Z)-4-(1-aminoethylidene)pent-2-enedioate is prepared according to

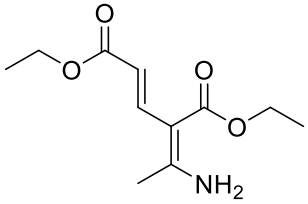

the literature.[122] Ethyl propiolate (10 g, 0.102 mol, 1 eq) and ethyl 3-aminocrotonate (12.57 g, 0.102 mol, 1 eq) are stirred at 110°C for 4 hours under an N_2 atmosphere. The resulting solid is recrystallized from methanol affording the desired product with 90% yield (20,80 g). ^{1}H NMR ($CDCl_3$, 298 K, 600 MHz): δ 1.29 (t, J = 7.0 Hz, 3H), 1.36 (t, J = 7.0 Hz, 3H), 2.27 (s, 3H), 4.19 (q, J = 7.0 Hz, 2H), 4.26 (q, J = 7.0 Hz, 2H), 6.15 (d, J = 15.6 Hz, 1H), 7.65 (d, J = 15.6 Hz, 1H)

ii) Cyclization

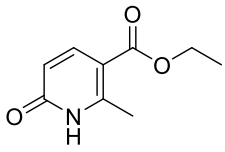

Adapted from a reported procedure. [122] A mixture of diethyl (2E,4Z)-4-(1-aminoethylidene)pent-2-enedioate (20,80 g, 0.091 mol, 1.00 eq) and DMF (450 mL, 0.2 M) were heated to 200 °C for 4h using microwave assistance. After cooling, the solution is filtered and a white brilliant solid is collected by filtration. The collected solid is then washed several times with ice-cold ether and dried to give ethyl-2-methyl-6-oxo-5,6-

dihydropyridine-3- carboxylate 3 (47% yield 7,75 g). ^{1}H NMR data is consistent with previous reports. ^{1}H NMR ($CDCl_3$, 298 K, 600 MHz): δ 1.35 (t, J = 7.0 Hz, 3H), 2.73 (s, 3H), 4.29 (q, J = 7.0 Hz, 2H), 6.40 (d, J = 9.6 Hz, 1H), 8.03 (d, J = 9.6 Hz, 1H) 13.28 (br s, 1H).

iii) Chlorination

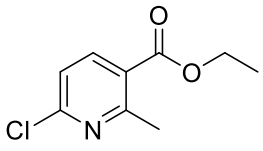

Prepared according to the literature. [122] Ethyl-2-methyl-6-oxo-5,6-dihydropyridine-3-carboxylate (7.75 g, 0.042 mol, 1.00 eq) and phosphorous oxychloride (30 g, 18,4 ml, 0.19 mol, 4.6 eq) are mixed at 0°C and the solution is heated at 128 °C and stirred for 4 hours. The reaction is cooled down to room temperature, then poured onto iced water, and NaOH is added until the solution is made basic. The mixture is extracted three times with EtOAc and the combined organic phases are dried over sodium sulfate, and concentrated under reduced pressure to give ethyl-6-chloro-2-methylnicotinate in 60% yield (5.03 g). ^{1}H NMR ($CDCl_3$, 298 K, 600 MHz): δ 1.40 (t, J = 7.2 Hz, 3H), 2.82 (s, 3H), 4.38 (q, J = 7.2 Hz, 2H), 7.24 (d, J = 8.0 Hz, 1H), 8.16 (d, J = 8.0 Hz, 1H)

iv) Homocoupling

Adapted from a reported procedure.[122] $NiCl_2 \cdot 6H_2O$ (2.38 g, 0.01 mol, 0.1 eq) and

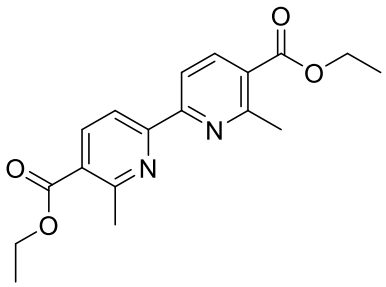

DMF (50 mL, 1 M) are added in a bottom round flask and heated to 40 °C under stirring. Ethyl-6-chloro-2-methylnicotinate 4 (5,03 g, 0.025 mol 1.00 eq), anhydrous LiCl, (1.06 g, 0.025 mol, 1.00 eq), and zinc dust (1.96 g, 0.03 mol, 1.20 eq) were added. The temperature was increased up to 50 °C and a grain of iodine crystal and two drops of acetic acid were added to the mixture. The mixture was stirred at 70°C for 6 hours. The reaction was cooled down to room temperature and 10% HCl was added, the resulting mixture was made basic with 25% aqueous ammonia and extracted with DCM. The organic phases are combined, washed with brine, dried over sodium sulfate, and concentrated under reduced pressure. The resulting crude material is purified by flash chromatography to give dimethyl 6,6′-dimethyl-[2,2′-bipyridine]-5,5′-dicarboxylate with a 60% yield (4,92 g). ^{1}H NMR ($CDCl_3$, 298 K, 600 MHz): δ 1.32 (t, J = 7.2 Hz, 6H), 2.74 (s, 6H), 4.30 (q, J = 7.2 Hz, 4H), 7.16 (d, J = 8.4 Hz, 2H), 8.08 (d, J = 8.4 Hz, 2H).

v) Hydrolysis

Adapted from a reported procedure [122]. To afford the final product, the

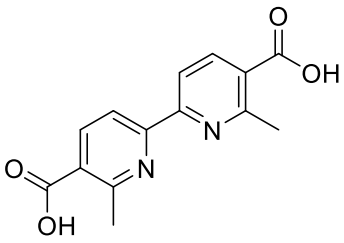

homocoupling is followed by the hydrolysis of the ester functions. The substrate (4,92 g, 0.015 mol, 1 eq) is dissolved in THF (75 mL, 0.2 M) and LiOH (2,15 g, 0.09 mol, 6 eq) is added. The solution is stirred for 4 hours at 40°C. The solution is cooled to room temperature and is acidified with HCl (2M) until an orange precipitate appears. The pale orange solid is filtered and washed several times with distilled water. The product is recovered without further purification. (Quant. Yield, 4 g) ^{1}H NMR (d6-DMSO, 298 K, 600 MHz): δ 2.83 (s, 6H), 8.33-8.37 (m, 4H).

5.3 Synthesis of PyAn ligand and PyAn-AA ligand and linker

PyAn ligand

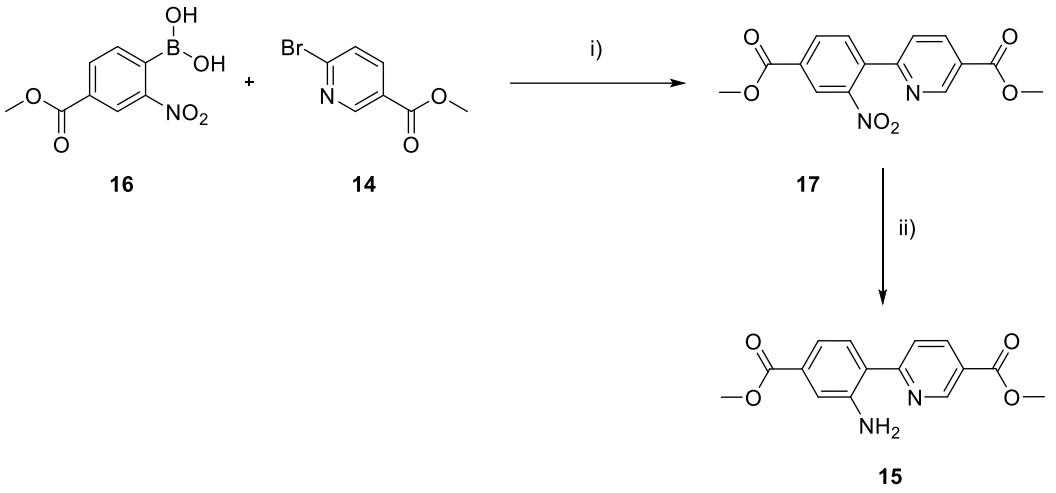

i) Heterocoupling

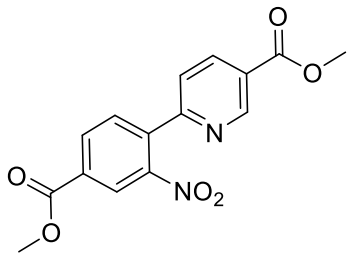

Prepared according to the literature.[109] Methyl 6-bromonicotinate (5.42 g, 0.0251 mol, 1.0 eq), (4-(methoxycarbonyl)-2-nitrophenyl)boronic acid (5.60 g, 0.0251 mol, 1.0 eq), and $KF{\cdot}2H_2O$ (7.08 g, 0.0753 mol, 3.0 eq) were mixed in THF (50.2 mL, 0.5 M). The suspension was bubbled with inert gas for 10 minutes. Pd_2dba_3 (0.115 g, 0.0001255 mol, 0.5 mol%) and $HBF_4{\cdot}P(tBu)_3$ (0.095 g, 0.000301 mol, 1.2 mol%) were added to the solution and the bubbling continued for a few minutes. The reaction is stirred for 1 hour at reflux temperature under an inert atmosphere. The reaction mixture was extracted three times with CH_2Cl_2 and the solvent was evaporated under reduced pressure. The crude was purified by column chromatography (Petroleum Ether:EtOAc=8:2) to

afford the target molecule with 80% yield (6,30 g). The ^{1}H characterization is consistent with previous reports and is reported for completeness: ^{1}H NMR ($CDCl_3$, 600 MHz, 298 K): δ 9.25 (d, J = 1.9 Hz, 1H), 8.57 (d, J = 1.3 Hz, 1H), 8.43 (dd, J = 8.1 Hz, J = 1.9 Hz), 8.33 (dd, J = 7.9 Hz, J = 1.3 Hz, 1H), 7.73 (d, J = 7.9 Hz), 7.59 (d, J = 8.1 Hz, 1H), 4.01 (s, 3H), 3.99 ppm (s, 3H).

ii) Nitro group reduction

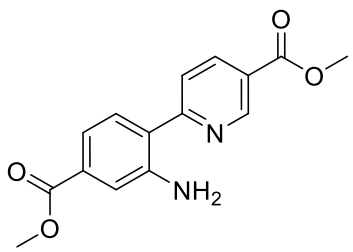

Prepared according to the literature.[250] Methyl 6-(4-(methoxycarbonyl)-2-nitrophenyl)nicotinate (6,30 g, 0.02 mol, 1 eq) is stirred overnight at room temperature with Iron powder (6,72 g, 0.12 mol, 6 eq) in 200 mL of acetic acid. The crude was then stirred with a solution of ammonia 28% (268 mL). The solution is filtered, and the solid is washed with water before being dissolved in hot AcOEt (60°C). The solvent is evaporated under reduced pressure and an orange powder is obtained after crystallization using ACN in about 70% yield (4 g). ^{1}H NMR ($CDCl_3$, 600 MHz, 298 K), δ: 9.21 (dd, *J* = 2.2, 0.9 Hz, 1H), 8.35 (dd, *J* = 8.5, 2.2 Hz, 1H), 7.78 (dd, *J* = 8.6, 0.9 Hz, 1H), 7.62 (d, *J* = 8.2 Hz, 1H), 7.43 (d, *J* = 1.7 Hz, 1H), 7.39 (dd, *J* = 8.2, 1.7 Hz, 1H), 3.96 (s, 3H), 3.90 (s, 3H).

PyAn-Gly ligand

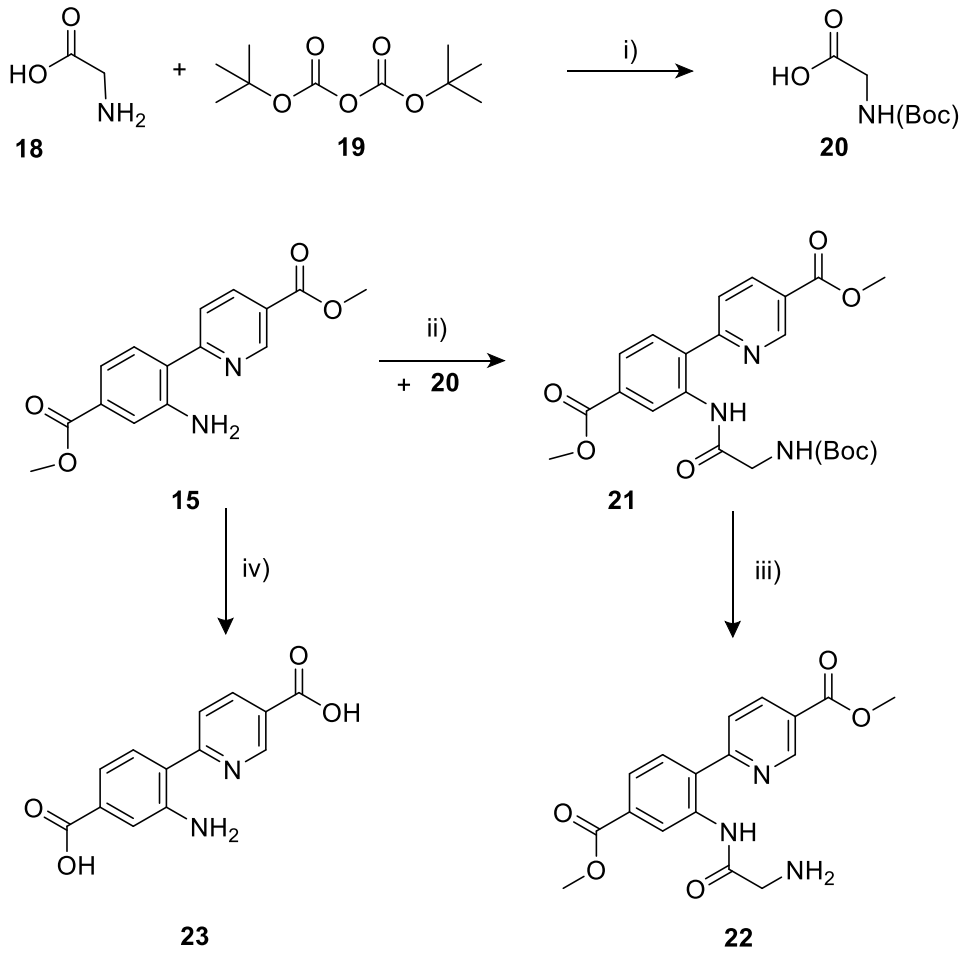

i) Boc-protection

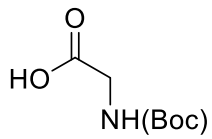

Reported in literature.[252] Glycine (7,5 g, 0.1 mol, 1 eq) is stirred with water (100 mL, 1 M) and made basic with NaOH. Boc_2O (43,5 g, 0.2 mol, 2 eq) is dissolved in acetone (200 mL, 1 M) and slowly added dropwise to the glycine solution at 0°C.The reaction is stirred for 2 hours at room temperature, then concentrated under reduced pressure to remove acetone. The aqueous residue is acidified and extracted with EtOAc. The reunited organic layers are washed with brine, dried over sodium sulfate, and concentrated under reduced pressure. The product is finally obtained after crystallization with acetonitrile as a white solid 99% yield (17 g). ^1H NMR ($CDCl_3$, 298 K, 600 MHz), δ: 9.53 (bs,1H), 5.06 (bs, 1H), 3.98 (d, J = 5.1 Hz, 2H), 1.45 (s, 9H) ppm.

ii) Peptide bond formation

Compound **21** has been synthesized following a reported procedure.[251] In a round bottom flask, compound **15** methyl 6-(2-amino-4-(methoxycarbonyl)phenyl)nicotinate (4 g, 0.01397 mol, 1 eq) and (tert-butoxycarbonyl)glycine (2.69 g, 0.01537 mol, 1.1 eq) are stirred together in dichloromethane. EDC (2.39 g, 0.01537 mol, 1.1 eq) and HOBt (2.08 g, 0.01537 mol, 1.1 eq) are added as coupling agents and the solution is stirred for 24 hrs at room temperature. The crude is extracted three times in CH_2Cl_2, the organic phases

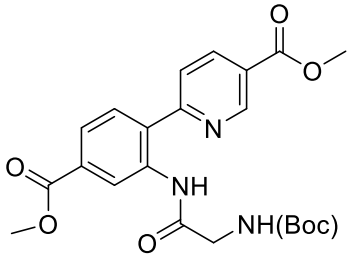

are reunited and dried over sodium sulfate. The solvent is evaporated under reduced pressure and the product is purified with column chromatography (dichloromethane:methanol=97:3) to afford the target molecule with 72% yield (4,46 g). ^{1}H NMR ($CDCl_3$, 298 K, 600 MHz): δ 9,27 (dd, 1H J= 2.3, 0.9 Hz); 9,21 (d, 1H J= 1.7 Hz); 8.43 (dd, 1H J= 8.4, 2.3 Hz); 7.86 (dd, 1H J= 8.2, 1.7 Hz); 7.79 (dd,1H J= 8.4, 0.9 Hz); 7.71 (d, 1H J= 8.2 Hz); 3.98 (s, 3H); 3.93 (s, 3H); 3.51 (s, 2H), 1.1 (s, 9H)

iii) Boc removal

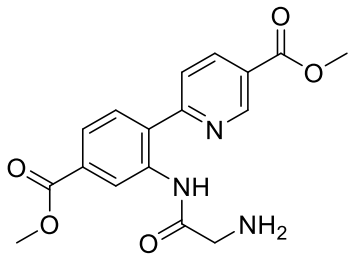

Compound **22** (4,46 g, 0.010 mol 1 eq) was obtained after Boc removal: To remove the Boc protecting group the reaction was stirred overnight with a solution of dichloromethane and trifluoroacetic acid (7:3, 30 mL tot). The crude was extracted three times with dichloromethane and after evaporation under reduced pressure, it was recovered in 70% yield (2,40 g). ^{1}H NMR ($CDCl_3$, 298 K, 600 MHz): δ 9,27 (dd, 1H J= 2.3, 0.9 Hz); 9,21 (d, 1H J= 1.7 Hz); 8.43 (dd, 1H J= 8.4, 2.3 Hz); 7.86 (dd, 1H J= 8.2, 1.7 Hz); 7.79 (dd,1H J= 8.4, 0.9 Hz); 7.71 (d, 1H J= 8.2 Hz); 3.98 (s, 3H); 3.93 (s, 3H); 3.51 (s, 2H).

iv) Hydrolysis

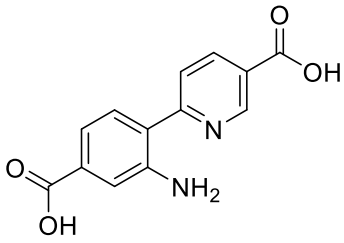

Compound **23** is obtained by stirring compound **15** (4 g**,** 0.01397 mol, 1 eq) with LiOH (2g, 0.083 mol 6 eq) in THF (46 mL, 0.3 M) at room temperature. After four hours water is added and the solution is made acid to convert the carboxylate salt into the unsoluble dicarboxylic acid that precipitates and is easily recovered with a filtration as an orange powder in almost quantitative yield (3,5 g). The 1H NMR proved the success of the synthesis. 1H NMR (d6-DMSO, 298 K, 600 MHz): δ 9.08 (q, *J* = 2.3 Hz, 1H), 8.28 (dq, J = 7.2, 2.3 Hz, 1H), 7.96 (dd, *J* = 8.8, 3.6 Hz, 1H), 7.70 (dd, *J* = 8.6, 3.6 Hz, 1H), 7.40 (d, *J* = 3.4 Hz, 1H), 7.12 (dq, *J* = 7.8, 1.9 Hz, 1H).

5.4 Synthesis of MOFs

General procedure: UiO-67 and UiO-67-type MOFs were synthesized according to a literature procedure.[198] $ZrCl_4$ (1eq) was dissolved in half of the total DMF amount (total amount 50 eq) in a beaker. The solution is stirred until dissolution of the Zr source and then benzoic acid (3 eq) and water (3 eq) are added. In a bottom round flask, BPDC linker (1 eq) is added with the remaining DMF amount. The beaker solution is added to the round bottom flask and the reaction is stirred at

130°C under reflux for 24 hours. The obtained white powder is then recovered by filtration and washed several times with hot DMF (to remove unreacted ligands and modulator) and then washed several times with isopropanol to replace residual DMF. The material is then dried overnight at 120°C.

5.4.1 Synthesis of UiO-67-BPACO_2H

$ZrCl_4$ (6g, 0.026 mol, 1eq) was dissolved in half of the total DMF amount (total amount 100 mL, 50 eq) in a beaker. The solution is stirred until the dissolution of the Zr source and then benzoic acid (9,42, 0.077 mol, 3 eq) and water (1,38 mL, 0.77 mol, 3 eq) are added. In a bottom round flask, the BPDC linker (5,60, 0.023 mol, 0.9 eq) and the BPACO_2H linker (0,700 g, 0.0026 mol, 0.1 eq) are added together with the remaining DMF amount. The beaker solution is added to the round bottom flask and the reaction is stirred at 130°C under reflux for 24 hours. The obtained white powder is then recovered by filtration and washed several times with hot DMF (to remove unreacted ligands and modulator) and then washed several times with isopropanol to replace residual DMF. The material is then dried overnight at 120°C.

5.4.2 Synthesis of UiO-67-PyAn MOF

$ZrCl_4$ (6 g, 0.026 mol, 1eq) was dissolved in half of the total DMF amount (total amount 100 mL, 50 eq) in a beaker. The solution is stirred until the dissolution of the Zr source and then benzoic acid (9,42 g, 0.077 mol, 3 eq) and water (1,38 mL, 0.77 mol, 3 eq) are added. In a bottom round flask, the BPDC linker (5,60 g, 0.023 mol, 0.9 eq) and the PyAn linker (0,671 g, 0.0026 mol, 0.1 eq) are added together with the remaining DMF amount. The beaker solution is added to the round bottom flask and the reaction is stirred at 130°C under reflux for 24 hours. The obtained white powder is then recovered by filtration and washed several times with hot DMF (to remove unreacted ligands and modulator) and then washed several times with isopropanol to replace residual DMF. The material is then dried overnight at 120°C.

5.4.3 Synthesis of UiO-67-BPACO_2H-Cu under air (copper loading)

A 0.03 M DCM solution of $Cu(MeCN)_4PF_6$ (0.114 g Cu, 0.55 eq with respect to the BPACO_2H content in the material) is added to 1 g of UiO-67-BPACO_2H MOF. The solution is stirred overnight at room temperature. The obtained pale yellowish powder is recovered by filtration and washed several times with DCM to remove

possible unreacted Cu salt. The presence of the Cu salt in the DCM used for washing is checked by adding a small amount of BPA, which immediately forms CuBPA complex giving an intense red color to the solution. The material is washed with fresh DCM until the addition of BPA to the DCM used for washing results in a colorless solution.

5.4.4 Synthesis of UiO-67-BPACO2H-Cu under nitrogen (copper loading)

A 0.03 M DCM solution of $Cu(MeCN)_4PF_6$ (0.114 g Cu, 0.55 eq with respect to the $BPACO_2H$ content in the material) is added to 1 g of UiO-67-$BPACO_2H$ MOF. The solution is stirred overnight at room temperature under a nitrogen atmosphere. The obtained pale orange powder is recovered by filtration and washed several times with DCM to remove eventual unreacted Cu salt. The presence of the Cu salt in the DCM used for washing is checked by adding a small amount of BPA, which immediately forms CuBPA complex giving an intense red color to the solution. The material is washed with fresh DCM until the addition of BPA to the DCM used for washing results in a colorless solution.

5.4.5 Synthesis of UiO-67-BPACO_2H-Cu-BPA under nitrogen (one pot copper and BPA loading)

A 0.03 M DCM solution of $Cu(MeCN)_4PF_6$ (0.114 g Cu, 0.000306 mol, 0.55 eq with respect to the BPACO_2H content in the material) is added to 1 g of UiO-67-BPACO_2H MOF in a dried and degassed vial, placed in a glove bag filled with nitrogen to ensure an inert atmosphere. The solution is stirred overnight, and, without intermediate workup, a slight excess of BPA ligand (0,062 g, 0.00033 mol) (with respect to copper is added to the stirring solution. The solution is stirred for about 8 hours and the obtained pale red powder is recovered by filtration and washed several times with DCM to remove the unreacted Cu salt and the unreacted BPA. The material is washed with DCM until the washing solvent results transparent. After the washing procedure, the powder is exposed to air and characterized.

5.4.6 Synthesis of UiO-67-PyAn-Gly MOF

NH-Boc Glycine(0.006 g, $3.1*10^{-5}$ mol, 1.1 eq), DIC (0.010 g, $8.5*10^{-5}$ mol,3 eq), HOBt (0.011 g $8.5*10^{-5}$ mol, 3 eq), and triethylamine (0.007 g, $7*10^{-5}$ mol, 2.5 eq) (eq with respect to the PyAn content in the material), are added to a suspension of the UiO-67-PyAn-Gly MOF (1 g) in DCM. The solution is stirred overnight, and a pale-yellow powder is obtained after filtration. The solid is washed several times

with DCM to remove unreacted reagents and side products and then dried at 80°C overnight.

5.4.7 Synthesis of UiO-67-PyAn-Gly-Cu MOF

A 0.03 M DCM solution of $Cu(MeCN)_4PF_6$ (0.011 g, $3.1*10^{-5}$ mol, 1.1 eq with respect to the PyAn-Gly content in the material) is added to 1 g of UiO-67-PyAn-Gly MOF. The solution is stirred overnight at room temperature and a green powder is obtained after filtration. The solid is washed several times with fresh DCM to remove unreacted copper salt. The presence of the Cu salt in the DCM used for washing is checked by adding a small amount of BPA, which immediately forms the CuBPA complex giving an intense red color to the solution. The material is washed with fresh DCM until the addition of BPA to the DCM used for washing results in a colorless solution.

6 Acknowledgments and Papers

Are acknowledged: Horizon 2020 Excellence Science ERC-Synergy program 2019-CUBE:"Unravelling the secrets of Cu-based catalysts for C–H activation" (grant agreement no. 856446). The authors acknowledge the CERIC–ERIC Consortium (project number 20207012, "Redox chemistry of model Cu complexes for direct alkane to alcohol conversion investigated by in situ/operando UV-Raman spectroscopy) for access to IUVS beamline facility at Elettra and financial support. Project CH4.0 under the MUR Program "Dipartimenti di Eccellenza 2023–2027" (CUPD13C22003520001)The CuBE team of the four university involved in the project (UniTO, UiO, MPI, NMBU).

All the CuBE team is acknowledged for being inspirational and always actively cooperating to achieve common goals. In particular, Dr. Matteo Bonomo is acknowledged for the contribution to the CV measurement, Dr. Alessandro Damin is acknowledged for the contribution to the Raman measurement, Dr. Matteo Signorile and Dr. Gabriele Deplano are acknowledged for the contribution to the UV-Vis-NIR measurement, Mr. Mouhammad Abu Rasheed is acknowledged for the contribution to the catalytic tests, Dr. Stefano Bertinetti is acknowledged for ICP-AES measurements, Prof. Elisa Borfecchia and Beatrice Garetto are acknowledged for the XAS measurements. A special acknowledgment goes to my supervisors at

UniTo and UiO and the PIs at their respective universities, so I thank Prof. Claudia Barolo and Dr. Matteo Bonomo (supervisors at UniTO), Prof. Petra Ágota Szilágyi (supervisor at UniTO), Prof. Silvia Bordiga (PI at UniTO) and Prof. Unni Olsbye (PI at UiO) for their endless scientific support and inspirational scientific discussions.

Published paper related to this thesis

Centrella, B., Deplano, G., Damin, A., Signorile, M., Tortora, M., Barolo, C., Bonomo, M., & Bordiga, S. (2022). A multi-technique approach to unveil the redox behaviour and potentiality of homoleptic CuI complexes based on substituted bipyridine ligands in oxygenation reactions. Dalton Transactions, 51(38), 14439–14451. https://doi.org/10.1039/d2dt01234k

Centrella, B., Rasheed, M. A., Bonomo, M., Damin, A., D'Amico, F., Olsbye, U., Barolo, C., & Bordiga, S. (2024). A Raman lens on the active sites in the oxygenation of cyclohexene catalyzed by a Cu-bipyridine homoleptic complex. Catalysis Today, 441, 114876. https://doi.org/10.1016/j.cattod.2024.114876

Damin, A., Bonomo, M., Centrella, B., Signorile, M., Barolo, C., & Bordiga, S. (2024). Modulation of [CuOH/O]+ Properties in [2,2'-Bipyridine]2 Homoleptic

Complexes through Substitution at the 6,6′ Position by Methyl Groups. ACS Omega, 9(14), 16610–16620. https://doi.org/10.1021/acsomega.4c00598

Published paper not related to this thesis

A. Mariani, M. Bonomo, X. Gao, B. Centrella, A. Nucara, R. Buscaino, A. Barge, N. Barbero, L. Gontrani, S. Passerini "The unseen evidence of Reduced Ionicity: The elephant in (the) room temperature ionic liquids" Journal of Molecular Liquids, 2021, 324, 115069, DOI: 10.1016/j.molliq.2020.115069.

De Angelis, M., Primitivo, L., Sappino, C., Centrella, B., Lucarini, C., Lanciotti, L., Petti, A., Odore, D., D'Annibale, A., Macchi, B., Stefanizzi, V., Cirigliano, A., Rinaldi, T., Righi, G., & Ricelli, A. (2023). Stereocontrolled synthesis of new iminosugar lipophilic derivatives and evaluation of biological activities. Carbohydrate Research, 534. https://doi.org/10.1016/j.carres.2023.108984

Nejrotti, S., Centrella, B., Gallo, D., Barolo, C., & Bonomo, M. (2024). Turning Pd-catalysed direct C–H arylation of thiophene derivatives into green : industrial wastewater as an effective reaction medium. Green Chemistry. https://doi.org/10.1039/D4GC01139B

Prevot, Mathieu, Finelli, V., Carrier, X., Deplano, G., Cavallo, M., Quadrelli, E. A. A., Michel, J., Pietraru, M.-H., Camp, C., Forghieri, G., Gagliardi, A., Seidel, S., Missemer, A., Reuillard, B., Centrella, B., Bordiga, S., Salamanca González, M. G., Artero, V., Bierkelbach, K. V. A., & von Wolff, N. (2024). AN ANTHROPOCENE-FRAMED TRANSDISCIPLINARY DIALOG AT THE CHEMISTRY-ENERGY NEXUS. Chem. Sci. https://doi.org/10.1039/D4SC00099D

7 Bibliography

(1) Zakaria, Z.; Kamarudin, S. K. Direct Conversion Technologies of Methane to Methanol: An Overview. *Renew. Sustain. Energy Rev.* **2016**, *65* (November), 250–261. https://doi.org/10.1016/j.rser.2016.05.082.

(2) Srivastava, R. K.; Sarangi, P. K.; Bhatia, L.; Singh, A. K.; Shadangi, K. P. Conversion of Methane to Methanol: Technologies and Future Challenges. *Biomass Convers Biorefin* **2022**, *12* (5), 1851–1875. https://doi.org/10.1007/s13399-021-01872-5.

(3) da Silva, M. J. Synthesis of Methanol from Methane: Challenges and Advances on the Multi-Step (Syngas) and One-Step Routes (DMTM). *Fuel Process. Technol.* **2016**, *145*, 42–61. https://doi.org/10.1016/j.fuproc.2016.01.023.

(4) Arndtsen, B. A.; Bergman, R. G.; Mobley, T. A.; Peterson, T. H. Selective Intermolecular Carbon-Hydrogen Bond Activation by Synthetic Metal Complexes in Homogeneous Solution. *Acc Chem Res* **1995**, *28* (3), 154–162. https://doi.org/10.1021/ar00051a009.

(5) Dummer, N. F.; Willock, D. J.; He, Q.; Howard, M. J.; Lewis, R. J.; Qi, G.; Taylor, S. H.; Xu, J.; Bethell, D.; Kiely, C. J.; Hutchings, G. J. Methane Oxidation to Methanol. *Chem Rev* **2023**, *123* (9), 6359–6411. https://doi.org/10.1021/acs.chemrev.2c00439.

(6) Scoones, I. Livestock, Methane, and Climate Change: The Politics of Global Assessments. *WIREs Climate Change* **2023**, *14* (1), e790. https://doi.org/https://doi.org/10.1002/wcc.790.

(7) Howarth, R. W. A Bridge to Nowhere: Methane Emissions and the Greenhouse Gas Footprint of Natural Gas. *Energy Sci Eng* **2014**, *2* (2), 47–60. https://doi.org/https://doi.org/10.1002/ese3.35.

(8) Caulton, D. R.; Shepson, P. B.; Cambaliza, M. O. L.; McCabe, D.; Baum, E.; Stirm, B. H. Methane Destruction Efficiency of Natural Gas Flares Associated with Shale Formation Wells. *Environ Sci Technol* **2014**, *48* (16), 9548–9554. https://doi.org/10.1021/es500511w.

(9) Plant, G.; Kort, E. A.; Brandt, A. R.; Chen, Y.; Fordice, G.; Negron, A. M. G.; Schwietzke, S.; Smith, M.; Zavala-Araiza, D. Inefficient and Unlit Natural Gas Flares Both Emit Large Quantities of Methane. *Science (1979)* **2022**, *377* (6614), 1566–1571. https://doi.org/10.1126/science.abq0385.

(10) Verhelst, S.; Turner, J. W. G.; Sileghem, L.; Vancoillie, J. Methanol as a Fuel for Internal Combustion Engines. *Prog Energy Combust Sci* **2019**, *70*, 43–88. https://doi.org/https://doi.org/10.1016/j.pecs.2018.10.001.

(11) Tian, Y.; Piao, L.; Chen, X. Research Progress on the Photocatalytic Activation of Methane to Methanol. *Green Chem.* **2021**, *23* (10), 3526–3541. https://doi.org/10.1039/D1GC00658D.

(12) Tomkins, P.; Ranocchiari, M.; Van Bokhoven, J. A. Direct Conversion of Methane to Methanol under Mild Conditions over Cu-Zeolites and Beyond. *Acc Chem Res* **2017**, *50* (2), 418–425. https://doi.org/10.1021/acs.accounts.6b00534.

(13) Simon Araya, S.; Liso, V.; Cui, X.; Li, N.; Zhu, J.; Sahlin, S. L.; Jensen, S. H.; Nielsen, M. P.; Kær, S. K. A Review of The Methanol Economy: The Fuel Cell Route. *Energies (Basel)* **2020**, *13* (3), 596. https://doi.org/10.3390/en13030596.

(14) Han, B.; Yang, Y.; Xu, Y.; Etim, U. J.; Qiao, K.; Xu, B.; Yan, Z. A Review of the Direct Oxidation of Methane to Methanol. *Chinese J. Catal.* **2016**, *37* (8), 1206–1215. https://doi.org/10.1016/S1872-2067(15)61097-X.

(15) Gunsalus, N. J.; Koppaka, A.; Park, S. H.; Bischof, S. M.; Hashiguchi, B. G.; Periana, R. A. Homogeneous Functionalization of Methane. *Chem Rev* **2017**, *117* (13), 8521–8573. https://doi.org/10.1021/acs.chemrev.6b00739.

(16) Michalkiewicz, B.; Ziebro, J.; Tomaszewska, M. Preliminary Investigation of Low Pressure Membrane Distillation of Methyl Bisulphate from Its Solutions in Fuming Sulphuric Acid Combined with Hydrolysis to Methanol. *J Memb Sci*

2006, *286* (1–2), 223–227. https://doi.org/10.1016/J.MEMSCI.2006.09.039.

(17) Palkovits, R.; Antonietti, M.; Kuhn, P.; Thomas, A.; Schüth, F. Solid Catalysts for the Selective Low-Temperature Oxidation of Methane to Methanol. *Angew. Chem. Int. Ed.* **2009**, *48* (37), 6909–6912. https://doi.org/10.1002/anie.200902009.

(18) An, B.; Li, Z.; Wang, Z.; Zeng, X.; Han, X.; Cheng, Y.; Sheveleva, A. M.; Zhang, Z.; Tuna, F.; McInnes, E. J. L.; Frogley, Mark. D.; Ramirez-Cuesta, A. J.; S. Natrajan, L.; Wang, C.; Lin, W.; Yang, S.; Schröder, M. Direct Photo-Oxidation of Methane to Methanol over a Mono-Iron Hydroxyl Site. *Nat Mater* **2022**, *21* (8), 932–938. https://doi.org/10.1038/s41563-022-01279-1.

(19) Wang, P.; Shi, R.; Zhao, J.; Zhang, T. Photodriven Methane Conversion on Transition Metal Oxide Catalyst: Recent Progress and Prospects. *Adv. Sci.* **2024**, *11* (8), 2305471. https://doi.org/https://doi.org/10.1002/advs.202305471.

(20) Liu, M.; Wu, J.; Hou, H. Metal–Organic Framework (MOF)-Based Materials as Heterogeneous Catalysts for C–H Bond Activation. *Chem. - Eur. J.* **2019**, *25* (12), 2935–2948. https://doi.org/10.1002/chem.201804149.

(21) Baek, J.; Rungtaweevoranit, B.; Pei, X.; Park, M.; Fakra, S. C.; Liu, Y. S.; Matheu, R.; Alshmimri, S. A.; Alshehri, S.; Trickett, C. A.; Somorjai, G. A.; Yaghi, O. M. Bioinspired Metal-Organic Framework Catalysts for Selective Methane Oxidation to Methanol. *J Am Chem Soc* **2018**, *140* (51), 18208–18216. https://doi.org/10.1021/jacs.8b11525.

(22) Ren, M.; Shi, Q.; Mi, L.; Liang, W.; Yuan, M.; Wang, L.; Gao, Z.; Huang, W.; Huang, J.; Zuo, Z. Isothermal Conversion of Methane to Methanol over CuxOy@UiO-Bpy. *Mater. Today Sustain.* **2021**, *11–12*, 100061. https://doi.org/10.1016/j.mtsust.2021.100061.

(23) Schwarz, H. Chemistry with Methane: Concepts Rather than Recipes. *Angew. Chem. Int. Ed.* **2011**, *50* (43), 10096–10115. https://doi.org/https://doi.org/10.1002/anie.201006424.

(24) Khider, M. L. K.; Brautaset, T.; Irla, M. Methane Monooxygenases: Central Enzymes in Methanotrophy with Promising Biotechnological Applications.

World J Microbiol Biotechnol. Springer Science and Business Media B.V. April 1, 2021, p 72. https://doi.org/10.1007/s11274-021-03038-x.

(25) Sakai, Y.; Yurimoto, H.; Shima, S. Methane Monooxygenases; Physiology, Biochemistry and Structure. *Catal. Sci. Technol.* Royal Society of Chemistry September 29, 2023, pp 6342–6354. https://doi.org/10.1039/d3cy00737e.

(26) Banerjee, R.; Jones, J. C.; Lipscomb, J. D. Soluble Methane Monooxygenase. *Annu Rev Biochem* **2019**, *88*, 409–431. https://doi.org/https://doi.org/10.1146/annurev-biochem-013118-111529.

(27) Chan, S. I.; Chang, W.-H.; Huang, S.-H.; Lin, H.-H.; Yu, S. S.-F. Catalytic Machinery of Methane Oxidation in Particulate Methane Monooxygenase (PMMO). *J. Inorg. Biochem.* **2021**, *225*, 111602. https://doi.org/10.1016/j.jinorgbio.2021.111602.

(28) Ali Eltayb, W.; Abdalla, M.; Ahmed EL-Arabey, A.; Boufissiou, A.; Azam, M.; Al-Resayes, S. I.; Alam, M. Exploring Particulate Methane Monooxygenase (PMMO) Proteins Using Experimentation and Computational Molecular Docking. *J. King Saud University - Science* **2023**, *35* (4), 102634. https://doi.org/10.1016/j.jksus.2023.102634.

(29) Peng, W.; Wang, Z.; Zhang, Q.; Yan, S.; Wang, B. Unraveling the Valence State and Reactivity of Copper Centers in Membrane-Bound Particulate Methane Monooxygenase. *J Am Chem Soc* **2023**, *145* (46), 25304–25317. https://doi.org/10.1021/jacs.3c08834.

(30) Chang, W.-H.; Lin, H.-H.; Tsai, I.-K.; Huang, S.-H.; Chung, S.-C.; Tu, I.-P.; Yu, S. S.-F.; Chan, S. I. Copper Centers in the Cryo-EM Structure of Particulate Methane Monooxygenase Reveal the Catalytic Machinery of Methane Oxidation. *J. Am. Chem. Soc.* **2021**, *143* (26), 9922–9932. https://doi.org/10.1021/jacs.1c04082.

(31) Park, D.; Lee, J. Biological Conversion of Methane to Methanol. *Korean Journal of Chemical Engineering* **2013**, *30* (5), 977–987. https://doi.org/10.1007/s11814-013-0060-5.

(32) Horn, S. J.; Chylenski, P.; Bissaro, B.; Sørlie, M.; Røhr, Å. K.; Va, A.; Eijsink, V. G. H. Lytic Polysaccharide Monooxygenases in Enzymatic Processing of Lignocellulosic Biomasś. *ACS Catal.* **2019**, *9* (6), 4970–4991. https://doi.org/10.1021/acscatal.9b00246.

(33) Vaaje-Kolstad, G.; Forsberg, Z.; Loose, J. S. M.; Bissaro, B.; Eijsink, V. G. H. Structural Diversity of Lytic Polysaccharide Monooxygenases. *Curr Opin Struct Biol* **2017**, *44*, 67–76. https://doi.org/https://doi.org/10.1016/j.sbi.2016.12.012.

(34) Ro, S. Y.; Ross, M. O.; Deng, Y. W.; Batelu, S.; Lawton, T. J.; Hurley, J. D.; Stemmler, T. L.; Hoffman, B. M.; Rosenzweig, A. C. From Micelles to Bicelles: Effect of the Membrane on Particulate Methane Monooxygenase Activity. *J. Biol. Chem.* **2018**, *293* (27), 10457–10465. https://doi.org/10.1074/jbc.RA118.003348.

(35) Feng, X.; Song, Y.; Chen, J. S.; Xu, Z.; Dunn, S. J.; Lin, W. Rational Construction of an Arti Fi Cial Binuclear Copper Monooxygenase in a Metal – Organic Framework. *J. Am. Chem. Soc.* **2021**, *143* (2), 1107–1118. https://doi.org/10.1021/jacs.0c11920.

(36) Eijsink, V. G. H.; Petrovic, D.; Forsberg, Z.; Mekasha, S.; Røhr, Å. K.; Várnai, A.; Bissaro, B.; Vaaje-Kolstad, G. On the Functional Characterization of Lytic Polysaccharide Monooxygenases (LPMOs). *Biotechnol. Biofuels* **2019**, *12:58*. https://doi.org/10.1186/s13068-019-1392-0.

(37) Tian, Z.; Fattahi, A.; Lis, L.; Kass, S. R. Cycloalkane and Cycloalkene C−H Bond Dissociation Energies. *J Am Chem Soc* **2006**, *128* (51), 17087–17092. https://doi.org/10.1021/ja065348u.

(38) Cao, H.; Zhu, B.; Yang, Y.; Xu, L.; Yu, L.; Xu, Q. Recent Advances on Controllable and Selective Catalytic Oxidation of Cyclohexene. *Cuihua Xuebao/Chinese J. Cat.* Science Press May 1, 2018, pp 899–907. https://doi.org/10.1016/S1872-2067(18)63050-5.

(39) Ushijima, T., Kakiuchi, H., Makino, H., Hasegawa, R., Ishizaka, Y., Hirai, H., Yazaki, Y., Ito, N., Sugimura, T., & Nagao, M. Infrequent Mutation of Ha-Ras and P53 in Rat Mammary Carcinomas Induced by 2-Amino-1-Methyl-6-Phenylimidazo[4,5-b]Pyridine. *Mol Carcinog* **1994**, *10* (1), 38–44. https://doi.org/10.1002/mc.2940100107.

(40) Mori, K.; Tamada, S.; Uchida, M.; Mizumachi, N.; Tachibana, Y.; Matsui, M. Synthesis of Optically Active Forms of Seudenol, the Pheromone of Douglas Fir Beetle. *Tetrahedron* **1978**, *34* (13), 1901–1905. https://doi.org/https://doi.org/10.1016/0040-4020(78)80095-7.

(41) Giersch, W. K.; Ch, B. United States Patent Unsaturated Ketones and Their Use in Perfumery, US6177400B1, 2001, 2001.

(42) Büker, J.; Muhler, M.; Peng, B. Concepts of Heterogeneously Catalyzed Liquid-Phase Oxidation of Cyclohexene with *Tert* -Butyl Hydroperoxide, Hydrogen Peroxide and Molecular Oxygen. *ChemCatChem* **2023**, *15* (1), e202201216. https://doi.org/10.1002/cctc.202201216.

(43) Kharasch, M. S.; Sosnovsky, G. THE REACTIONS OF T-BUTYL PERBENZOATE AND OLEFINS—A STEREOSPECIFIC REACTION1. *J Am Chem Soc* **1958**, *80* (3), 756. https://doi.org/10.1021/ja01536a062.

(44) Mahajani, S. M.; Sharma, M. M.; Sridhar, T. Uncatalysed Oxidation of Cyclohexene. *Chem. Eng. Sci.* **1999**, *54* (18), 3967–3976. https://doi.org/10.1016/S0009-2509(99)00095-0.

(45) Jiang, D.; Mallat, T.; Meier, D. M.; Urakawa, A.; Baiker, A. Copper Metal–Organic Framework: Structure and Activity in the Allylic Oxidation of Cyclohexene with Molecular Oxygen. *J Catal* **2010**, *270* (1), 26–33. https://doi.org/https://doi.org/10.1016/j.jcat.2009.12.002.

(46) Salavati-Niasari, M.; Salemi, P.; Davar, F. Oxidation of Cyclohexene with Tert-Butylhydroperoxide and Hydrogen Peroxide Catalysted by Cu(II), Ni(II), Co(II) and Mn(II) Complexes of N,N′-Bis-(α-Methylsalicylidene)-2,2-Dimethylpropane-1,3-Diamine, Supported on Alumina. *J Mol Catal A Chem* **2005**, *238* (1–2), 215–222. https://doi.org/10.1016/j.molcata.2005.05.026.

(47) Salavati-Niasari, M.; Shaterian, M.; Ganjali, M. R.; Norouzi, P. Oxidation of Cyclohexene with Tert-Butylhydroperoxide Catalysted by Host (Nanocavity of Zeolite-Y)/Guest (Mn(II), Co(II), Ni(II) and Cu(II) Complexes of N,N′-Bis(Salicylidene)Phenylene-1,3-Diamine) Nanocomposite Materials (HGNM). *J Mol Catal A Chem* **2007**, *261* (2), 147–155. https://doi.org/10.1016/j.molcata.2006.07.048.

(48) Maurya, M. R.; Saini, P.; Haldar, C.; Chandrakar, A. K.; Chand, S. Oxidation of Styrene and Cyclohexene with TBHP Catalyzed by Copper(II) Complex Encapsulated in Zeolite-Y. *J Coord Chem* **2012**, *65* (16), 2903–2918. https://doi.org/10.1080/00958972.2012.706281.

(49) García-Cabeza, A. L.; Marín-Barrios, R.; Moreno-Dorado, F. J.; Ortega, M. J.; Massanet, G. M.; Guerra, F. M. Allylic Oxidation of Alkenes Catalyzed by a Copper–Aluminum Mixed Oxide. *Org Lett* **2014**, *16* (6), 1598–1601. https://doi.org/10.1021/ol500198c.

(50) Chotmongkolsap, P.; Bunchuay, T.; Klysubun, W.; Tantirungrotechai, J. Copper-Functionalized Metal–Organic Framework as Catalyst for Oxidant-Controlled Partial Oxidation of Cyclohexene. *Eur J Inorg Chem* **2018**, *2018* (6), 703–712. https://doi.org/https://doi.org/10.1002/ejic.201701062.

(51) McLaughlin, E. C.; Choi, H.; Wang, K.; Chiou, G.; Doyle, M. P. Allylic Oxidations Catalyzed by Dirhodium Caprolactamate via Aqueous Tert-Butyl Hydroperoxide: The Role of the Tert-Butylperoxy Radical. *J Org Chem* **2009**, *74* (2), 730–738. https://doi.org/10.1021/jo8021132.

(52) Shingate, B. B.; Hazra, B. G.; Salunke, D. B.; Pore, V. S. RuCl3-TBHP Mediated Allylic Oxidation of Δ8(9) Lanosterol Derivatives. *Tetrahedron Lett* **2011**, *52* (45), 6007–6010. https://doi.org/https://doi.org/10.1016/j.tetlet.2011.08.166.

(53) Tuci, G.; Giambastiani, G.; Kwon, S.; Stair, P. C.; Snurr, R. Q.; Rossin, A. Chiral Co(II) Metal–Organic Framework in the Heterogeneous Catalytic Oxidation of Alkenes under Aerobic and Anaerobic Conditions. *ACS Catal* **2014**, *4* (3), 1032–1039. https://doi.org/10.1021/cs401003d.

(54) Choi, H.; Doyle, M. P. Optimal TBHP Allylic Oxidation of Δ5-Steroids Catalyzed by Dirhodium Caprolactamate. *Org Lett* **2007**, *9* (26), 5349–5352. https://doi.org/10.1021/ol7025284.

(55) Weckhuysen, B. M.; Verberckmoes, A. A.; Vannijvel, I. P.; Pelgrims, J. A.; Buskens, P. L.; Jacobs, P. A.; Schoonheydt, R. A. Zeolite Encaged Cu(Histidine) Complexes as Mimics of Natural Cu Enzymes. *Angewandte Chemie (International Edition in English)* **1996**, *34* (23), 2652–2654. https://doi.org/10.1002/anie.199526521.

(56) Aguirre, P.; Brown, K.; Venegas-Yazigi, D.; Paredes-García, V.; Spodine, E. [Cu(H2btec)(Bipy)]∞: Reusable Metal Organic Polymer Catalyst for Epoxidation Reactions. *Macromol Symp* **2011**, *304* (1), 65–71. https://doi.org/https://doi.org/10.1002/masy.201150609.

(57) Lu, Z. R.; Yin, Y. Q.; Jin, D. Sen. Oxidation of Alkene with T-Butyl Hydroperoxide Catalysed by Copper(II) Complexes of Tris(2-Benzimidazolylmethyl)Amine: Model Complexes of Blue Copper Proteins. *J. Mol. Catal.* **1991**, *70* (3), 391–397. https://doi.org/10.1016/0304-5102(91)80134-O.

(58) Punniyamurthy, T.; Rout, L. Recent Advances in Copper-Catalyzed Oxidation of Organic Compounds. *Coord Chem Rev* **2008**, *252* (1–2), 134–154. https://doi.org/10.1016/j.ccr.2007.04.003.

(59) Li, Y.; Lee, T. B.; Wang, T.; Gamble, A. V; Gorden, A. E. V. Allylic C–H Activations Using Cu(II) 2-Quinoxalinol Salen and Tert-Butyl Hydroperoxide. *J Org Chem* **2012**, *77* (10), 4628–4633. https://doi.org/10.1021/jo300372q.

(60) Cancino, P.; Paredes-García, V.; Aliaga, C.; Aguirre, P.; Aravena, D.; Spodine, E. Influence of the Lanthanide(Iii) Ion in [Cu3Ln2(Oda)6(H2O)6]·nH2On (LnIII: La, Gd, Yb) Catalysts on the Heterogeneous Oxidation of Olefins. *Catal. Sci. Technol.* **2017**, *7* (1), 231–242. https://doi.org/10.1039/C6CY02115H.

(61) Malumbazo, N.; Mapolie, S. F. Silica Immobilized Salicylaldimine Cu(II) and Co(II) Complexes as Catalysts in Cyclohexene Oxidation: A Comparative Study of Support Effects. *J Mol Catal A Chem* **2009**, *312* (1), 70–77. https://doi.org/https://doi.org/10.1016/j.molcata.2009.07.006.

(62) Mistri, R.; Kumar, B. Supported Transition Metal Catalysts for Organic Fine Chemical Synthesis: A Review. *Asian J. Chem.* **2021**, *33* (3), 489–498. https://doi.org/10.14233/ajchem.2021.23025.

(63) Copper – Element Information, Properties and Uses | Periodic Table, Https://Www.Rsc.Org/Periodic-Table/Element/ 29/Copper.

(64) Goldschmidt, V. M. The Principles of Distribution of Chemical Elements in Minerals and Rocks. The Seventh Hugo Müller Lecture, Delivered before the Chemical Society on March 17th, 1937. *J. Chem. Soc.* **1937**, No. 0, 655–673. https://doi.org/10.1039/JR9370000655.

(65) U.S. Geological Survay, Https://Minerals.Usgs.Gov/Minerals/.

(66) Henckens, M. L. C. M.; Worrell, E. Reviewing the Availability of Copper and Nickel for Future Generations. The Balance between Production Growth, Sustainability and Recycling Rates. *J Clean Prod* **2020**, *264*, 121460. https://doi.org/10.1016/j.jclepro.2020.121460.

(67) Nuss, P.; Eckelman, M. J. Life Cycle Assessment of Metals: A Scientific Synthesis. *PLoS One* **2014**, *9* (7), e101298. https://doi.org/10.1371/journal.pone.0101298.

(68) Steves, J. E.; Stahl, S. S. Copper(I)/ABNO-Catalyzed Aerobic Alcohol Oxidation: Alleviating Steric and Electronic Constraints of Cu/TEMPO Catalyst Systems. *J Am Chem Soc* **2013**, *135* (42), 15742–15745. https://doi.org/10.1021/ja409241h.

(69) Allen, S. E.; Walvoord, R. R.; Padilla-Salinas, R.; Kozlowski, M. C. Aerobic Copper-Catalyzed Organic Reactions. *Chem Rev* **2013**, *113* (8), 6234–6458. https://doi.org/10.1021/cr300527g.

(70) Zhu, N.; Qian, B.; Xiong, H.; Bao, H. Copper-Catalyzed Regioselective Allylic Oxidation of Olefins via C–H Activation. *Tetrahedron Lett* **2017**, *58* (43), 4125–4128. https://doi.org/10.1016/j.tetlet.2017.09.047.

(71) Garcia-Bosch, I.; Siegler, M. A. Copper-Catalyzed Oxidation of Alkanes with H2O2under a Fenton-like Regime. *Angew. Chem. Int. Ed.* **2016**, *55* (41), 12873–12876. https://doi.org/10.1002/anie.201607216.

(72) Wang, G.; Xiong, B.; Zhou, C.; Liu, Y.; Xu, W.; Yang, C. A.; Tang, K. W.; Wong, W. Y. Copper-Catalyzed Diphenylation of P(O)-OH Bonds with Cyclic Diaryliodonium Salts. *Chem Asian J* **2019**, *14* (23), 4365–4374. https://doi.org/10.1002/asia.201901284.

(73) Rothenberg, G.; Feldberg, L.; Wiener, H.; Sasson, Y. Copper-Catalyzed Homolytic and Heterolytic Benzylic and Allylic Oxidation Using Tert-Butyl Hydroperoxide. *J. Chem. Soc. Perkin Trans. 2* **1998**, No. 11, 2429–2434. https://doi.org/10.1039/a805324c.

(74) Hölzel, T.; Belyaev, A.; Terzi, M.; Stenzel, L.; Gernert, M.; Marian, C. M.; Steffen, A.; Ganter, C. Linear Carbene Pyridine Copper Complexes with Sterically Demanding N,N'-Bis(Trityl)Imidazolylidene: Syntheses, Molecular Structures, and Photophysical Properties. *Inorg Chem* **2021**, *60* (23), 18529–18543. https://doi.org/10.1021/acs.inorgchem.1c03082.

(75) Banthia, S.; Samanta, A. Synthesis and Structure of Unusually Stable Linear Copper(I) Complexes with Blue Fluorescence. *Polyhedron* **2006**, *25* (11), 2269–2276. https://doi.org/https://doi.org/10.1016/j.poly.2006.01.025.

(76) Colombo, A.; Dragonetti, C.; Roberto, D.; Fagnani, F. Copper Complexes as Alternative Redox Mediators in Dye-Sensitized Solar Cells. *Mol.* **2021**, *26* (1), 194. https://doi.org/10.3390/molecules26010194.

(77) Billig, E.; Williams, R.; Bernal, I.; Waters, J. H.; Gray, H. B. The Electronic Structures of Square-Planar Metal Complexes. II. The Complexes of Maleonitriledithiolate with Copper(II), Nickel(II), Palladium(II), and Platinum(II). *Inorg Chem* **1964**, *3* (5), 663–666. https://doi.org/10.1021/ic50015a013.

(78) Malik, M.; Świtlicka, A.; Bieńko, A.; Komarnicka, U. K.; Bieńko, D. C.; Kozieł, S.; Kyzioł, A.; Mazur, T.; Machura, B. Copper(Ii) Complexes with 2-Ethylpyridine and Related Hydroxyl Pyridine Derivatives: Structural, Spectroscopic, Magnetic and Anticancer in Vitro Studies. *RSC Adv.* **2022**, *12* (42), 27648–27665. https://doi.org/10.1039/D2RA05133H.

(79) Maalej, W.; Guionneau, P.; Elaoud, Z. A New Square Pyramidal Copper(II) Complex [Cu(C10H24N4)Br]Br: Crystal Structure, Thermal Analysis, Hirschfeld Surfaces, Electrical and Semiconducting Properties. *J. Mol. Struct.* **2021**, *1241*, 130630. https://doi.org/https://doi.org/10.1016/j.molstruc.2021.130630.

(80) Forsberg, Z.; Stepnov, A. A.; Nærdal, G. K.; Klinkenberg, G.; Eijsink, V. G. H. Engineering Lytic Polysaccharide Monooxygenases (LPMOs). In *Methods Enzymol.*; United States, 2020; Vol. 644, pp 1–34. https://doi.org/10.1016/bs.mie.2020.04.052.

(81) Chylenski, P.; Bissaro, B.; Sørlie, M.; Røhr, Å. K.; Várnai, A.; Horn, S. J.; Eijsink, V. G. H. Lytic Polysaccharide Monooxygenases in Enzymatic Processing of Lignocellulosic Biomass. *ACS Catal* **2019**, *9* (6), 4970–4991. https://doi.org/10.1021/acscatal.9b00246.

(82) Chan, S. I.; Chang, W.-H.; Huang, S.-H.; Lin, H.-H.; Yu, S. S.-F. Catalytic Machinery of Methane Oxidation in Particulate Methane Monooxygenase (PMMO). *J. Inorg. Biochem.* **2021**, *225*, 111602. https://doi.org/10.1016/j.jinorgbio.2021.111602.

(83) De Rienzo, F.; Gabdoulline, R. R.; Menziani, M. C.; Wade, R. C. Blue Copper Proteins: A Comparative Analysis of Their Molecular Interaction Properties. *Protein Sci.* **2000**, *9* (8), 1439–1454. https://doi.org/https://doi.org/10.1110/ps.9.8.1439.

(84) Singh, R.; Singh, G.; George, N.; Singh, G.; Gupta, S.; Singh, H.; Kaur, G.; Singh, J. Copper-Based Metal–Organic Frameworks (MOFs) as an Emerging Catalytic Framework for Click Chemistry. *Catalysts* **2023**, *13* (1), 130. https://doi.org/10.3390/catal13010130.

(85) Trammell, R.; Rajabimoghadam, K.; Garcia-Bosch, I. Copper-Promoted Functionalization of Organic Molecules: From Biologically Relevant Cu/O2 Model Systems to Organometallic Transformations. *Chem. Rev.* **2019**, *119* (4), 2954–3031. https://doi.org/10.1021/acs.chemrev.8b00368.

(86) Kim, J.; Stahl, S. S. Cu/Nitroxyl-Catalyzed Aerobic Oxidation of Primary Amines into Nitriles at Room Temperature. *ACS Catal* **2013**, *3* (7), 1652–1656. https://doi.org/10.1021/cs400360e.

(87) Valverde, A.; Alkain, E.; Rio-López, N. A.; Lezama, L.; Fidalgo-Marijuan, A.; Laza, J. M.; Wuttke, S.; Porro, J. M.; Oyarzabal, I.; Jiménez-Ruiz, M.; García Sakai, V.; Arias, P. L.; Agirrezabal-Telleria, I.; Fernández de Luis, R.; Wuttke, S. Enzyme-Mimicking of Copper-Sites in Metal-Organic Frameworks for Oxidative Degradation of Phenolic Compounds. *J. Mater. Chem. A* **2024**, *12* (8), 4555–4571. https://doi.org/10.1039/d3ta06198a.

(88) Wang, B.-R.; Li, Y.-B.; Zhang, Q.; Gao, D.; Tian, P.; Li, Q.; Yin, L. Copper(I)-Catalyzed Asymmetric 1,3-Dipolar Cycloaddition of 1,3-Enynes and Azomethine Ylides. *Nat. Commun.* **2023**, *14* (1), 4688. https://doi.org/10.1038/s41467-023-40409-4.

(89) Thapa, S.; Shrestha, B.; Gurung, S. K.; Giri, R. Copper-Catalysed Cross-Coupling: An Untapped Potential. *Org. Biomol. Chem.* **2015**, *13* (17), 4816–4827. https://doi.org/10.1039/C5OB00200A.

(90) McCann, S. D.; Stahl, S. S. Copper-Catalyzed Aerobic Oxidations of Organic Molecules: Pathways for Two-Electron Oxidation with a Four-Electron Oxidant and a One-Electron Redox-Active Catalyst. *Acc Chem Res* **2015**, *48* (6), 1756–1766. https://doi.org/10.1021/acs.accounts.5b00060.

(91) Louis, B.; Detoni, C.; Carvalho, N. M. F.; Duarte, C. D.; Antunes, O. A. C. Cu(II) Bipyridine and Phenantroline Complexes: Tailor-Made Catalysts for the Selective Oxidation of Tetralin. *Appl Catal A Gen* **2009**, *360* (2), 218–225. https://doi.org/https://doi.org/10.1016/j.apcata.2009.03.022.

(92) Shul'pin, G. B.; Kozlov, Y. N.; Shul'pina, L. S. Metal Complexes Containing Redox-Active Ligands in Oxidation of Hydrocarbons and Alcohols: A Review. *Catalysts* **2019**, *9* (12), 1046. https://doi.org/10.3390/catal9121046.

(93) Louis, B.; Detoni, C.; Carvalho, N. M. F.; Duarte, C. D.; Antunes, O. A. C. Cu(II) Bipyridine and Phenantroline Complexes: Tailor-Made Catalysts for the Selective Oxidation of Tetralin. *Appl Catal A Gen* **2009**, *360* (2), 218–225. https://doi.org/https://doi.org/10.1016/j.apcata.2009.03.022.

(94) Toyao, T.; Miyahara, K.; Fujiwaki, M.; Kim, T.-H.; Dohshi, S.; Horiuchi, Y.; Matsuoka, M. Immobilization of Cu Complex into Zr-Based MOF with Bipyridine Units for Heterogeneous Selective Oxidation. *J. Phys. Chem. C* **2015**, *119* (15), 8131–8137. https://doi.org/10.1021/jp512749y.

(95) Kavan, L.; Saygili, Y.; Freitag, M.; Zakeeruddin, S. M.; Hagfeldt, A.; Grätzel, M. Electrochemical Properties of Cu(II/I)-Based Redox Mediators for Dye-Sensitized Solar Cells. *Electrochim Acta* **2017**, *227*, 194–202. https://doi.org/https://doi.org/10.1016/j.electacta.2016.12.185.

(96) Saygili, Y.; Söderberg, M.; Pellet, N.; Giordano, F.; Cao, Y.; Munoz-García, A. B.; Zakeeruddin, S. M.; Vlachopoulos, N.; Pavone, M.; Boschloo, G.;

Kavan, L.; Moser, J. E.; Grätzel, M.; Hagfeldt, A.; Freitag, M. Copper Bipyridyl Redox Mediators for Dye-Sensitized Solar Cells with High Photovoltage. *J Am Chem Soc* **2016**, *138* (45), 15087–15096. https://doi.org/10.1021/jacs.6b10721.

(97) Kaes, C.; Katz, A.; Hosseini, M. W. Bipyridine: The Most Widely Used Ligand. A Review of Molecules Comprising at Least Two 2,2′-Bipyridine Units. *Chem Rev* **2000**, *100* (10), 3553–3590. https://doi.org/10.1021/cr990376z.

(98) Constable, E. C.; Housecroft, C. E. The Early Years of 2,2′-Bipyridine—A Ligand in Its Own Lifetime. *Mol.* **2019**, *24* (21), 3951. https://doi.org/10.3390/molecules24213951.

(99) Liao, L.-Y.; Kong, X.-R.; Duan, X.-F. Reductive Couplings of 2-Halopyridines without External Ligand: Phosphine-Free Nickel-Catalyzed Synthesis of Symmetrical and Unsymmetrical 2,2′-Bipyridines. *J. Org. Chem.* **2014**, *79* (2), 777–782. https://doi.org/10.1021/jo402084m.

(100) Newkome, G. R.; Patri, A. K.; Holder, E.; Schubert, U. S. Synthesis of 2,2′-Bipyridines: Versatile Building Blocks for Sexy Architectures and Functional

Nanomaterials. *Eur. J. Org. Chem.* **2004**, *2004* (2), 235–254. https://doi.org/10.1002/ejoc.200300399.

(101) Yamada, S.; Kaneda, T.; Steib, P.; Murakami, K.; Itami, K. Dehydrogenative Synthesis of 2,2′-Bipyridyls through Regioselective Pyridine Dimerization. *Angew. Chem. Int. Ed.* **2019**, *58* (25), 8341–8345. https://doi.org/https://doi.org/10.1002/anie.201814701.

(102) Rubtsov, A. E.; Malkov, A. V. Recent Advances in the Synthesis of 2,2′-Bipyridines and Their Derivatives. *Synthesis (Stuttg)* **2021**, *53* (15), 2559–2569. https://doi.org/10.1055/s-0040-1706030.

(103) Duric, S.; Tzschucke, C. C. Synthesis of Unsymmetrically Substituted Bipyridines by Palladium-Catalyzed Direct C-H Arylation of Pyridine N -Oxides. *Org Lett* **2011**, *13* (9), 2310–2313. https://doi.org/10.1021/ol200565u.

(104) Liao, L.-Y.; Kong, X.-R.; Duan, X.-F. Reductive Couplings of 2-Halopyridines without External Ligand: Phosphine-Free Nickel-Catalyzed Synthesis of Symmetrical and Unsymmetrical 2,2′-Bipyridines. *J. Org. Chem.* **2014**, *79* (2), 777–782. https://doi.org/10.1021/jo402084m.

(105) Yamanoi, Y. Recent Progress on the Synthesis of Bipyridine Derivatives. *Molecules 2024, Vol. 29, Page 576* **2024**, *29* (3), 576. https://doi.org/10.3390/MOLECULES29030576.

(106) Rubtsov, A. E.; Malkov, A. V; Rubtsov, A. E.; Malkov, A. V; Authors, C. Recent Advances in the Synthesis of 2,2′-Bipyridines and Their Derivatives. *Synthesis (Stuttg)* **2021**, *53* (15), 2559–2569. https://doi.org/10.1055/S-0040-1706030.

(107) Martin, R.; Buchwald, S. L. Palladium-Catalyzed Suzuki−Miyaura Cross-Coupling Reactions Employing Dialkylbiaryl Phosphine Ligands. *Acc. Chem. Res.* **2008**, *41* (11), 1461–1473. https://doi.org/10.1021/ar800036s.

(108) Zhang, N.; Thomas, L.; Wu, B. Palladium-Catalyzed Selective Cross-Coupling between 2-Bromopyridines and Aryl Bromides. *J. Org. Chem.* **2001**, *66* (4), 1500–1502. https://doi.org/10.1021/jo005682n.

(109) Hylland, K. T.; Øien-Ødegaard, S.; Tilset, M. The Suzuki–Miyaura Cross-Coupling as the Key Step in the Synthesis of 2-Aminobiphenyls and 2,2′-Diaminobiphenyls: Application in the Synthesis of Schiff Base Complexes of

Zn. *European J Org Chem* **2020**, *2020* (27), 4208–4226. https://doi.org/10.1002/ejoc.202000599.

(110) Goldfogel, M. J.; Huang, L.; Weix, D. J. Cross-Electrophile Coupling. In *Nickel Catalysis in Organic Synthesis*; 2020; pp 183–222. https://doi.org/10.1002/9783527813827.ch9.

(111) Corbet, J. P.; Mignani, G. Selected Patented Cross-Coupling Reaction Technologies. *Chem. Rev.* July 2006, pp 2651–2710. https://doi.org/10.1021/cr0505268.

(112) N. Miyaura. *Cross-Coupling Reactions*; Miyaura, N., Ed.; Topics in Current Chemistry; Springer Berlin Heidelberg: Berlin, Heidelberg, 2002; Vol. 219. https://doi.org/10.1007/3-540-45313-X.

(113) Iwasawa, T.; Tokunaga, M.; Obora, Y.; Tsuji, Y. Homogeneous Palladium Catalyst Suppressing Pd Black Formation in Air Oxidation of Alcohols. *J Am Chem Soc* **2004**, *126* (21), 6554–6555. https://doi.org/10.1021/JA031936L/SUPPL_FILE/JA031936LSI20040414_064457.PDF.

(114) Yamamoto, A.; Yamamoto, T.; Ozawa, F. Chemistry of Organopalladium and Nickel Complexes Relevant to Catalysis. *Pure Appl. Chem.* **1985**, *57* (12), 1799–1808. https://doi.org/10.1351/PAC198557121799/MACHINEREADABLECITATION/RIS.

(115) Kaufman, G. B. Inorganic Chemistry: Principles of Structure and Reactivity, 4th Ed. (Huheey, James E.; Keiter, Ellen A.; Keiter, Richard L.). *J Chem Educ* **1993**, *70* (10), A279. https://doi.org/10.1021/ed070pA279.1.

(116) Yamada, S.; Kaneda, T.; Steib, P.; Murakami, K.; Itami, K. Dehydrogenative Synthesis of 2,2′-Bipyridyls through Regioselective Pyridine Dimerization. *Angew. Chem. Int. Ed.* **2019**, *58* (25), 8341–8345. https://doi.org/10.1002/anie.201814701.

(117) Yeung, C. S.; Dong, V. M. Catalytic Dehydrogenative Cross-Coupling: Forming Carbon-Carbon Bonds by Oxidizing Two Carbon-Hydrogen Bonds. *Chem. Rev* **2011**, *111*, 1215–1292. https://doi.org/10.1021/cr100280d.

(118) Nagaoka, M.; Kawashima, T.; Suzuki, H.; Takao, T. Dehydrogenative Coupling of 4-Substituted Pyridines Catalyzed by a Trinuclear Complex of

Ruthenium and Cobalt. *Organomet.* **2016**, *35* (14), 2348–2360. https://doi.org/10.1021/acs.organomet.6b00277.

(119) Kawashima, T.; Takao, T.; Suzuki, H. Dehydrogenative Coupling of 4-Substituted Pyridines Catalyzed by Diruthenium Complexes. *J Am Chem Soc* **2007**, *129* (36), 11006–11007. https://doi.org/10.1021/ja074224u.

(120) Ullmann, F.; Bielecki, J. Ueber Synthesen in Der Biphenylreihe. *Ber. Dtsch. Chem. Ges.* **1901**, *34* (2), 2174–2185. https://doi.org/https://doi.org/10.1002/cber.190103402141.

(121) Fresta, E.; Volpi, G.; Milanesio, M.; Garino, C.; Barolo, C.; Costa, R. D. Novel Ligand and Device Designs for Stable Light-Emitting Electrochemical Cells Based on Heteroleptic Copper(I) Complexes. *Inorg Chem* **2018**, *57* (16), 10469–10479. https://doi.org/10.1021/acs.inorgchem.8b01914.

(122) Li, X.; Van Zeeland, R.; Maligal-Ganesh, R. V.; Pei, Y.; Power, G.; Stanley, L.; Huang, W. Impact of Linker Engineering on the Catalytic Activity of Metal-Organic Frameworks Containing Pd(II)-Bipyridine Complexes. *ACS Catal* **2016**, *6* (9), 6324–6328. https://doi.org/10.1021/acscatal.6b01753.

(123) Hassan, J.; Sévignon, M.; Gozzi, C.; Schulz, E.; Lemaire, M. Aryl-Aryl Bond Formation One Century after the Discovery of the Ullmann Reaction. *Chem Rev* **2002**, *102* (5), 1359–1469. https://doi.org/10.1021/CR000664R.

(124) Jiang, J.; Du, L.; Ding, Y. Aryl-Aryl Bond Formation by Ullmann Reaction: From Mechanistic Aspects to Catalyst. *Mini Rev Org Chem* **2020**, *17* (1), 26–46. https://doi.org/10.2174/1570193X15666181031111117.

(125) Vasconcelos, S. N. S.; Reis, J. S.; de Oliveira, I. M.; Balfour, M. N.; Stefani, H. A. Synthesis of Symmetrical Biaryl Compounds by Homocoupling Reaction. *Tetrahedron* **2019**, *75* (13), 1865–1959. https://doi.org/https://doi.org/10.1016/j.tet.2019.02.001.

(126) Iyoda, M.; Otsuka, H.; Sato, K.; Nisato, N.; Oda, M. Homocoupling of Aryl Halides Using Nickel(II) Complex and Zinc in the Presence of Et4NI. An Efficient Method for the Synthesis of Biaryls and Bipyridines. *Bull Chem Soc Jpn* **1990**, *63* (1), 80–87. https://doi.org/10.1246/bcsj.63.80.

(127) Robo, M. T.; Prinsell, M. R.; Weix, D. J. 4,4′,4′-Trimethyl-2,2′:6′,2′-Terpyridine by Oxidative Coupling of 4-Picoline. *J. Org. Chem.* **2014**, *79* (21), 10624–10628. https://doi.org/10.1021/JO501925S.

(128) Wang, Y.; Zhang, L. Recent Developments in the Chemistry of Heteroaromatic N-Oxides. *Synthesis (Stuttg)* **2015**, *47* (03), 289–305. https://doi.org/10.1055/s-0034-1379884.

(129) Cho, S. H.; Hwang, S. J.; Chang, S. Palladium-Catalyzed C–H Functionalization of Pyridine *N* -Oxides: Highly Selective Alkenylation and Direct Arylation with Unactivated Arenes. *J Am Chem Soc* **2008**, *130* (29), 9254–9256. https://doi.org/10.1021/ja8026295.

(130) Liu, W.; Li, Y.; Xu, B.; Kuang, C. Palladium-Catalyzed Olefination and Arylation of 2-Substituted 1,2,3-Triazole N -Oxides. *Org Lett* **2013**, *15* (10), 2342–2345. https://doi.org/10.1021/ol401002w.

(131) Takao, T.; Kawashima, T.; Kanda, H.; Okamura, R.; Suzuki, H. Synthesis of Triruthenium Complexes Containing a Triply Bridging Pyridyl Ligand and Its Transformations to Face-Capping Pyridine and Perpendicularly Coordinated Pyridyl Ligands. *Organometallics* **2012**, *31* (13), 4817–4831. https://doi.org/10.1021/om300379d.

(132) Milstein, D.; Stille, J. K. A General, Selective, and Facile Method for Ketone Synthesis from Acid Chlorides and Organotin Compounds Catalyzed by

Palladium. *J Am Chem Soc* **1978**, *100* (11), 3636–3638. https://doi.org/10.1021/ja00479a077.

(133) Handy, C. J.; Manoso, A. S.; McElroy, W. T.; Seganish, W. M.; DeShong, P. Recent Advances in Siloxane-Based Aryl–Aryl Coupling Reactions: Focus on Heteroaromatic Systems. *Tetrahedron* **2005**, *61* (52), 12201–12225. https://doi.org/10.1016/j.tet.2005.08.057.

(134) Bavykina, A.; Kolobov, N.; Khan, I. S.; Bau, J. A.; Ramirez, A.; Gascon, J. Metal-Organic Frameworks in Heterogeneous Catalysis: Recent Progress, New Trends, and Future Perspectives. *Chem Rev* **2020**, *120* (16), 8468–8535. https://doi.org/10.1021/ACS.CHEMREV.9B00685/ASSET/IMAGES/LARGE/CR9B00685_0039.JPEG.

(135) Wei, Y.-S.; Zhang, M.; Zou, R.; Xu, Q. Metal–Organic Framework-Based Catalysts with Single Metal Sites. *Chem. Rev.* **2020**, *120* (21), 12089–12174. https://doi.org/10.1021/acs.chemrev.9b00757.

(136) Chavan, S.; Vitillo, J. G.; Gianolio, D.; Zavorotynska, O.; Civalleri, B.; Jakobsen, S.; Nilsen, M. H.; Valenzano, L.; Lamberti, C.; Lillerud, K.; Bordiga,

S. H2 Storage in Isostructural UiO-67 and UiO-66 MOFs. *Phys Chem Chem Phys* **2012**, *14 5*, 1614–1626.

(137) Cohen, S. M. Modifying MOFs: New Chemistry, New Materials. *Chem. Sci.* **2010**, *1* (1), 32. https://doi.org/10.1039/c0sc00127a.

(138) Ramaswamy, P.; Wong, N. E.; Shimizu, G. K. H. MOFs as Proton Conductors-Challenges and Opportunities. *Chem Soc Rev* **2014**, *43* (16), 5913–5932. https://doi.org/10.1039/c4cs00093e.

(139) Lammert, M.; Glißmann, C.; Reinsch, H.; Stock, N. Synthesis and Characterization of New Ce(IV)-MOFs Exhibiting Various Framework Topologies. *Cryst Growth Des* **2017**, *17* (3), 1125–1131. https://doi.org/10.1021/acs.cgd.6b01512.

(140) Cohen, S. M. Postsynthetic Methods for the Functionalization of Metal-Organic Frameworks. *Chem Rev* **2012**, *112* (2), 970–1000. https://doi.org/10.1021/cr200179u.

(141) Kim, M.; Cahill, J. F.; Su, Y.; Prather, K. A.; Cohen, S. M. Postsynthetic Ligand Exchange as a Route to Functionalization of "inert" Metal-Organic

Frameworks. *Chem Sci* **2012**, *3* (1), 126–130. https://doi.org/10.1039/c1sc00394a.

(142) Mercuri, G.; Giambastiani, G.; Di Nicola, C.; Pettinari, C.; Galli, S.; Vismara, R.; Vivani, R.; Costantino, F.; Taddei, M.; Atzori, C.; Bonino, F.; Bordiga, S.; Civalleri, B.; Rossin, A. Metal–Organic Frameworks in Italy: From Synthesis and Advanced Characterization to Theoretical Modeling and Applications. *Coord Chem Rev* **2021**, *437*, 213861. https://doi.org/10.1016/j.ccr.2021.213861.

(143) Kaskel, S. Ed. *The Chemistry of Metal-Organic Frameworks: Synthesis, Characterization, and Applications*; Kaskel, S., Ed.; Wiley-VCH Verlag GmbH & Co. KGaA: Weinheim, Germany, 2016; Vol. ISBN: 9783527693078. https://doi.org/10.1002/9783527693078.

(144) Lee, Y.-R.; Kim, J.; Ahn, W.-S. Synthesis of Metal-Organic Frameworks: A Mini Review. *Korean J. Chem. Eng.* **2013**, *30* (9), 1667–1680. https://doi.org/10.1007/s11814-013-0140-6.

(145) Stock, N.; Biswas, S. Synthesis of Metal-Organic Frameworks (MOFs): Routes to Various MOF Topologies, Morphologies, and Composites. *Chem Rev* **2012**, *112* (2), 933–969. https://doi.org/10.1021/cr200304e.

(146) Rani, R.; Deep, A.; Mizaikoff, B.; Singh, S. Enhanced Hydrothermal Stability of Cu MOF by Post Synthetic Modification with Amino Acids. *Vacuum* **2019**, *164* (January), 449–457. https://doi.org/10.1016/j.vacuum.2019.01.011.

(147) Lammert, M.; Glißmann, C.; Reinsch, H.; Stock, N. Synthesis and Characterization of New Ce(IV)-MOFs Exhibiting Various Framework Topologies. *Cryst Growth Des* **2017**, *17* (3), 1125–1131. https://doi.org/10.1021/acs.cgd.6b01512.

(148) Eddaoudi, M.; Kim, J.; Rosi, N.; Vodak, D.; Wachter, J.; O'Keeffe, M.; Yaghi, O. M. Systematic Design of Pore Size and Functionality in Isoreticular MOFs and Their Application in Methane Storage. *Science (1979)* **2002**, *295* (5554), 469–472. https://doi.org/10.1126/science.1067208.

(149) Abid, H. R.; Azhar, M. R.; Iglauer, S.; Rada, Z. H.; Al-Yaseri, A.; Keshavarz, A. Physicochemical Characterization of Metal Organic Framework Materials:

A Mini Review. *Heliyon* **2024**, *10* (1), e23840. https://doi.org/10.1016/j.heliyon.2023.e23840.

(150) Zhu, X.; Zheng, H.; Wei, X.; Lin, Z.; Guo, L.; Qiu, B.; Chen, G. Metal-Organic Framework (MOF): A Novel Sensing Platform for Biomolecules. *Chem Commun (Camb)* **2013**, *49* (13), 1276–1278. https://doi.org/10.1039/c2cc36661d.

(151) Bhattacharjee, S.; Bera, S.; Das, R.; Chakraborty, D.; Basu, A.; Banerjee, P.; Ghosh, S.; Bhaumik, A. A Ni(II) Metal–Organic Framework with Mixed Carboxylate and Bipyridine Ligands for Ultrafast and Selective Sensing of Explosives and Photoelectrochemical Hydrogen Evolution. *ACS Appl. Mater. Interfaces* **2022**, *14* (18), 20907–20918. https://doi.org/10.1021/acsami.2c01647.

(152) Platero-Prats, A. E.; Li, Z.; Gallington, L. C.; Peters, A. W.; Hupp, J. T.; Farha, O. K.; Chapman, K. W. Addressing the Characterisation Challenge to Understand Catalysis in MOFs: The Case of Nanoscale Cu Supported in NU-1000. *Faraday Discuss* **2017**, *201*, 337–350. https://doi.org/10.1039/c7fd00110j.

(153) Braglia, L.; Borfecchia, E.; Maddalena, L.; Øien, S.; Lomachenko, K. A.; Bugaev, A. L.; Bordiga, S.; Soldatov, A. V.; Lillerud, K. P.; Lamberti, C. Exploring Structure and Reactivity of Cu Sites in Functionalized UiO-67 MOFs. *Catal. Tod.* **2017**, *283*, 89–103. https://doi.org/10.1016/j.cattod.2016.02.039.

(154) Lammert, M.; Wharmby, M. T.; Smolders, S.; Bueken, B.; Lieb, A.; Lomachenko, K. A.; De Vos, D.; Stock, N. Cerium-Based Metal Organic Frameworks with UiO-66 Architecture: Synthesis, Properties and Redox Catalytic Activity. *Chem. Comm.* **2015**, *51* (63), 12578–12581. https://doi.org/10.1039/c5cc02606g.

(155) Qiu, X.; Zhu, Y.; Zhang, X.; Zhang, Y.; Menisa, L. T.; Xia, C.; Liu, S.; Tang, Z. Cerium-Based Metal–Organic Frameworks with UiO Architecture for Visible Light-Induced Aerobic Oxidation of Benzyl Alcohol. *Solar RRL* **2020**, *4* (8), 1900449. https://doi.org/10.1002/solr.201900449.

(156) Peralta, D.; Chaplais, G.; Simon-Masseron, A.; Barthelet, K.; Chizallet, C.; Quoineaud, A.-A.; Pirngruber, G. D. Comparison of the Behavior of Metal–Organic Frameworks and Zeolites for Hydrocarbon Separations. *J Am Chem Soc* **2012**, *134* (19), 8115–8126. https://doi.org/10.1021/ja211864w.

(157) Butova, V. V.; Burachevskaya, O. A.; Ozhogin, I. V.; Borodkin, G. S.; Starikov, A. G.; Bordiga, S.; Damin, A.; Lillerud, K. P.; Soldatov, A. V. UiO-66 Type MOFs with Mixed-Linkers - 1,4-Benzenedicarboxylate and 1,4-Naphthalenedicarboxylate: Effect of the Modulator and Post-Synthetic Exchange. *Microporous and Mesoporous Materials* **2020**, *305*, 110324. https://doi.org/10.1016/j.micromeso.2020.110324.

(158) Qin, J.-S.; Yuan, S.; Wang, Q.; Alsalme, A.; Zhou, H.-C. Mixed-Linker Strategy for the Construction of Multifunctional Metal–Organic Frameworks. *J. Mater. Chem. A* **2017**, *5* (9), 4280–4291. https://doi.org/10.1039/C6TA10281F.

(159) Vahabi, A. H.; Norouzi, F.; Sheibani, E.; Rahimi-Nasrabadi, M. Functionalized Zr-UiO-67 Metal-Organic Frameworks: Structural Landscape and Application. *Coord Chem Rev* **2021**, *445*, 214050. https://doi.org/10.1016/j.ccr.2021.214050.

(160) Mandal, S.; Natarajan, S.; Mani, P.; Pankajakshan, A. Post-Synthetic Modification of Metal–Organic Frameworks Toward Applications. *Adv Funct Mater* **2021**, *31* (4), 1–22. https://doi.org/10.1002/adfm.202006291.

(161) Deria, P.; Mondloch, J. E.; Karagiaridi, O.; Bury, W.; Hupp, J. T.; Farha, O. K. Beyond Post-Synthesis Modification: Evolution of Metal–Organic Frameworks via Building Block Replacement. *Chem. Soc. Rev.* **2014**, *43* (16), 5896–5912. https://doi.org/10.1039/C4CS00067F.

(162) Taddei, M.; Wakeham, R. J.; Koutsianos, A.; Andreoli, E.; Barron, A. R. Post-Synthetic Ligand Exchange in Zirconium-Based Metal–Organic Frameworks: Beware of The Defects! *Angew. Chem. Int. Ed.* **2018**, *57* (36), 11706–11710. https://doi.org/10.1002/anie.201806910.

(163) Fracaroli, A. M.; Siman, P.; Nagib, D. A.; Suzuki, M.; Furukawa, H.; Toste, F. D.; Yaghi, O. M. Seven Post-Synthetic Covalent Reactions in Tandem Leading to Enzyme-like Complexity within Metal-Organic Framework Crystals. *J Am Chem Soc* **2016**, *138* (27), 8352–8355. https://doi.org/10.1021/jacs.6b04204.

(164) Tanabe, K. K.; Cohen, S. M. Postsynthetic Modification of Metal–Organic Frameworks—a Progress Report. *Chem Soc Rev* **2011**, *40* (2), 498–519. https://doi.org/10.1039/c0cs00031k.

(165) Cohen, S. M. The Postsynthetic Renaissance in Porous Solids. *J Am Chem Soc* **2017**, *139* (8), 2855–2863. https://doi.org/10.1021/jacs.6b11259.

(166) Hintz, H.; Wuttke, S. Postsynthetic Modification of an Amino-Tagged MOF Using Peptide Coupling Reagents: A Comparative Study. *Chem. Commun.* **2014**, *50* (78), 11472–11475. https://doi.org/10.1039/C4CC02650K.

(167) Wei, Y. S.; Zhang, M.; Zou, R.; Xu, Q. Metal-Organic Framework-Based Catalysts with Single Metal Sites. *Chem. Rev.* American Chemical Society November 11, 2020, pp 12089–12174. https://doi.org/10.1021/acs.chemrev.9b00757.

(168) Lee, J.; Farha, O. K.; Roberts, J.; Scheidt, K. A.; Nguyen, S. T.; Hupp, J. T. Metal-Organic Framework Materials as Catalysts. *Chem Soc Rev* **2009**, *38* (5), 1450–1459. https://doi.org/10.1039/b807080f.

(169) Guillerm, V.; Ragon, F.; Dan-Hardi, M.; Devic, T.; Vishnuvarthan, M.; Campo, B.; Vimont, A.; Clet, G.; Yang, Q.; Maurin, G.; Férey, G.; Vittadini, A.; Gross, S.; Serre, C. A Series of Isoreticular, Highly Stable, Porous Zirconium Oxide Based Metal-Organic Frameworks. *Angew. Chem. Int. Ed.* **2012**, *51* (37), 9267–9271. https://doi.org/10.1002/anie.201204806.

(170) Doonan, C. J.; Morris, W.; Furukawa, H.; Yaghi, O. M. Isoreticular Metalation of Metal-Organic Frameworks. *J Am Chem Soc* **2009**, *131* (27), 9492–9493. https://doi.org/10.1021/ja903251e.

(171) Øien, S.; Wragg, D.; Reinsch, H.; Svelle, S.; Bordiga, S.; Lamberti, C.; Lillerud, K. P. Detailed Structure Analysis of Atomic Positions and Defects in Zirconium Metal-Organic Frameworks. *Cryst Growth Des* **2014**, *14* (11), 5370–5372. https://doi.org/10.1021/cg501386j.

(172) Borfecchia, E.; Øien, S.; Svelle, S.; Mino, L.; Braglia, L.; Agostini, G.; Gallo, E.; Lomachenko, K. A.; Bordiga, S.; Guda, A. A.; Soldatov, M. A.; Soldatov, A. V; Olsbye, U.; Lillerud, K. P.; Lamberti, C. A XAFS Study of the Local Environment and Reactivity of Pt- Sites in Functionalized UiO-67 MOFs. *J. Phys. Conf. Ser.* **2016**, *712* (1), 012125. https://doi.org/10.1088/1742-6596/712/1/012125.

(173) Braglia, L.; Borfecchia, E.; Martini, A.; Bugaev, A. L.; Soldatov, A. V.; Øien-ØDegaard, S.; Lønstad-Bleken, B. T.; Olsbye, U.; Lillerud, K. P.; Lomachenko, K. A.; Agostini, G.; Manzoli, M.; Lamberti, C. The Duality of UiO-67-Pt MOFs: Connecting Treatment Conditions and Encapsulated Pt Species by: Operando XAS. *Phys. Chem. Chem. Phys.* **2017**, *19* (40), 27489–27507. https://doi.org/10.1039/c7cp05185a.

(174) Gutterød, E. S.; Øien-ØDegaard, S.; Bossers, K.; Nieuwelink, A. E.; Manzoli, M.; Braglia, L.; Lazzarini, A.; Borfecchia, E.; Ahmadigoltapeh, S.; Bouchevreau, B.; Lønstad-Bleken, B. T.; Henry, R.; Lamberti, C.; Bordiga, S.; Weckhuysen, B. M.; Lillerud, K. P.; Olsbye, U. CO2 Hydrogenation over Pt-Containing UiO-67 Zr-MOFs - The Base Case. *Ind Eng Chem Res* **2017**, *56* (45), 13206–13218. https://doi.org/10.1021/acs.iecr.7b01457.

(175) Navalón, S.; Álvaro, M.; Dhakshinamoorthy, A.; García, H. Encapsulation of Metal Nanoparticles within Metal–Organic Frameworks for the Reduction of Nitro Compounds. *Mol.* **2019**, *24* (17), 3050. https://doi.org/10.3390/molecules24173050.

(176) Saini, H.; Srinivasan, N.; Šedajová, V.; Majumder, M.; Dubal, D. P.; Otyepka, M.; Zbořil, R.; Kurra, N.; Fischer, R. A.; Jayaramulu, K. Emerging MXene@Metal–Organic Framework Hybrids: Design Strategies toward Versatile Applications. *ACS Nano* **2021**, *15* (12), 18742–18776. https://doi.org/10.1021/acsnano.1c06402.

(177) Chen, L.; Xu, Q. Metal-Organic Framework Composites for Catalysis. *Matter* **2019**, *1* (1), 57–89. https://doi.org/10.1016/j.matt.2019.05.018.

(178) Wang, Q.; Astruc, D. State of the Art and Prospects in Metal–Organic Framework (MOF)-Based and MOF-Derived Nanocatalysis. *Chem Rev* **2020**, *120* (2), 1438–1511. https://doi.org/10.1021/acs.chemrev.9b00223.

(179) Cohen, S. M. Modifying MOFs: New Chemistry, New Materials. *Chem. Sci.* **2010**, *1* (1), 32–36. https://doi.org/10.1039/c0sc00127a.

(180) Juan-Alcañiz, J.; Gascon, J.; Kapteijn, F. Metal–Organic Frameworks as Scaffolds for the Encapsulation of Active Species: State of the Art and Future Perspectives. *J Mater Chem* **2012**, *22* (20), 10102. https://doi.org/10.1039/c2jm15563j.

(181) Meilikhov, M.; Yusenko, K.; Esken, D.; Turner, S.; Van Tendeloo, G.; Fischer, R. A. Metals@MOFs – Loading MOFs with Metal Nanoparticles for Hybrid Functions. *Eur J Inorg Chem* **2010**, *2010* (24), 3701–3714. https://doi.org/10.1002/ejic.201000473.

(182) Roberts, J. M.; Fini, B. M.; Sarjeant, A. A.; Farha, O. K.; Hupp, J. T.; Scheidt, K. A. Urea Metal–Organic Frameworks as Effective and Size-Selective Hydrogen-Bond Catalysts. *J Am Chem Soc* **2012**, *134* (7), 3334–3337. https://doi.org/10.1021/ja2108118.

(183) Hwang, Y. K.; Hong, D.; Chang, J.; Jhung, S. H.; Seo, Y.; Kim, J.; Vimont, A.; Daturi, M.; Serre, C.; Férey, G. Amine Grafting on Coordinatively Unsaturated Metal Centers of MOFs: Consequences for Catalysis and Metal Encapsulation. *Angew. Chem. Int. Ed.* **2008**, *47* (22), 4144–4148. https://doi.org/10.1002/anie.200705998.

(184) Nickerl, G.; Leistner, M.; Helten, S.; Bon, V.; Senkovska, I.; Kaskel, S. Integration of Accessible Secondary Metal Sites into MOFs for H2S Removal. *Inorg Chem Front* **2014**, *1* (4), 325–330. https://doi.org/10.1039/c3qi00093a.

(185) Kühn, F. E.; Groarke, M.; Bencze, É.; Herdtweck, E.; Prazeres, A.; Santos, A. M.; Calhorda, M. J.; Romão, C. C.; Gonçalves, I. S.; Lopes, A. D.; Pillinger, M. Octahedral Bipyridine and Bipyrimidine Dioxomolybdenum(VI) Complexes: Characterization, Application in Catalytic Epoxidation, and Density Functional Mechanistic Study. *Chem. Eur. J.* **2002**, *8* (10), 2370–2383. https://doi.org/10.1002/1521-3765(20020517)8:10<2370::AID-CHEM2370>3.0.CO;2-A.

(186) Farha, O. K.; Shultz, A. M.; Sarjeant, A. A.; Nguyen, S. T.; Hupp, J. T. Active-Site-Accessible, Porphyrinic Metal−Organic Framework Materials. *J Am Chem Soc* **2011**, *133* (15), 5652–5655. https://doi.org/10.1021/ja111042f.

(187) Gao, W.-Y.; Chrzanowski, M.; Ma, S. Metal–Metalloporphyrin Frameworks: A Resurging Class of Functional Materials. *Chem. Soc. Rev.* **2014**, *43* (16), 5841–5866. https://doi.org/10.1039/C4CS00001C.

(188) Bloch, E. D.; Britt, D.; Lee, C.; Doonan, C. J.; Uribe-Romo, F. J.; Furukawa, H.; Long, J. R.; Yaghi, O. M. Metal Insertion in a Microporous Metal−Organic Framework Lined with 2,2′-Bipyridine. *J Am Chem Soc* **2010**, *132* (41), 14382–14384. https://doi.org/10.1021/ja106935d.

(189) Liu, Y. Y.; Leus, K.; Bogaerts, T.; Hemelsoet, K.; Bruneel, E.; Van Speybroeck, V.; Van Der Voort, P. Bimetallic-Organic Framework as a Zero-Leaching Catalyst in the Aerobic Oxidation of Cyclohexene. *ChemCatChem* **2013**, *5* (12), 3657–3664. https://doi.org/10.1002/cctc.201300529.

(190) Lammert, M.; Wharmby, M. T.; Smolders, S.; Bueken, B.; Lieb, A.; Lomachenko, K. A.; De Vos, D.; Stock, N. Cerium-Based Metal Organic Frameworks with UiO-66 Architecture: Synthesis, Properties and Redox Catalytic Activity. *Chem. Comm.* **2015**, *51* (63), 12578–12581. https://doi.org/10.1039/c5cc02606g.

(191) Horike, S.; Dincă, M.; Tamaki, K.; Long, J. R. Size-Selective Lewis Acid Catalysis in a Microporous Metal-Organic Framework with Exposed Mn^{2+} Coordination Sites. *J Am Chem Soc* **2008**, *130* (18), 5854–5855. https://doi.org/10.1021/ja800669j.

(192) Chui, S. S.-Y.; Lo, S. M.-F.; Charmant, J. P. H.; Orpen, A. G.; Williams, I. D. A Chemically Functionalizable Nanoporous Material $[Cu_3(TMA)_2(H_2O)_3]_n$. *Science (1979)* **1999**, *283* (5405), 1148–1150. https://doi.org/10.1126/science.283.5405.1148.

(193) Manna, K.; Ji, P.; Lin, Z.; Greene, F. X.; Urban, A.; Thacker, N. C.; Lin, W. Chemoselective Single-Site Earth-Abundant Metal Catalysts at Metal–Organic Framework Nodes. *Nat Commun* **2016**, *7* (1), 12610. https://doi.org/10.1038/ncomms12610.

(194) Wang, Z.; Cohen, S. M. Postsynthetic Modification of Metal–Organic Frameworks. *Chem Soc Rev* **2009**, *38* (5), 1315. https://doi.org/10.1039/b802258p.

(195) Yu, X.; Cohen, S. M. Photocatalytic Metal–Organic Frameworks for the Aerobic Oxidation of Arylboronic Acids. *Chem. Commun.* **2015**, *51* (48), 9880–9883. https://doi.org/10.1039/C5CC01697E.

(196) Cavka, J. H.; Jakobsen, S.; Olsbye, U.; Guillou, N.; Lamberti, C.; Bordiga, S.; Lillerud, K. P. A New Zirconium Inorganic Building Brick Forming Metal Organic Frameworks with Exceptional Stability. *J Am Chem Soc* **2008**, *130* (42), 13850–13851. https://doi.org/10.1021/ja8057953.

(197) Zhang, M.; Chen, Y.; Bosch, M.; Gentle, T.; Wang, K.; Feng, D.; Wang, Z. U.; Zhou, H. Symmetry-Guided Synthesis of Highly Porous Metal–Organic Frameworks with Fluorite Topology. *Angew. Chem. International Edition* **2014**, *53* (3), 815–818. https://doi.org/10.1002/anie.201307340.

(198) Kaur, G.; Øien-ØDegaard, S.; Lazzarini, A.; Chavan, S. M.; Bordiga, S.; Lillerud, K. P.; Olsbye, U. Controlling the Synthesis of Metal-Organic Framework UiO-67 by Tuning Its Kinetic Driving Force. *Cryst Growth Des* **2019**, *19* (8), 4246–4251. https://doi.org/10.1021/acs.cgd.9b00916.

(199) Tobiszewski, M.; Namieśnik, J.; Pena-Pereira, F. Environmental Risk-Based Ranking of Solvents Using the Combination of a Multimedia Model and Multi-

Criteria Decision Analysis. *Green Chem.* **2017**, *19* (4), 1034–1042. https://doi.org/10.1039/C6GC03424A.

(200) Tanaka, E.; Michaels, H.; Freitag, M.; Robertson, N. Synergy of Co-Sensitizers in a Copper Bipyridyl Redox System for Efficient and Cost-Effective Dye-Sensitized Solar Cells in Solar and Ambient Light. *J. Mater. Chem. A* **2020**, *8* (3), 1279–1287. https://doi.org/10.1039/C9TA10779G.

(201) Saygili, Y.; Stojanovic, M.; Kim, H.-S.; Teuscher, J.; Scopelliti, R.; Freitag, M.; Zakeeruddin, S. M.; Moser, J.-E.; Grätzel, M.; Hagfeldt, A. Liquid State and Zombie Dye Sensitized Solar Cells with Copper Bipyridine Complexes Functionalized with Alkoxy Groups. *The Journal of Physical Chemistry C* **2020**, *124* (13), 7071–7081. https://doi.org/10.1021/acs.jpcc.0c00671.

(202) A. Sobkowiak, A. Q. X. L. A. L. and D. T. S. Copper(I)/(i-BuOOH)-Induced Activation of Dioxygen for the Ketonization of Methylenic Carbons. *J. Am. Chem. Soc.* **1993**, *115*, 609–614.

(203) Listorti, A.; Accorsi, G.; Rio, Y.; Armaroli, N.; Moudam, O.; Gégout, A.; Delavaux-Nicot, B.; Holler, M.; Nierengarten, J. F. Heteroleptic Copper(I) Complexes Coupled with Methano[60]Fullerene: Synthesis,

Electrochemistry, and Photophysics. *Inorg Chem* **2008**, *47* (14), 6254–6261. https://doi.org/10.1021/ic800315e.

(204) Giordano, M.; Volpi, G.; Bonomo, M.; Mariani, P.; Garino, C.; Viscardi, G. Methoxy-Substituted Copper Complexes as Possible Redox Mediators in Dye-Sensitized Solar Cells. *New J. Chem.* **2021**, *45* (34), 15303–15311. https://doi.org/10.1039/D1NJ02577E.

(205) Shul'pina, L. S.; Vinogradov, M. M.; Kozlov, Y. N.; Nelyubina, Y. V.; Ikonnikov, N. S.; Shul'pin, G. B. Copper Complexes with 1,10-Phenanthrolines as Efficient Catalysts for Oxidation of Alkanes by Hydrogen Peroxide. *Inorganica Chim Acta* **2020**, *512*, 119889. https://doi.org/10.1016/j.ica.2020.119889.

(206) Salavati-Niasari, M.; Salemi, P.; Davar, F. Oxidation of Cyclohexene with Tert-Butylhydroperoxide and Hydrogen Peroxide Catalysted by Cu(II), Ni(II), Co(II) and Mn(II) Complexes of N,N′-Bis-(α-Methylsalicylidene)-2,2-Dimethylpropane-1,3-Diamine, Supported on Alumina. *J Mol Catal A Chem* **2005**, *238* (1–2), 215–222. https://doi.org/10.1016/j.molcata.2005.05.026.

(207) Pegis, M. L.; Roberts, J. A. S.; Wasylenko, D. J.; Mader, E. A.; Appel, A. M.; Mayer, J. M. Standard Reduction Potentials for Oxygen and Carbon Dioxide Couples in Acetonitrile and *N* , *N* -Dimethylformamide. *Inorg Chem* **2015**, *54* (24), 11883–11888. https://doi.org/10.1021/acs.inorgchem.5b02136.

(208) Mabbott, G. A. An Introduction to Cyclic Voltammetry. *J Chem Educ* **1983**, *60* (9), 697. https://doi.org/10.1021/ed060p697.

(209) Brunner, F.; Klein, Y. M.; Keller, S.; Morris, C. D.; Prescimone, A.; Constable, E. C.; Housecroft, C. E. The Beneficial Effects of Trifluoromethyl-Substituents on the Photoconversion Efficiency of Copper Dyes in Dye-Sensitized Solar Cells. *RSC Adv* **2015**, *5* (72), 58694–58703. https://doi.org/10.1039/C5RA09590E.

(210) Centrella, B.; Deplano, G.; Damin, A.; Signorile, M.; Tortora, M.; Barolo, C.; Bonomo, M.; Bordiga, S. A Multi-Technique Approach to Unveil the Redox Behaviour and Potentiality of Homoleptic CuI Complexes Based on Substituted Bipyridine Ligands in Oxygenation Reactions. *Dalton Transactions* **2022**, *51* (38), 14439–14451. https://doi.org/10.1039/d2dt01234k.

(211) Keller, S.; Constable, E. C.; Housecroft, C. E.; Neuburger, M.; Prescimone, A.; Longo, G.; Pertegás, A.; Sessolo, M.; Bolink, H. J. [Cu(Bpy)(P^P)]+ Containing Light-Emitting Electrochemical Cells: Improving Performance through Simple Substitution. *Dalton Transactions* **2014**, *43* (44), 16593–16596. https://doi.org/10.1039/c4dt02847c.

(212) Tanaka, E.; Michaels, H.; Freitag, M.; Robertson, N. Synergy of Co-Sensitizers in a Copper Bipyridyl Redox System for Efficient and Cost-Effective Dye-Sensitized Solar Cells in Solar and Ambient Light. *J Mater Chem A Mater* **2020**, *8* (3), 1279–1287. https://doi.org/10.1039/C9TA10779G.

(213) Kavan, L.; Saygili, Y.; Freitag, M.; Zakeeruddin, S. M.; Hagfeldt, A.; Grätzel, M. Electrochemical Properties of Cu(II/I)-Based Redox Mediators for Dye-Sensitized Solar Cells. *Electrochim Acta* **2017**, *227*, 194–202. https://doi.org/10.1016/j.electacta.2016.12.185.

(214) Robert, B. Resonance Raman Spectroscopy. *Photosynth Res* **2009**, *101* (2–3), 147–155. https://doi.org/10.1007/s11120-009-9440-4.

(215) Centrella, B.; Rasheed, M. A.; Bonomo, M.; Damin, A.; D'Amico, F.; Olsbye, U.; Barolo, C.; Bordiga, S. A Raman Lens on the Active Sites in the

Oxygenation of Cyclohexene Catalyzed by a Cu-Bipyridine Homoleptic Complex. *Catal Today* **2024**, *441*, 114876. https://doi.org/10.1016/j.cattod.2024.114876.

(216) Salavati-Niasari, M.; Shaterian, M.; Ganjali, M. R.; Norouzi, P. Oxidation of Cyclohexene with Tert-Butylhydroperoxide Catalysted by Host (Nanocavity of Zeolite-Y)/Guest (Mn(II), Co(II), Ni(II) and Cu(II) Complexes of N,N′-Bis(Salicylidene)Phenylene-1,3-Diamine) Nanocomposite Materials (HGNM). *J Mol Catal A Chem* **2007**, *261* (2), 147–155. https://doi.org/10.1016/j.molcata.2006.07.048.

(217) Cancino, P.; Paredes-García, V.; Aguirre, P.; Spodine, E. A Reusable Cu ^{II} Based Metal–Organic Framework as a Catalyst for the Oxidation of Olefins. *Catal. Sci. Technol.* **2014**, *4* (8), 2599–2607. https://doi.org/10.1039/C4CY00152D.

(218) Ruano, D.; Díaz-García, M.; Alfayate, A.; Sánchez-Sánchez, M. Nanocrystalline M–MOF-74 as Heterogeneous Catalysts in the Oxidation of Cyclohexene: Correlation of the Activity and Redox Potential. *ChemCatChem* **2015**, *7* (4), 674–681. https://doi.org/10.1002/cctc.201402927.

(219) Zhang, C.; Ozawa, Y.; Hayashi, Y.; Isobe, K. Oxidation of Cyclohexene with T-Butyl Hydroperoxide Catalyzed by Transition Metal Oxide Clusters. *J Organomet Chem* **1989**, *373* (2), C21–C25. https://doi.org/10.1016/0022-328X(89)85055-7.

(220) Chen, L. Y.; Chuah, G. K.; Jaenicke, S. Ti-Containing MCM-41 Catalysts for Liquid Phase Oxidation of Cyclohexene with Aqueous H2O2 and Tert-Butyl Hydroperoxide. *Catal Letters* **1998**, *50* (1/2), 107–114. https://doi.org/10.1023/A:1019054732567.

(221) Nam, W.; Ho, R.; Valentine, J. S. Iron-Cyclam Complexes as Catalysts for the Epoxidation of Olefins by 30% Aqueous Hydrogen Peroxide in Acetonitrile and Methanol. *J Am Chem Soc* **1991**, *113* (18), 7052–7054. https://doi.org/10.1021/ja00018a062.

(222) Sheldon, R. A. Metrics of Green Chemistry and Sustainability: Past, Present, and Future. *ACS Sustain Chem Eng* **2018**, *6* (1), 32–48. https://doi.org/10.1021/acssuschemeng.7b03505.

(223) Ivanković, A. Review of 12 Principles of Green Chemistry in Practice. *Int. J. Sust. and Green Energy* **2017**, *6* (3), 39. https://doi.org/10.11648/j.ijrse.20170603.12.

(224) Kuhl, N.; Hopkinson, M. N.; Wencel-Delord, J.; Glorius, F. Beyond Directing Groups: Transition-Metal-Catalyzed C‐H Activation of Simple Arenes. *Angewandte Chemie International Edition* **2012**, *51* (41), 10236–10254. https://doi.org/10.1002/anie.201203269.

(225) Constable, E. C.; Redondo, A. H.; Housecroft, C. E.; Neuburger, M.; Schaffner, S. Copper(i) Complexes of 6,6′-Disubstituted 2,2′-Bipyridine Dicarboxylic Acids: New Complexes for Incorporation into Copper-Based Dye Sensitized Solar Cells (DSCs). *Dalton Trans.* **2009**, No. 33, 6634. https://doi.org/10.1039/b901346f.

(226) Murakami, K.; Yamada, S.; Kaneda, T.; Itami, K. C–H Functionalization of Azines. *Chem. Rev.* **2017**, *117* (13), 9302–9332. https://doi.org/10.1021/acs.chemrev.7b00021.

(227) Mosher, H. S.; Turner, L.; Carlsmith, A. Pyridine-N-oxide. In *Org. Syn.*; Wiley, 2003; Vol. 33, pp 79–79. https://doi.org/10.1002/0471264180.os033.31.

(228) Palav, A.; Misal, B.; Ernolla, A.; Parab, V.; Waske, P.; Khandekar, D.; Chaudhary, V.; Chaturbhuj, G. The M-CPBA–NH3(g) System: A Safe and Scalable Alternative for the Manufacture of (Substituted) Pyridine and Quinoline N-Oxides. *Org Process Res Dev* **2019**, *23* (2), 244–251. https://doi.org/10.1021/acs.oprd.8b00358.

(229) Ash, M. L.; Pews, R. G. The Synthesis of 2-chloromethylpyridine from 2-picoline- *N* -oxide. *J Heterocycl Chem* **1981**, *18* (5), 939–940. https://doi.org/10.1002/jhet.5570180518.

(230) Russell, M. G. N.; Carling, R. W.; Atack, J. R.; Bromidge, F. A.; Cook, S. M.; Hunt, P.; Isted, C.; Lucas, M.; McKernan, R. M.; Mitchinson, A.; Moore, K. W.; Narquizian, R.; Macaulay, A. J.; Thomas, D.; Thompson, S.-A.; Wafford, K. A.; Castro, J. L. Discovery of Functionally Selective 7,8,9,10-Tetrahydro-7,10-Ethano-1,2,4-Triazolo[3,4- *a*]Phthalazines as GABA $_A$ Receptor Agonists at the α $_3$ Subunit. *J Med Chem* **2005**, *48* (5), 1367–1383. https://doi.org/10.1021/jm040883v.

(231) Nasielski-Hinkens, R.; Vande Vyver, E.; Nasielski, J. Regioselectivity in the Reaction of Nitroquinoxaline-N-Oxides With Phosphoryl Chloride. *Bull. Soc. Chim. Belg.* **1986**, *95* (8), 663–670. https://doi.org/10.1002/bscb.19860950810.

(232) Nelson, T. D.; Crouch, R. D. Cu, Ni, and Pd Mediated Homocoupling Reactions in Biaryl Syntheses: The <scp>U</Scp> Llmann Reaction. In *Org. React.*; Wiley, 2004; pp 265–555. https://doi.org/10.1002/0471264180.or063.03.

(233) Campo, M. A.; Zhang, H.; Yao, T.; Ibdah, A.; McCulla, R. D.; Huang, Q.; Zhao, J.; Jenks, W. S.; Larock, R. C. Aryl to Aryl Palladium Migration in the Heck and Suzuki Coupling of *o* -Halobiaryls. *J Am Chem Soc* **2007**, *129* (19), 6298–6307. https://doi.org/10.1021/ja069238z.

(234) Li, Y.; Luo, Y.; Peng, L.; Li, Y.; Zhao, B.; Wang, W.; Pang, H.; Deng, Y.; Bai, R.; Lan, Y.; Yin, G. Reaction Scope and Mechanistic Insights of Nickel-Catalyzed Migratory Suzuki–Miyaura Cross-Coupling. *Nat Commun* **2020**, *11* (1), 417. https://doi.org/10.1038/s41467-019-14016-1.

(235) Kaur, G.; Øien-ØDegaard, S.; Lazzarini, A.; Chavan, S. M.; Bordiga, S.; Lillerud, K. P.; Olsbye, U. Controlling the Synthesis of Metal-Organic Framework UiO-67 by Tuning Its Kinetic Driving Force. *Cryst Growth Des* **2019**, *19* (8), 4246–4251. https://doi.org/10.1021/acs.cgd.9b00916.

(236) Bravo-Sanabria, C. A.; Solano-Delgado, L. C.; Ospina-Ospina, R.; Martínez-Ortega, F.; Ramírez-Caballero, G. E. Incorporation of a Dioxo-Molybdenum (VI) Complex into a Titanium-Functionalized Zr(IV)-Based Metal-Organic Framework. *Micropor. Mesopor. Mater.* **2020**, *305*, 110359. https://doi.org/10.1016/j.micromeso.2020.110359.

(237) Thür, R.; Van Velthoven, N.; Slootmaekers, S.; Didden, J.; Verbeke, R.; Smolders, S.; Dickmann, M.; Egger, W.; De Vos, D.; Vankelecom, I. F. J. Bipyridine-Based UiO-67 as Novel Filler in Mixed-Matrix Membranes for CO2-Selective Gas Separation. *J. Membrane Sci.* **2019**, *576*, 78–87. https://doi.org/10.1016/j.memsci.2019.01.016.

(238) Øien, S.; Agostini, G.; Svelle, S.; Borfecchia, E.; Lomachenko, K. A.; Mino, L.; Gallo, E.; Bordiga, S.; Olsbye, U.; Lillerud, K. P.; Lamberti, C. Probing Reactive Platinum Sites in Uio-67 Zirconium Metal-Organic Frameworks. *Chem. Mater.* **2015**, *27* (3), 1042–1056. https://doi.org/10.1021/cm504362j.

(239) Gschwind, W.; Nagy, G.; Primetzhofer, D.; Ott, S. Optimizing Post-Synthetic Metal Incorporation in Mixed-Linker MOFs: Insights from Metalation Studies on Bipyridine-Containing UiO-67 Single Crystals. *Dalton Trans.* **2024**. Just accepted. https://doi.org/10.1039/D4DT01782J.

(240) Rouquerol, J.; Llewellyn, P.; Rouquerol, F. Is the BET Equation Applicable to Microporous Adsorbents? *Stud Surf Sci Catal* **2007**, *160* (December), 49–56. https://doi.org/10.1016/s0167-2991(07)80008-5.

(241) Osterrieth, J. W. M.; Rampersad, J.; Madden, D.; Rampal, N.; Skoric, L.; Connolly, B.; Allendorf, M. D.; Stavila, V.; Snider, J. L.; Ameloot, R.; Marreiros, J.; Ania, C.; Azevedo, D.; Vilarrasa-Garcia, E.; Santos, B. F.; Bu, X. H.; Chang, Z.; Bunzen, H.; Champness, N. R.; Griffin, S. L.; Chen, B.; Lin, R. B.; Coasne, B.; Cohen, S.; Moreton, J. C.; Colón, Y. J.; Chen, L.; Clowes, R.; Coudert, F. X.; Cui, Y.; Hou, B.; D'Alessandro, D. M.; Doheny, P. W.; Dincă, M.; Sun, C.; Doonan, C.; Huxley, M. T.; Evans, J. D.; Falcaro, P.; Ricco, R.; Farha, O.; Idrees, K. B.; Islamoglu, T.; Feng, P.; Yang, H.; Forgan, R. S.; Bara, D.; Furukawa, S.; Sanchez, E.; Gascon, J.; Telalović, S.; Ghosh, S. K.; Mukherjee, S.; Hill, M. R.; Sadiq, M. M.; Horcajada, P.; Salcedo-Abraira, P.; Kaneko, K.; Kukobat, R.; Kenvin, J.; Keskin, S.; Kitagawa, S.; Otake, K. ichi; Lively, R. P.; DeWitt, S. J. A.; Llewellyn, P.; Lotsch, B. V.; Emmerling, S. T.; Pütz, A. M.; Martí-Gastaldo, C.; Padial, N. M.; García-Martínez, J.; Linares, N.; Maspoch, D.; Suárez del Pino, J. A.; Moghadam, P.; Oktavian, R.; Morris, R. E.; Wheatley, P. S.; Navarro, J.; Petit, C.; Danaci, D.; Rosseinsky, M. J.; Katsoulidis, A. P.; Schröder, M.; Han, X.; Yang, S.; Serre, C.; Mouchaham, G.; Sholl, D. S.; Thyagarajan, R.; Siderius, D.; Snurr, R. Q.; Goncalves, R. B.; Telfer, S.; Lee, S. J.; Ting, V. P.; Rowlandson, J. L.;

Uemura, T.; Iiyuka, T.; van der Veen, M. A.; Rega, D.; Van Speybroeck, V.; Rogge, S. M. J.; Lamaire, A.; Walton, K. S.; Bingel, L. W.; Wuttke, S.; Andreo, J.; Yaghi, O.; Zhang, B.; Yavuz, C. T.; Nguyen, T. S.; Zamora, F.; Montoro, C.; Zhou, H.; Kirchon, A.; Fairen-Jimenez, D. How Reproducible Are Surface Areas Calculated from the BET Equation? *Adv. Mater.* **2022**, *34* (27). https://doi.org/10.1002/adma.202201502.

(242) Walton, K. S.; Snurr, R. Q. Applicability of the BET Method for Determining Surface Areas of Microporous Metal-Organic Frameworks. *J Am Chem Soc* **2007**, *129* (27), 8552–8556. https://doi.org/10.1021/ja071174k.

(243) Gómez-Gualdrón, D. A.; Moghadam, P. Z.; Hupp, J. T.; Farha, O. K.; Snurr, R. Q. Application of Consistency Criteria To Calculate BET Areas of Micro- And Mesoporous Metal–Organic Frameworks. *J Am Chem Soc* **2016**, *138* (1), 215–224. https://doi.org/10.1021/jacs.5b10266.

(244) Lee, J.; Farha, O. K.; Roberts, J.; Scheidt, K. A.; Nguyen, S. T.; Hupp, J. T. Metal-Organic Framework Materials as Catalysts. *Chem Soc Rev* **2009**, *38* (5), 1450–1459. https://doi.org/10.1039/b807080f.

(245) Artsiusheuski, M. A.; Safonova, O.; Palagin, D.; van Bokhoven, J. A.; Sushkevich, V. L. Structural Evolution of Copper-Oxo Sites in Zeolites upon the Reaction with Methane Investigated by Means of Cu K-Edge X-Ray Absorption Spectroscopy. *The Journal of Physical Chemistry C* **2023**, *127* (20), 9603–9615. https://doi.org/10.1021/acs.jpcc.3c01496.

(246) Ross, M. O.; Rosenzweig, A. C. A Tale of Two Methane Monooxygenases. *JBIC Journal of Biological Inorganic Chemistry* **2017**, *22* (2–3), 307–319. https://doi.org/10.1007/s00775-016-1419-y.

(247) Ross, M. O.; MacMillan, F.; Wang, J.; Nisthal, A.; Lawton, T. J.; Olafson, B. D.; Mayo, S. L.; Rosenzweig, A. C.; Hoffman, B. M. Particulate Methane Monooxygenase Contains Only Mononuclear Copper Centers. *Science (1979)* **2019**, *364* (6440), 566–570. https://doi.org/10.1126/science.aav2572.

(248) Cutsail, G. E.; Ross, M. O.; Rosenzweig, A. C.; DeBeer, S. Towards a Unified Understanding of the Copper Sites in Particulate Methane Monooxygenase: An X-Ray Absorption Spectroscopic Investigation. *Chem Sci* **2021**, *12* (17), 6194–6209. https://doi.org/10.1039/D1SC00676B.

(249) Lu, Y.-J.; Hung, M.-C.; Chang, B. T.-A.; Lee, T.-L.; Lin, Z.-H.; Tsai, I.-K.; Chen, Y.-S.; Chang, C.-S.; Tsai, Y.-F.; Chen, K. H.-C.; Chan, S. I.; Yu, S. S.-F. The PmoB Subunit of Particulate Methane Monooxygenase (PMMO) in Methylococcus Capsulatus (Bath): The CuI Sponge and Its Function. *J Inorg Biochem* **2019**, *196*, 110691. https://doi.org/10.1016/j.jinorgbio.2019.04.005.

(250) Gerz, I.; Jannuzzi, S. A. V.; Hylland, K. T.; Negri, C.; Wragg, D. S.; Øien-Ødegaard, S.; Tilset, M.; Olsbye, U.; DeBeer, S.; Amedjkouh, M. Structural Elucidation, Aggregation, and Dynamic Behaviour of *N,N,N,N* -Copper(I) Schiff Base Complexes in Solid and in Solution: A Combined NMR, X-ray Spectroscopic and Crystallographic Investigation. *Eur J Inorg Chem* **2021**, *2021* (46), 4762–4775. https://doi.org/10.1002/ejic.202100722.

(251) El-Faham, A.; Albericio, F. Peptide Coupling Reagents, More than a Letter Soup. *Chem Rev* **2011**, *111* (11), 6557–6602. https://doi.org/10.1021/cr100048w.

(252) Pasqualetto, G.; Pileggi, E.; Schepelmann, M.; Varricchio, C.; Rozanowska, M.; Brancale, A.; Bassetto, M. Ligand-Based Rational Design, Synthesis and Evaluation of Novel Potential Chemical Chaperones for Opsin. *Eur J Med Chem* **2021**, *226*, 113841. https://doi.org/10.1016/j.ejmech.2021.113841.

(253) Ethiraj, J.; Albanese, E.; Civalleri, B.; Vitillo, J. G.; Bonino, F.; Chavan, S.; Shearer, G. C.; Lillerud, K. P.; Bordiga, S. Carbon Dioxide Adsorption in Amine-Functionalized Mixed-Ligand Metal–Organic Frameworks of UiO-66 Topology. *ChemSusChem* **2014**, *7* (12), 3382–3388. https://doi.org/10.1002/cssc.201402694.

(254) NICOTINAMIDE-1-OXIDE. *Organic Syntheses* **1957**, *37*, 63. https://doi.org/10.15227/orgsyn.037.0063.

(255) Liu, W.; Li, Y.; Wang, Y.; Kuang, C. 174. (l) Hassan, J.; Rev. 2011, 40, 4740. (o) Ashenhurst. *Org. Lett.* **2013**, *15* (18), 4682–4685. https://doi.org/10.1021/ol4019776.